Structure of nano-crystalline apatite in bone and bone-analogous materials

Dissertation zur Erlangung des Doktorgrades
an der Fakultät für Geowissenschaften
der Ludwig-Maximilians-Universität München

Vorgelegt von
Balázs Kocsis

München, 09. September, 2020

Erstgutachter: Prof. Dr. Wolfgang W. Schmahl
Zweitgutachter: Prof. Dr. Guntram Jordan
Tag der mündlichen Prüfung: 15.04.2021

"What we observe is not nature itself,
but nature exposed to our method of questioning."
– Werner Heisenberg

Kurzfassung

Das Knochengewebe der Wirbeltiere unterstützt zahlreiche biomechanische Prozesse wie Fortbewegung, Nahrungszerkleinerung oder Atmung und ist gleichzeitig ein wichtiger Teil der physiologischen Prozesse. Das Gewebe besteht größtenteils aus organischem Kollagen und anorganischem Carbonat-Calciumphosphat-Apatit im nanokristallinen Zustand. Aus kristallographischer und mineralogischer Sicht sind die Bildung und der Zustand dieser kristallinen Struktur und ihr Verbund mit dem Kollagen von höchster Relevanz.

In dieser Dissertation wird das Knochenmaterial ex vivo untersucht. Die Probennahme und Vorbereitung ges Materials für die Untersuchung können möglicherweise zu Veränderungen des ursprünglichen Zustands des Knochenmaterials führen. Aus diesem Grund werden verschiedene Veränderungsexperimente durchgeführt, um die kristallographischen und mikrostrukturellen Veränderungen auf der Ebene von Ångstrom bis Nanometern abzubilden. In dieser Studie werden auch Referenzmaterialien aus umweltverändertem Knochenmaterial im archaeologischen Kontext, sowie geologische und synthetisierte knochenanaloge Materialien als Ergänzung für die Veränderungskontextforschung aufgenommen.

Aufgrund des nanokristallinen Zustands des Knochenapatits stoßen die Bewertungsmethoden an ihre Grenzen in Bezug auf die Auflösung kleiner Unterschiede im gemessenen Signal. Die Ergebnisse der kristallographischen und mikrostrukturellen Analyse des Knochenbiominerals und seiner analogen Materialien werden mit Schwerpunkt auf der Charakterisierung des anorganischen nanokristallinen Bestandteils vorgestellt. Der Fokus liegt auf der Interpretation gemessener Röntgenpulverbeugungs- und Schwingungsspektroskopiemuster. Die vorgestellten Ergebnisse zeigen, dass die mikrostrukturellen Parameter von Kristallitgröße (d.h. Größe der kohärent streuenden Domäne) und Microstrain (statistische Variation der Gitterparameter über die Probe) getrennt untersucht werden können. Die Entkopplung der mikrostrukturellen Parameter bei Anwendung der Rietveld-Verfeinerungsmethode könnte aber auch Auswirkungen auf die Interpretation der Ergebnisse haben.

Das erste Kapitel bietet eine Einführung in das Thema des nanokristallinen Carbonat-Calciumphosphat-Apatits im Knochenmaterial von Säugetieren sowie Hintergrundkonzepte, die für die Interpretation der Ergebnisse in den späteren Kapiteln erforderlich sind. Theoretische Aspekte für die angewandten Charakterisierungstechniken umfassen eine heuristische Behandlung der Mikrostrukturanalyse von Röntgenpulverbeugungsmustern, Totalstreuungsmethoden und Schwingungsspektroskopie.

Der Vergleich des Röntgenpulverbeugungsmusters (*X-ray powder diffraction XRPD*) und der Bewertung der Atompaarverteilungsfunktion (*atomic pair distribution function PDF*) verschiedener Knochenmaterialien wird in Kapitel 2 erörtert. Dieses Kapitel befasst sich mit dem Problem der Modellierung kleiner Unterschiede in den Beugungsmustern (Rietveld- und PDF-Anpassung) von Knochenmaterialmessungen. Die Ergebnisse zeigen, dass aus den XRPD-Mustern eine geringe Variation zwischen den Säugetierarten abgeleitet werden kann. Weitere Ergebnisse zeigen, dass die Probenvorbereitung in einigen Fällen leichte Veränderungen hervorrufen kann. Während der Probenvorbereitung für weitere Experimente durchläuft das aus dem lebenden Organismus extrahierte Knochenmaterial mehrere Bearbeitungschritte. Veränderungen könnten durch die chemischen Wasch- und Trocknungsprozesse entstehen.

In Kapitel 3 sind Ergebnisse eigener Softwareentwicklung für die automatisierte Rietveld Verfeinerung demonstriert. Mit der Codeimplementierung kann über die automatisierte Rietveld-Methode systematisch eine größere Anzahl von Beugungsmustern ausgewertet und kristallografische Modellhypothesen verglichen werden. Die Handhabung einer größeren Anzahl von Beugungsmustern stellt eine Herausforderung für eine konsistente und zuverlässige Bewertung dar. Die manuelle Auswertung erhöht die Wahrscheinlichkeit systematischer Fehler durch subjektive Einflüsse und Ergebnis-Streuung durch inkonsistente Verfeinerungs-Strategien. Der Code ermöglicht dagegen das automatisierte Testen und Vergleichen von Verfeinerungsstrategien, sowie das Testen von Strukturhypothesen. Die Reproduzierbarkeit der Bewertungsergebnisse wird durch skriptierte Strategien erreicht, die jeden Verfeinerungsschritt mit Parameterwerten erfassen.

Knochenmaterial verschiedener Spezies, Skelettelemente in ihrem Originalzustand und die Abhängigkeit von der Probenvorbereitung wurden in den Kapiteln eins bis drei erörtert. Parallel zum ursprünglichen Zustand der Kristallite im Knochenmaterial wurden Referenzmaterialien untersucht, die analog zum kristallchemischen und mikrostrukturellen Zustand des nanokristallinen kohlensäurehaltigen Knochenapatits verwendet wurden.

Die Referenzmaterialien sind:

1. umweltverändertes Knochenmaterial (Kapitel 4);
2. geologische Referenzmineralien (Kapitel 5);
3. experimentell veränderter Originalknochen (Kapitel 6);
4. synthetisierte knochenanaloge Materialien (Kapitel 7).

In Kapitel 4 wurden die Referenzmaterialien umweltveränderter Knochenproben im Rahmen anthropologischer Untersuchungen analysiert, um innerhalb einer Forschergruppe ein separates Teilprojekt der Isotopenanalyse zu

unterstützen. Die Isotopenforschung verwendet ausgewählte archaeologische Knochenmaterialproben aus unterschiedlichem archaeologischen Kontext in Bezug auf sowohl archaeologische Kulturstufen als auch geographischem Fundort, der mit unterschiedlichen Böden einhergeht. Zur Ergänzung wurde Calciumphosphat-Apatit geologischen Ursprungs betrachtet und mit anderen Referenzmaterialien verglichen (Kapitel 5).

Experimente zur Veränderung des Knochenmaterials werden in Kapitel 6 beschrieben. Diese Experimentserien haben das Ziel, die Veränderungen der kristallographischen Struktur und Mikrostruktur durch das Wachstum der Calciumphosphat-Apatit-Kristallite nachzuvollziehen. Die Ergebnisse des Experiments bringen mikrostrukturelle und strukturelle Parameter in eine Zeitreihe der Behandlungsdauer unter hydrothermalen Bedingungen und Temperaturreihen des Temperns ein.

Kapitel 7 erweitert die Forschung des nanokristallinen carbonathaltigen Calciumphosphat-Apatits mit synthetisierten knochenanalogen Materialien mit Schwerpunkt auf amorphem Calciumphosphat (ACP) als Vorstufe für die Bildung der nanokristallinen Calciumphosphatphase. Es wurden Synthesewege untersucht, die das Endprodukt als Weiterbearbeitung von ACP aus wässriger Fällung ergeben. Ein zweistufiger Syntheseweg wird festgelegt, um einen Einblick in den Mechanismus der kristallinen Apatitbildung in wässrigem Medium zu erhalten.

Das letzte Kapitel 8 vervollständigt den Rahmen der Arbeit mit einer zusammenfassenden Schlussfolgerung und Vorschlägen für die weitere zukünftige Forschung. Darüber hinaus enthält der Anhang einen Abschnitt mit Einzelheiten zum WPPM-Ansatz (Whole-Powder Pattern Modeling), zum Williamson-Hall-Plot und zum entwickelten Python-Code für die automatisierte Rietveld-Verfeinerung.

Abstract

Bone tissue supports vertebrates in various biomechanical functions such as locomotion, consumption of food, or breathing and it is at the same time an important part of the physiological processes. The tissue is constituted of organic collagen and inorganic carbonate calcium-phosphate apatite in nanocrystalline state. From the crystallographic and mineralogical point of view, the formation and state of this crystalline structure and its entanglement with the collagen are of the highest relevance.

In this thesis, the examined bone material was investigated ex-vivo. The extraction and preparation of samples for analysis could lead to changes in the original state of the bone material. For this reason, various alteration experiments have been carried out to map the crystallographic and microstructural changes on the level from Ångstrom to nanometers. This study also includes reference materials from environmentally altered bone material in an archaeological context, geological materials, as well as synthesized bone-analogous materials as a supplement.

Due to the nanocrystalline state of the bone apatite, the evaluation methods reach their limits in resolving small differences in the measured signal. The results of the crystallographic and microstructural analysis of the bone biomineral and its analogous materials are presented with a focus on the characterization of the inorganic nanocrystalline component. The focus is on the interpretation of measured X-ray powder diffraction and vibration spectroscopy patterns. The presented results show that the microstructural parameters of crystallite size (i.e. size of the coherently diffracting domain) and microstrain (i.e. statistical variations of the lattice parameters across the sample) can be examined separately, but the decoupling can be shown to have effect on the obtained results while applying the Rietveld refinement method on X-ray powder diffraction measurements.

The first chapter provides an introduction to the topic of nanocrystalline carbonated-calcium-phosphate apatite found in bone material of mammals and provides background concepts necessary for the interpretation of the results presented in the later chapters. Theoretical aspects for the applied characterisation techniques are included providing a heuristic treatment of microstructural analysis of X-ray powder diffraction patterns, total scattering methods and vibrational spectroscopy.

Comparison of X-ray powder diffraction pattern and atomic pair distribution function evaluation of various bone materials is discussed in Chapter 2. The chapter is focused on the problem of the possibility to model (Rietveld and PDF fit) small differences in the diffraction patterns of bone material. The results show that small interspecies variation can be inferred from the XRPD patterns. During the sample

preparation for further experiments, the bone material that is extracted from the living organism undergoes processes of chemical washing and drying. The results show that in some cases the preparation method may introduce alterations.

In Chapter 3 results of own software development is demonstrated that utilizes the Rietveld methods in an automated fashion. With the code implementation it is possible to systematically evaluate a larger number of diffraction patterns and compare crystallographic model hypotheses. Handling a larger number of diffraction patterns is a challenge for a consistent and reliable evaluation. Manual evaluation rises the probability of systematic errors due to subjective influences and scatter of results due to inconsistent refinement strategies. The code, however, enables consistent testing and comparison of different refinement strategies, as well as structural hypothesis testing in an automated manner. Reproducibility of the evaluation results is achieved via scripted refinement strategies that capture each refinement step with parameter values.

The original bone material of different species, skeletal elements and sample preparation dependence has been discussed in the first three chapters. In order to put the results in context reference materials have been added to the research. The reference materials have been investigated in parallel to the original state of the crystallites in bone material as analogue for the understanding of the crystal-chemical and microstructural state of the nanocrystalline carbonated bone apatite. The reference materials are:

1. environmentally altered bone material (Chapter 4);
2. geological minerals of reference (Chapter 5);
3. experimentally altered original bone (Chapter 6);
4. synthesized bone-analogous materials (Chapter 7).

In Chapter 4 the reference materials of environmentally modified bone samples were analysed as part of anthropological studies in order to support a separate project in a *Forschergruppe* which was dedicated to isotope analysis. The research used selected bone material samples from an archaeological context that originate from different cultural epochs and different geographical areas with different soil conditions. In addition, calcium-phosphate-apatite of geological origin was considered and compared with other reference materials (Chapter 5).

In Chapter 6 the results of bone material alteration experiments are described. The aim of these series of experiments is to understand the changes in the crystallographic structure and microstructure due to the growth of the calcium phosphate-apatite crystallites. The results of the experiment bring microstructural and structural parameters into a time series of the treatment duration under hydrothermal conditions and temperature series of the annealing (cremation) processes.

Chapter 7 extends the research of the nanocrystalline carbonated-calcium-phosphate apatite with synthesized bone-analogous materials with a focus on amorphous calcium phosphate (ACP) as a precursor for the formation of the nanocrystalline calcium phosphate phase. Synthesis routes were investigated that resulted in nanocrystalline bone analogous calcium-phosphate apatite by post processing of ACP, which was originally obtained from aqueous precipitation. A two-step synthesis route is established in order to gain an insight into the mechanism of crystalline apatite formation in an aqueous medium.

The last Chapter 8 completes the frame of the thesis with a concluding discussion and sugestions for further future research. In addition, details of WPPM (whole-powder pattern modelling) approach, Williamson-Hall plot and the developed python code for automated Rietveld refinement are included in the appendix section.

List of abbreviations

ACP	amorphous calcium phosphate
C-Ap	carbonate bearing calcium-phosphate apatite
CCP	carbonated calcium-phosphate with hydroxylapatite structure
DFT	density functional theorem
HAP	hydroxylapatite
FAP	fluorapatite
FTIR	Fourier transform infrared spectroscopy
FWHM	full width at half maximum
LRO	Long -range order
NMR	Nuclear magnetic resonance
OCP	octa-calcium-phosphate structure
PDF	Pair distribution function (atomic pair distribution function)
RS	Raman spectroscopy
SRO	Short-range order
TEM	Transmission electron microscopy
XRPD	X-ray powder diffraction
WA	Warren-Averbach
WH	Williamson-Hall
WPPF	whole powder pattern fitting
WPPM	whole powder pattern modelling

Content

Chapter 1
Introduction

1.1 Context and general aspects

Biological evolution on Earth resulted in the development of biomineralized tissue of bone. Through the aeons the function of the bone organ was optimized for load bearing and weight support of the organism, and other relevant physiological regulatory functions as well. The bone tissue exhibits a hierarchically organized structure with high complexity ranging from Ångstroms to centimetre length-scales. At the base of the hierarchy reside the entangled collagen fibres and the nanocrystalline carbonated calcium-phophate apatite biomineral. The function of bone composite material, as well as the state of the inorganic nanocrystallites is controlled by genetic, physiological, as well as metabolic processes. Great amount of research is focused on the understanding of the complex bone formation on multiple hierarchical levels. Nevertheless, the focus of this thesis is only on the inorganic part of the bone material, where the bone samples have been investigated ex-vivo.

The objects of the study are various bone samples obtained from different animal species, anatomical skeletal elements, naturally and experimentally altered bone material, as well as synthesised bone analogous materials. In order to examine the properties of the intrinsic bone biomineral it is necessary to extract it from the living organism and preserve it. Therefore, at the time of the examination the bone material is not any more in its native state as the preparation for measurements may introduce potential alterations. Experimental simulation (via synthesis) of the biomineral was included in the research in order to devise a model for the inorganic crystallite structure in the form of bone-analogous material. For this reason bone analogous materials have been synthesised, with the aim to resemble the crystallographic properties of the original inorganic nanocrystallites found in the bone material. Further aims of the synthesis experiments were to examine the relation of the nucleation and growth of the carbonated calcium-phosphate apatite phase. Geological minerals of hydroxylapatite, fluorapatite and carbonated-apatites have been included in the study in order to investigate the coexistence of isostructural phases and incorporated ionic variations in the crystallographic models.

Physical and mechanical properties in general are often related to strain, dislocations, stacking faults, chemical disorder, etc. For example, dislocations and stacking faults can stabilize a certain structure or phases, while chemical disorder or

substitution of elements can give rise to electric and magnetic properties to otherwise neutral configurations. In order to support the weight of the organism, the bone material has to have adequately toughness, which is primarily provided by the nanocrystallites of carbonated calium-phosphate apatite. Therefore, microstructural parameters such as microstrain and the crystallite size (and distribution) are of a great relevance.

In order to get insight about the microstructural and chemical nature of the inorganic crystallites of the bone material, fundamental characterization techniques are usually applied such as X-ray powder diffraction (XRPD), spectroscopic techniques Fourier transform infrared (FTIR) and Raman spectroscopy (RS). Interpretation of the measured data can still produce ambiguous results. Quality of the measured signal (noise ratio, resolution) can be a source of misinterpretation. In the scope of the thesis work emphasis had been given to the interpretation of XRPD reflection broadening effects and peak broadening sources. A combination of methods was applied in order to reinforce the analysis and facilitate accuracy and more complete understanding. Rietveld refinements and the pair distribution function (PDF) analysis was carried out next to the investigation of the relation of spectroscopic peak width and position.

The interpretation of peaks (diffraction and spectroscopic) using structure optimization algorithms strongly depends on the starting conditions (or the “initial guess”) of the structure parameters. A hypothesis of the crystalline structure, space group, phase or vibrational band composition is in any case only the starting point of the evaluation. In the Rietveld refinement, a step-wise approach to optimize crystallographic parameters can be referred to as the 'refinement strategy'. It is comprised of a sequence of steps that leads to a solution for a structure. However, this bears a bias toward preferred solutions as there are no formal ways to do exhaustive search in the parameter space and control the optimization algorithms (Fig1.1).

Figure 1.1: Einstein deriving his famous equation; image by S.Harris

1.2 Biomineralization in bone material

Bone is an example of bio-mineralised tissue. It is a composite of collagen fibres and inorganic nano-meter sized crystallites. These nano-crystallites are chemically identified as carbonated-calcium-phosphate-apatite (CCP) (LeGeros et al., 1968; Legeros et al., 1967), with a hexagonal hydroxylapatite average structure (Ca_{10-x} $[(PO_4)_{6-2x}$ $(CO_3)_{2-x}]$ OH_{2-x} / CO_3) (Wopenka and Pasteris, 2005). A commonly accepted solution for the location of the carbonate group are: (1.) carbonate ions can partially replace the phosphate group (B-type); (2.) and/or OH^- (A-type) (Tonegawa et al., 2010; Wopenka and Pasteris, 2005). Determination of the location of the carbonate group in the bone-apatite structure is not trivial even when combined observation techniques are used (Fleet, 2014).

A significant contribution to the understanding of the structural incorporation of the carbonate CO_3^{2-} position and crystal-chemistry implication has been done by Fleet and co-workers (Fleet and Liu, 2007, 2004) on single crystals of carbonated-HAP, synthesized at high pressure and temperature. However, thorough and meticulous studies of XRPD and FTIR on both synthetic and natural bone material were not able to resolve the preferred carbonate location in the structure (Fleet, 2014).

Octa-calcium phosphate (OCP) was described as a stacked formation of ideally ordered structure of apatite with layers of hydrated non-apatitic calcium-phosphate in-between the layers (Brown, 1962; Brown et al., 1962). The presence and structure of OCP is discussed even in recent literature (Suzuki, 2010). Arellano et al. investigated synthesis routes and characterization of the OCP (Arellano-Jiménez et al., 2009). The stability of the OCP phase was examined through conversion

experiments, notably by Bigi et al, and Xin et al. (Bigi et al., 1990; Xin et al., 2006). Although, discussions about OCP are present in the literature, a conclusive evidence of its relation to the bone calcium-phosphate apatite is still not fabricated.

In strict sense, the calcium-phosphate apatite is hexagonal as an average structure, which is stabilized by alternating the order of the anions in the channel position (anionic column) of the crystal structure (Hughes et al., 1989., Kohn et al., 2002 and references therein). Often the structure of hydroxylapatite is taken as a model for the inorganic nanocrystallites found in bone material. It is believed that in contrary to geological minerals of hydroxylapatite, the biominerals formed in bones are stabilized by the presence of carbonate and/or calcium deficiency in the unit cell (Wopenka and Pasteris, 2005).

The nanocrystallites have a platelet-like habitus (5.8nm x 28nm x 19nm) reported from TEM (Schwarcz et al., 2014). Crystallite sizes in animal bone are regarded to vary in the range of some tens of nano meters depending on the species and skeletal element in question (Currey, 2001). It is debated in literature, whether the shape of a crystallite habitus is needle or platelet-like. The reported differences arose partially due to the applied examination technique. Namely, microscopy based methods report platelet-like crystallites, while diffraction based methods resulted needle-like coherently scattering domains (Kohn et al., 2002 chapter11 p439-440). Furthermore, diffraction methods cannot give information about the habitus of the crystallite directly, but only about the coherent domain lengths.

NMR studies report that the nano crystallites are often presented as a core-shell type material, where the inner crystalline part is constituted of nanometer sized crystalline domains and the outer shell is a water-mediated hydrogen-phosphate (HPO_4^{2-}) layer with no long range order (Wang et al., 2013). This idea appears in the work of Eichert et al. as well (Eichert et al., 2009). Eichert also characterised FTIR spectra of several calcium-phosphates and introduced a notation of "non-apatitic" bands to highlight that the structure at the nano scale has different spectral features relative to hydroxylapatite (Eichert et al., 2005).

Due to such complexities and the entangled nature of the bone material, its research has noticeably branched into many research directions. A major research direction is towards improving biomedical applications (Palmer et al., 2008). The research field of biomimetics focuses on producing enhanced materials based on models from nature. Bone analogous calcium-phosphates are used to produce functional materials with superior properties than the natural structures. For example foam-type materials based on the model of hierarchical structure of bone material have been developed that show improved mechanical properties with respect to the original bone (Wegst et al., 2015). Other research directions target the nanocrystalline structure itself, focusing on additives and protein influence on the crystalline properties during crystal formation and growth. Amorphous calcium-

phosphate (ACP) has been recognized as a precursor for the formation of the nanocrystalline calcium-phosphate of the bone biomineral (Gower, 2008; Mahamid et al., 2008; Xie et al., 2014), but there are reports where this is debated (Johnsson and Nancollas, 1992). Moreover, it has been reported that ACP forms in intracellular regions of the bone cells (Betts et al., 1975; Harries et al., 1987). The importance of ACP in the biomineralization systems can be seen in the studies of cation incorporation in ACP, as in the case of beaver tooth Mg-bearing ACP (Gordon et al., 2015). Other investigations are aimed at synthetic ACP in order to learn more about the fundamental structure of the amorphous phase and also to answer the question about the nucleation and crystal growth of the nanocrystalline HAP phase.

Posner made significant contributions to the understanding of the amorphous and nanocrystalline structure of calcium-phosphates and bone biomineral by applying the pair distribution function (Betts et al., 1975; Betts and Posner, 1974; Posner et al., 1980; Posner and Betts, 1975). Based on his findings he proposed the existence of calcium-phosphate clusters (named after the author – Posner's cluster), which describe the ordering of the phosphate tetrahedra around calcium ions in the amorphous phase.

Medical applications include bone material replacements, fillings and biocompatible coating of metal implants. In the case of elemental Mg metal bone replacement, the question of magnesium incorporation in the nanocrystalline structure is discussed (Grünewald et al., 2016).

Synthesis of bone analogous materials using various additives (proteins) under various conditions (hydrothermal, pressure, temperature etc.) is relevant due to the interest of enhanced biocompatible materials for bone replacement and in dentistry. Tailoring the crystallite morphology is well investigated in the example of small proteins of citrate (Hu et al., 2010; Taylor and Kirkley, 1967; Xie and Nancollas, 2010).

Innovative methods combine XRD analysis with tomography-type measurement techniques to capture diffraction patterns as the sample is irradiated from all angles. From the scan each slice can be evaluated using Rietveld refinements and parameters such as microstructure size and strain can be visualized across the entire sample (Frølich et al., 2016; Leemreize et al., 2014, 2013). Tomography based techniques have applied to other measurement method as well. Recent results of Gordon at al. show that atom probe tomography can give insight of the spatial distribution of chemical elements. In the mentioned report (Gordon et al., 2015) the spread of magnesium in the amorphous part of the beaver tooth demonstrates the high importance and future impact of tomography in bone research. Another example of tomography-coupled techniques was reported by Jacques et al., where the authors report on the use of automated atomic pair distribution function analysis on tomography scan acquisition data (Jacques et al., 2013).

1.3 Characterization techniques used

In order to describe and characterize bone and its analogous a combination of diffraction (XRPD, PDF) and vibrational spectroscopy (FTIR, RS) techniques have been used. The research laid out in the following chapters is centred around the problem of measurement interpretation and data evaluation using the listed measuring techniques.

In this section a heuristic treatment of theoretical concepts are given as a context for the bone and bone analogous materials investigation.

1.3.1 Classical powder diffraction

By observing the X-ray powder diffraction pattern of bone material it is evident that there is:

- a significant reduction of intensity with respect to a well crystalline reference
- very broad, but still distinguishable Bragg diffraction peaks
- a significant background contribution.

In vertebrate long bones, the crystallites have a preferred c-axis orientation leading to the development of planes in a(b) direction* (Aizawa et al., 2013). Variations between different types of bone, various skeletal elements and animal species were investigated, among others by Rogers and Zioupos (Rogers and Zioupos, 1999), who conducted full-profile Rietveld micro-structural analysis assuming spherical crystallites on a dozen of randomly selected animal species. Hyper-mineralization of the *mesoplodon densirostris* whale's rostrum skeletal element highlights the ranges of different states of the bone material (Li et al., 2013). XRPD peaks show significantly more differentiation and narrowing, hinting less degree of microstrain and/or larger crystallite domains than the usual average bovine femur reference. An exceptional example of hydroxylapatite bio-mineralization of a non-vertebrate organism was reported in mantis shrimp clubs, that show has high values for toughness (Weaver et al., 2012). Beckett reports a survey of more then a dozen various vertebrate species bone material comparisons (Beckett et al., 2011).

Possibilities of the characterization methods used to extract information relevant to natural and experimentally induced alterations are discussed by Peters et al. (Peters et al., 2000).

Diffraction measurements gathered in the scope of the research were conducted with the goal to describe the crystallographic structure of the bone and bone analogous materials. As the incoming radiation interacts with the electron cloud around the atoms constructive and destructive interference create a pattern from

* in the hexagonal symmetry the a and b axis are identical

which the position of the atoms in the unit cell can be determine. This task would be trivial if the phase of the diffracted waves could be obtainable. Therefore, in order to interpret diffraction measurements an initial structural model in generated and via optimization the model is refined. There are a number of approaches: direct space methods, reciprocal space methods, direct methods ab-initio structure solution and density-function-theory calculations. All methods are based on the ideal crystal structure approximation, stating that the space is filled with repeating units with translational periodicity and long range order. In the case of the bone and bone-analogous calcium-phosphate nanocrystallites a complete interpretation of a measured diffraction pattern should include potential short-range order, atomic disorder, and unit cell lattice discrepancies (microstrain).

Analysing the Bragg peaks of diffraction patterns

Bragg peaks of the diffraction pattern contain information of all structural parameters by their position and relative intensity. They describe the state of the bulk crystalline structure with long-range order and translational periodicity. The width of the peaks contains information about the coherently scattering length (size) and the variance of the unit cell lattice constants (microstrain).

In general the evaluations of powder diffraction patterns can be approached in several ways: single peaks fitting, full diffraction pattern analysis, Fourier transform based methods, as well and the pair distribution function analysis. Paradigms of powder diffraction evaluation methods are listed following Scardi's classification, that differentiates the approach to retrieve structural information, and the treatment of microstructural parameters (Scardi et al., 2010):

(1.) Peak profile analysis with analytic functions

In this approach the diffraction pattern trace is approximated by a model that is constituted of a combination of analytical distribution functions (Gaussian, Cauchy-Lorentzian or pseudo-Voigt functions). The parameters of the model functions are then interpreted with assigned physical meaning. An example of peak-fitting of powder diffraction patterns of bone can be seen in the work of Handschin and Stern (Handschin and Stern, 1995). In their report a fit on selected reflections diffraction maxima (002, 210, 300 and 310) was carried out and domain size estimates were given based on the width of these Bragg peaks only.

(2.) Warren-Averbach (WA) approach

Warren and Averbach introduced a way of powder diffraction peak analysis based on discrete Fourier transform of the diffraction pattern peak profile (Warren and Averbach, 1950). They derive the column length for a cubic system by transforming the measured data (diffraction peak) directly. Fourier transform is a

mathematical transformation that returns the constituting sinusoid component of a periodic signal. The measured diffraction profile is Fourier transformed as a sum of the sine and cosine terms, where only the cosine term A_n is considered and the sine term B_n neglected. A general starting equation is (eq.1.1):

$$P_{hkl} = \sum_{n=-\infty}^{n=+\infty} (A_n cos(2\pi nhkl)) + B_n sin(2\pi nhkl)) \qquad \text{(Equation 1.1)}$$

where P_{hkl} is the measured pattern (intensity). Further on, the A_n is interpreted as the product of coherently diffracting domains and a distortion (or disorder) coefficient $A_n = A_n^s \cdot A_n^d$. In their method, the cosine part of the Fourier series coefficients are sorted and from the extrapolation of the initial slope a domain size value is derived.

Posner et al. applied the Warren-Averbach method on fluorinated bone samples and analysed the 002 reflection (Posner et al., 1963). Their analysis was conducted exclusively on the 002 reflection since this reflection is a separate peak without overlapping in the diffraction pattern of bone samples in the hexagonal apatite structure in general. More studies of the diffraction patterns of bone or bone analogous materials based on Warren-Averbach method are in general missing in the literature. A possible reason is that the heavy overlapping of the diffraction profiles in addition to the finite size broadening of the nano-crystallites does not permit interpretation without problems.

(3.) Whole powder pattern fitting - WPPF

According to this approach, the powder pattern is first fitted with analytical profile functions after which the profile function of each peak is analysed separately (Dinnebier, 2008; Mittemeijer and Scardi, 2004). This approach allows Warren-Averbach-type analysis of the peaks since the peak profile functions have been made available. This way it is possible to evaluate the estimated peak profile of overlapping peaks. However, the problem of overlapping peaks remains unsolved, since the peak fitting cannot give an unambiguous result and is dependent on initial conditions (Dong and Scardi, 2000).

Peak shape functions are chosen according to the type of statistical distribution that the broadening source might exhibit. The first attempt to model the diffraction peaks by analytical functions was worked out by Caglioti, who gave an empirical equation for the diffraction peak profile (Caglioti et al., 1958) that is used till today. It is used to retrieve the angle (or scattering vector) dependence of the full- width-of-half-maximum (essentially the peak width but not shape), as well as to map the intrinsic broadening of the measuring instrument (instrumental resolution). Even though the applied statistical distribution functions have strict meaning, their

application, however, does not necessarily have one. For example, the size and strain effects behave according to the central limit theorem (allowing the usage of a Gaussian function), which implies that a mean value for size and strain must exist. Crystallographically relevant aspects of statistical distribution function are discussed by Scardi and Leoni (Scardi and Leoni, 2001). The most often used analytical function for a Bragg peak is a pseudo-Voigt (de Keijser et al., 1982), as well as asymmetric pseudo-Voigt in order to include axial divergence (Thompson et al., 1987). Software that utilizes this approach are the most common (FullProf, Jana, Gsas, Topas, etc.).

(4.) Whole powder pattern modelling - WPPM

An alternative method to examine powder diffraction patterns is through Fourier transformation and profile pattern synthesis described in literature as whole powder pattern modelling (WPPM) (Leoni et al., 2004; Scardi et al., 2010; Scardi and Leoni, 2006, 2002). The main argument for its purpose is that the broadening of the diffraction peaks is not interpreted using analytical functions. Instead a full pattern model is generated based on a direct parametrization of the microstructural effects that contribute to the diffraction peak broadening. It combines instrumental broadening and the sample's intrinsic microstructural properties. For each effect (size, dislocation, stacking faults, etc.) it generates a full pattern which is summed in Fourier space to avoid a convolution process in real space (Leoni et al., 2006). It then refines directly the parameters that describe the effects in the powder pattern synthesis. The result is matched against the provided experimental pattern in a least square optimization algorithm. Technically, the method requires the set of reflections with their integrated intensities and it does not require crystallographic information about atomic positions, thermal factors, nor site occupancies. Authors Scardi and Leoni developed special software for the implementation of this method, the “PM2k” software (Scardi and Leoni, 2002).

Theoretical treatments of the crystallite size distribution have been given by Kril and Birringer (Kril and Birringer, 1998), however, the application in standard software is not implemented, except in the “PM2k” software solution. Some results of the WPPM approach applied in the evaluation of bone biomineral diffraction patterns is given in appendix A3-p197.

Sources of Bragg peak broadening can be of various origin, although, they are in general divided into two categories: finite size and strain - commonly referred to as “apparent size” and microstrain, respectively. The type of the broadening source is inferred by its reflection order dependence (or reflection angle dependence).

(1.) Finite size

An illustration of the diffraction planes and the conditions of reflection is

shown in Fig.1.2. The finite size of the coherently scattering (diffracting) domain L_{hkl} can be written as the product of p number of inter-planar distances d_{hkl}:

$$L_{hkl} = p \cdot d_{hkl} \qquad \text{(Equation 1.2)}$$

The path difference of a diffracted photon (Δ) can be given with respect to the diffraction angle variance (γ) (Dinnebier, 2008, Klug and Alexander, 1974)*

$$\begin{aligned} \Delta &= 2d\sin(\theta+\gamma) \\ &= n\lambda\ cos\gamma\ +\ sin\gamma\ 2d\cos\theta \end{aligned} \qquad \text{(Equation 1.3)}$$

Including the phase difference ($\delta\phi = 2\pi\ \Delta/\lambda$) and neglecting the $n\lambda cos\gamma$ term from eq.1.3, the substitution of the path difference gives over all p planes:

$$\delta\phi\ =\ p(4\pi\gamma\ d\ cos\theta/\lambda) \qquad \text{(Equation 1.4)}$$

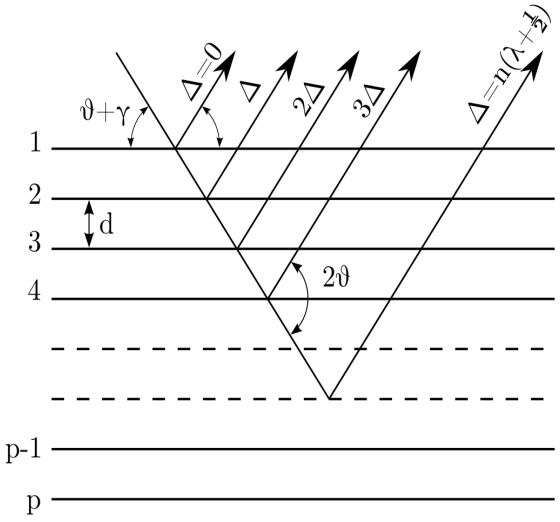

Figure 1.2: Path difference of the diffracted photon. The length of the coherently diffracting domain is denoted as p. Image from Dinnebier (2008)

Substituting 1.2 into equation 1.4 and rearranging, the misalignment angle can be expressed as a function of size of the crystallite (L_{hkl}) and the phase difference between top and bottom planes ($\delta\phi$).

As the coherently scattering (diffracting) domain is decreasing in size, the angle of misalignment is increasing. By rearranging equation 1.4 the equation for the misalignment angle is:

* use trigonometric identity for sum of angles and the Bragg equation $n\lambda = 2dsin\theta$

$$\gamma \;=\; (\lambda\delta\phi)/(\;4\pi L_{hkl} cos\theta) \qquad \text{(Equation 1.5)}$$

When the condition of destructive interference is met, equation 1.5 becomes:

$$\gamma \;=\; \lambda/(\;4\;L_{hkl} cos\theta) \qquad \text{(Equation 1.6)}$$

Redefining the angle of misalignment into diffraction angles ($\gamma \rightarrow \beta$):

$$\beta_{hkl} \;=\; K\;\lambda/(\;L_{hkl} cos\theta) \qquad \text{(Equation 1.7)}$$

The obtained equation 1.7 is well know as Scherrer's equation for size contribution to diffraction peak broadening. The coefficient K is expressed as a parameter that includes the geometry of the crystallites, i.e. in case of approximated sphere shaped domains K is 0.98. This approximation however does not consider a particle size distribution. Determination of the coherently diffracting domain size from powder diffraction methods is commonly based on the Scherrer's equation. Microstructural characterization based on these assumptions are widely used, for example in the determination of chemical synthesis mechanisms from diffraction line broadening Delgado-López et al., 2012, Ibsen et al., 2016, Rusu et al., 2005).

Integral breadth description

The integral breadth (β) is taken as an empirical ratio of the powder diffraction peak area (integrated intensity) and the peaks maximum measured intensity:

$$\beta = \frac{\int_{-\infty}^{\infty} I(s)ds}{I_0} \qquad \text{(Equation 1.8)}$$

which results in Scherrer's equation eq.1.7 after the integration of the interference-function (after Scardi, P. in Dinnebier, 2008 chapter 13.). However, the presence of different domain sizes (size distribution), and also irregular shapes of the domains have an affect on the peak profile as well. In general, the shape of the crystallites can be approximated as spheres (isotropic) or ellipsoid (anisotropic). The size distribution is approximated as the volume-weighted mean size $\langle L_{hkl}\rangle_V$, or practically the apparent domain size as:

$$\beta = \frac{\lambda}{\langle L_{hkl}\rangle_V cos\theta} \qquad \text{(Equation 1.9)}$$

if the integral breadth is a function of angle $\beta(2\theta)$.

An area-weighted mean size is defined by Warren and Averbach (Warren and Averbach, 1950) as $\langle L_{hkl} \rangle_S$ and is given as:

$$\frac{dA_L}{dL}\Big|_{L=0} = \frac{-1}{\langle L_{hkl} \rangle_S} \qquad \text{(Equation 1.10)}$$

where A_L are the Fourier coefficients of the Fourier transform of the intensities I (expressed as the proportional relation summed over all domain sizes)

$$I \propto \sum_{L=-\infty}^{\infty} A_L e^{2\pi i L} \qquad \text{(Equation 1.11)}$$

(2.) Microstrain

Independently to the finite size contribution, a diffraction peak can be broadened due to "microstrain" as well. The cause for this effect can be chemical disorder, dislocation, stacking faults and similar can produce random fluctuations in the long range order and periodicity of the unit cells (illustrated in Fig.1.3). In general terms, microstrain (ϵ) can be described as the variation of the lattice constants (Δd and single lattice constant value d):

$$\epsilon = \frac{\Delta d}{d} \qquad \text{(Equation 1.12)}$$

By taking the total derivative of the Bragg equation $n\lambda = 2dsin(\theta)$ (with respect to the inter-planar distances $d_{hkl}$and the angle θ) at a constant wavelength and keeping the delta terms the following equation can be written:

$$0 = \frac{\partial}{\partial d} 2dsin\theta \Delta d + \frac{\partial}{\partial \theta} 2dsin\theta \Delta\theta \qquad \text{(Equation 1.13)}$$

$$0 = 2\ \Delta d\ sin\theta + 2d\ \Delta\theta\ cos\theta$$

By expressing Δd from eq.1.12 and inserting it into eq.1.13 we obtain:

$$-\epsilon\ tan\theta = \Delta\theta \qquad \text{(Equation 1.14)}$$

Defined through the integral breadth:

$$\beta(2\theta)\ \propto\ \sqrt{\langle \epsilon^2 \rangle}\ tan\theta \qquad \text{(Equation 1.15)}$$

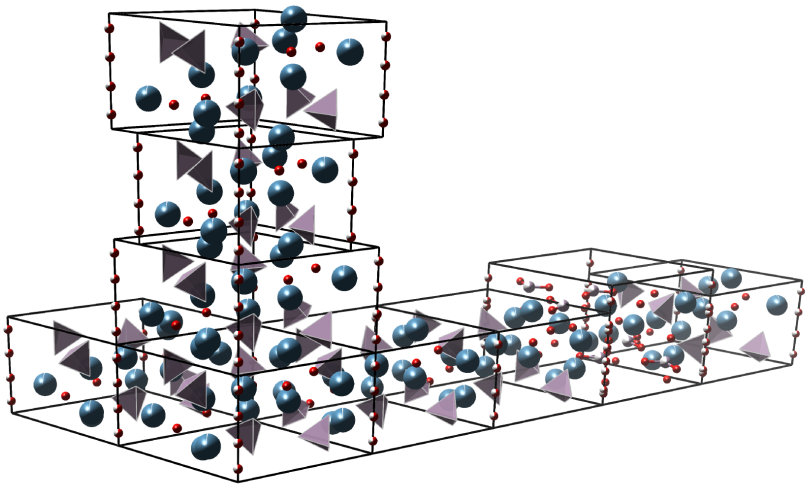

Figure 1.3: Schematic illustration of microstrain as unit cells with lattice constants randomly different from the average.

Equation 1.15 written as the integral breadth in reciprocal space has the *sin* dependence:

$$\beta(s) \propto \frac{2sin\theta_{hkl}}{\lambda} \qquad \text{(Equation 1.16)}$$

which leads to the Williamson-Hall (WH) interpretation of the broadening. According to WH, the size contribution to the diffraction peak broadening is reflection independent while the microstrain increases with higher order reflections* (Ungár, 2001; Ungár et al., 1999). Formally expressed as a convolution ($\otimes$):

$$\beta(2\theta) \approx \frac{cos\theta}{L_{hkl}} \otimes \epsilon \cdot tan\theta \qquad \text{(Equation 1.17)}$$

In the presence of a size distribution of an unique shape of domains (Scardi and Leoni, 2006), the eq.1.17 can be written as:

$$\beta \approx \frac{1}{\langle L \rangle_V} + 2.5\sqrt{\langle \epsilon^2 \rangle} \cdot d^*_{hkl} \qquad \text{(Equation 1.18)}$$

where the term $\sqrt{\langle \epsilon^2 \rangle}$ is the root-mean-square strain defined by Stokes and Wilson (Stokes and Wilson, 1944). In practice, as implemented in "FullProf", the microstrain is calculated as the maximum strain, which is empirically given as $1.25 \cdot \sqrt{\langle \epsilon^2 \rangle}$. The

* the WH interpretation in the case of anisotropic size and microstrain are futher discussed in appendix A4-p201

details of the software implementation in “FullProf” are provided in appendix A1-p190).

Remarks

The interpretation of the X-ray powder diffraction pattern peak profile broadening sources has been widely discussed in the literature (Audebrand and Louër, 2004; Kojdecki, 2004; Tian and Atzmon, 1999). The broadening sources have different diffraction order dependence. Overlapping peaks, correlation of strain, size and lattice constants represent a difficulty in the separation of the broadening sources. More subtle relations of the atomic site occupancy and the microstrain are also possible, as atomic occupancy (substitution, vacancies) may distort the unit cell locally.

Mittemeijer writes about the state-of-the-art of powder diffraction in 2008 “...analysis of strain broadening is a field of currently strong activity...” (Mittemeijer and Welzel, 2008). Latest development include Bayesian statistic evaluation of the distribution of values in a multi-parameter space optimized using Markov-chain Monte Carlo sampling (Fancher et al., 2016; Gagin and Levin, 2015; Lesniewski et al., 2016; Wiessner and Angerer, 2014)

Alternatives for the application of the Warren-Averbach method for separation of size and strain broadening have been evaluated by van Berkum (van Berkum et al., 1994). Special cases are defined where based on the assumption about the sample's properties (pure strain case, broadening that is only due size effect, uniform or random strain etc.), where linear or logarithmic expansion of the Fourier coefficients is more appropriate. Berkum et al. also stated that: “..in practice, each time an analysis is performed the results must be tested against common (physical) sense and all information available on the specimens.“ (van Berkum et al., 1994). The importance of testing the uncertainties was summarised by Tian and Billinge (Tian and Billinge, 2011). In Chapter 3, an approach is described that automates the Rietveld method with focus on conducting a refinement systematically and equally for a series of initial models and strategies reducing biased evaluations.

1.3.2 Total scattering analysis

In the case of the nanocrystallites in bones, structural characterization from powder diffraction is problematic due to extensive finite size broadening. Retrieval of atomic position, mean-atomic displacement factors and site occupancy factors is questionable on poorly resolved Bragg peaks. In order to extend the amount of optimized structural information from diffraction experiments, the atomic pair distribution function can be analysed in addition. Deviations of atomic positions from the ideal position in long-range order (LRO) description can be modelled in total

scattering experiments.

The incoming radiation can interact with the material in a multitude of ways (coherent or incoherent scattering, multiple scattering events, absorption, etc.). Bragg peaks bear the information about the presence of a structure with attributes showing translational symmetry and long range order. Data evaluation methods such as the Rietveld refinement type methods interprate only the coherent part of the diffraction signal, through analytical bell-shaped probability distribution functions (Gaussian, Lorentzian sum functions or Voigt-type). Microstructural analysis is derived from the width of the applied analytical distribution functions. Even though finite size effect and microstrain are the sources of broadening of Bragg peaks, their correlation or cause-and-effect relation to the non-coherent part of the captured signal is often not analysed in the classical structure optimization methods such as the Rietveld refinement.

High photon-flux synchrotron source and a dedicated instrumental set-up allowing measurement of high momentum transfer vector values are necessary for good quality total scattering data. Such a measurement allows analytical modelling of physical effects (such as Compton scattering, fluorescence, multiple scattering, Laue diffuse scattering etc.) and makes the subtraction of signal from the diffraction pattern possible. The rest of the scattering signal is then transformed and analysed.

Total scattering and the atomic pair distribution function

In the analysis of Bragg peaks, the local deviation of the lattice constants from the average value is assigned to microstrain, a parameter that is retrieved from the Bragg peak width. In the case that the atomic arrangement deviates from the long-range order and periodicity, conditions for coherent interference apply no more and the resulted signal is scattered in diffuse manner. It is to be distinguished from Laue diffuse scattering which occurs normally in every case when different atom types are presents in the material and is due to the difference in atomic form factors (Egami and Billinge, 2003 p.141,p159).

In the Rietveld refinement only the Bragg reflections are analysed and the structure factor does not contain any term for diffuse scattering. The diffuse scattering is mostly incorporated into the background term, which in the Rietveld methods does not have physical meaning. However, the background correlates with, and affects parameters such as the mean atomic displacement factors, atomic position values, scale, and also the phase fraction (in multiphase refinements). Neglecting the information content of this signal can have significant influence on the interpretation of measured diffraction patterns of non-ideal crystalline materials. For this reason the method of analysis through the total scattering was attempted through the analysis of the atomic pair distribution function (PDF).

Total scattering measurement and data transformation

Total scattering measurements are interpreted in the context of physical phenomena potentially contributing to the measured intensity. This can be illustrated with equation 1.19:

$$I_M(Q) = a(Q)I_C(Q) + b(Q) \qquad \text{(Equation 1.19)}$$

where the measured intensity I_M is correlated to the coherent scattering through signal from non-structural origin $a(Q), b(Q)$ (Farrow and Billinge, 2009) as the function of the momentum transfer vector, denoted here as Q referring to $\vec{q} = p_{\vec{final}} - p_{\vec{init}}$ expressed in wavenumber units $Q = k_{final} - k_{init}$ where $k = q/\hbar$; $k = 2\pi/\lambda$. Factors that affect the measured intensity are: the inelastic incoherent Compton scattering, the signal from the sample container material, which act as additive factor (term $b(Q)$). Some factors that multiply the coherent signal are the polarization, self-absorption and multiple scattering (term $a(Q)$).

The first step is to extract the coherently diffracted signal from the measured signal. This is achieved by modelling each contribution and subtracting it from the total pattern. The obtained coherent scattering is then transformed into the total scattering structure factor $S(Q)$ as:

$$S(Q) = \frac{I_C(Q) - < f(Q)^2 > + < f(Q) >^2}{< f(Q) >^2} \qquad \text{(Equation 1.20)}$$

$$S(Q) - 1 = \frac{I_C(Q)}{< f(Q) >^2} - \frac{< f(Q)^2 >}{< f(Q) >^2} \qquad \text{(Equation 1.21)}$$

In the case of X-ray radiation $< f(Q) >$ is the average atomic form factor for all atom types in the composition (chemical formula of the material).

The atomic pair distribution function G(r) is obtained from the total scattering structure factor via the Fourier transform of the S(Q):

$$G(r) = 2/\int_{Q_{max}}^{Q_{min}} Q(S(Q) - 1)sin(Q)rdQ \qquad \text{(Equation 1.22)}$$

Formal derivation of the eq.1.22 G(r) is given in (Farrow and Billinge, 2009; Juhás et al., 2013).

Modelling the PDF function and fitting the measured data

The PDF analysis belongs to the category of a direct space methods as the solution is carried out in real space (r) after the Fourier-transform of the measured signal. For the interpretation of the obtained pair distribution function pattern from

the measurement, an initial crystallographic model is used as a starting point. From the model a hypothetical PDF pattern is generated, matched against the measured pattern, and the parameters of the model are optimized. The pair distribution function can be calculated using the bond length distribution $\delta(r - r_{ij})$ weighted by the scattering factor of all atoms ($b_{i,j}$) and the average scattering factor ($< b >$) from the initial model structure:

$$G(r) = \frac{1}{Nr} \sum_i \sum_{j \neq i} [\frac{b_i b_j}{< b >^2} \delta(r - r_{ij})] - 4\pi r \rho_0 \qquad \text{(Equation 1.23)}$$

Equation 1.23 is derived from the expression as the $4\pi r$ weighted difference of the atomic pair density $\rho(r)$ (function of distance) and the atomic number density (ρ_0):

$$G(r) = 4\pi r(\rho(r) - \rho_0) \qquad \text{(Equation 1.24)}$$

where:

$$\rho(r) = \frac{1}{4\pi r^2 N} \sum_i \sum_{j \neq i} [\frac{b_i b_j}{< b >^2} \delta(r - r_{ij})] \qquad \text{(Equation 1.25)}$$

The width of the peaks can be modelled by Gaussian distribution functions where the width of the distribution function (σ_{ij}) is defined (in the case of the used software "PDFGui" eq.1.26) containing contributions from thermal, zero point displacements, and static disorder. The peak width originating from the structural anisotropic displacement factors (σ'_{ij}) is multiplied by the square-root of the correlated motion of the atoms, which contributes to peak narrowing (or broadening). Terms δ_1 and δ_2 (eq.1.26) are parameters assigned for the effects of correlated thermal motion and they describe the low and high temperature case, respectively. Term Q_{broad} is a parameter to adjust instrumental resolution.

$$\sigma_{ij} = \sigma'_{ij} \sqrt{1 - \frac{\delta_1}{r_{ij}} - \frac{\delta_2}{r_{ij}^2} + Q_{broad}^2 r_{ij}^2} \qquad \text{(Equation 1.26)}$$

Eq.1.26 is specific to the software implementation that is used in this thesis "PDFGui" (Farrow et al., 2007).

Lastly, "termination ripple" effect is convoluted into the calculated PDF that scales as:

$$sin(Q_{max} \cdot r)/r \qquad \text{(Equation 1.27)}$$

where Q_{max} is the upper limit of integration in the Fourier-transform. It is also a

parameter that is experiment specific and limited by the set-up of the instrument used and the capabilities of the radiation source (X-ray or neutron source).

As a result the inter atomic distances can be derived from the optimization of the hypothetical model to fit the measured pattern. Other alternative methodical approaches to obtain the same result are based on large-scale Reverse Monte Carlo simulations.

Authors Egami and Billinge (Egami and Billinge, 2012) argue about the applicability of the Rietveld analysis in the case of nano-crystallites and highlight the importance of the atomic pair distribution function for the analysis of local atomic disorder. In their interpretation the PDF analysis is aimed at studying the local atomic disorder as a distribution of inter atomic distances. Microstrain, a parameter characteristic for Rietveld refinement, on the other hand, describes the disorder on the level of unit cell lattice constants, and therefore is missing from the PDF analysis.

1.3.3 Vibrational spectroscopy based techniques

FTIR and Raman spectroscopy are techniques used to investigate the covalent bond structure and properties of materials. In bone research mid-range FTIR (400-4000cm^{-1}) is used very frequently to quantify the phosphate bands state, hydroxylation, as well as to identify the presence of carbonate. Quantification of carbonate from FTIR spectra is a task that does not have a straightforward approach. Raman scattering microscopy in bone research is also established, although the fluorescence effect represents a major limitation in some cases. The classical approach to retrieve information from vibrational spectra is by using the spectral deconvolution method, a non-linear least square fit which uses distribution functions assigned to bands of the vibrational modes of the covalent bonds (Antonakos et al., 2007; Vandecandelaere et al., 2012, Grunewald 2014-5-6). In general the band positions and assignment to modes in reference structures (such as the HAP) has been determined using isotope substitution, and factor group analysis (Adler, 1964; DeAngelis et al., 1972). Contemporary challenges are the evaluation of complex cases of hydrated layers, HPO_4^{2-} presence, as well as the interpretation of the spectroscopic band broadening, and the clarification of the assigned distribution function. Recent development of computer codes using force field and DFT calculations are attempting to calculate the spectroscopic properties and model a vibrational spectra, although, calculated values are often still in cases about tens of wavenumber in offset from experimentally obtained values (Corno et al., 2006; Pedone et al., 2007; Yi et al., 2014; Yin and Stott, 2003). In theoretical modelling the peak shapes are usually approximated with Gaussian functions, neglecting the complexity arising from microstructural properties such as size, chemical disorder or discrepancy in the

regularity in the material.

In order to describe the atomic structure of the bone material, vibrational spectroscopy is also used as complementary technique to X-ray or neutron diffraction. FTIR and Raman spectroscopy can yield vital information about symmetry breaking of the rigid unit of phosphate tetrahedra in the crystallographic structure of bone biomineral, hinting on the ionic environment change and potentially relate to microstructural effects. The FTIR measures the permanent dipole moment of the bonds through the absorption of the electromagnetic radiation. Raman spectroscopy measures the polarizability of the bond as the difference of the incoming and scattered light. These techniques yield spectra with fingerprint-like characteristic peaks (bands) of chemical compounds. Appearance of peaks in experimental series is usually a sign of local symmetry breaking, for example due to a distortion of coordination polyhedra. A field in spectroscopy called factor group analysis focuses on the mathematical aspects of the possible application of group theory to symmetry breaking problems. Appearance of IR inactive modes due to the distortion of the phosphate tetrahedra in the calcium-phosphates and HAP has been analysed by DeAngelis et al. as well as by McCue et al. (DeAngelis et al., 1972; McCue and Malinowski, 1981). Adler analysed the symmetry break of the phosphate tetrahedra in several apatite structures and classified the resulting symmetry class of the distorted tetrahedra (Adler, 1964). Point symmetry lowering in the P-O tetrahedra from C^{2}_{6h} to C_{3h} has spectral implications in the form of appearing vibrational bands in the spectral trace (Adler, 1964; Antonakos et al., 2007). The peak positions and their shift from reference values (band position of known compounds) or theoretically predicted values can give insight about the ionic surroundings of the bonds. The profile of the peaks is broadened primarily due to natural broadening, having a Gaussian nature (central limit theorem), however, additional broadening effects can be caused by micro-structural deviations present in the material.

Band assignment

Identification of vibrational bands in the measured spectrum of calcium-phosphate apatite has been explored by isotope substitution and peak shift evaluation methods more than half a century ago among others by Adler and Fowler (Adler, 1964; Fowler, 1974; Fowler et al., 1966). Recent detailed study of spectral bands and modes for the HAP structure have been investigated experimentally by (Antonakos et al., 2007; Miller et al., 2001; Rehman and Bonfield, 1997). Recent theoretical calculations show, however, that calculated band positions can differ by a few wavenumbers up to tens of wavenumbers from band positions in experimental measurements (Bhat et al., 2014; Corno et al., 2010, 2006; Pedone et al., 2007; Yi et al., 2014). The effect of carbonate content on spectral bands have been studied by Awonusi el at. (Awonusi et al., 2007). Splitting of infra-red bands associated to

carbonate in the evolution of the bone with age was conducted by Rey et al. (Rey et al., 1991a, 1990, 1989). Literature references of band positions of HAP and vibrational modes in biological samples are listed in Table 1.1.

Broadening of spectroscopic peaks

Sources of spectroscopic band broadening are at first attributed to natural broadening due to the Doppler-effect, finite lifetime of phonons, and secondly due to size and disorder of the material's structure. Theoretical description of sources that produce observable broadening in spectral lines are described by the phonon confinement model and the elastic spheres model (Arora et al., 2007, Gouadec and Colomban, 2007). According to the phonon confinement model, the source for the broadening can be various combinations of effects including effects of finite crystallite size, chemical disorder (substitution), dislocations, presence of grain boundaries, etc. (Gouadec and Colomban, 2007, Gupta and Jha, 2009).

Mul et al. investigated the broadening of the vibrational spectral lines in experimentally measured spectra of calcium-phosphates with respect to carbonate content (Mul et al., 1986, 1988; Balan et al., 2010)

Spectral decomposition[*]

The measured spectrum represents the sum of peak profiles of individual vibrational bands. In order to retrieve the state of the vibrational bands, the spectral trace is modelled by bell-shaped statistical functions during the band assignment. For each vibrational band a Gauss and Lorentzian sum function is used where the character of the distribution function is a free parameter that defines the ratio in the sum function. The method is limited by the lack of structural symmetry constraints that could constrain the optimization process. Another limitation of peak fitting is due to the hyperparameters of the non-linear least-square fitting algorithm such as the dampening factors, soft constants, value intervals (box restraints) influencing the convergence of the fit and can introduce biased, non complete or even over-fitted results. The limitation of spectroscopic peak fitting was discussed among others by Maddams (1980), Gans and Gill, (1980) where the authors highlight that the peak fitting method should not be used as an exploration tool, as it only optimizes an initial structural hypothesis.

* Spectral decomposition – synonymous in the literature with spectral deconvolution. Further discussion of the terminology in appendix A1

Table 1.1: Table of observed as well as calculated bands and modes for reference structures (R and IR). Table in parts constructed with values after Elliott (Kohn et al., 2002 chapter 11); additional references are provided

HAP with C	theoretical calculations	in biological systems	lit. IR	lit. Raman
PO_4^{3-}	ν_1=938 (R) ν_2=420 (R) ν_3=1017 (Ir,R) ν_4=567 (Ir,R) (Corno et al., 2006)	930 (R) 550-650 (Ir,R)	ν_1=962 ν_2=462 ν_3=1091,1042 ν_4=566,603, 632 (Rehman and Bonfield, 1997)	ν_1=963 ν_2=433-449 ν_3=1048 ν_4=580,591 (Cuscó et al., 1998)
HPO_4^{2-}	no calculated values found	P-(OH) 870 (Berry, 1967) very close to ν_2CO_3 ν_3-mod 1020(Rey et al., 1991c) 1100 1145 1110 1125 ν_4-mod 530-530 (Rey et al., 1990) 540-550	878 (Young and Holcomb, 1984) 530-540 (Miller et al., 2001)	1049
CO_3^{2-}	ν_1=1063 (R) ν_2=879 (Ir) ν_3=1415 (Ir,R) ν_4=680 (Ir,R)	ν_2 is non-deg,; if split CO_3^{-2} is in different ionic environments dichroism (C-O)$\parallel$ c 1465, 1412, 873 ν_{3b} sym (C-O)$\perp$c 1545, 1450, 880 ν_{3a} asym	(Rey et al., 1991b) (Penel et al., 1998)	
OH^- /H_2O	stretching 3570 libration 630 water stretching and bending: 2700-3700 1640	3571-3572	3571	3571

1.3.4 Determination of the chemical composition of the bone material

Although successful electron-microprobe results on the chemical constituents of the inorganic part of the bone material have been reported (Li et al., 2013; Li and Pasteris, 2014), reliable determination of carbonate content in the nanocrystallite of the bone remains intractable partially due to the amount of organic molecules presence. Separation the bone composite to its constituents (collagen and inorganic nano-crystallites) by means of chemical washing or rinsing inevitably induces an unknown amount of alterations of the inorganic crystalline part as side effect. For example, inorganic crystallites of the bone material were extracted and studies under TEM by (Cuisinier et al., 1987; Ziv and Weiner, 1994) and later by (McNally et al., 2013; Reznikov et al., 2014; Schwarcz et al., 2014). However, their conclusions do not merge into an unambiguous description about the crystallite size. The influence of the sample preparation methods on the results remains the topic of scientific discussion. For these reasons microstructural analysis of the bone material requires a thorough evaluation including size and strain effects, crystallite size anisotropy, chemical composition etc..

1.4 Outline of the thesis

Samples of several animal species and skeletal elements have been included in order to search for a representative sample of the bone material (Chapter 2). For several experiments crushed *bos taurus* femur bone material was used, as starting material (see Chapter 6). A set of reference samples was devised in order to cover a large bandwidth of structural alterations of the calcium-phosphate nanocrystallites in the bone and bone analogous materials (Chapter 4). Samples of geological minerals have been put on parallel with mineralization in biological system, such as in bone (Chapter 5). Synthetic bone-analogous materials have been produced in an attempt to model and recreate the observed properties of the extracted reference bone material (Chapter 7).

In the work presented in this thesis the main focus of the research was on the exploration of the microstructure and atomic structure relation in bone, and bone-analogous materials. Accent has been put on the modelling of the obtained measurement data using combining classical characterization-, with innovative methods, in some occasions in a on-traditional way. The measurements have been evaluated with the attempt to thoroughly investigate the underlying relation of intrinsic properties to bias, systematic errors and established assumptions. In the case of XRPD evaluation using the Rietveld method a structural hypothesis testing and structural refinement strategy comparison approach has been devised. (Chapter 3).

Chapter 2
Diffraction patterns of various bone samples

Powdered bone sample of three animal species *mesoplodon densirostris, ovis aries* and *bos taurus,* have been empirically compared based on observations from the measured diffraction data. Two anatomically different skeletal elements of the *ovis aries* have been included in the comparison: *os petrosum* - inner ear bone and *os occipitale* – basal vertebra. In this chapter a phenomenological comparison of dense mammalian bone samples are given from the diffraction patter analysis point of view. In addition the transformation of the diffraction patterns to the pair distribution function data is demonstrated and described. The measured diffraction pattern data has been compared in order to identify interspecies and skeletal element variations. Results of the bone sample preparation protocols comparison shows that the original bone material can be affected.

2.1 Intrinsic observable differences in the crystalline state of the bone biomineral

It is reasonable to assume that biological evolution optimized the functionality of the anatomical skeletal elements. From this assumption follows that the microstructure and thus the properties of the inorganic nanocrystallites of the bone material have been specifically tuned to fit the purpose of the bone tissue. Interspecies differences of the inorganic nanocrystallites of bone have been studied on a variety of species, where the crystallite sizes in animal bone have been observed to vary in the range of tens of nanometers depending on the species and skeletal element in question (Bertazzo and Bertran, 2006; Currey, 2001; Rogers and Zioupos, 1999).

2.1.1 Choice of samples

The *bos taurus* and *ovis aries* samples have been chosen as an example of a common bone reference material. These samples are widely available and accessible to obtain. A sample of *mesoplodon densirostris* was included in the comparison as an example for its significantly different crystalline state. Samples of the *mesoplodon*

densirostris skeletal element have been described as hyper-mineralized bone material by Li et al. (Li et al., 2013).

A comparison of diffraction patterns of diverse skeletal elements and various animal species collected under same measuring conditions are shown in Fig.2.1.

2.1.2 Discussion on the powder diffraction patterns

The complex nature of biological apatites has been highlighted already in the 60's by Elliott (Elliott, 1969). Although HAP is often used as the starting model for the evaluation of diffraction patterns of bone material, guest ions can be in incorporated into the structure and can have structure stabilizing effect. Ionic substitution can be interpreted as microstrain in the diffraction pattern evaluation. The microstructural properties such as microstrain can originate from inhomogeneities in the amount of Ca (in calcium deficient structures), or the presence of carbonate in the system, hence the relation of the site occupancies and microstrain needs to be addressed. Determination of site occupancy variation requires reliable high resolution data. The impact of calcium deficiency in the apatite structure has been thoroughly investigated by Wilson, Elliott and co-authors (Wilson et al., 2005) and it may play a role in the interpretation of the average symmetry as hexagonal (Hughes, 2015; Wopenka and Pasteris, 2005; Hughes et al., 1989) rather than monoclinic (Suetsugu and Tanaka, 2002). Investigation of the carbonate content in bone-apatite nanocrystallites from the PDF function was pioneered by Posner (Posner et al., 1980). In his work, it is demonstrated that even small carbonate content up to 3-4wt% was able to produce observable differences in the PDF pattern.

Interpretation of chemical variability is challenging in averaged powdered bone material samples. Inhomogeneities in the chemical composition of the crystalline structure can influence the measured average values depending on the bone material sampling location (anatomical position of the bone segment). Therefore a single Ca-to-P ratio value may not necessarily apply for all regions of the investigated skeletal element. In the case when the whole skeletal element is completely crushed and pulverized, a mechanical average is obtained, which can leave to interpretation bias due to sampling and averaging of the powder material.

The measured powder diffraction patterns hint to microstructural or structural variety between the compared bone samples (Fig.2.1). Slight differences in the diffraction pattern peak shape and relative peak intensity changes can be observed in the case of *mesoplodon densirostris*, while the samples of *ovis aries* and *bos taurus,* and two anatomically different skeletal elements of the *ovis aries* appear almost identical.

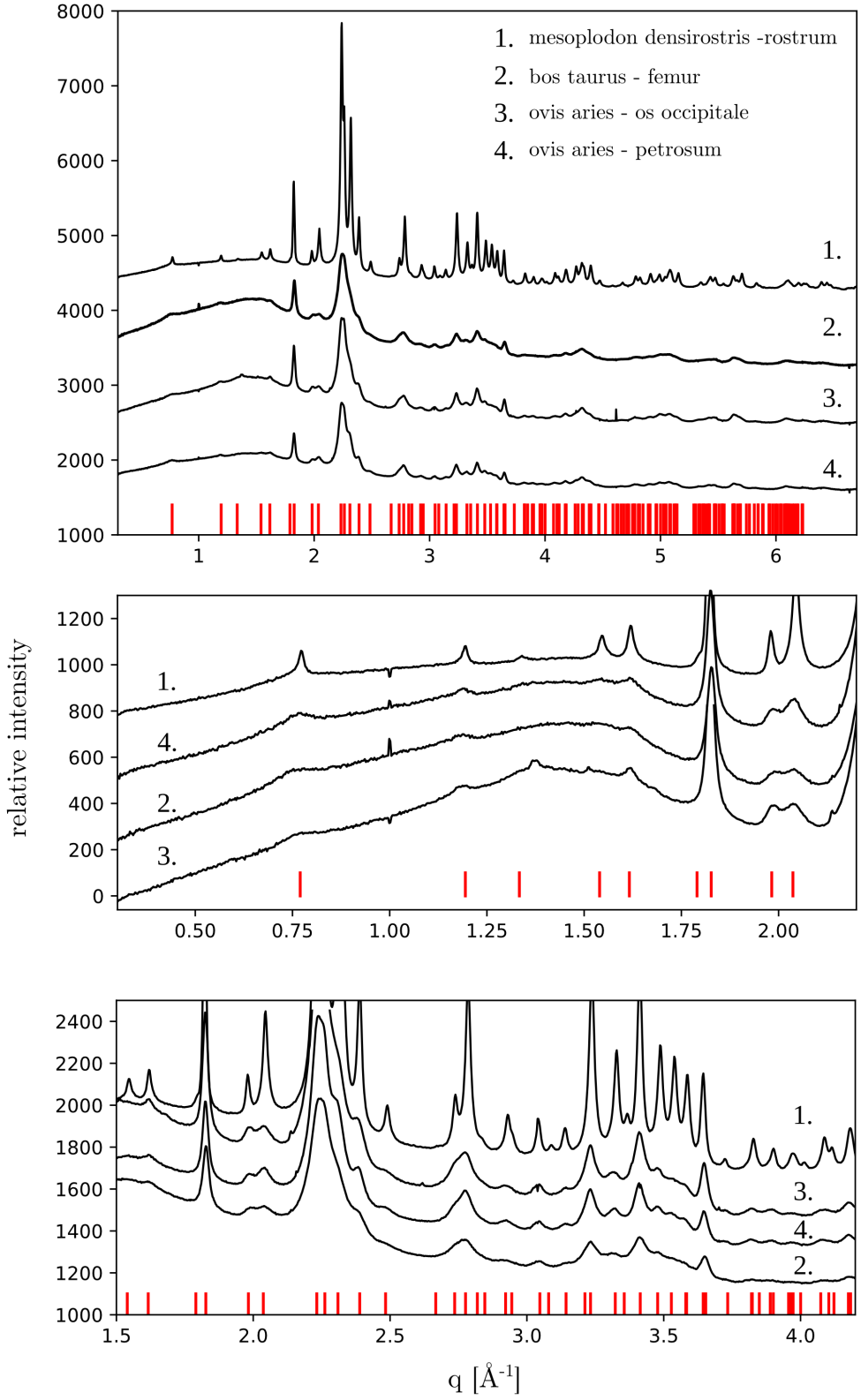

Figure 2.1: Diffraction patterns of various animal species and skeletal elements. Reference peak positions of the hydroxylapatite are marked below the patterns.

2.1.3 Pair distribution function patterns

The XRD patterns were gathered at the DESY synchrotron facility in Hamburg. The material in capillaries of 1mm diameter were illuminated with 60keV photons of 0.20727nm wavelength. The data was collected on Perkin-Elmer 2D detectors of 0.5x0.5m dimension and pixel size of 200microns (0.2x0.2mm).

The measurement was carried out in two stages, two sample-detector distances in order to: 1. get a dataset of high Q-space (momentum transfer vector space) resolution by using short sample-detector distance; 2. get high angular resolution in reciprocal space to resolve the peak of the first reflections (in reciprocal space). Comparison of the same sample with the two measuring distances is shown in the lower plot of Fig.2.2.

Long sample-detector distance measurements (Fig.2.1) are intended for Rietveld method analysis, while the short sample-detector distance patterns (Fig.2.2) are intended for the atomic pair distribution function (PDF) analysis. Magnified regions of the diffraction patters show differences for example of Bragg peaks near $2Å^{-1}$ (middle plot Fig.2.1).

To obtain the pair distribution function G(r), the diffraction pattern needs to be transformed adequately. On the upper and middle plot in Fig. 2.2 the diffraction pattern is shown in relative counts on the y-axis. The high Q-space region is magnified to emphasise the peak features (middle plot in Fig.2.2). This region shows multiple features, but the counts are by an order of magnitude smaller than in the case of dominant Bragg peaks in the region up to $5Å^{-1}$. A scaled comparison of the high Q-space dataset and low Q-space dataset of the same sample is shown on the lower plot of Fig.2.2. Although the high Q-space measurement can capture more structural information, the low Q-space dataset has superior angular resolution.

The preparation of the data requires subtraction of incoherent, as well as the empty sample holder contribution to the signal. In Fig.2.3 the calculated Compton energy dependant signal contribution as well as the Laue diffuse scattering is plotted. The intensity plot is converted into the total scattering amplitude signal (lower row in Fig.2.3). The signal is reasonably well normalized, which can be seen as the tail of the signal oscillates around unity (magnified region on S(q) inset plot of Fig.2.3). The Fourier transform of the S(q) was conducted with the upper integration limit of $18Å^{-1}$ resulting the G(r) shown in the lower right in Fig.2.3. Additionally results of the PDF conversion are compared with respecto to the software implementation used “pdfgetx2” and “pdfgetx3” [*]. Manual tinkering with the correction factors is done in "pdfgetx2", while “pdfgetx3” uses automated algorithms for scaling and optimization.

* tested only for historical relevance, pdfgetx2 is the older version while pdfgetx3 is newer

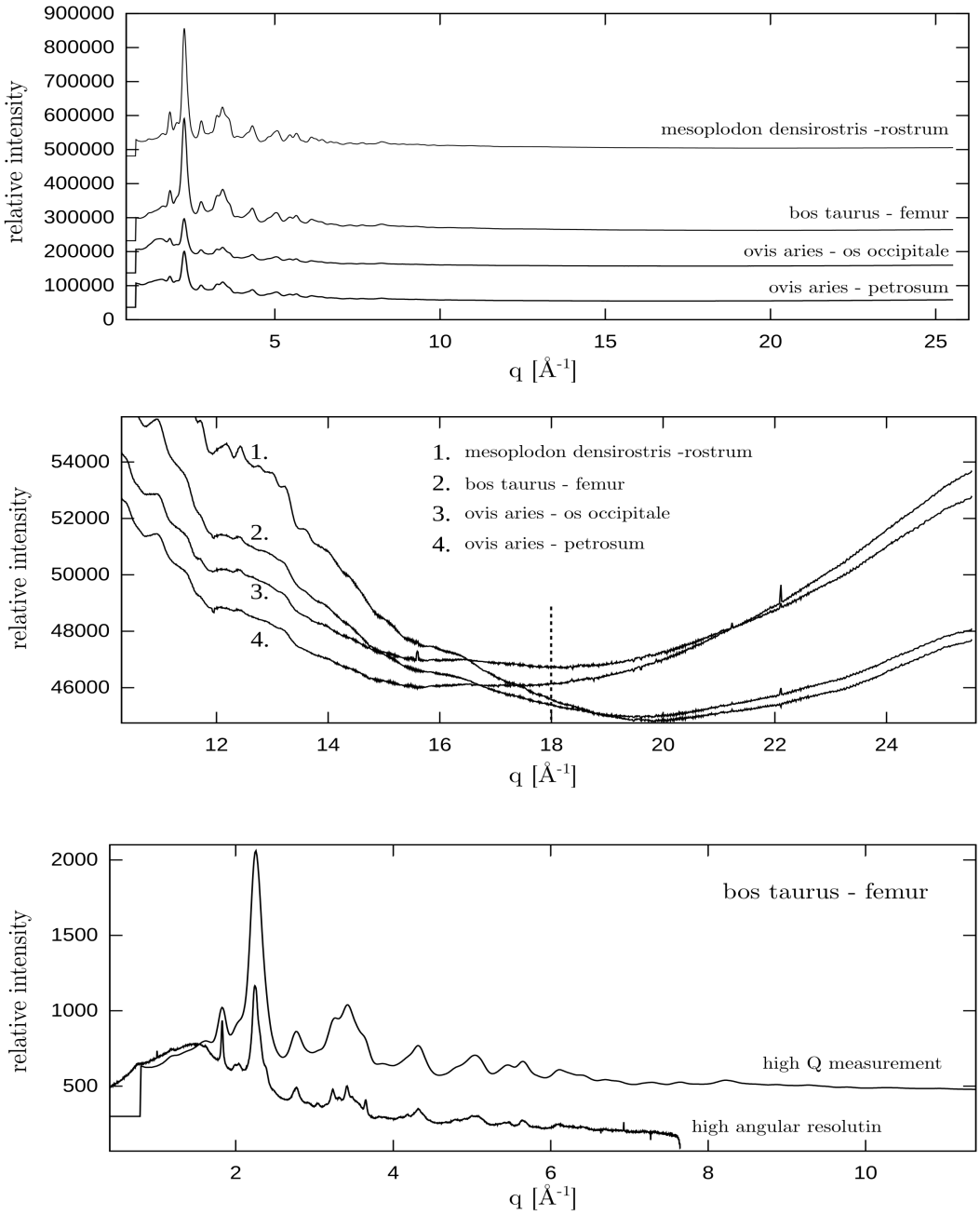

Figure 2.2: Diffraction measurement with various settings. Upper plot: measurement with high Q-space resolution for the evaluation of the pair distribution function; middle plot: magnified region of the upper limit for the Fourier transform (qmax=18Å^{-1}); lower plot: comparison of high Q-space resolution and measurement with high angular resolution (int. scaled).

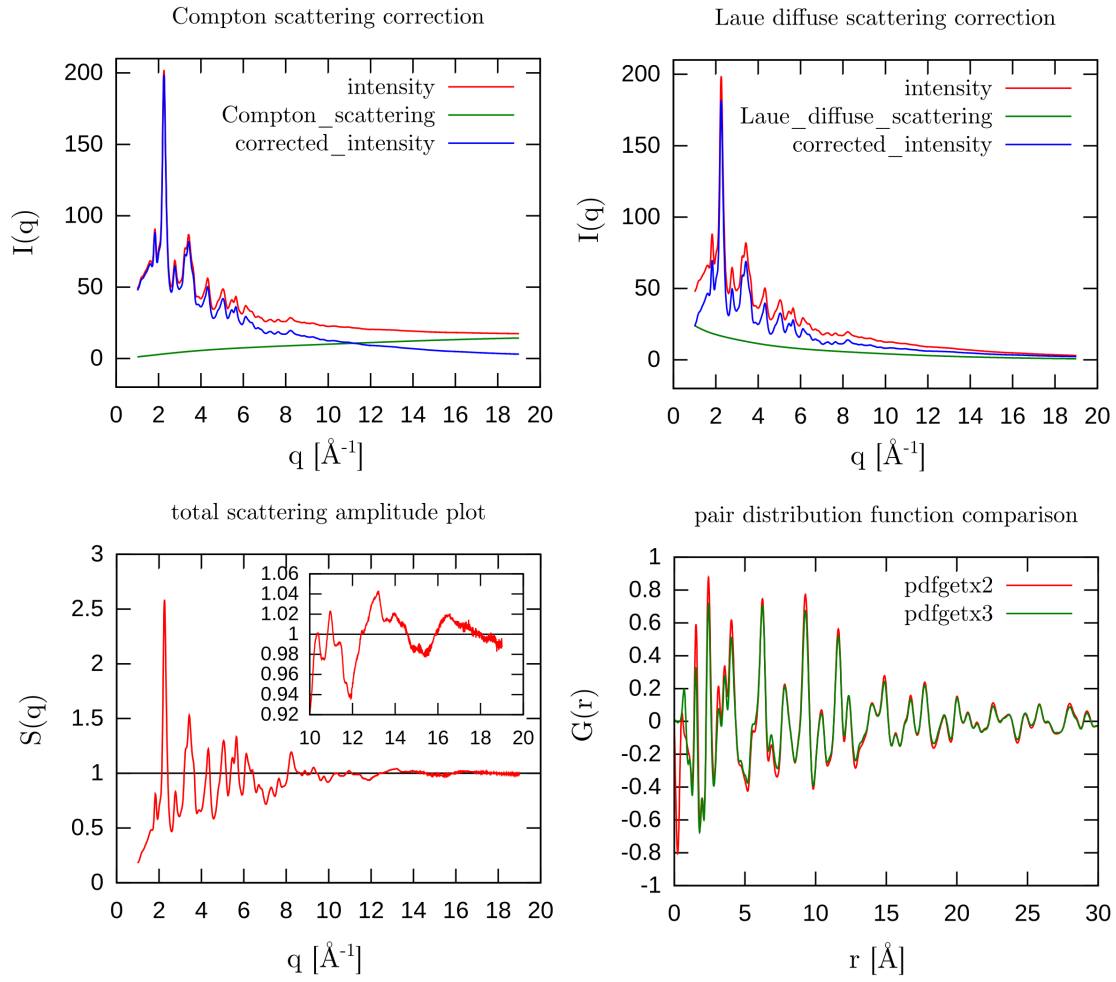

Figure 2.3: Transformation of the high-q resolution dataset of the *bos taurus* bone sample. Upper plot: intensity correction I(q) for Compton and Laue diffuse scattering contribution; lower left plot: total scattering amplitude plot S(q) with inset plot of the magnified high q region (10-20Å^{-1}) shows that the signal indeed oscillates around S(q)=1; lower right: the atomic pair distribution function G(r) where the results of the obtained PDF are compared, "pdfgetx2" plot is obtained by manual tinkering with correction factors, while the "pdfgetx3" result uses automated algorithms.

The PDF function of the various animal species bone samples is shown on the upper plot in Fig.2.4. Differences in the G(r) of several sampling attempts of one bone skeletal element is shown on the lower plot. From the plot of the G(r) of the examined animal species it can be concluded that there is no significant difference in peak position or peak breadth, but slight differences in peak amplitudes. This suggests that the atomic structure and inter-atomic distances are about the same for every bone sample. However, it needs to be mentioned that for the data

transformation the same chemical composition was used for every dataset. Slight differences in scaling could lead to differences in the PDF function. In the case of examined bone samples the chemical composition and precise stoichiometric values are missing and therefore values are hypothesised. Further investigation of the chemical composition on the PDF function requires additional measurements and extended analysis.

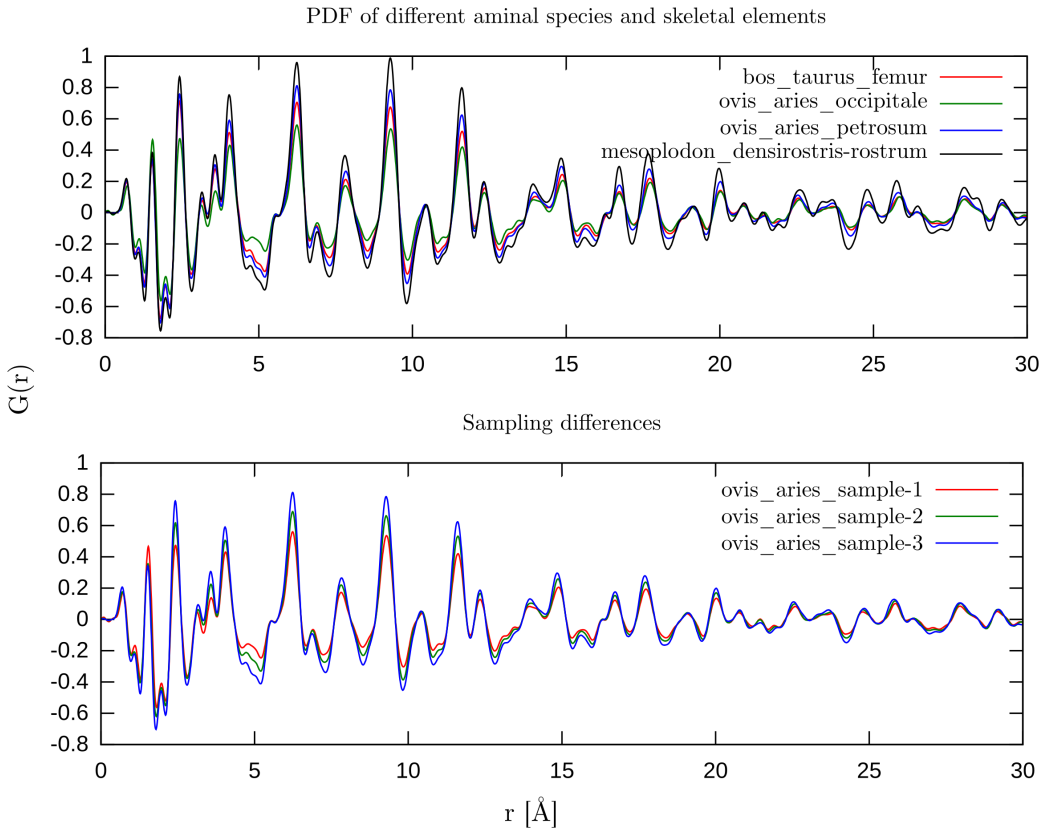

Figure 2.4: Comparison of the transformed diffraction patterns of the examined species. Upper plot: interspecies comparison; lower plot: sampling difference on the same species and same skeletal element.

2.2 Induced alteration due to preparation and extraction of bone samples

The preparation procedures for the extraction of the inorganic component of the bone material may inevitably cause moderate or severe changes on the microstructure and crystal-chemical structure of the nanocrystallites. Comparison of sample preparation procedures executed on the identical starting material (pulverized

bovine femur) is compared. Procedures including acid washing are used in order to dissolve outer layers of bone material while sample preparation of the bone material for stable isotope ratio measurement. These sample preparation procedures will be relevant for the experiments and analysis of the environmentally altered bone samples in Chapter 4. It is expected that this treatment removes exogenous isotope material by keeping the original (indigenous) isotope ratios intact. Procedures including washing with HCl, HCOOH and NaOCl are applied specifically for measurement of strontium and lead isotope values. The acid treatment is intended to serve as a surface cleaning method. De-proteination using sodium-hypochloride is a sample preparation procedure that is expected to remove organic material leaving the inorganic calcium-phosphate properties for examination.

2.2.1 Sample preparation procedures

A complete *femur* skeletal element of *bos taurus* was obtained in fresh state. After the removal of organic tissue the remaining hard bone material was washed with deionized water in an ultrasonic bath. The long bone section of the *femur* was cut into small cubes of approximately $2cm^3$ and washed in a soxhlet apparatus. After the washing and drying of the bone cubes, they were crushed to powder state and sieved through a $100\mu m$ filter. Further on, this material is referred to as the reference state of the bone material. Preparation of the bone material with HCOOH and HCl was conducted on the cube bone pieces, where they were washed with 98% concentrated HCOOH in one case, and 37% HCl in the other case both for 5min duration. After the acid wash, the material was rinsed with deionized water until a neutral pH was achieved. The bone pieces were then crushed and pulverized. In the de-proteination procedure, 4% diluted NaOCl (sodium-hypochloride) was used on the already powdered material, where 100mg of powder was soaked with 5ml of sodium-hypochloride for 2 days. The procedure was repeated for an additional day with new solution.

2.2.2 Results of diffraction data comparison

Comparison of the low q resolution diffraction patterns of the various sample preparation procedures and the reference starting material is given in Fig.2.6. A comparison of the PDF function is given in Fig.2.5. Visual observation of the examined data suggests that there are subtle differences from sample to sample. The impact of HCOOH and HCl treatment is barely resolvable from the diffraction data, while the de-proteination has significant change in the microstructure (Fig.2.6) and the amplitudes of the PDF function (Fig.2.5).

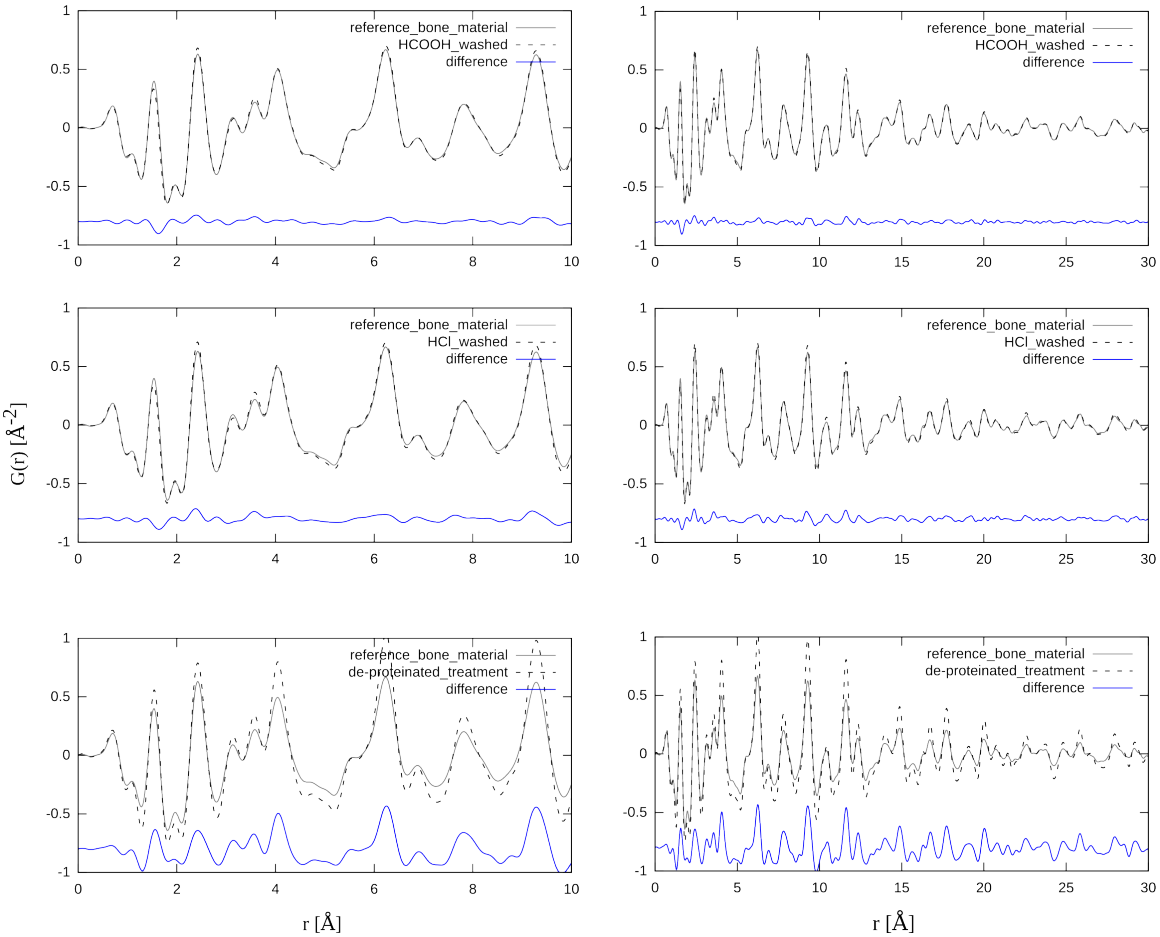

Figure 2.5: Atomic pair distribution G(r) plot of the different bone washing preparation treatments directly compared to reference preparation using pure water. Upper row - HCOOH acid preparation described in the text; Middle row - HCl preparation; Lower row - result of NaOCl de-proteination procedure; In each plot the relative difference from the reference bone sample is shown. The reference bone sample was prepared with only water washing. The difference curve represents the subtraction of the PDF patterns from the reference sample PDF. Plots on the left column are the section from 0 to 10Å, the right column shows the full pattern up to 30Å.

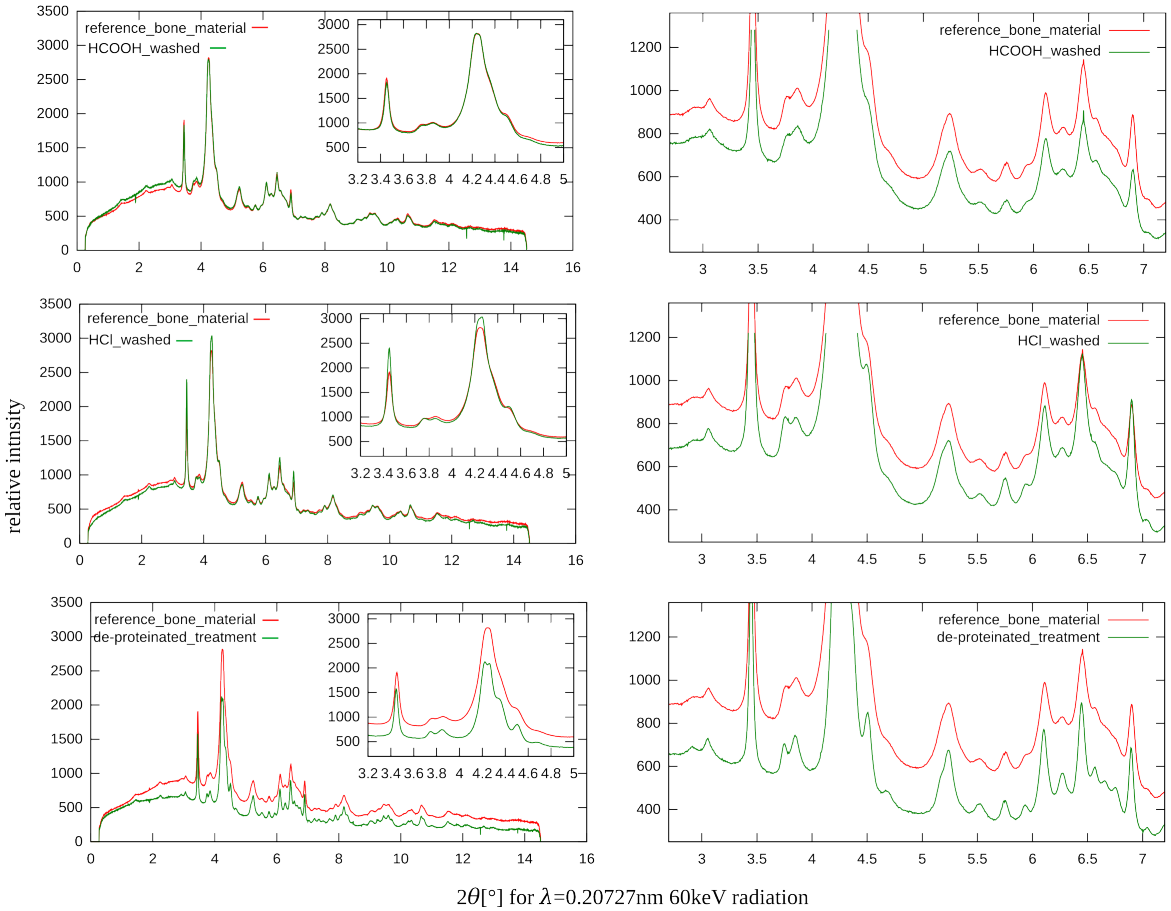

Figure 2.6: Diffraction pattern of bone material samples that have been exposed to different washing treatments. The reference (initial material) is shown on each plot (with red line). Upper row - HCOOH acid preparation described in the text; Middle row - HCl preparation; Lower row - result of NaOCl de-proteination procedure; In each plot the reference bone sample is plotted for visual comparison.

2.3 Conclusion

Powdered bone samples of three animal species *mesoplodon densirostris, ovis aries* and *bos taurus,* and two anatomically different skeletal elements of the *ovis aries* (os *petrosum* – inner ear bone and *os occipitale* – basal vertebra) have been empirically compared based on observations from the measured diffraction data. In addition the transformation of the diffraction patterns to the pair distribution function data is demonstrated and described. The comparison of the diffraction and PDF patterns suggest that the difference between species can range from significantly different (as in the case of the *mesoplodon desirostris*) to almost indistinguishable. The difference between the skeletal element is very mild, which may be due to the sample powder averaging.

More extensive variation in the diffraction pattern data can be seen in the case of the chemically washed samples. The large difference seen in the bone sample prepared with NaOCl washing may be due to long exposure to water. It may also be due to the fact that this washing/cleaning methods were performed on already crushed and pulverized material and so a large interaction surface was available for the reaction. The HCl and HCOOH washed sample have been prepared as centimetre sized bone chunks and were pulverized later. The aspect of water influence on the material will be further investigated in Chapter 7, when synthetic bone-analogous materials will be discussed and the transformation of amorphous calcium-phosphate into HAP will be discussed.

Visual comparison of the data as a difference from the dataset of the reference bone sample is possible in a direct way only for the PDF-s while the patterns are normalized. In the case of the angle-dependent diffraction pattern (in reciprocal-space) the counts are relative and not-normalized. A direct comparison of peak-features can be done in speculative manner. Quantitative and qualitative evaluation using calculation methods such as the Rietveld method is needed to adequately compare these diffraction patterns. Structural model testing is explored in the following Chapter 3, where an automated way of systematic evaluation is presented on selected examples that illustrate the evaluation and modelling possibilities. Nevertheless, the very small differences between these investigated samples are very problematic to quantify and unambiguously prove via any characterization technique and data evaluation method.

In continuation, experimental alteration of bone samples have been conducted. Natural bone alteration experiments are investigated and described in Chapter 6. In the altered states the Bragg peaks appear more resolved allowing more accurate evaluation. As the altered state of the material stem from the original properties, observations made on the altered state can allow inference about the original state.

Chapter 3
Automated Rietveld refinement

"The purpose of computing is insight, not numbers."
– Richard Hamming, mathematician

3.1 Approach

The problem of false minimum is well known in the field of diffraction pattern analysis and crystallographic structure optimization methods. Also, deriving the solution can end in a state where some of the parameters don't have physically meaningful values. The usual approach to bridge these issues is by applying refinement strategies. A "refinement strategy" can be seen as a predefined sequence of refinement steps. A widely accepted approach to the Rietveld refinement is a "step-by-step" execution of unlocking parameters of interest and so consecutively increase the number of parameters toward a better model-to-data fit. In such a scenario it is usual to encounter bifurcation points, from which the refinement sequence can be different leading to alternative outcomes, break down, or produce unrealistic results.

General refinement step sequences are known as a basic template to evade non-converging refinements. They rely mostly on the experience and familiarity of the user with the investigated crystallographic system and measurement conditions. The question of a universally "correct" template of refinement step sequence had been widely investigated (Dinnebier, 2008; Pecharsky and Zavalij, 2009; Young, 1993 p32-36). In practice, however, usually a lot of try-and-error work is applied to get an acceptable result. The sequence and the choice of the refined parameters can, indeed, have an influence on the final result. Schwarzenbach argues that the "...use of established procedures in widely distributed software may be as harmful as the natural tendency of most people to prefer results in agreement with preconceived ideas" (Schwarzenbach et al., 1989).

To achieve acceptable values for the interpretation of the diffraction patterns one can define a set of best suiting sequence of refinement steps that solves the structure in question. However, this approach could potentially lead to unresolved systematic errors that can not be easily tracked. Automatizing the Rietveld refinement evaluation approach, not only the refinement steps can be executed automatically, but also different refinement sequences can be tested and compared. This way the problem of systematic errors and biases by the conductor of the

refinement can be at least made transparent.

3.1.1 Existing solutions

Rietveld refinement software such as "GSAS" (Toby and Von Dreele, 2013) and "FullProf" (Rodríquez-Carvajal and Roisnel, 2004, Rodríguez-Carvajal, 1993) allow the possibility of wrapping the core functions of the software, using them as the refinement engine. Solutions such as the "Sr-Rietveld" (Tian et al., 2010) uses both 'FullProf' and 'GSAS' to conduct refinements. It can be used to follow up the flow of the refinement and parameter behaviour in real-time through a graphical user interface. This solution can also compare the results of different refinements. According to the description of "Topas Academic" (Coelho, 2007), it can be used for parametrized refinement and strategies testing as well. However, the TOPAS software was unavailable in the scope of the research, as it requires a paid licence. GSAS can be used as the refinement engine through macro files as in "Gsas-language" by Vogel (Vogel, 2011). The latest contribution to automated Rietveld refinement was by (Frølich and Birkedal, 2015) who wrote a MATLAB wrapper 'MultiRef' around GSAS for evaluating thousands of diffraction patterns from XRD tomography.

3.1.2 Concept of the automation with "AlgoRun"

In order to explore the stability of a Rietveld refinement solution a python script "AlgoRun" was written that uses "FullProf"-s refinement engine. Originally "FullProf" can handle multiple file refinements (by applying the same **.pcr* file to many diffraction pattern files), however, it does not have a feature for refinement strategy comparison and stepwise execution of refinements on single and/or multiple datasets and using several crystallographic models. The code described in this thesis extends "FullProf"-s functionality by accessing the refinement control file (**.pcr* file) and directly modifying it programmaticaly. In this way one can test: 1) many variations of the **.pcr* file onto one diffraction pattern, where the modification of the **.pcr* file can be parametrized as well, 2) evaluation of many diffraction patterns all with various, altered **.pcr* files.

The script requires a working **.pcr* file as a start. The code makes automated text editing of the refinement control file (**.pcr*) and conducts refinement runs. The **.pcr* file is altered according to a strategy contained in a special file (**.ctrl* file), where the refinement instructions are stored in step-wise order. This file contains essentially the "recipe" for the refinement. Each step executes a refinement with a specific alteration to the control file. The work-flow conceptually follows the manual try-and-error approach, but with the advantage that the refinement instructions are documented and read from a text-file (the **.ctrl* file), which can be generated,

altered, modified and revisited at any time. More details about the code and its availability in appendix A2-p193.

The output files of each refinement are organized and each refinement step can be reviewed separately. Utilizing organized and systematic refinement strategies in an automatized manner the validity of the found local minimum of the result can be evaluated with respect to the way it was obtained. The approach presented here focuses on the testing of the refinement and the validity of the resulting parameter values from the refinement. Application can cover:

- parameter control and refinement strategies comparisons
- structural model or phase mixture hypothesis testing
- refinement solution comparison and classification
- introducing perturbations on parameters
- test various parameter combinations in the form of an automated strategy comparison

The global optimization least squares algorithm returns a set of parameter values that produce the best match to the measured dataset. If the values for each free parameter are in a reasonable range, the refinement is accepted as valid based on assumptions about what a correct value should be. Whether the obtained values are accurate with acceptable precision is debatable and it is depending on the initial assumptions. Since the evaluation of diffraction patterns is interpretation dependent there is no absolute solution, but only accepted solutions. With the proposed refinement strategy testing approach this argument is explored.

The "AlgoRun" script can also be used for the evaluation of a larger number of diffraction patters, in case the number of patterns exceeds the capacity of manually refining them one-by-one. It is possible to run every refinement using any number n of different strategies with various refinement steps (schematically shown in Fig.3.1). Furthermore, it is possible to test m number of structural models, with n number of strategies on any number of diffraction patterns.

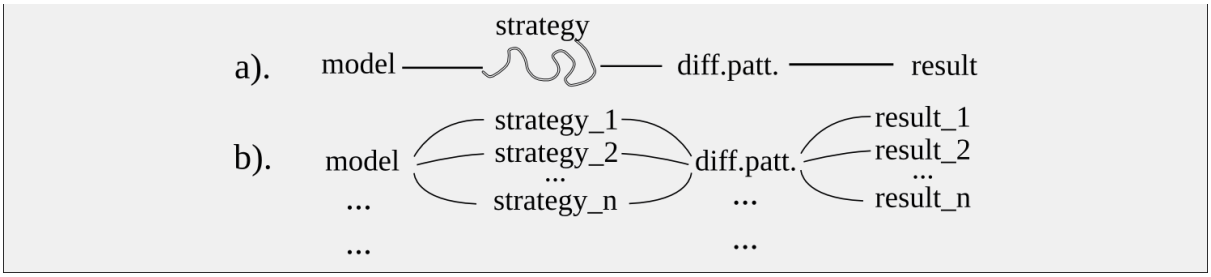

Figure 3.1: Combination of models, strategies in diffraction pattern evaluation.
a). direct route of manual refinement with try-and-error approach, b). a set of strategies is applied on the diffraction pattern using a crystallographic model (assumption). It produces equal number of results as the number of strategies. m-number of models can be tested (compared) with n different strategies producing m*n number of results on a single diffraction pattern. Ultimately, several structural models can be used to refine a large number of diffraction patterns, for each with n number of strategies.

Generally, the optimization algorithm can be run for an arbitrary number of iterations. Usually a convergence criterion is set and depending on the end of the iteration cycles the state of the refinement is judged as converged or not-yet converging. The speed how fast a global optimisation process can search in the parameter space can be usually also controlled by defining the distance for the next random value in the least-square fit. Due to this reference frame, there can be a significant difference in the result in the case where the initial values of the introduced parameters differ significantly from the accurate ones. A usual way to practically handle this situation is to lock all relevant parameters before introducing a new additional parameter to the refinement. This rises the question of the releasing sequence and the order of the parameters introduction. In the case where a large number of parameters is made available for optimization the likelihood that the refinement will reach a false minima is significantly greater. For this reason the "AlgoRun" code makes all combinations of the given parameters and explores which case of the introduction sequence and combination yields the most matching refinement. A set of rules are necessary in this case to distinguish between non-physical solutions (local minima) and solutions with parameter values in an acceptable range. However, it is to be emphasised that any set of rules contain the bias of the conductor towards expected results and it is therefore not fully objective. After the execution of all the refinements, the reliability factors are listed out and sorted in descending order. Each result is now evaluated according a set of rules to judge the validity of the result. Such rules can be constituted of: no negative values of the mean square atomic displacement factors, sign of the U,V and W parameter values has to be positive (U), negative (V), positive (W), specified inter-atomic distances have to be inside an acceptable value range, etc.. All these criteria can be

easily checked when the values of the parameters are extracted from the output files.

In order to have an insight on the effect of different free parameter combinations and their sequence of introduction, a set of strategies is composed. A set of strategies is formed by combining blocks of refinement steps. Each strategy is formed of a set of steps that the refinement will go through. After all the refinements are done their output is collected in a database. Even though two refinements can have the same number and same free parameters, their sequence of introduction to the refinement can yield different parameter values. If the refinement produced values for parameters that contradict the defined rules, the solution is rejected and the next best matching refinement in the sorted list is considered.

In a constrained fit, such as the Rietveld refinement, the state of the parameter can be free or locked (fixed) to a certain value while iterating through the optimization cycles. Switching between the attributes can be considered as a search algorithm. In this approach a difference can be made between the following cases: 1. "switch on-off" case, where a parameter is let free for a given number of refinement cycles and then fixed (locked); 2. "dragging the parameter", where the parameter is let free at a certain step and kept so; 3. "let free at the end" case, where at the end all relevant parameters are let free following the assumption that by doing so the system will find it's true global minimum. These approaches can be readily moulded into strategies and tested which has more merit and effectiveness.

3.2 Example 1.: Lanthanum-hexaborate NIST standard material

In microstructural analysis from powder diffraction patterns, the broadening of profile functions is analysed. However, the contribution of the instrumental broadening has to be deconvoluted from the intrinsic signal of the investigated material. There are in general two ways to deal with the deconvolution: 1. measuring a known material (standard material) and mapping the broadening of the instrument and deconvoluted from the pattern of the actual sample; 2. fundamental parameter approach (FPA), where the instrumental broadening is modelled using values of the optical set-up of the instrument – the contribution is calculated analytically and deconvoluted for every measurement. In this thesis the first method is applied and the lanthanum-hexaborate standard material is used to obtain the instrumental resolution file.

In the case of the known standard material of LaB_6, there are only a few parameters that are accessible for the refinement, these are: background polynomials, Cagliotti profile function parameters, one fractional coordinate of the boron atom position, overall temperature factor or the temperature factor for the lanthanum and boron atom. It is to be expected that the result of a refinement with different number

of background coefficients will have a great impact on the results, especially with respect to the correlation of the temperature factors and atomic positions. It is impossible to guess the right order and number of background parameters and its correlation with the rest of the parameters since the background signal largely depends on the measuring instrument set-up and measuring conditions. Moreover it is modelled as a polynomial series with no physical meaning assigned to the coefficients.

Further on, a comparison of LaB_6 refinement on measurements with a laboratory type X-ray source (Cu-tube) measured with a 1D detector in reflection mode and synchrotron transmission mode measurement with a 2D detector using kapton as well as boro-glass capillary will be discussed. Refinement strategies containing various numbers of background parameters have been devised and the fit results are compared. The strategies vary in the sequence of free parameters introduction to the refinement as well as in the order which they are locking to a value. After running all the refinements the results for each strategy refinement are extracted, sorted and filtered using defined rules: thermal factors between 1 and 0, positive U,W,X,Y coefficient and negative profile shape parameter V. Refinement of synchrotron data in boro-glass capillary resulted with a strategy containing 12 background, U,V,W,X, sample displacement, boron atomic position and mean thermal displacement factor and lanthanum thermal factor. This set and order of parameters resulted in the lowest residual chi^2 factor, while satisfying all rules. The reliability factors are: Rwp=9.66, Re=3.41, chi^2=8.05, Rf=1.96 with number of free parameters Npar=20. Synchrotron data of LaB_6 in kapton capillary resulted in a best fit with the same strategy. The obtained reliability factors were: Rwp=9.03, Re=4.61, chi^2=3.832, Rf=1.99 with Npar=20. In the case of the Cu-tube radiation the best strategy was the same as for the synchrotron data refinement. The reliability factors are Rwp=19, Re=14.8, chi^2=1.65, Rf=2.28 with Npar=20.

The refinements are plotted in Fig.3.2. Both synchrotron measurements have a more complex background signal that requires a higher number of coefficients to model it adequately. In the case of the Cu-tube the high number of the background coefficients may be redundant. From the obtained results and from the plot of the fit, it can be seen that the signal-to-noise ratio is obviously significantly different due to the different photon flux of the used sources. Due to this fact the copper-tube source smears the actual background line introducing ambiguity. This can be inferred from the reliability factors as well where the smaller value of chi2 may signify over-fitting.

Nevertheless, this example demonstrates that the refinement of standard material can be automated in full extent even in the case of different measuring settings. For further microstructural analysis of the bone samples the instrumental resolution file is obtained from the fitted Cagliotti's profile function parameters (U,V,W).

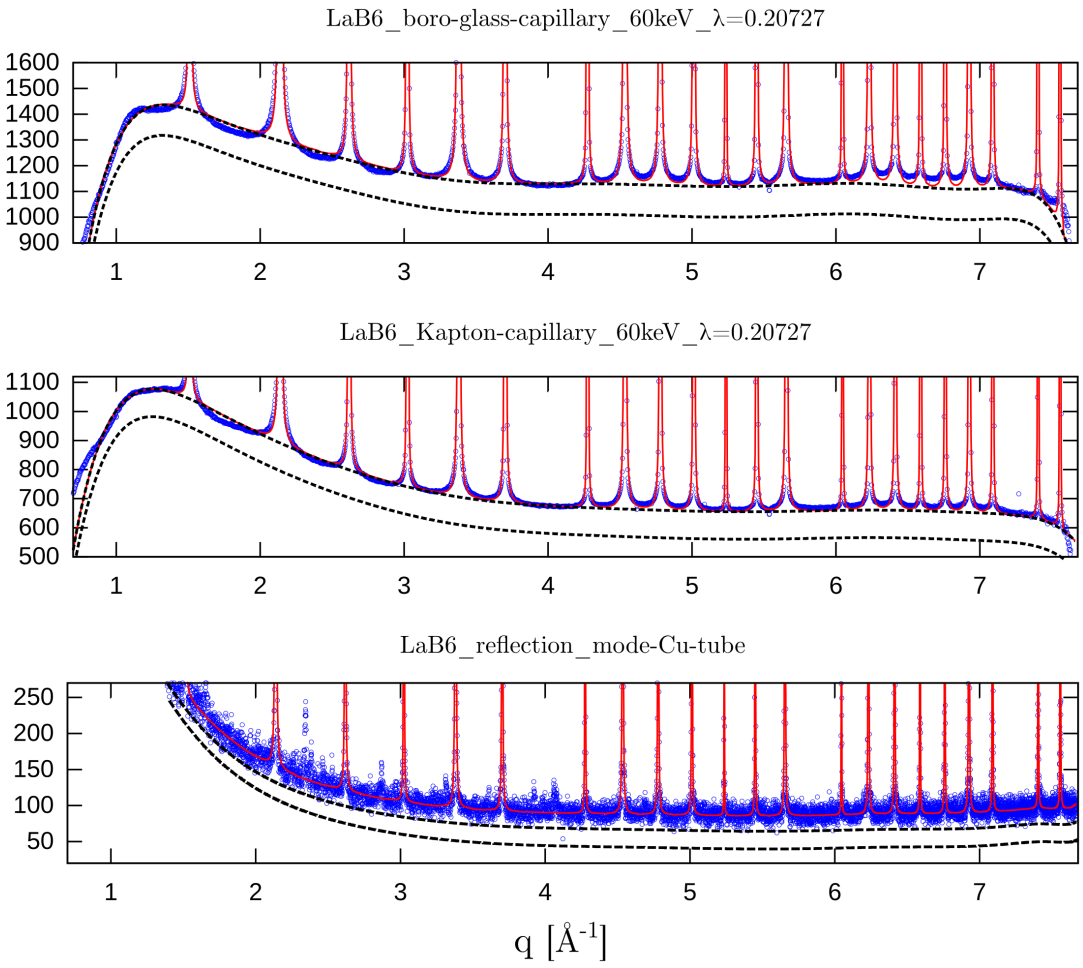

Figure 3.2: Results of automated refinement of NIST standard material on different instruments. The background signal is additionally shifted for viewing clarity (lower dashed line).

3.3 Example 2.: Refinement of bone material using soft constraints with various sigma values

In general "soft-constraints" in Rietveld refinement software represent additionally defined constraints between parameters, that limit the value of a parameter with a defined variance (usually denoted as sigma).

In this example a diffraction pattern of *bos taurus* femur and the *mesoplodon densirostris* rostrum bone samples are refined using various strategies with different soft constraint variance (increasing sigma values of the constraint). A refinement of the atomic position value for specific atom-to-atom distance (P-O) is fixed to a hypothesised value and different sigma vales are set (0.02, 0.008, 0.002). If the sigma value is too big, the obtained bond distances can result in unrealistic values, a false

local minimum of the refinement. On the contrary, if the sigma value is too narrow, the initial guess can be considered too strict. By using soft-constraints rigid body structural units are assumed, which in this case are the phosphate tetrahedra.

The obtained results are summarised in table 3.1 and the diffraction patterns of the refinements are shown for the case of σ=0.002 in Fig.3.3. The rules used to classify the results in this example are: positive isotropic mean displacement factors (Biso) with values below Biso>=2; P-O bond distances (P1-O1, P1-O2 and P1-O3) in range from 1.5 to 1.58 Å.

Table 3.1: Comparison of refinement results on two datasets (bos taurus and mesoplodon densirostris) with different variance (σ) of the P-O bond distance soft constraint.

		σ=0.002	σ=0.008	σ=0.02
Species: Bos taurus *skel. el.*: femur	strategy	#90	#88	#86
	Rwp chi^2	11 0.181	11 0.178	12.1 0.212
Species: mesoplodon densirostris *skel. el:* rostrum	strategy	#90	#86	#86
	Rwp chi^2	14.7 1.2	15.7 1.37	15.7 1.37

The strategies in Table3.1. are partially identical in the number of background parameters (12), lattice constants, anisotropic size and isotropic strain refined parameter introduction sequence. The difference is in accessing the Ca, P and O atomic position parameters. The strategy number #90 gradually introduces the P and O position parameters, locking them all before accessing the Ca position refinement. At the end the P and O are all let free again. Strategies #88 and #86 are different from strategy #90 as they access the P, O positions to be refined in one step. They differ also in the last step, where the Ca atoms are not refined in #86, while in #88 they are refined.

From this example the following conclusions can be drawn: (1.) as the sigma value increases the reliability factors increase as well. This indicates that with greater variance on the P-O distance (refined as the phosphorous and oxygen atom positions), the fit tends to be less reliable. This further signifies that when the parameters of P and O positions are allowed to shift more severely, the fit tends to slip into a more unrealistic result due to correlation between the parameters of the fit. (2.) the diffraction pattern of *bos taurus* shows a much greater broadening relative to the *mesoplodon densirostris.* The obtained chi^2 factors for the fit of the *bos taurus* samples (0.181, 0.178, 0.212) are very low and this might be considered as over-fitted.

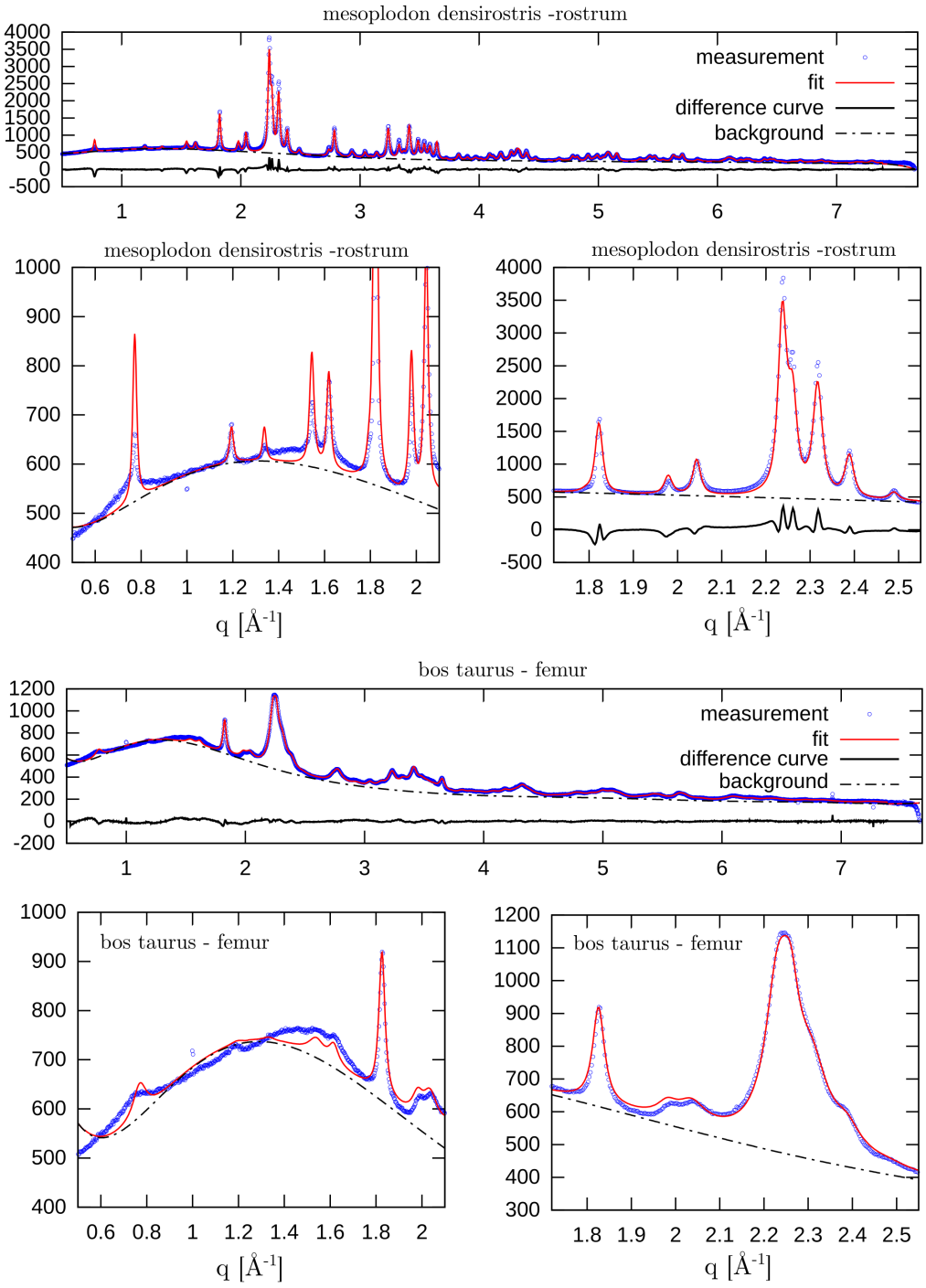

Figure 3.3: Rietveld refinement plots for bone samples of *bos taurus* and *mesoplodon densirostris* using the same crystallographic model in both cases. The sigma parameters of the constraints on P-O bond distances is 0.002. Zoomed in sections are shown for region 0.6 - 2, and 1.8 - 2.5 Å^{-1}. All vertical axes are relative intensities – scaling of the plots can be inferred from the axis values. The background behaviour appears unusual suggesting artefacts (detector, settings) of the acquisition at the synchrotron facility.

3.4 Example 3.: Structural model comparison

In case when the initial structure is not strictly known or formulated it is of importance to compare various crystallographic models during the evaluation.

In the COD (crystallographic open database) there are 178 reported structures matching a search using the chemical composition of Ca,P,O with optional H,C,F,Na,Mg,Cl and Sr. 107 of those are described in hexagonal, 54 monoclinic, 7 triclinic, 5 tetragonal and 5 as orthorhombic system. If we reduce the search to only calcium-phosphates as Ca,P,O with optional C and H then there are 31 hexagonal, 34 monoclinic, 4 triclinic, 2 tetragonal and 1 orthorhombic structures. However, the crystallographic information files (cif) obtained from this database are on many instances duplicated and not uniquely named. For this reason the ICSD database will be used further on.

In the ICSD (inorganic crystal structure database) the queries were conducted using the chemical composition and total number of atoms while listing out hexagonal and monoclinic models. In the scope of this thesis the obtained structure information files are clustered in 3 groups:
[G1.] Hexagonal structures with $P6_3/m$ space group that contain Ca,P,O,C,H and can incorporate other elements such as Na, Mg, Sr, Cl, F. This group contains 27 database entries which are carbonated apatite structures, Na-,Mg- bearing apatite structures etc.
[G2.] Hexagonal structures with $P6_3/m$ space group that contain only 4 elements Ca, O, P, H. This group counts 103 entries from the ICSD database. In this group are all the strictly hydroxylapatite structures.
[G3.] Monoclinic structures with 4 elements in total containing only Ca,P,O,H. This group contains 16 entries.

Two bone measurement evaluations will be presented here as an example of the automated Rietveld using models from the database. It is possible to run refinements using all of the structural models with the exact same refinement strategy on one or many datasets (diffraction patterns of various bone samples). Furthermore, it is possible to make phase mixture models with minor non-apatitic secondary phases (where the structural parameters of the secondary phase are kept fixed) in order to systematically and reliably compare them.

3.4.1 Hexagonal $P6_3/m$ structural models with ionic substitution

In the first approach only hexagonal structural models were used that have other elements next to Ca-P-O, such as C, H, Na, Mg, etc. (group G1). Refinements using all models from the first group (G1) – the hexagonal (space group $P6_3/m$) as single phase have been conducted in 80 ways (strategies), where each strategy varies in the number of background parameters, profile broadening parameters and atomic

positions in different sequences.

In table 3.2 the "top-list" of the obtained lowest chi^2 refinements that satisfy the filter rules is given. These rules are: accept refinement that produced P-O bond length between 1.56Å and 1.5Å in the phosphate tetrahedra; apparent domain sizes between 1000 and 0Å and with no strain. The refinement with the smallest chi^2 is shown in Fig. 3.4.

Table 3.2: Comparison results for two bone sample refinements using 80 strategies and 27 structural models of hexagonal space group $P6_3/m$ - (G1)

bos taurus femur					
	Chi2	ICSD entry	reference	chemical sum formula from ICSD entry	strategy
1.	0.237	171551	Fleet 2004a	$C_{0.22}$ $H_{1.562}$ Ca_5 $O_{13.514}$ $P_{2.823}$	61
2.	0.246	150311	Fleet 2004b	$C_{0.66}$ $H_{3.032}$ Ca_{10} $O_{27.572}$ $P_{5.64}$	61
3.	0.249	150311	Fleet 2004b	$C_{0.66}$ $H_{3.032}$ Ca_{10} $O_{27.572}$ $P_{5.64}$	61
4.	0.256	171550	Fleet 2004a	$C_{0.26}$ $H_{1.59}$ Ca_5 $O_{13.686}$ $P_{2.829}$	61
5.	0.269	171549	Fleet 2004a	$C_{0.01}$ $H_{1.3}$ Ca_5 $O_{13.33}$ P_3	61
10.	0.32	87677	Wilson 1999	$C_{0.57}$ $H_{2.18}$ $Ca_{9.412}$ $Mg_{0.049}$ $Na_{0.21}$ $O_{25.61}$ $P_{5.43}$	68
19.	0.36	87683	Wilson 1999	$C_{0.79}$ $H_{2.05}$ $Ca_{9.442}$ $Mg_{0.049}$ $Na_{0.211}$ $O_{25.26}$ $P_{5.21}$	48
mesoplodon densirostris rostrum					
1.	1.27	171549	Fleet 2004a	$C_{0.01}$ $H_{1.3}$ Ca_5 $O_{13.33}$ P_3	61
2.	1.28	171549	Fleet 2004a	$C_{0.01}$ $H_{1.3}$ Ca_5 $O_{13.33}$ P_3	41
3.	1.303	171549	Fleet 2004a	$C_{0.01}$ $H_{1.3}$ Ca_5 $O_{13.33}$ P_3	66
4.	1.304	171549	Fleet 2004a	$C_{0.01}$ $H_{1.3}$ Ca_5 $O_{13.33}$ P_3	21
5.	1.312	171549	Fleet 2004a	$C_{0.01}$ $H_{1.3}$ Ca_5 $O_{13.33}$ P_3	46

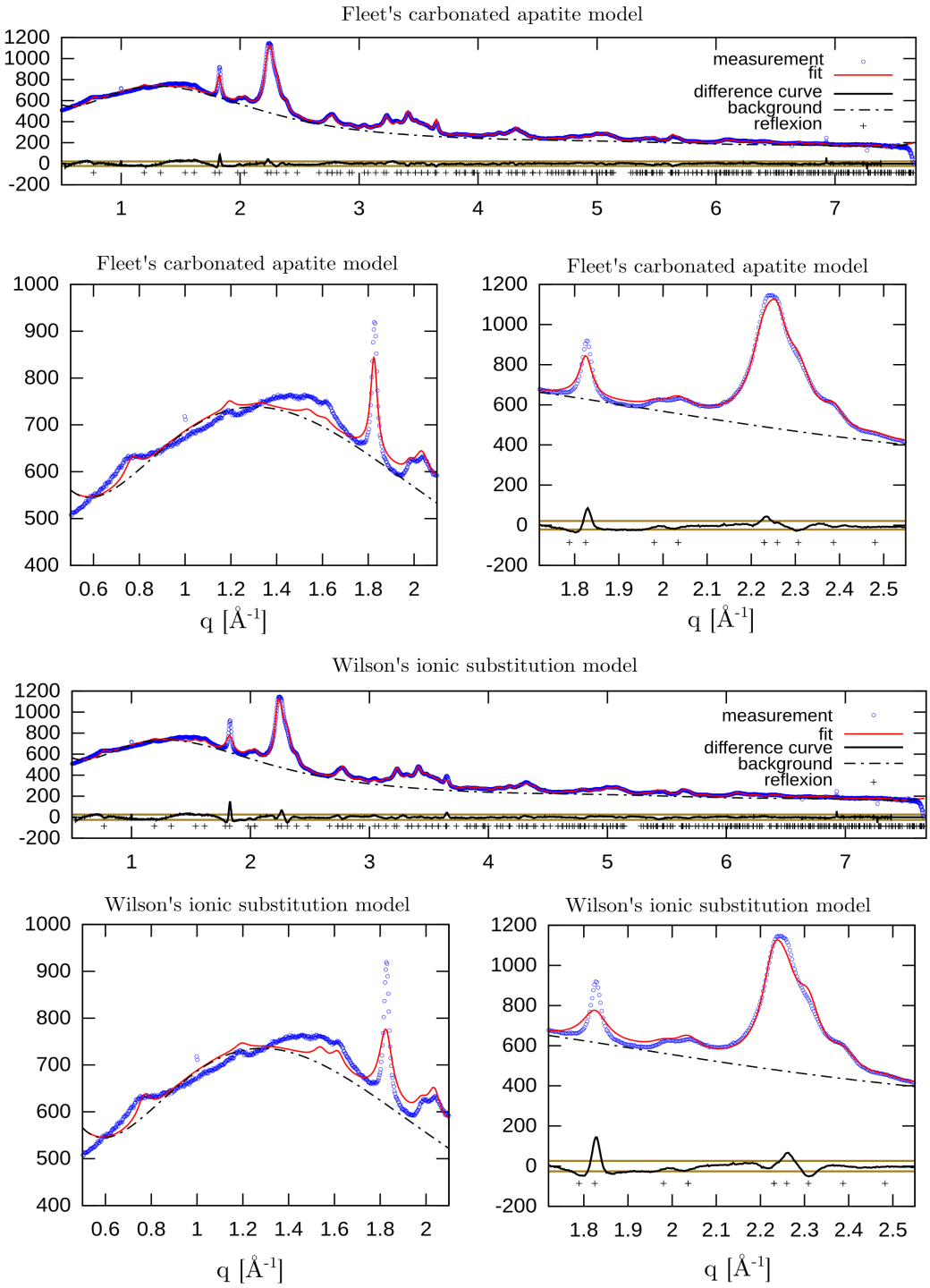

Figure 3.4: Comparison of the refinement structural models on the *bos taurus* femur diffraction pattern using Fleet's carbonated-apatite model (upper plots) and Wilson's cation substitution on calcium sites (lower plots). Zoomed in sections are shown for region 0.6 - 2, and 1.8 - 2.5 $Å^{-1}$. All vertical axis are relative intensities – scaling of the plots can be inferred from the axis values The unusual background suggests artefacts (detector, settings) of the acquisition at the synchrotron facility.

From Table 3.2 it can be seen that the diffraction pattern for the *bos taurus* femur is modelled very well with the carbonated apatite model of Fleet et al. (2004a). This is true also in the case of diffraction pattern of the *mesoplodon densirostris* (showing more developed peaks). Interestingly, the database entry of Wilson et al. (1999) the apatite structure accommodates other cation in the structure next to carbonate anion. In Fig.3.5 the difference of the fit models are compared after the refinement. Model of Fleet et al. results with a fit with narrower peak for the 00l reflections.

The results suggest that the broad diffraction Bragg peaks of bone samples are very accurately (to a certain degree) modelled using carbonated structures. However, original bone material does contain other cations as well (Na,Mg, etc.). Refinements with structural models incorporating other cations as well produced slightly worse reliability factors.

The model comparison shows that there is no unique single phase average structure in the database that can adequately describe the hypothesised crystal chemistry of the bone material samples examined in this example.

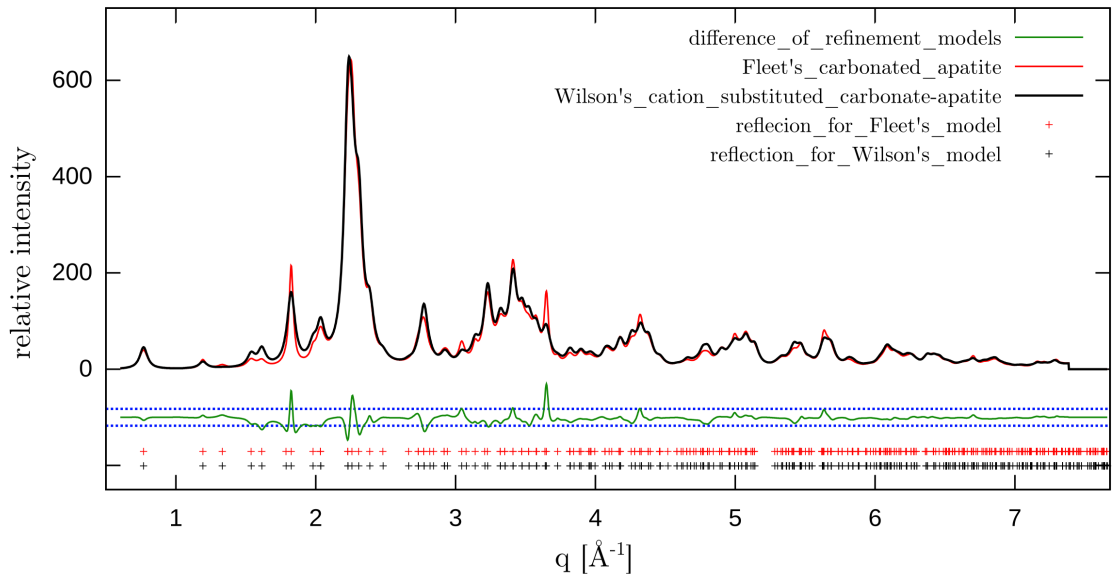

Figure 3.5: Difference of the resulting fit curve of the two refinements: carbonated-apatite (Fleet's model) and cation substitution on calcium sites (Wilson's model). The background is subtracted from the fit-curves. The blue dashed lines represent 2 standard deviation limits from the residual mean.

3.4.2 Monoclinic structural models of Ca-P-O-H composition

In the second approach, the two bone diffraction patterns have been refined using monoclinic structural models (group G3 described above). These refinements have been conducted without accessing atomic parameters due to the numerous atom sites. In each case only background, lattice and peak profile broadening parameters have been refined. The obtained results are listed in Table 3.3.

Comparing the results from Tables 3.2 and 3.3, it can be seen that the chi^2 values are somewhat higher then in the case of hexagonal model refinements, but it is still nearly an acceptable model. It also needs consideration that no atomic positions have been refined in the monoclinic model. This model might also have ionic substitutions which have not been examined in the scope of this example. The best matching monoclinic model is graphically show in Figure 3.6.

Table 3.3: Comparison results for two bone sample refinements using 80 strategies and 16 monoclinic structural models – (database search group G3)

bos taurus femur						
	Chi2	ICSD entry	reference	chemical sum formula from ICSD entry	space group	strategy
1.	0.323	34457	Elliott 1973	$Ca_5\ O_{13}\ P_3\ H_1$	P 1 1 21/b	29
2.	0.323	34457	Elliott 1973	$Ca_5\ O_{13}\ P_3\ H_1$	P 1 1 21/b	25
3.	0.328	34457	Elliott 1973	$Ca_5\ O_{13}\ P_3\ H_1$	P 1 1 21/b	24
4.	0.338	50656	Ikoma 1999	$Ca_5\ O_{13}\ P_3\ H_1$	P 1 1 21/b	25
5.	0.338	50656	Ikoma 1999	$Ca_5\ O_{13}\ P_3\ H_1$	P 1 1 21/b	29
9.	0.346	93932	Suetsugu 2001	$Ca_5\ O_{13}\ P_3\ H_1$	P 1 1 21/b	25
mesoplodon densirostris rostrum						
1.	2.01	34457	Elliott 1973	$Ca_5\ O_{13}\ P_3\ H_1$	P 1 1 21/b	29
2.	2.01	34457	Elliott 1973	$Ca_5\ O_{13}\ P_3\ H_1$	P 1 1 21/b	25
3.	2.02	34457	Elliott 1973	$Ca_5\ O_{13}\ P_3\ H_1$	P 1 1 21/b	21
4.	2.024	34457	Elliott 1973	$Ca_5\ O_{13}\ P_3\ H_1$	P 1 1 21/b	17
5.	2.06	34457	Elliott 1973	$Ca_5\ O_{13}\ P_3\ H_1$	P 1 1 21/b	13

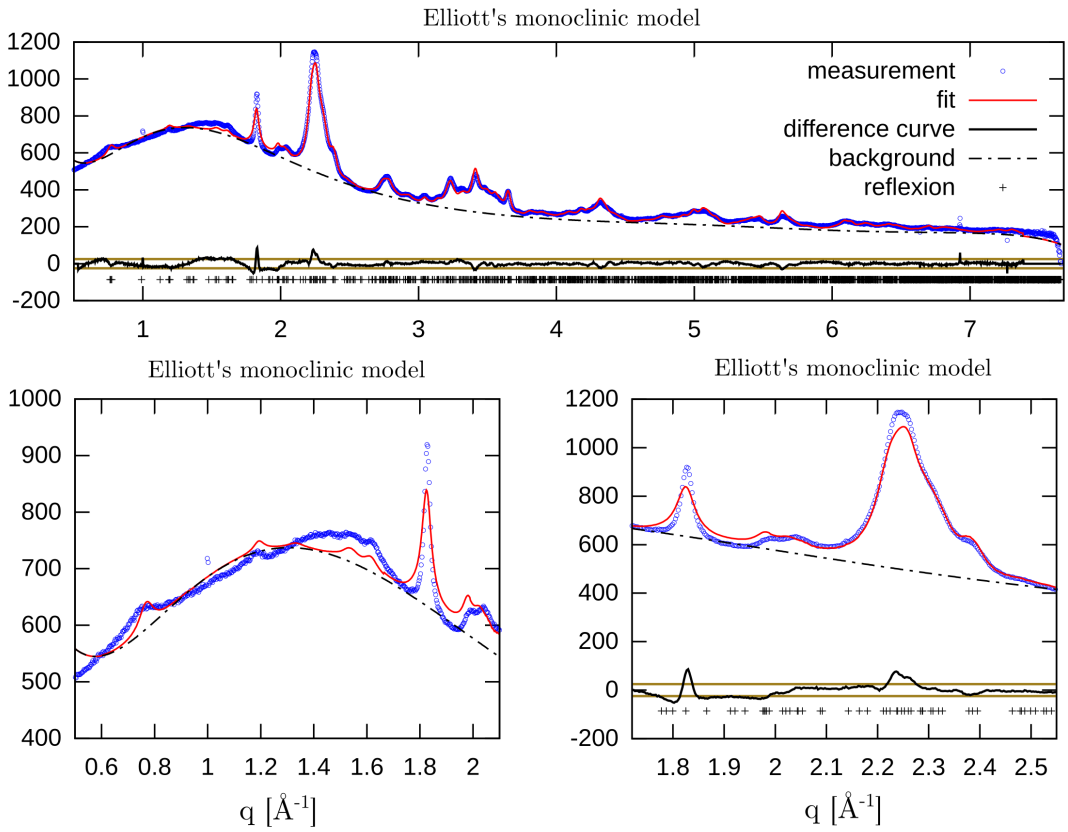

Figure 3.6: Refinement with a monoclinic structural model of Elliott (1973)

3.4.3 Hexagonal structures of Ca-P-O-H composition

Structural models of hydroxylapatite phase have been also tested (G2 group from above). 103 reported hexagonal $P6_3/m$ structures of only Ca-P-O-H composition yields results summarized in Table 3.4.

By comparing the reliability factors in Table 3.2 and Table 3.4, it can be concluded the reference bone of the *bos taurus* femur is better fit using Fleet et al.-s carbonated model, than the hydroxylapatite, and even the calcium deficient-hydroxylapatite structural models. The best fit in both structural model groups was achieved using the same strategy (denoted here as #61). However, the diffraction pattern of the *mesoplodon densirostris* rostrum has been better refined using non-carbonated models of hydroxylapatite. This would indicate that the rostrum sample contains less carbonate, but it might also be that the result is due to the better crystalline state (narrower peaks, less overlapping).

Table 3.4: Results of hydroxylapatite (HAP) structural model comparison

bos taurus femur					
	Chi2	ICSD entry	reference	chemical sum formula from ICSD entry	strategy
1.	0.251	154312	Stork 2005	$H_{0.48}$ $Ca_{4.992}$ $O_{12.48}$ P_3	61
2.	0.255	169499	Tanaka 2010	H_1 Ca_{10} $O_{25.5}$ P_6	61
3.	0.258	154306	Stork 2005	$H_{0.69}$ $Ca_{5.04}$ $O_{12.69}$ P_3	61
4.	0.259	154314	Stork 2005	$H_{0.684}$ $Ca_{4.992}$ $O_{12.684}$ P_3	61
5.	0.262	154307	Stork 2005	$H_{0.726}$ $Ca_{5.04}$ $O_{12.726}$ P_3	61
mesoplodon densirostris rostrum					
1.	1.22	87670	Wilson 1999	$H_{3.748}$ $Ca_{10.132}$ $O_{27.088}$ $P_{5.958}$	61
2.	1.22	87670	Wilson 1999	$H_{3.748}$ $Ca_{10.132}$ $O_{27.088}$ $P_{5.958}$	41
3.	1.231	87670	Wilson 1999	$H_{3.748}$ $Ca_{10.132}$ $O_{27.088}$ $P_{5.958}$	21
4.	1.232	87671	Wilson 1999	$H_{3.39}$ $Ca_{10.084}$ $O_{27.15}$ $P_{5.94}$	61
5.	1.233	87670	Wilson 1999	$H_{3.748}$ $Ca_{10.132}$ $O_{27.088}$ $P_{5.958}$	41

3.4.4 Phase mixture models – hexagonal and monoclinic

Two phase mixtures refinements converged in almost all of the cases to a result with over 99wt% hexagonal phase with virtually no monoclinic phase. This can be interpreted as a consequence of the correlation between the free parameters in the fit. When there is no additional constraint or restrain it is practically impossible to resolve the monoclinic from and hexagonal phases using the Rietveld method alone in the case of powder diffraction on bone samples.

3.4.5 Concluding discussion on the structural model comparison

When using a one-phase crystallographic structural model, it is not possible to obtain a unique and unambiguous structural solution fit in case of the examined powdered bone samples. This conclusion is derived from the observation that there are no combinations in the set of available parameters that will optimize the structural fit to a satisfactory refinement. Better match can be obtained at the expense of some parameters taking on unrealistic values.

The applied refinement strategy appears to result in moderate changes in the resulting parameter values. However, the evaluation of the refinement, in the presented approach depends on the chosen set of rules for the acceptance of the obtained parameter values. When the refinement of several strategies, models or

datasets are compared, the “top-list” of solutions can change depending on the intervals of values set in the rules. In the examples presented, the P-O distance rule was chosen between 1.56Å and 1.5Å, which is an assumption. There might be another better fit, with slightly higher P-O distance that was disregarded (in the presented example this wasn't the case). The meaning of the obtained result therefore heavily depends on the previous assumption made prior to the refinement. The “AlgoRun” code highlights only the flexibility of the method and suggest the strict consideration of the preconceived assumptions.

The refinement plots in all examples show discrepancy regions around the 002 reflection (strong peak near 1.8$Å^{-1}$ in Fig3.3.-3.6.). It appears that this is in some relation to the background signal. It is also possible that systematic errors occurred while positioning the sample during measurement, or it is a contribution from the sample holder capillary. The overall difference between the measured diffraction pattern and the models suggests that simple models with a unique average structure might not be appropriate for modelling the bone material powder samples. Domain size distribution, size anisotropy and local deviation from the long range order might have a combined effect that produces diffraction pattern features that would require extended evaluation methods reaching beyond the classical Rietveld method.

3.5 Conclusion and discussion

The inability to solve the phase problem in structure refinement requires optimization methods in order to match and retrieve improved structural information from measurements. Although optimization algorithms are very efficient, they are bound to the initial conditions (starting model, parameter values). The quality of the optimization can only be as good as the initial structural model. Nevertheless, diffraction based structure solving methods play a major role in the research of crystalline and non-crystalline matter on the fundamental level.

3.5.1 Optimization algorithms

An alternative for least-squares fit are direct methods for structure solution. This can be defined as a large number of parameter combinations used to calculate a diffraction pattern that is then matched against the measured diffraction pattern. Summary discussions on structure solving methods are given, for example, by Černý and Favre-Nicolin (2007), and Wagner (1978). First principle methods are based on Monte-Carlo algorithms to find the most suited hypothesised structure. Recently Markov-Chain Monte Carlo (MCMC) methods have been coupled with Bayesian

inference as an alternative for the estimation of the standard errors of the structural parameters (Gagin and Levin, 2015). This approach maps the parameter space by combining given values ranges of the parameters that are selected randomly by the MCMC. The uncertainties are given as probability functions instead of an estimated error. This method needs a large number of simulations in order to have valid statistical evaluation. Giving the result in terms of an uncertainty distribution (as in the article of Gagin and Levin, 2015), it would be more difficult to interpret when comparing the solutions for samples in experimental series as it could result in different parameter sets, value range, or multi-modal uncertainty distribution in subsequent datasets.

As the Rietveld method, on the other hand, relies on the residual minimization (eq.3.1) it can converge to a non-physical solution depending on the algorithm control (convergence criteria, search dampening factors, number of iterations). An additional limitation of the Rietveld method represents the choice of the convergence criteria, data transformation, excluded regions, damping factors in the optimization algorithm and the number of iterations to reach convergence.

$$\chi^2 = \sum_{i=1}^{n} w_i \{y_i - y_{c,i}\}^2 \qquad \text{(Equation 3.1)}$$

The advantage of exhaustive parameter space search is the resulting distribution of uncertainties in contrary to the non-linear least square fitting, where the reliability factors are highly influenced by the data quality (signal-to-noise ratio). By exploring the parameter space it is more likely that the uncertainties of the parameter values are accurately mapped. In the case of a large number of structural parameters, the MCMC-Bayesian method would require larger computational resources (and time). However, MCMC and Bayesian methods still need the initial guess and the value ranges of the parameters limiting the maximum obtainable accuracy. The initial parameters set, or values ranges can still be under-, or overestimated. A comparison of different models would still be required for hypothesis testing. The Rietveld method is still more practical and faster in optimizing the initial starting conditions. In the case that the standard deviation precision is not the decisive factor for the interpretation of experimental results and sample comparison, the uncertainties obtained with the Rietveld method can be considered reliable.

Application of Bayesian inference in crystallography has been researched in other context as well (Sivia and David, 1994, Armstrong et al., 2004).

3.5.2 Global minimum vs. local minima

The concept of an optimal solution in the parameter landscape can be visualized as a minimum (fig.3.7). Local minima can reflect the range of the acceptable solution and ideally they should be easily distinguishable. A global minimum in this reference corresponds to the lowest value of the cost-function (in this case Rw or chi^2) of all recognized local minima. In principle a global minimum is distinct and well separated from other solutions with higher chi^2 values. It may be that a stable solution might not signify a global minimum – the refinement is stuck in a false minimum.

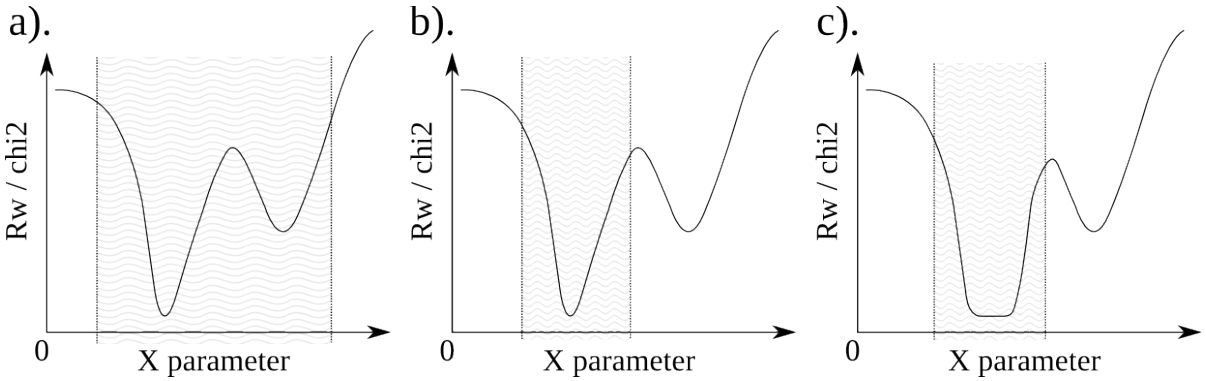

Figure 3.7: One dimensional optimization profiles.
a). bimodal or multi-modal distribution solutions -range of acceptable variable values too big, b). one global minimum in the acceptable range of values for the parameter. This represents the expected response or result, c.) multiple apparent equally good results.

3.5.3 Outlook and further possibilities

Parametrization of broadening and atomic site occupancies

In bone material a calcium-to-phosphorus ratio of 1.8 is usually considered (Li and Pasteris, 2014). In synthetic calcium-phosphate apatites the ratio is closer to the ideal stoichiometric value of 1.66 (Bolis et al., 2012). Sources of the ratio variance can be diverse, such as calcium deficiency, ionic substitution (A-,B-,AB-type carbonate substitution), sodium, magnesium incorporation etc.. Parametrizing the values of the site occupancy of phosphorus and calcium positions, the impact of the ionic exchange can be described. The term parametrization here is adapted with the meaning of systematic change of a refinement parameter value. The values can be generated following any function and altered systematically in a predefined value range. For example, the parameter of site occupancy values can be systematically varied as a fixed parameter and the refinements response can be observed as a

relation of the fixed site occupancy values. Furthermore, this way the calcium-to-phosphor ratio and its correlation with the bond distances of the phosphate tetrahedra and Ca-O polyhedra can be accessed.

In the apatite structure the calcium atoms can take two different sites 6h and 4f (Hughes et al., 1989). Calcium forms two different coordination polyhedra with the oxygen atoms. The 6h site has coordination number 7, and the 4f site has coordination number 9. The volume of these polyhedra can indicate ionic substitutions, or the average amount of calcium deficiency. An expected positive linear correlation with between the Ca-O polyhedral volume and site occupancy should exist. Since the volume of the polyhedra is calculated with respect to the unit cell volume, the relation between the lattice constants and the Ca-O polyhedra are to be expected.

Lattice constants could be obtained prior to the Rietveld refinement by a Le Bail-type (Le Bail et al., 1988) or Pawley-type (Pawley, 1981) refinement, as these neglect any structural information and instrumental parameters. The obtained unit cell constants could be used as the initial guess in Rietveld refinement. However, profile matching procedures tend to be problematic in the case of severely overlapping and broadened peaks. Since the profile matching has less constraints in the refinement than the Rietveld method, profile matching is therefore less stable when the number of refined parameter is higher (by including peak shape parameters or microstructural parameters).

The "AlgoRun" code can be improved by implementing decision-making-algorithms that, for example, add a secondary structural phase from a list of potential phases based on the residual of the fit. This could be helpful in situations where a larger number of measurements need to be compared but where the phase composition can vary.

Coupling the atomic pair distribution function analysis with the Rietveld method by sharing the structural information between the two approaches could be devised. This should improve microstructural analysis in the Rietveld method and increase the reliability of the lattice constants. Optimized atomic positions from the PDF analysis could be fed-back to the Rietveld refinement. However, the Rietveld method requires strict atomic positions through symmetry constraints. The PDF analysis approach used in this thesis, however, uses the crystallographic structural information (provided on the from of the CIF files) as the starting initial guess for the evaluation of the PDF function via least-squares optimization algorithm over the asymmetric unit cell (P1), where each individual atom in the unit cell can shift its position. This forms an additional degree of freedom, in order to address short range order. Furthermore, the lattice constants obtained in the PDF analysis, can differ in general from those obtained from Rietveld refinement. As the inter-atomic distances depend on the value of the lattice constant in the geometrical calculation of bond

lengths, a change in the unit cell dimension can affect the obtained inter-atomic distances.

Chapter 4
Reference material 1. - Analysis of bone exposed to environmental influence of soil condition

As part of the "Transalpine mobility and cultural transfer" project 64 bone samples of various animal species were examined in the context of the environmental influence on the state of the inorganic crystalline material. The DFG, German Research Foundation (Deutsche Forschungsgemeinschaft) project was aimed at researching prehistoric human mobility in the Alpine-region during the Bronze-, and Iron-age. The samples have been randomly selected from a larger number of registered archaeological finds originating from diverse environmental, geological, geographical and archaeological background. The biological carbonated calcium-phosphate apatite of bone material samples have been investigated in altered state*.

In the focus of the research is the evaluation of the relation between crystallographic parameters and archaeological context of the examined altered bone samples. Correlations with previously determined properties of the samples such as the presumed bone species, skeletal element, and age of the archaeological bone find are evaluated. Strontium-isotope ratio analysis results have been also used for the estimation of the viability of a combined crystallographic and isotope research.

4.1 Context and aim

Strontium isotope analysis and crystallographic parameters

The main topic of the "Transalpine mobility and cultural transfer" project was to establish a geological map based on the strontium isotope fractionation values, that can support the tracing of humans and their stock mobility in the time frame from 3200BC till 800AD. The Sr-isotope values have been measured on bone material in archaeological context, since strontium can substitute calcium atoms in the apatite structure of the bone material. In order to distinguish between calcium-phosphate

* Altered bone material – here bone material that was exposed to soil environment and an unknown number of physical, chemical cycles of essentially post-processing. More on the discussion of terminology in appendix A1 p190.

phases that belong to the indigenous bone material differentiated from other strontium-bearing calcium-phosphate phases or strontium containing material, crystallographic analysis of the samples was required with the aim to prove the originality of the bone material. It is the underlying hypothesis of the study that the inside of the bone samples is less prone to environmental influences, and so the isotope signature remains true and unaltered. This way the strontium isotope fractionation values can be considered as the intrinsic values that are representative of the original bone material. The indigenous strontium values correspond to the geological environment values that have been incorporated into the bone structure during the growth of the bone. For this reason, in the study only mechanically cleaned samples have been examined, where the outer surface of the altered bone samples have been removed.

In general, X-ray diffraction methods can not identify the trace element quantities of strontium substitution into the positions of the calcium atoms incorporated in the crystallographic structure of the unit cell. However, if we consider a certain discrepancy with respect to the ideal lattice constants of the bone apatite, a distortion of the unit cell at the case of Sr substitution might manifest itself as strain, so a Rietveld refinement parameter of microstrain could be used to describe similar effects.

Rokita et al. studied strontium doped hydroxylapatite with maximum 0.5wt% of strontium and in their report the authors state that they did not find any evidence that strontium has any influence on the hydroxylapatite under X-ray diffraction. In their study emphasis was given to the question whether the local atomic structure is modified due to strontium replacing calcium atoms. Furthermore, Rokita et al. states that the evaluation of strontium incorporation into the crystallographic structure of bone material requires local atomic structure methods (Rokita et al., 1993). Other evidence shows that strontium acts as retardant for the growth of hydroxylapatite crystallites (Root, 1990). Methods as the pair distribution function analysis of the diffraction patterns have not been applied in the frame of this work for the evaluation of the bone samples from archaeological context.

Archaeological context

In the case of environmentally altered bone material from the archaeological record the intrinsic differences in the bone material with respect to skeletal element, individual age, or presence of bone material altering diseases is unknown. It is not know what is the combined effect of all the possible influences that can affect the bone material, before and after its placement in a certain geological and soil environments (Hughes, 2015). Piga et al. reports on difficulties in the attempts to distinguish between human and animal bones by applying X-ray diffraction technique alone (Piga et al., 2013). Trueman et al. argues about the impossibility of relating

age of the bone sample (piece of skeletal element) as an object and the microstructural state of the bone material (Trueman et al., 2008). The same authors have been investigating the incorporation of rare-earth elements into the bone material and they reported experimental evidence that the uptake of rare-earth elements can be significant and non-negligible (Trueman et al., 2011, 2004). Research about the spatial distribution of the rare-earth element across the skeletal element's cross sections have been reported by Tütken et al. (Tütken et al., 2008; Tütken and Vennemann, 2011). Monge et al. report the evidence of whitlockite, a formation which includes magnesium in the crystallographic structure (Monge et al., 2014). Our samples did not show any evidence of the whitlockite phase.

Hydroxylapatite as a proxy

Theoretical treatment of crystal-chemistry of the calcium-phosphate mineral of the bone material can be approximated using the crystallographic structure of hydroxylapatite and carbonated calcium hydroxylapatite (Hughes et al., in 1989). However, later on the same author considered that the details of the atomic arrangement of the apatite structure are not fully clear (Hughes, 2015). This underlines the complexity of the structure and hints to great care at the evaluation of the crystal chemistry of the nano crystallites of altered bone material from various influence factors.

In the hexagonal symmetry description of the bone-apatite ($P6_3/m$), reduction of the occupancy factors of the two calcium sites (Wickhoff position 4f and 6h) is not equal. Rietveld refinement on various calcium deficient apatite structures show that the reduction of calcium site occupancy could arguably be interpreted as variance of the unit cell parameters (Wilson et al., 2005). This again could be further associated to the presence of microstrain in the system. Microstrain is calculated as part of the interpretation of the line-broadening of the diffraction peaks of the powder diffraction measurements.

Presence and implications of OH^- and CO_3^{2-} are discussed in later chapter in the case of other sample-sets. Detailed investigation of the hydroxyl-, and carbonate group presence in the crystallographic structure of the investigated bone samples in the "Transalpine mobility and culture transfer" project have not been conducted in the frame of this thesis.

Microstrain and size effect

The archaeological bone shows increased long range order as the diffraction peaks show more narrower and sharper peaks than the diffraction peaks of the fresh and unaltered bone material.

Ionic exchange can produce a local distortion in the crystallographic unit cell, which can me described and interpreted as a global parameter of microstrain in the

Rietveld method of diffraction pattern interpretation, although, microstrain causing factors can by numerous. Microstrain as part of the X-ray peak broadening interpretations is a rough parameter to prove ionic exchange in the unit cell, but it still can be a useful classification metric.

Domain size and microstrain are both inferred from the diffraction peak broadening. The approach of separating the two and/or incorporating one or another into the structure refinement will influence the obtained results significantly. The two effects contributing to the behaviour of the peak broadening have different diffraction angle dependence (Mittemeijer and Welzel, 2008). Severely overlapping broad Bragg peaks can be evaluated using distribution functions applied as peak-fitting of individual diffraction peaks from the whole diffraction patter (Handschin and Stern, 1995). The relation of size and strain and their correlation in the X-ray powder diffraction peak broadening was investigated in depth by Baig et al., with an approach for the size and strain effect separation (Baig et al., 1999). Their conclusion was that that both size and strain have Lorentzian character, while anisotropic peak broadening was not possible for the software they used. Further on, for the environmentally altered bone samples models with anisotropic size parameters were used alongside a isotropic microstrain parameter for the diffraction peak broadening evaluation.

Lattice constants

Previous attempt of XRD comparative study of archaeological bone has shown that the lattice parameters of the crystallographic unit cell have a specific behaviour namely that the a(b)-axis show a linear correlation with increasing unit cell volume, and that the c-axis is behaving more randomly (Stathopoulou et al., 2008). The results of the Rietveld refinement of bone samples of the "Transalpine mobility and culture transfer" project show concordance with the previous results of Stathopoulou et al.. However, the variance of the obtained lattice constants differs for the unit cell axis a and c of the hexagonal apatite structure.

4.2 Sample preparation and measurement

A piece of compact bone was cut from the skeletal element and the endosteal and periosteal surfaces were mechanically removed by grinding. The sample was then ultrasonically washed in deionized water (35 kHz), whereby the water was changed every 5 minutes after which the sample was air dried. The bone piece was de-fatted for 5 hours with diethylether in a Soxhlet apparatus and air dried again. After that, the samples were etched in an ultrasound bath (35 kHz) to chemically remove all inner and outer surfaces. For a subsequent measurement of stable strontium isotopic ratios, this acid wash was performed for 5 minutes in concentrated HCOOH (98%,

ultra-pure quality), for a measurement of lead stable isotopic ratios for 10 minutes in concentrated HCl (37%, supra-pure quality). Samples were then washed in distilled water aided by ultrasound until the pH of the distilled water was reached. The weight of the sample was recorded before it was ashed in a muffle furnace for 12 hours at 800°C under oxidizing conditions. After cooling to room temperature, the weight of the sample was recorded again to calculate the mineral yield. Finally, the sample was homogenized to a fine powder in a ball mill and sieved with a 100µm mash-size sieve.

The XRPD patterns were gathered on a General Electric Powder Diffractometer in a Bragg-Brentano set up in reflection mode. Cu_{Kapha1} radiation was used with a Ge(111) monochromator and a 1mm divergence slit. Additionally "knife-edge" slit was used directly over the sample surface at 3mm height for air-scattering reduction. In the case of bone material, this additional slit also reduces the high diffuse scattering at low angles. The data was analysed using the "Fullprof" software package (Rodríquez-Carvajal and Roisnel, 2004) (see appendix A5).

4.3 Rietveld refinement results

In Chapter 3 several crystallographic models have been applied and tested by comparing the fit results. In the case of the archaeological samples the chosen approach was to use one specific crystallographic model (hydroxylapatite) for the fit of all samples. This approach allows to compare the differences between the samples, instead of searching the best possible fit between all possible crystallographic models comparatively. As a starting crystallographic structure model a hydroxylapatite of ideal stoichiometry $Ca_{10}[PO_4]_6OH$ (HAP) was used (Wilson et al., 2006). The refinement of the diffraction patterns of 64 samples was done in an automated manner using the "AlgoRun" code introduced in Chapter 3. All refinement steps were conducted in the same sequence enabling direct comparison of the crystallographic parameters. The obtained refinement results are aggregated and plotted in a scatter matrix, in order to visually explore correlations between the crystallographic parameters (Fig.4.1).

All samples have been refined with a secondary phase of calcite included into the refinement model. Most of the sample have negligible values of calcite (less than 1%wt), only a few sample outlier can be spotted that have much higher calcite secondary phase weight fraction than most of the samples. The calcite phase microstructural analysis of the line broadening of the calcite phase show nano-meter sized calcite crystallites in the case of the outlier, high calcite weight percent bone samples.

From the figure 4.1 we can see that the strontium isotope ratio is uncorrelated with crystallographic parameters, as expected. The strong correlation appearing

between the unit cell volume and lattice constant a is due to the trivial unit cell volume calculation. The matrix plot allows to identify the relation that with increasing values of the lattice constants the values of microstrain are decreasing. Furthermore, parameters of microstrain and domain sizes (size along a-, and c-axis) also show an apparent correlation, although with more variance.

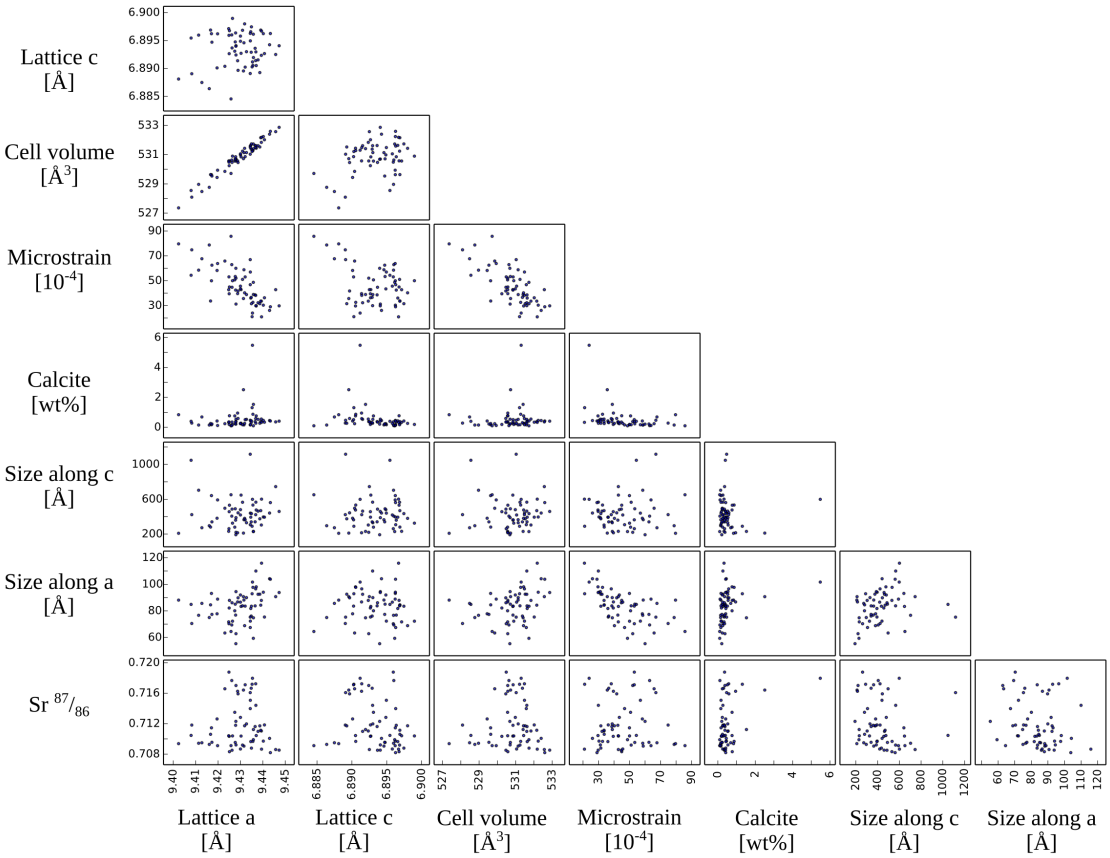

Figure 4.1: Correlation matrix-plot showing the relation between selected crystallographic parameters of lattice constants, microstrain, crystallite domain size along and axis. Strontium isotope ratio relations values are also included in the scatter-plots. Each sub-plot represents a visual information about the correlation of two parameters.

4.3.1 Microstructural analysis

Broadening of the reflections due to finite size is considered as anisotropic and it is modelled with a generalized quadratic form. The strain effect is approximated as a Gaussian distribution, so the contribution of the microstrain to the broadening of the reflection is isotropic. A phenomenological description of isotropic microstrain can be given as hkl-reflection independent lattice parameter variation expressed as a root-

mean-square-strain (RMSS). The values are given as the maximum RMSS, as the highest possible value of the lattice parameter deviation.

Crystallite size distribution is not accessible within the scope of the integral breadth method based Rietveld refinement, however, it is reasonable to expect that in natural nanocrystalline material of bone, a distribution of some kind exists due to the arguable difference between extra-fibrilar and inter-fibrillar crystallites (Dumont et al., 2011; Stock, 2015).

Figure 4.2 shows the relation of microstrain with parameters of the unit cell (volume and lattice constants) as well as the apparent domain size along the a-, and c-axis. In each scatter plot the animal species groups are shown in different colours (red - *sus domesticus*, green - *bos taurus*, yellow - *cervus elaphus*). In addition the bubble size represents the relative domain size along the c-axis. The correlation between microstrain and lattice constant should be trivial, since the variation in the unit cell lengths causes microstrain.

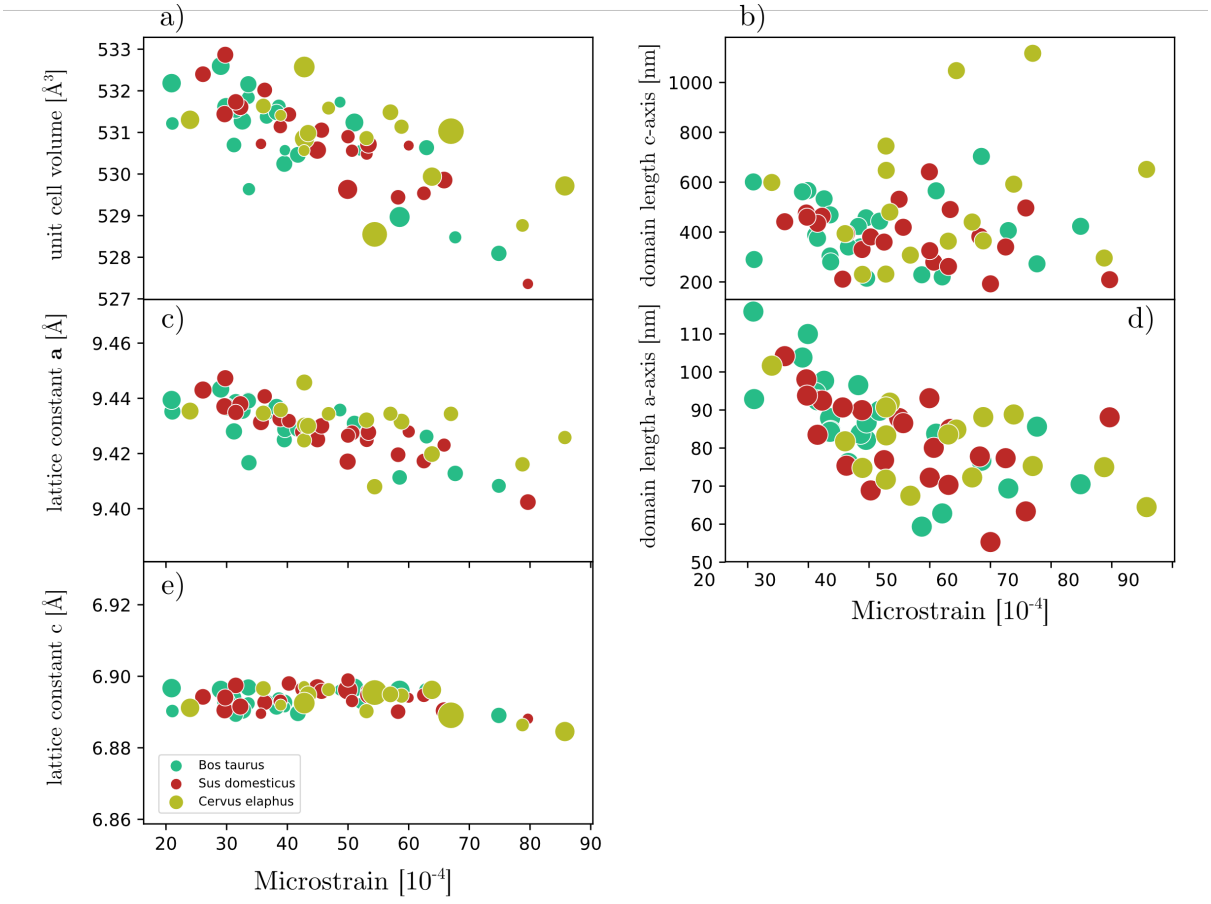

Figure 4.2: Correlation of microstrain with unit cell volume, lattice constants and apparent domain size along a-axis and c-axis. In each scatter plot the animal species groups are shown in colours (red - *sus domesticus*, green - *bos taurus*, yellow - *cervus elaphus*). The bubble size represents the relative domain size along the c-axis.

In general, from the examined samples and from the results shown in Fig.4.2a, it can be concluded that samples with small unit cell volume have higher microstrain – as the irregularity between the unit cells is bigger (higher values of microstrain), the average crystallographic unit cell size is apparently smaller.

The negative slope that is seen in the unit cell volume relation with microstrain must originate from the lattice constant a, as the c axis values appears to be less prone to reflect change with microstrain – its value remains almost the same for any value of microstrain (Fig.4.2e).

Results of linear regression of the unit cell volume relation with the microstrain (Table 4.1) shows that the variance in the scatter of the unit cell volume values for each animal species is slightly different between the three species groups.

Table 4.1: Resulting parameters of the linear regression of the microstrain and unit cell volume ($V = a < \epsilon > +b$) for 64 samples and different animal species groups

	r-value	std error	a (slope)	b (intercept)[Å^3]
sus domesticus	0.887	1.289	-11.1(0.7)	5924(385)
bos taurus	0.731	2.069	-10.1(1.2)	5426(619)
cervus elaphus	0.614	3.526	-10(2)	5504(1054)

The number of samples for each of the three species is different. The standard deviation is the highest for the species of *cervus elaphus*. Lower values of the standard deviation are obtained for the species which are domesticated. This could be explained with the higher mobility of the wild animals, diversity of the food, or in the case of domesticated animals, the environment of the keeping.

The relation of the domain sizes across all 64 samples have been evaluated with respect to the lattice constants in Fig.4.3. From the figure it can be concluded that there is no apparent high correlation between the domain lengths along the a-, and c-axis and the lattice constants.

In all the sub-plots of figure 4.3 the bubble size represents the microstrain. The values have been scaled for better visualization by an exponential factor* $pointsize = e^{microstrain/15}$. The obtained plots in Fig.4.3 show that the samples with lower values of the lattice constants have higher values of microstrain (bigger bubbles), in the case when the lattice constant are plotted with respect to the domain sizes.

* plotting microstrain values as bubble size with values $e^{microstrain/15}$ was obtained empirically

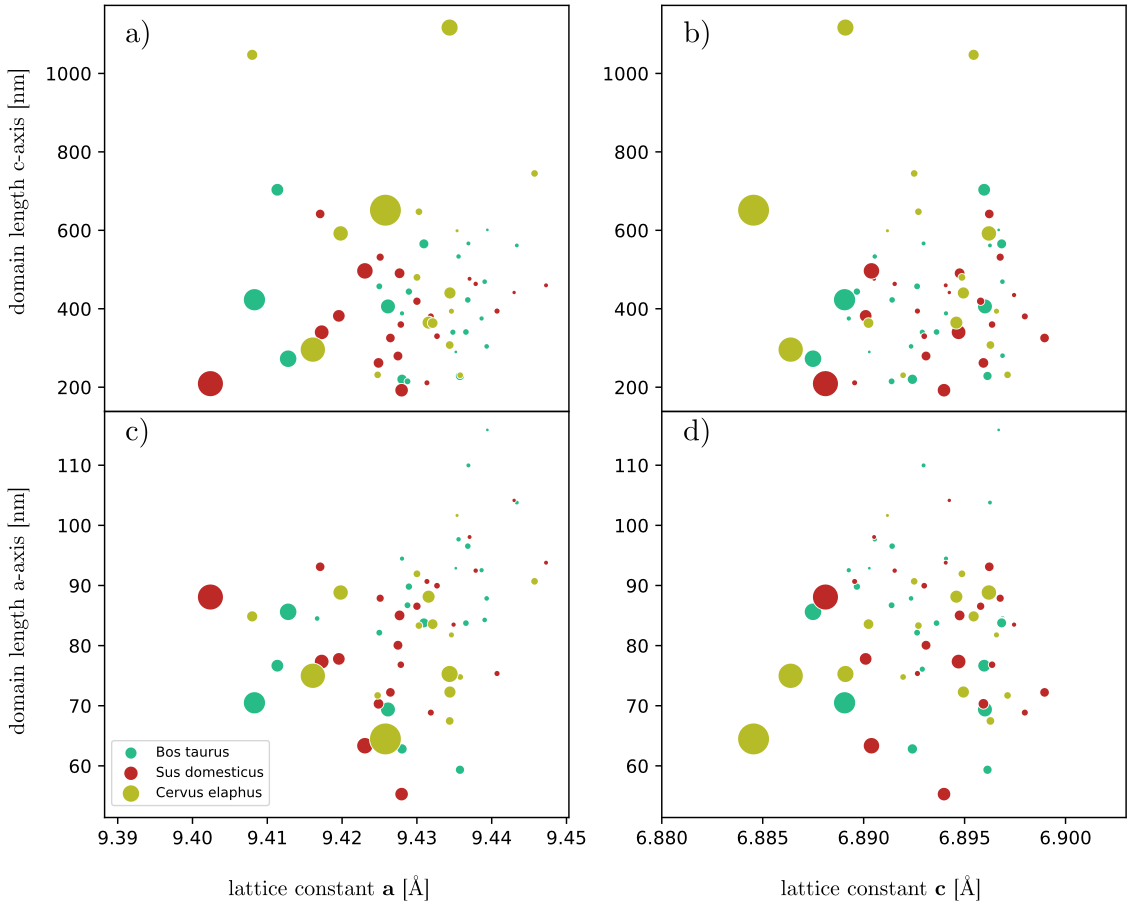

Figure 4.3: Relation of the lattice constants and the apparent domain size along a-, and c-axis. The size of the bubbles corresponds to the exponentially scaled value of the microstrain for each sample (point on the scatter-plot).

4.3.2 Lattice parameters

Report of a study done on larger number of diverse archaeological bone samples shows that the lattice parameters a(b) and c correlate differently with respect to the unit cell volume (Stathopoulou et al., 2008). The same linear trend in the relation of the of lattice parameter and the unit cell volume can be observed here as well (Fig.4.4).

The unit cell volume in a hexagonal system is calculated as a product of the squared value for the a-axis and a linear term for c-axis (times the sinus of the angle of 120°). Therefore, small variation of the a-axis values will return greater unit cell volume change, while variation of the c-axis lattice constant influences the unit cell volume linearly. Therefore, the correlation of the lattice parameters with the unit cell volume is trivial. However, in this study the correlation occurs between random samples, indicating that the trivial relation of the unit cell volume and the lattice

constants is unfolded over all examined samples. Moreover, the trends in the scatter plot show a linear dependence of the lattice constant a with respect to unit cell volume (Fig.4.4a), and no specific correlation with respect the lattice constant c (Fig.4.4b). The variance of lattice constant values for the a-axis is about 0.53%, and for the c-axis is 0.22% of the mean value, meaning that the unit cell dimensions vary double as much in a-axis than the values for the c-axis.

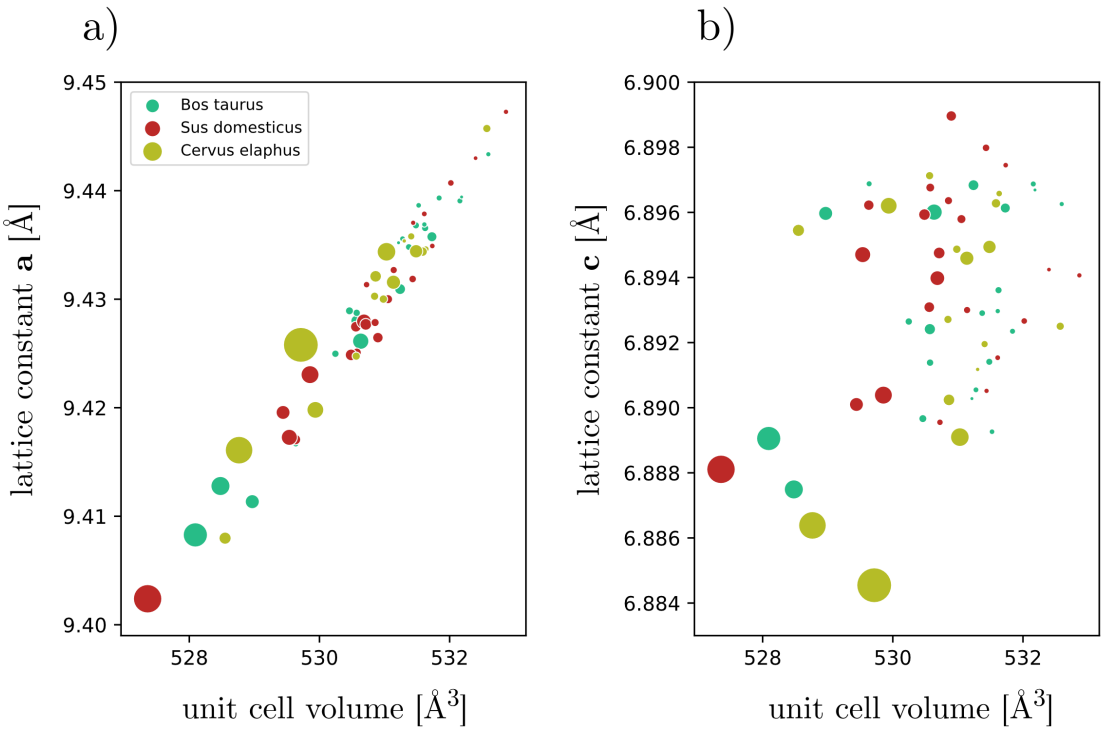

Figure 4.4: Relation of the lattice constants and the unit cell volume. The size of the bubbles corresponds to the exponentially scaled value of the microstrain for each sample (point on the scatter-plot).

4.3.3 Ageing of the bone material

As the samples are exposed to the soil environment for extended periods of time measured in thousands of years the material altering process can be essentially described as ageing. However, no correlation of the unit-cell volume, nor the crystallite size with archaeologically determined age has been seen in the examined samples (Fig.4.5). On figure 4.5 the box-plot represents the distribution of unit cell volume values of sample with respect to the age-range assigned from archaeological context, where the mean value and the first quantile form the box and the second quantile is marked with a bar. Most of the samples fell into the age category of 850BC – 15BC. Additionally, it needs to be mentioned that no quantitative

determination (measurement) of the samples age was carried out, such as carbon dating. Instead the age is approximated from the archaeological context.

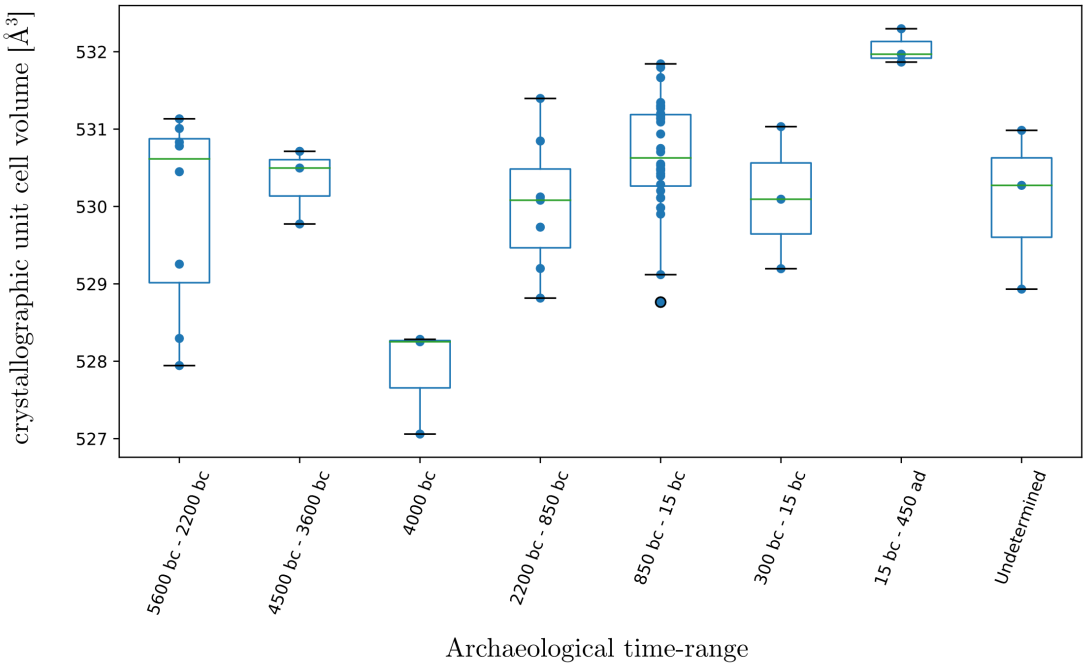

Figure 4.5: Box-plot of the crystallite sizes of the samples in correlation with the determined archaeological age of the samples. The age categories are based on estimation from the archaeological context. Only the age category of 850BC-15BC has more then 10 data points, while the other have only a few. There is an "Undetermined" category as well for samples which at the moment of evaluation did not have a archaeological age estimate (3 data points).

The result of the lack of archaeological age dependence of the crystallographic parameters might be due to a combination of extrinsic and intrinsic factors. Extrinsic factors may include humidity, and soil pH at the archaeological site that may affect the alteration reaction in an unpredictable way. Intrinsic factors may be intra-species and across-species variations of the crystallographic parameters of the bone mineral that can lead to difference in the ageing conditions.

4.3.4 Occupancy factors

In the crystal structure of hydroxylapatite (hexagonal symmetry space group $P6_3/m$) the calcium atoms can occupy two sites (Ca1 4f, and Ca2 6h) and they form different coordination polyhedra (Kay et al., 1964). Accessing these parameters from the Rietveld refinement of powder X-ray diffraction is challenging and can even be

put into question. Nevertheless, the refinement of broad diffraction peaks of the bone samples from archaeological context have been attempted. The results show scattering of obtained occupancy values, but week correlations with other parameters of the crystallographic model can still be inferred (Fig.4.6).

Site occupancies relation to microstructural parameters

In the Rietveld refinements the broadening effect was modelled with anisotropic size and isotropic strain (reflection independent) contribution. The assumption that the presence of microstrain can be interpreted as a parameter that hints to the correlation of calcium site occupancy variations was investigated. The results of linear regression of microstructural parameters with occupancy are summarized in Table 4.2 and correspond to Figure 4.6.

Table 4.2: Results of the linear regression of the occupancy values for the two calcium sites with respect to microstrain and domain sizes along c-, and a-axis, respectively.

	Ca1 (4f)		Ca2 (6h)	
	r-value	std error	r-value	std error
microstrain	0.779	0.366	0.553	0.843
domain size c-axis	0.252	6.440	0.318	10.93
domain size a-axis	0.758	0.290	0.567	0.635

The results suggest that the occupancy values of the calcium site 4f are apparently more correlated to the microstrain and the domain size along the a-axis (Fig.4.6 plots a,c,e), while the calcium site 6h shows more random like behaviour with more variance with respect to the microstructural parameters (Fig.4.6 plots b,d,f). The relation of microstrain and the calcium site occupancies percentage is visually evident when from plot c,d,e,f in Fig.4.6, where the bubble size is plotted using the scaled values of microstrain for each sample – as the calcium site occupancy values are decreasing, the microstrain values show increasing trend.

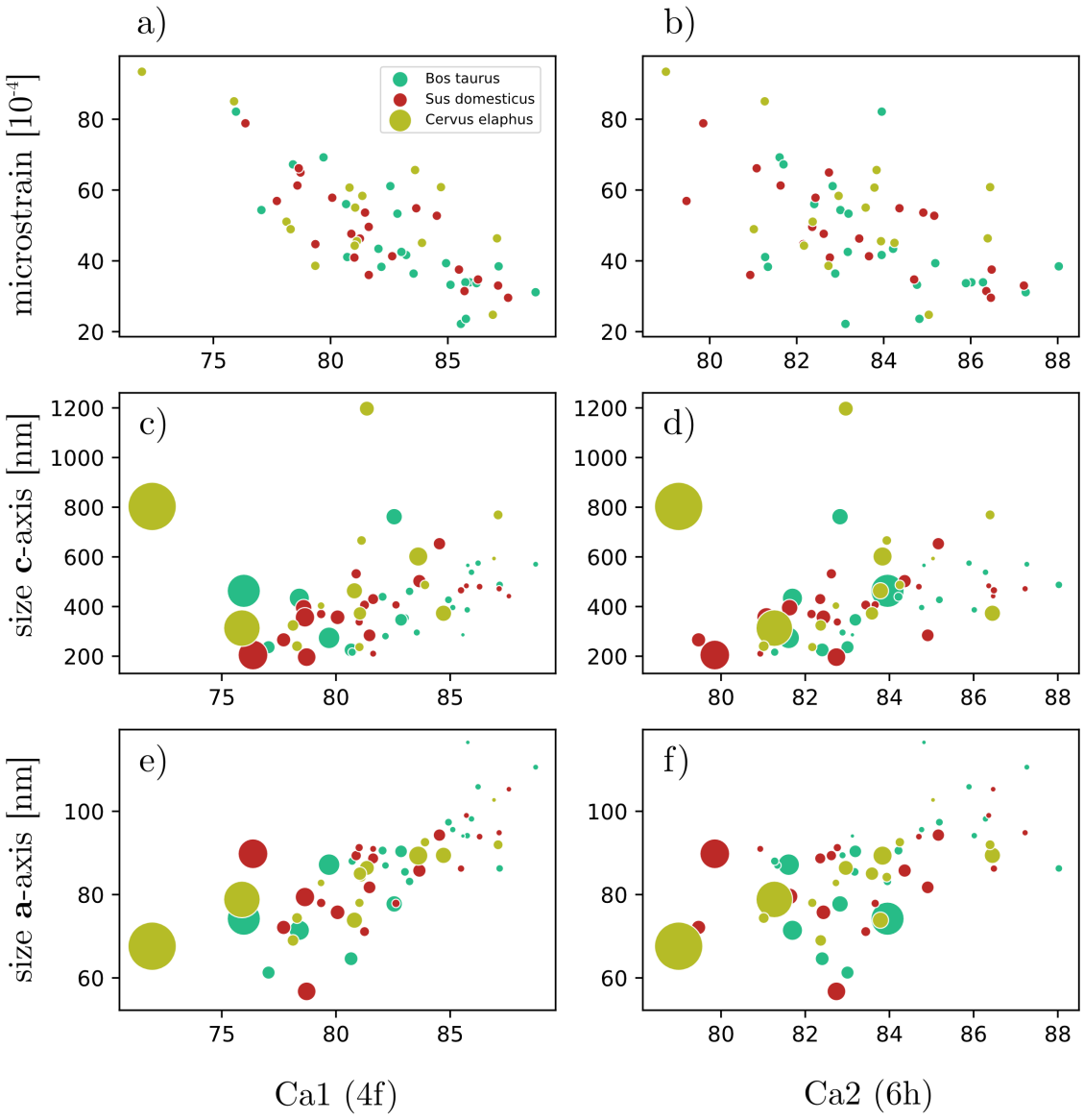

Figure 4.6: Occupancy factors of the two calcium sites in relation with the microstrain parameter, apparent domain size in a-, and c-axis direction. The occupancy values for the calcium are expressed in percentage of the total (full) stoichiometry in the crystallographic unit cell. On plots c-f the bubble size corresponds to the microstrain values, which are also shown on plots a-b.

4.3.5 P-O distances in the phosphate tetrahedra

In the used structure refinement software ("FullProf") the calculation of the inter-atomic distance and angles is based on the bond valence and bond distance relation derived by Brown and Altermatt (1985). The bond valence (s) carries the meaning of the strength of the bond and is defined through tabulated values of empirical variables d_o and B. The d_o is specific for anion-cation bond, while the distance d is a free parameter for the structure optimization. The relation of the bond valence and bond distance can be expressed as is eq.4.1.

$$s = e^{(d_0 - d)/B} \qquad \text{(Equation 4.1)}$$

In the automatic refinement of the 64 samples the atomic positions of the calcium, phosphor and the tetrahedra building oxygen atoms were refined without rigid body restrains and other constrains. For the description and interpretation of the tetrahedra distortion the P-O distances were investigated for emerging patterns in the sample population (Fig.4.7). The patterns that suggest strong correlations were examined in detail and are shown in Fig.4.8.

Yi et al. reports results of theoretical calculations of the Raman spectroscopic shifts that show the bond lengths in the phosphate tetrahedra and Raman peak position shifts are highly correlation (Yi et al., 2014). Yi at al. elaborates that inter-atomic distance values between P and O can be obtained from the band position in the spectral trances from experimental spectroscopic measurements.

Presence of carbonate ions can produce measurable effect of the P-O distances in neighbouring tetrahedra and potentially influence the average values independently of the occupied site (A-, or B-type substitution). Further resulting that the lattice parameters variations can be dependent on the amount of the incorporated CO_3^{2-} (Wopenka and Pasteris, 2005). Mul et al. give experimental evidence that the peak width of the P–O symmetric stretching vibration in the Raman spectrum depends on the amount of the carbonate substitution in the apatite lattice (Mul et al., 1986, 1988). Leventouri at al. compared P-O bond lengths from neutron diffraction of natural and synthetic apatites (Leventouri et al., 2001), where the variation of the bond distances are assigned solely to a contribution of the carbonate content in the apatite structure.

Next to the carbonate incorporation, cation substitution has also an influence on the bond distances of the P-O tetrahedra as well. Cation substitution might also lead to frequency inversion in measured FTIR spectra due to the repulsion forces between nearest oxygen atoms in contiguous tetrahedra. The repulsion between oxygen atoms linked through a mutually shared cation affects the molecular vibration frequencies. If a calcium atom in the apatite structure is substituted by a larger

cation, the oxygen atoms in adjoining tetrahedra are brought closer together resulting in a shortening of the P-O distances and a corresponding increase in the vibration frequencies of the PO_4^{3-} ion (Adler, 1964). The values of bond lengths are eventually affected by the presence of larger or smaller cations and have been extensively studied (Kohn et al., 2002). Trivially, ionic exchange has impact on the calcium coordination polyhedra as well.

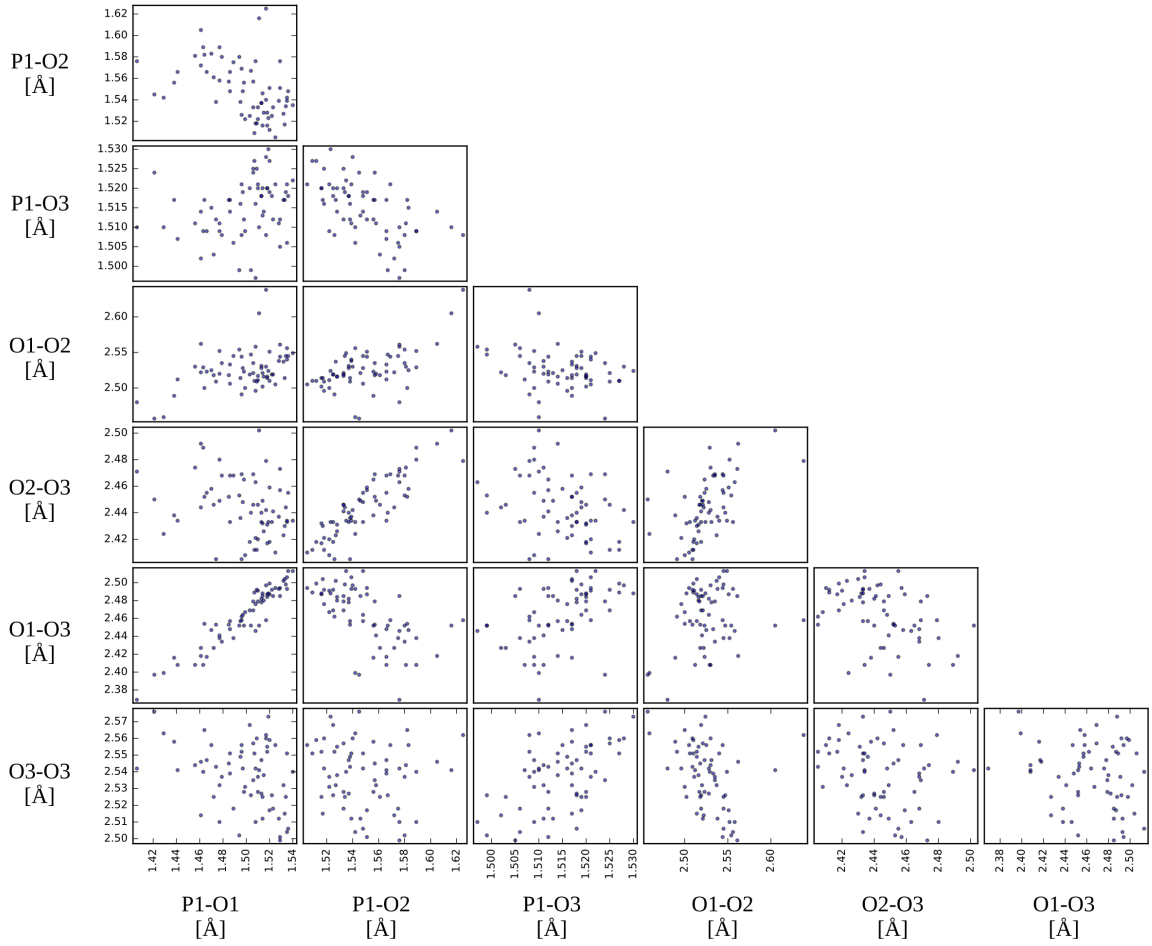

Figure 4.7: Matrix plot of the inter-atomic distances of the phosphate tetrahedra. The individual sub-plots show the distance of the center atom and the tetrahedral vertices (P-O), as well as the distances between each vertex site specific oxygen-oxygen atom. The notation of the O1 (6h), O2 (6h) and O3 (12i) correspond to the oxygen sites in the crystallographic unit cell of the hydroxylapatite.

In his study, Hughes reports that refinements using hydroxylapatite with the hexagonal symmetry (Hughes et al., 1990) including anisotropic mean square displacement factors, the obtained inter atomic distances in the distorted tetrahedra are between 1.528 – 1.540 Å for the P-O bonds.

Baur investigated and compared more than 129 reported crystallographic

structures containing the phosphate tetrahedral unit and extracted the P-O distances in order to evaluate the distribution of inter atomic distances (Baur, 1974). His study was not exclusive on hydroxylapatite, but rather all apatite structures with different degrees of distortion on the phosphate tetrahedral unit (Kohn et al., 2002 p124). From the work of Baur the P-O distance average values for the whole tetrahedra are in the range from 1.506-1.572Å. While the individual phosphor-to-oxygen distances (each vertex) range from 1.412 to 1.662 Å. The O-O distances average to 2.458 – 2.552 Å, while individual oxygen-oxygen values between the vertices of the phosphate tetrahedra range from 2.317-2.620 Å.

The analysis of the P-O distance values from the results of the Rietveld refinement of the 64 samples of the environmentally altered bone sample in the frame of the "Transalpine mobility and culture transfer" project are plotted as a scatter-matrix in Fig.4.7. The obtained P-O distance have been aggregated and plotted in a scatter matrix with respect to each site in the crystallographic model in order to visually explore correlations between the crystallographic parameters. This scatter-plot-matrix allows quick visual identification of apparent correlations between vertex-to-vertex, and vertex-to-center atom distances. Inter-atomic distance in the tetrahedra show slight, or no apparent relation except in the case of apparent correlation between P-O1, P-O2 and O1-O3, O2-O3 (the notation corresponds to O1 (6h), O2 (6h) and O3 (12i) in the crystallographic unit cell of the hydroxylapatite). This high correlation had been further investigated (Fig.4.8). Figure 4.8 shows scatter-plots of the P-O, and O-O distances where each data-point represents a different sample's center-to-vertex and vertex-to-vertex values of the phosphate tetrahedra. The influence factor of the structural change is unknown, therefore any correlation pattern can by either an unidentified alteration factor, or a sign of a systematic error.

On sub-plots *a* and *b* of Fig.4.8 it can be seen that with the increase of the P-O1 distance the corresponding O1-O3 and O1-O2 bond length increases as well, while the O2-O3 length decreases. For the sorted values of P-O2 distances the trend lines are apparently inverse when the O1-O3 and O2-O3 values are plotted. Illustrations of the tetrahedra with arrows indicating the shifts of the atomic positions are given in Fig.4.8 *c* and *d*. From the trend line of the center-to-vertex distance relation plot (Fig4.8 *e* and *f*) it can be seen that the most stable distance in the tetrahedra is the P-O3, while the P-O1 and P-O2 share inverse relation (as one increases the other decreases).

From the correlation plot of the bond distances (Fig.4.8) and the comparison of the literature values it can be seen that for some samples the P-O lengths (obtained from the Rietveld refinement) are outside the range found in the literature. On closer inspection of the refinements that produce outlier values with respect to the literature inter-atomic distances, it can be concluded that the diffraction peaks of

the measurement are less developed and show broader peaks indicating a complex microstructure and small domain lengths. In those cases the diffraction pattern does not offer enough peak differentiation which would be needed to access atomic position refinements meaningfully. The low inter atomic P-O distance values in the tetrahedra can be therefore assigned to systematic errors and correlating parameters in the execution of the Rietveld refinement.

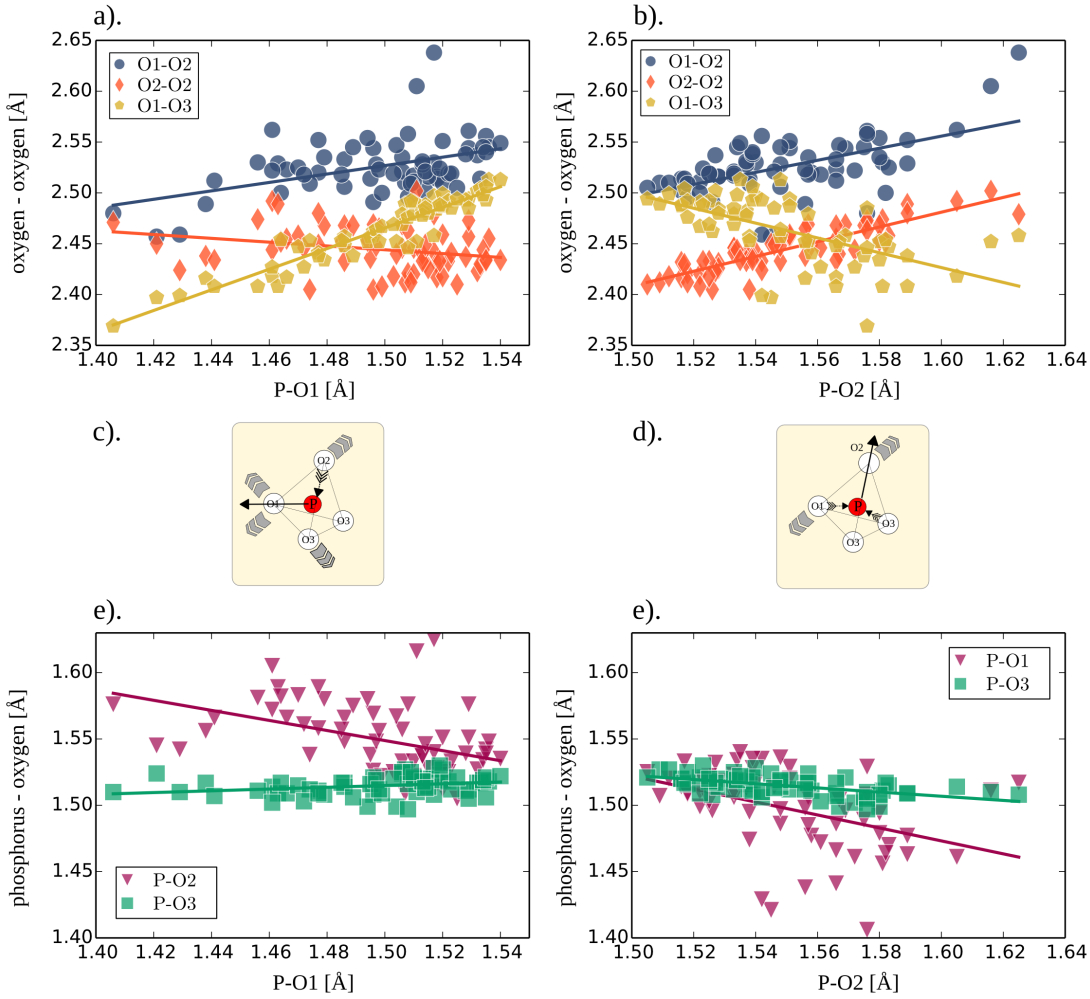

Figure 4.8: Phosphorus-oxygen distances in the phosphate tetrahedra structural unit. The correlation of inter-atomic distances in the phosphate tetrahedra in the sample population of the bone samples of diverse archaeological context. a) Oxygen-oxygen distances as a function of the P-O1 distance; b) Oxygen-oxygen distances as a function of the P-O2 distance; c and d) illustration of the observed trends from a and b, respectively; The trends between the center-to-vertex distances in the phosphate tetrahedra are shown in e and f, as a function of P-O1 and P-O2, respectively.

In addition, the obtained bond angles have been extracted from the refinement results and are summarized in Table 4.3. The angle between the two vertices and a center atom in the ideal Platonic tetrahedron is 109.47° (Brittin, 1945). In the unit cell of apatite (hydroxyl or carbonated) the phosphate tetrahedra are distorted, leading also to variation in the angle values. In Table 4.3 angles for a reference hydroxylapatite structure of Wilson et al. (Wilson et al., 2006) are also given as a comparison.

Table 4.3: The mean value and value range (minimum and maximum) of the O-P-O angles in the phosphate tetrahedra in the examined 64 different samples. The values of the starting (reference) structure of hydroxylapatite is given as well. Only the vertex-center-vertex angles are given for brevity.

∡(O-P-O)[°]	O1-P-O2	O1-P-$O3_1$	O1-P-$O3_2$	O2-P-$O3_1$	O2-P-$O3_2$	$O3_1$-P-$O3_2$
mean	111.95(63)	109.7(6)	109.7(6)	105.8(6)	105.8(6)	114(1)
min	111.4	108.3	108.3	104.1	104.1	111.3
max	114.2	110.7	110.7	106.9	106.9	116.3
HAP reference structure	110.96	112.0	112.0	107.46	107.46	106.7

4.4 Concluding discussion

In the presented study, an approach was made to correlate crystallographic parameters and archaeological contexts. Emerging correlations of lattice parameters, crystallite size and microstrain, as well as site occupancies can be observed based on the interpretation of the measurements. However, the influence factor that caused the structural change is in general unknown (unknown environment, alteration cycles and similar), therefore any correlation pattern that emerges can by either a not yet identified alteration factor, a sign of systematic error, or combination of both. Chemical composition analysis had not been conducted on these samples.

The results show that although the Rietveld fit resembles high apparent matching of the model to the data (with acceptable reliability factors), local in-detail inspection of the diffraction patterns shows only very slight deviations of the peak profiles and peak background, as well as occasional not matching single peaks in most of the samples.

The reliability factors of the Rietveld refinement have not been included into the analysis for the reason that in this case they can not be used to compare the fit

for all samples. The physical material constitution and the state of the powder samples shows a high variety and therefore not all samples could be prepared equally for all samples regardless of maximum care and diligence. The state of the sample is influenced by the degradation stage of the bone material, its soil environment, and similar factors. The condition of the powdered bone material varies from sample to sample (particle size and distribution from the grinding procedure), and influences the measurement and the diffraction pattern. Different levels of noise in the diffraction pattern from sample to sample renders the reliability factors meaningless for a direct comparison between the refinement of these samples.

The discovered correlations may not be in cause and effect relation, and in any case would depend on the number of examined samples. Future studies should include a greater number of samples in order to adequately distinguish outliers and identify sample group mean values. In addition, information about the environment, such as soil sample composition, additional locality description, hydrological surrounding would enrich the database and correlation could be examined regarding more parameters.

The complex influence of the environment and ageing-time in any case can not be reconstructed. Complete understanding of the bone nanocrystallites altering factors and sequence of influence requires more additional studies. Examination of the bone material from archaeological context is actually yielding the information about the preservation state of the bone and its nanocrystallites despite the alteration processes (bone material that survived chemical dissolution, biological degradation, and all possible destruction effects was investigated).

It could be speculated that formation of layered crystalline domains can occur, where the core could be the indigenous crystalline material that formed during the life of the organism, and an outer layer forming post-mortem additional crystallite growth. The conditions for the outer layer growth could be potentially different from the crystallite growth in the living organism. In addition, growth of the nanocrystallites inside the living organism is physiologically and genetically controlled, whereas secondary growth of the crystallites in soil or other environmental conditions is purely chemically induced. The growth controlling factors are biological degradation, presence of water, soil pH and ionic environment through elemental composition of the medium surrounding the nanocrystallites.

Some of the results from this chapter have been published in Grupe et al. (2015), Schmahl et al. (2016) and Schmahl et al. (2017).

Chapter 5
Reference material 2. - Peak profile analysis of geological minerals

5.1 Context and aim

Analysis of geological minerals of calcium-phosphate apatite have been taken into consideration as reference material to the bone of non-biological origin. Samples of nominal hydroxylapatite and fluorapatite minerals have been examined by combined diffraction and spectroscopic studies. Nominal carbonated-hydroxyl-apatite geological minerals, as well as synthetic hydroxylapatite and brushite (as an example of non-apatite Ca-phosphate) have been also included into the comparison in order to examine and compare the PO_4^{3-} vibrational spectroscopy region between the samples. A list of sample and descriptions is provided in Table 5.1.

According to the classical (strict) description of the average hexagonal calcium-apatite structure a concept of the "anionic column" is defined along the c-axis of the hexagonal crystallographic model (Hughes et al., 1989). Incorporation of F^-, Cl^- ions next to the OH^- can play a role of structure stabilization. Geological apatite shows various proportions of OH^- and F^- within the channel site (Pan and Fleet, 2002; Wopenka and Pasteris, 2005). End members of fluor-, and hydroxyl-apatites have well known structures and can be identified spectroscopically by the presence of a peak near $3570cm^{-1}$ in the FTIR spectra (Cant et al., 1971; Rehman and Bonfield, 1997). A shift in the position of this peak can be used to distinguish the presence of F^-, Cl^-, or OH^- in the anionic column.

In general, the interpretation of a possible phase mixture of these structurally identical apatites can be challenging, such as a mixture of fluorapatite and hydroxylapatite, which have different unit cell parameters with the same average hexagonal symmetry structure (Hughes et al., 1989; Jeanjean et al., 1996; Sudarsanan and Young, 1969). In the case of a two phase mixture of fluorapatite and hydroxylapatite, analytical techniques such as diffraction would show peak position similarity due to the similarity of the crystallographic models of the two structures, resulting in a profile shape resembling that of a broadened diffraction peak.

Spectroscopic features of the samples listed in Table 5.1, had been analysed using FTIR spectroscopy parallel to Rietveld refinement of X-ray powder diffraction patterns. A combined approach of complementary techniques is necessary to identify and distinguish isostructural apatites (hexagonal symmetry apatite structure).

Table 5.1: Sample abbreviation and additional information of origin and description of synthesised calcium-phosphates.

Sample name acronym	Nominal description
C-HyAp	Carbonated apatite from the Bavarian Mineralogical State collection. Sample is considered as dahlite (referring to carbonate-bearing hydroxylapatite), while presence of carbonated fluorapatite (francolite) is also plausible.
HyAp	Non-carbonated hydroxylapatite that shows multiple peaks in the OH^- stretching vibrational mode region. Sample referred to as "Snarum" by its origin locality name.
F-Ap	Fluorapatite – large, yellow coloured samples. FTIR of the OH^- stretching vibrational modes show a small peak (relative to the rest of the spectrum) distinctive for $F\cdots OH^-$ bonds.
S-(C)-HyAp	Synthetic (carbonated)-hydroxylapatite synthesized from calcium-nitrate and ammonium-hydrogen-phosphate under atmospheric conditions with access to CO_2 from the air and water.
S-brush	Synthetic brushite precipitated from the reaction of highly concentrated (>1M) calcium-nitrate and ammonium-hydrogen-phosphate aqueous solutions.

In general, the measured FTIR spectra for the investigated samples show diverse spectral trace features in the phosphate vibrational regions, as well as differences in peak positions in the OH^- stretching mode region where additional peaks can be observed. In the comparison of geological mineral samples differences appear in the characteristic vibrational band region of OH^- (near 3570cm^{-1}) implying complexity of the state of the anionic column (referring to the ordering of the OH^- and other anions such as F^-, Cl^- along the c-axis of the apatite structure). In the case of fluorapatite and synthetic hydroxylapatite, characteristic vibrational modes were identified in the spectral trace at their expected wavenumber positions, while in the case of the geological mineral of nominal hydroxylapatite (HyAp sample "Snarum"), a differentiated spectral trace has been identified near the OH^- stretchering mode (3570cm^{-1}), hinting to the potential presence of anions other than OH^- (Fig.5.2 b).

Rietveld analysis was used to describe the diffraction peak shapes in order to distinguish possible phase mixtures or diffraction peak broadening effects related to microstructure (crystallite size and microstrain). The obtained diffraction patterns

have been evaluated and tested with respect to specific crystallographic models and potential phase mixtures of hydroxylapatite and flourapatite. Alternative crystallographic models to hexagonal apatite such as the monoclinic model have been also evaluated. Further on, scenarios with multi-phase evaluation have been included into the analysis as well.

The XRPD diffraction peaks of the geological mineral of nominal hydroxyl-apatite (HyAp sample "Snarum") sample show slightly broadened peaks, implying rather a microstrain related cause than a finite size effect. It was assumed that the possibility for the existence of a nano phase in the examined geological mineral sample is low. However, in the case of two-phase model with isostructural phases having similar unit cell constants, the diffraction peaks of both structures could appear very close to each other and seemingly appear as one broad peak in the diffraction pattern trace. By inspecting the XRPD profile of the HyAp sample it can be inferred that some reflections might appear close to each other without forming separated (or split) peaks. In the investigation a laboratory X-ray source was used for the measurements. Additional higher precision synchrotron X-ray source data measurements, however, did not reveal more resolved information about peak separation. For samples such as the HyAp nominal hydroxylapatite, the results show that the best fit is achieved with a phase mixture refinement approach of fluorapatite and hydroxylapatite, in comparison to refinements with only single-phase scenarios with microstrain and finite size broadening model. In the sample of geological mineral of nominal hydroxyl-apatite (HyAp sample "Snarum"), the hydroxylapatite and fluorapatite can segregate to form domains. Ionic substitution would imply total miscibility, which would manifest as a diffraction peak broadening effect interpreted via microstrain.

Point-measurements under electron microprobe analysis in wavelength-dispersive spectroscopy mode (EMP/WDX) confirm regions with fluorine concentration of up to 3wt%, as well as regions with ppm amounts of fluorine content for the sample of geological mineral of nominal hydroxyl-apatite HyAp. However, in the case of this sample clear differentiation into distinct domains of pure hydroxyl or fluorapatite could not be inferred based on the electron microprobe measurements. Formations of interlocking regions of diverse fluorine content were not observed.

5.2 Sample preparation and methods of measurement

Preparation of geological mineral samples included crushing and milling in a hand mortar and sieving through a 100µm mash sieve. The synthetic samples have been precipitated from an aqueous solution of calcium-nitrate-tetrahydrate and diammonium-phosphate at low temperature (80 ° C). The synthetic brushite was precipitated from high concentrations (1M) of the same reactants as an instantaneous

reaction, without stirring and no pH control at room temperature.

FTIR measurements were carried out on a Bruker Equinox instrument. The spectrum was collected with a resolution of 4cm^{-1}, in the range from 400-4000cm^{-1} with a sum of 128 scans. Samples were prepared by mixing 1.4mg of sample material with 200mg of KBr and pressed to a pellet.

The XRPD patterns were gathered on a General Electric Powder Diffractometer in a Bragg-Brentano set up with $Cu_{Kalpha1}$ radiation, monochromator Ge-111, was used with a Soller slit and a divergence slit of 1mm opening. 1D-stripe detector Metero1D was used to collect the counts with an angle coverage of 6°. Synchrotron data was collected at the DESY-P07 using a flat-panel detector.

5.3 Results of FTIR spectroscopy

The measured spectral traces of the samples listed in Table 5.1 are shown in relative scaling of the absorbance in Fig.5.1. Scaled and magnified regions of the FTIR spectral trace of measured geological and synthetic apatites and brushite in the spectral range from 400-4000cm^{-1} has been cut into sub-regions for the evaluation shown in Fig.5.2. Each sub-region covers a range of the vibrational bands of ionic groups for $\nu_4PO_4^{3-}$ vibrational region, OH^- vibrational region, spectral region range 1300-1900cm^{-1} showing the characteristic carbonate modes of $\nu_3CO_3^{2-}$, and the region of the ν_3 and ν_1 of the PO_4^{3-} of the apatite minerals. In the case of sample HyAp and F-Ap the carbonate vibrational modes are absent. The sample of synthetic brushite is also included in the plot for visual comparison as a non-apatitic structure, and was not evaluated in the spectral decomposition.

The numbered peaks in the spectral trace in Fig.5.2a correspond to the positions of the $\nu_4PO_4^{3-}$ modes in the hydroxylapatite apatite structure, with the peak of the $\nu_2PO_4^{3-}$ at 470cm^{-1} as well. The examined samples show diverse shouldering and hidden peak presence. Results of the spectral decomposition of each sample are further discussed in section 5.3.1.

The direct comparison of the the OH^- region of the sample show appearance of various peaks (Fig5.2.b). The coexistence of separated peaks near 3570cm^{-1} in the HyAp nominal hydoxylapatite sample suggests that diverse anionic column occupation domains may exist (F^-, OH^-, Cl^-). Interestingly the spectral trace peak marked with number 2 in Fig.5.2.b appears at the same wavenumber in samples of C-HyAp and F-Ap as well. The synthetic hydoxylapatite and the HyAp samples have only the peak numbered with 3. The results of the spectral decomposition of this region are discussed in section 5.3.3 and the enumeration of peaks is given in Table 5.5.

The strong carbonate $\nu_3CO_3^{2-}$ band peaks at 1414cm^{-1} and 1450cm^{-1} are present in the sample of C-HyAp and S-(C)-HyAp, while they are absent in HyAp and F-Ap

samples (Fig.5.3c). The spectral region of the ν_3 and ν_1 of the PO_4^{3-} are shown in Fig.5.3d.

In the evaluation of the spectral trace the background signal was individually modelled for each sample and subtracted prior to the fit procedure. Parameters of the peak functions of the bands were obtained using the spectral decomposition method with the Gaussian and Lorentzian sum function in the "PeakFit" software.

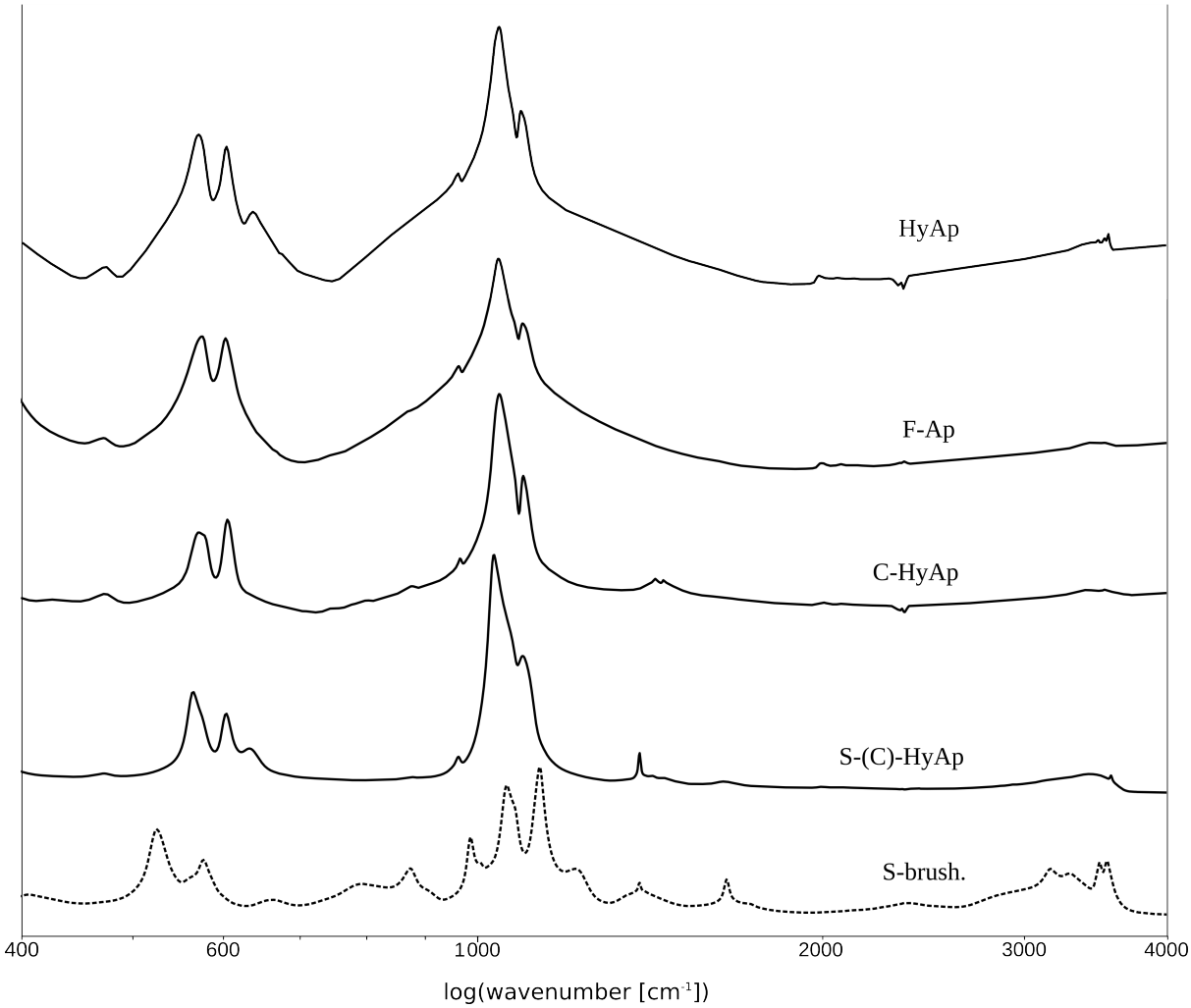

Figure 5.1: Visual comparison of measured FTIR spectral trace of the geological and synthetic minerals. The naming of the samples is according to the Table 5.1. On the abscissa the scale of the wavenumber values is logarithmic for better illustration. On the ordinate the absorbance vales are plotted. For better visual scale the absorbance values have been arbitrarily scaled between the samples. The S-brush synthetic brushite is plotted with a dashed line, as this sample does not have the apatitic structure as the rest of the samples.

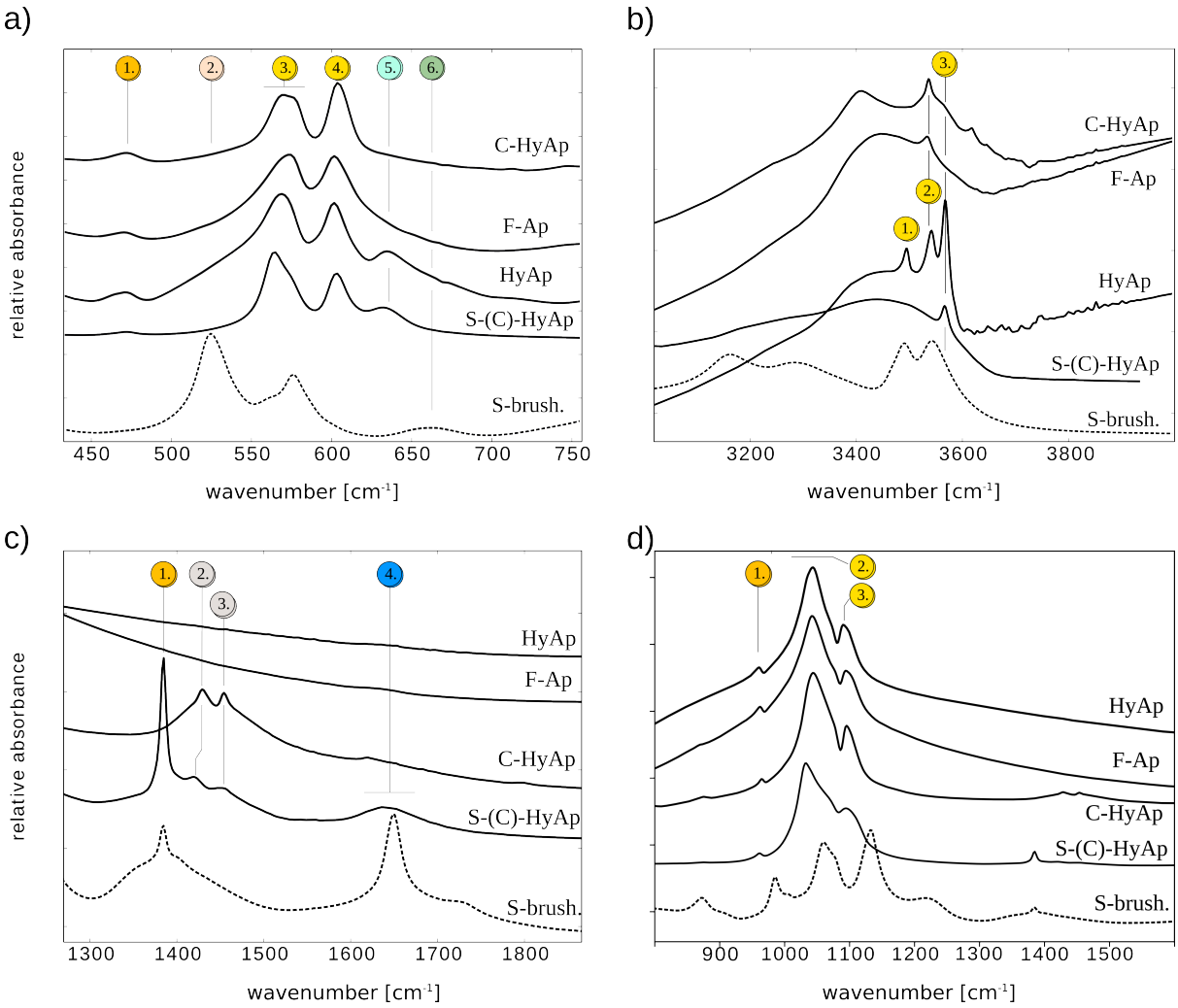

Figure 5.2: Scaled and magnified regions of the FTIR spectral trace of measured geological and synthetic apatites and brushite a) ν_2 (at 470cm^{-1}) and ν_4 PO_4^{3-} vibrational region; b) OH^- vibrational region; c) Spectral region range 1300-1900cm^{-1} showing the characteristic carbonate modes of $\nu_3CO_3^{2-}$; d) Spectral region of the ν_3 and ν_1 of the PO_4^{3-}. In the case of sample HyAp and F-Ap the carbonate vibrational modes are absent. The S-brush synthetic brushite is plotted with a dashed line, as this sample does not have the apatitic structure as the rest of the samples.

5.3.1 Comparison of the $\nu_4PO_4^{3-}$ asymmetric bending vibrational mode

The main IR-active vibrational bands for the P-O bond in the phosphate tetrahedral unit is the ν_4 (T2 asymmetric bending) region of the apatite structure. Theoretical calculations of the frequencies for $\nu_4PO_4^{3-}$ are given with a band at 566cm^{-1} (A), 602cm^{-1} (E1 representation) and a third (E1) at 632cm^{-1} (Corno et al., 2006). Experimental work by Miller et al. (Miller et al., 2001) also shows these band's values appearing in the $\nu_4PO_4^{3-}$ region. Labelling of the spectral trace peaks

and the corresponding band assignment according to the literature is provided in Table 5.3.

The spectral decomposition and the profile function of the band of the ν_4 region for the compared samples are show in Fig.5.3. The results show differences in obtained values of the peak positions. The values of the fit parameters obtained from spectral decompositions are listed in Table 5.2. The obtained values for all samples vary around the center values of 565cm^{1}, 576cm^{1} and 603cm^{1}, deduced from the spectral decomposition of measured spectra.

Brushite is included into the comparison as an example of a non-apatitic P-O vibrational mode. It has a strong peak at 528cm^{-1}, a hidden peak at 535cm^{-1}, peak near 560cm^{-1}, a strong peak near 580cm^{-1}, and a shallow-broad peak centred near 660cm^{-1}.

Table 5.2: Peak centre position in the $v_4PO_4^{3-}$ after the spectral decomposition

Band Peak centre [cm^{-1}]	C-HyAp	F-Ap	HyAp	S-(C)-HyAp	S-brush	Band**/ Peak centre [cm^{-1}]
Hidden peak L	546.77	538.57	545.65	541.36	528.94	HPO_4^{2-} O-P-O
A1 *	567.25	561.04	569.47	563.24	535.39	HPO_4^{2-} O-P-O
A1 *	577.73	574.48	Not possible to resolve	574.42	558.45	HPO_4^{2-} O-P-O
E1 *	604.37	601.79	602.06	603.3	557.05	HPO_4^{2-} O-P-O
OH^- libration	-	-	633.18	633.49	661.93	H_2O libration (W2)
Hidden peak R	621.74	615.4	668.26			

* band notation from (Corno et al., 2006);
** band notation from (Hirsch et al., 2014)

Table 5.3: Region of phosphate $\nu_4PO_4^{3-}$. The wavenumber notation corresponds to peak numbering in Fig.5.2a.

Wave number notation	C-HyAp	FAp	HyAp	Synthetic brushite	Synthetic HyAp	bond	reference
(1.)	vb	vb	vb,sh	-	w,vb	$\nu_2PO_4^{3-}$	Antonakos et al., 2007
(2.)	-	h	h	vs	-	Non-apatitic	Drouet et al., 2009, Vandecandelaere et al., 2012
(3.)	vs	vs	vs	vs	s,h	$\nu_4PO_4^{3-}$	Corno et al., 2006, Hirsch et al., 2014, Miller et al. 2001
(4.)	vs	vs	vs	-	vs	$\nu_4PO_4^{3-}$	
(5.)	-	h	s	-	s_{broad}	OH^- libration	Bhat et al., 2014, Cant et al., 1971, González-Díaz and Hidalgo, 1976a, González-Díaz and Hidalgo, 1976b
(6.)	-	-	h	w, vb	-	Non-apatitic	Drouet et al., 2009, Vandecandelaere et al., 2012

* vs = very strong; s = strong; w= weak; sh = shoulder; h = hidden; vb =very broad

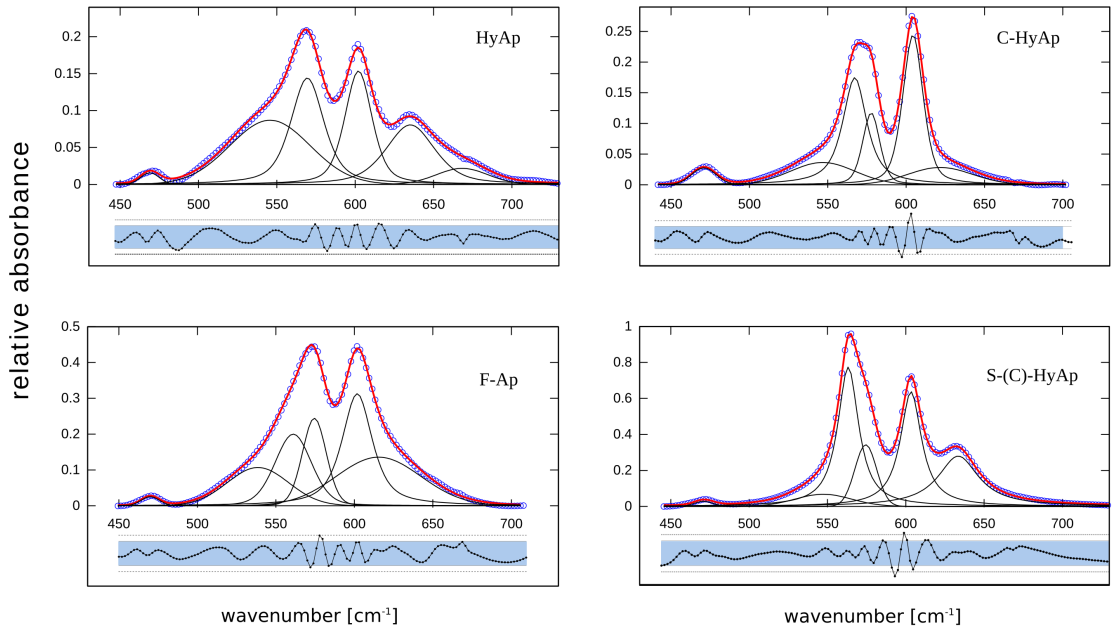

Figure 5.3: Spectral decomposition of the the $\nu_4PO_4^{3-}$ region for the sample of HyAp (adjusted r^2=0.9996), F-Ap (adjusted r^2=0.9995), C-HyAp (adjusted r^2=0.9991) and S-(C)-HyAp (adjusted r^2=0.9997). The lower section of each plot shows the magnified difference curve of the model and the fit. Limits of 2 and 3 standard deviations from the mean of the residual values denoted with blue band and dotted line, respectively.

5.3.2 Comparison of the carbonate vibrational modes $\nu_3 CO_3^{2-}$

Bands that can be associated to the characteristic CO_3^{2-} vibrational modes present in experimentally measured apatite samples are listed in Table 5.4 in correspondence with peak numbering in Fig.5.2c.

The FTIR spectra indicate that the carbonate group is absent in the nominal hydroxylapatite (HyAp) sample, as well as in fluorapatite (F-Ap). The characteristic bands at 1415cm^{-1} and 1450cm^{-1} appear in the spectral trace of the carbonated-fluor-apatite (C-HyAp) as well as in the sample of synthetic S-(C)-HyAp (see Fig.5.2c.). In the case of the C-HyAp sample a significant broadened background is also observable below these bands. The synthetic carbonate bearing hydroxylapatite (S-(C)-HyAp) shows small and broad bands of $\nu_3 CO_3^{2-}$, but also a very sharp and intense band at 1380cm^{-1}.

Table 5.4: Region of $\nu_3 CO_3^{2-}$. wavenumber notation corresponds to peak labelling in Fig.5.2.

Wave number notation	C-HyAp [cm^{-1}]	F-Ap	HyAp	Synthetic brushite [cm^{-1}]	Synthetic HyAp [cm^{-1}]	bond	reference
(1.)	-	-	-	s 1381	vs 1381	C-H	(Chen et al., 2002) (Rodríguez-Lorenzo et al., 2003) (Panda et al., 2003)
(2.)	1414					C-O	(Pasteris et al., 2012) (Antonakos et al., 2007)
(3.)	1450					C-O	
(4.)	-	-	-	1650	vb 1650	H_2O bending W(1)	(Drouet et al., 2009) (Hirsch et al., 2014)

* vs = very strong; s = strong; w= weak; sh = shoulder; h = hidden; vb =very broad

5.3.3 Comparison of the OH^- vibrational modes

The presence of OH^- in the structure of calcium-phosphate apatite can be readily identified by the presence of the characteristic peak near 3571cm^{-1}. Literature values are listed in Table 5.5. The spectral decomposition is graphically illustrated on the sample of nominal hydroxylapatite (HyAp) in Fig.5.4. Spectral decomposition of this spectral region was attempted in two approaches with different modelling of the background signal (background subtraction), as well as different spectral range of the fit. In the first approach the bands of water vibrational modes have been included in the fit as well (Fig.5.4a-b), while in the second approach only the exact region of the characteristic peaks have been evaluated over a smaller spectral range (Fig.5.4c).

The presence of OH^- in the structure of calcium-phosphate apatite can be also identified by the presence of a band near 630cm^{-1}. The band assignment was based on theoretical calculations of the torsion bands of water applying the potential functions by González-Díaz and Hidalgo. In their report the authors show that the band at 630cm^{-1} can be assigned to the libration* of the OH^- bond (González-Díaz and Hidalgo, 1976a). This band appears in the spectral trace of the "Snarum"-apatite sample (HyAp), as well as in the synthetic hydroxylapatite (S-(C)-HyAp). In the fluorapatite mineral (F-Ap) this peaks is evidently missing (Fig.5.2.a), however a broad background peak is needed in the spectral decomposition that is centred at 615.4cm^{-1} after the fitting procedure (Fig.5.3).

Table 5.5: Characteristic peaks of the OH^- vibrational region; wavenumber notation corresponds to peak numbering in Fig.5.2b.

Wave number [cm^{-1}]	C-HAp	FAp	HAp	Synthetic brushite	Synthetic HAp	bond	reference
(1.)	-	-	vs 3495	vs	-	H_2O stretch W(2)	(Hirsch et al., 2014)
(2.)	w 3537	w 3534	vs 3541	-	-	$F\cdots OH^-$	(Cant et al., 1971)
(3.)	sh 3562	-	vs 3569	-	h 3564 ; s 3571	OH^- stretch	(Rehman and Bonfield, 1997) (Pedone et al., 2007)

* vs = very strong; s = strong; w= weak; sh = shoulder; h = hidden; vb =very broad

The comparison of fluorapatite (F-Ap) and hydroxylapatite (HyAp) in the spectral region from 2500-4000cm^{-1} (Fig.5.2b) shows a peak centre position at 3541.8cm^{-1} for the sample of F-Ap, and 3569.1cm^{-1} for the synthetic-carbonate bearing hydorxylapatite (S-(C)-HyAp) sample. The peaks are marked by numbers (1) and (2) in Fig.5.2b. as F-Ap and S-(C)-HyAp, respectively. Values with literature references are provided in Table 5.5. In the case of the nominal hydroxylapatite (HyAp) sample the OH^- stretching mode is at 3569cm^{-1} (marked with number 3 in Fig.5.2b), and the vibrational mode assigned to $F\cdots OH^-$ is at 3541cm^{-1} (marked with number 2 in Fig.5.2b). From the simultaneous presence of these bands in the sample of HyAp, it can be concluded that there is a simultaneous presence of an OH^- band and $F\cdots OH^-$ bearing domains of hydroxylapatite and fluorapatite phases, which are present as a phase mixture in the measured sample volume.

* libration is a movement where the molecules with nearly fixed orientation sways or rotates back and forth. A molecule or atom can undergo libation if its orientation is constricted.

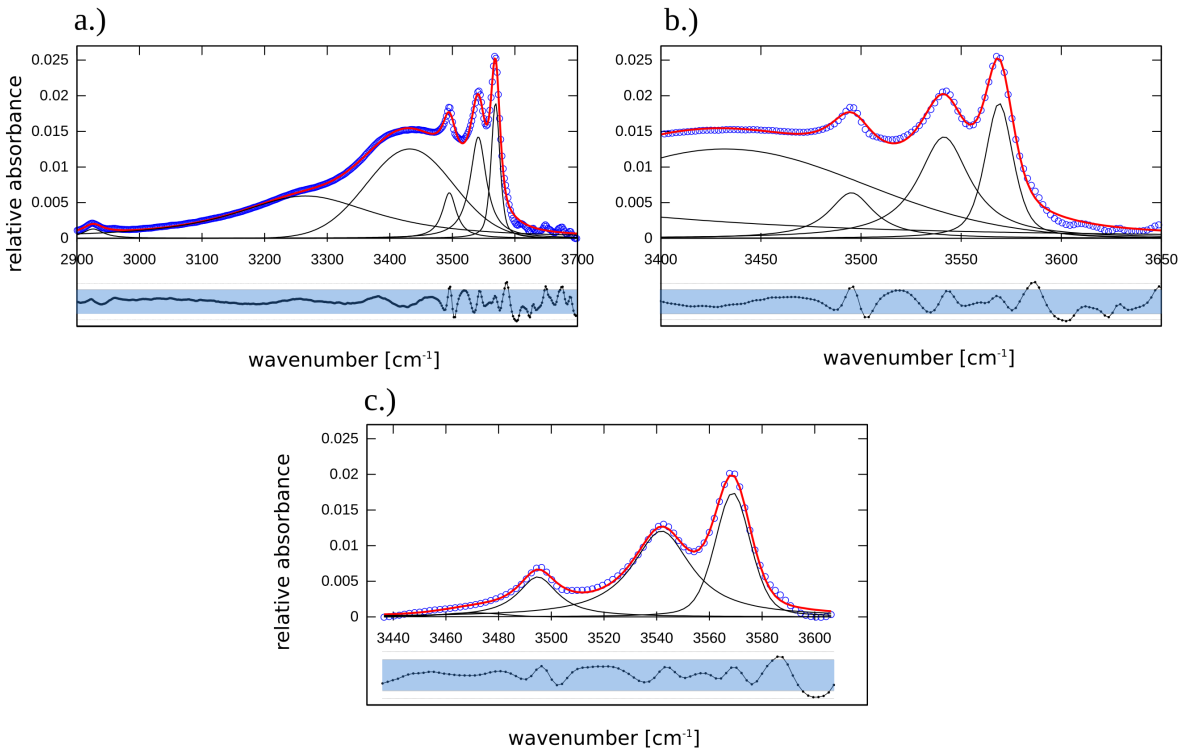

Figure 5.4: Spectral region of OH- vibration modes for the HyAp sample. a.) first approach of fit - overall view of the band positions in the spectral range from 2900-3700cm^{-1} ; b.) enlarged section of the plot on a. ; c) second approach of fit,where only the spectral range range from 3400-3650cm^{-1} has been taken into account. In the second case the background subtraction was only for the section of the three peaks shown. The peak at 3568.9cm^{-1} is identified as the OH^- stretching mode of hydroxylapatite structure, while the band at 3541.8cm^{-1} is assigned to the F···OH^- bond in fluorapatite. The direct comparison of the spectral region is shown in Fig.5.2b.

5.4 Results of XRPD pattern analysis

Result of the applied X-ray diffraction methods were not able to quantify small amounts of carbonate in the crystallographic structure. The focus in this section is therefore more on the evaluation of the phase mixture hypothesis by the means of powder diffraction illustrated on the nominal hydroxylapatite (HyAp) sample.

The difference of lattice constants of hydroxylapatite and fluorapatite hexagonal apatite structure would contribute to a non-trivial diffraction peak shape in the measured diffraction pattern. The hypothesis that microstrain related effect could cause the broadening of the observed peak profile (shape) in the diffraction pattern is also tested. The assigned physical meaning for the presence of microstrain

could be speculated as a distribution of fluorine that affects the lattice constants, locally producing inhomogeneities between the unit cells. This argument is still fully in agreement with the model of anionic column given by Hughes et al. (1989), where the fluorine can replace the OH^- groups (or vice versa). Furthermore, any amount of F^- and the OH^- in the anionic column (channel position in the apatite structure) would produce broadening in the corresponding vibrational modes in the FTIR spectrum as well.

In order to investigate the influence of the crystallographic model choice, Rietveld refinement of three crystallographic models have been evaluated on the same measurement dataset of the HyAp sample: 1.) single phase of hexagonal hydroxylapatite (with microstrain broadening included); 2.) monoclinic hydroxylapatite structure; and 3.) two-phase mixture of hexagonal hydroxylapatite and fluorapatite. In Table 5.6 the reference structures are listed as well and the lattice constants of the initial structure and the result of the refinement. The results show that the best fit was obtained for the two-phase model. The monoclinic hydroxylapatite shows also a reasonably good fit even for some of the very small peaks that are observable only by closer inspection. Nevertheless, this result can not confirm the monoclinic model due to the limited number of parameters used in the refinement (for example the atomic positions were not refined).

Table 5.6: Database references for apatite structures used in the Rietveld refinement with reported unit cell lattice constants and the comparison with the refined values

Model	Name	Reference of the initial structure and database code	Lattice constants [Å]	
			from reference	refinement results
Single phase Hexagonal	Hydroxylapatite	Sudarsanan and Young, 1969 COD 96-901-1095	a= 9.4240 c= 6.8790	a= 9.42717(14) c= 6.86309(2)
Single phase Monoclinic	Pentacalcium tris(phosphate(V)) hydroxide	Espanol et al., 2010 COD 96-721-7893	a= 9.426 b= 18.856 c= 6.887 γ= 119.8°	a= 9.4307(2) b= 18.8317(4) c= 6.8738(1) γ= 119.841(1)°
Two-phase	Hydroxylapatite	Sudarsanan and Young, 1969 COD 96-901-1095	a= 9.4240 c= 6.8790	a= 9.42718(14) c= 6.8613(2)
	Fluorapatite	Hughes et al., 1989 COD 96-900-1233	a= 9.3973 c= 6.8782	a= 9.4040(2) c= 6.8644(5)

5.4.1 Single phase with hexagonal model

The nominal hydroxylapatite (HyAp) sample was modelled with a hexagonal hydroxylapatite structure including microstrain broadening parameter, as the diffraction pattern of the sample shows broad peaks relative to the instrumental resolution profile. Broadening due to finite size of the crystallites was not assumed, since the samples have been grind manually and no presence of nanocrystalline phase is expected. This assumption leaves microstrain as an alternative source for the observed broadening of the peaks in this model. However, even with the microstrain included as a free parameter, the refinement could not model the shape of the diffraction peaks in full extent correctly. Nevertheless, the overall fit is adequate (Fig.5.5).

In Table 5.6 a comparison of the initial structures and the end results of the refinements have been given. For the single hexagonal phase the structure solution given by Sudarsanan and Young (1969) a very good match was obtained for the lattice constants along the a(b)-axis, however, in the case of the c-axis the difference from the initial model is significant.

The parameter of isotropic microstrain resulted in the values of 0.145%, corresponding to a maximum length variance of about 0.014Å for the values of the a(b)-axis, and 0.01Å length variance for the values of lattice constants along the c-axis. Interpretation of this result suggests that isotropic microstrain affects the longer axis in greater extent, which is contrary to expected results. The anionic column (channel sites) are expected to be more prone to host or exchange ions. Due to this assumption it is expected that microstrain would be more affecting the shorter axis (c-axis), resulting higher variance. However, this hypothesis could be tested only in an anisotropic strain refinement. Such a refinement had been unfortunately failing to converge and to produce reasonable results.

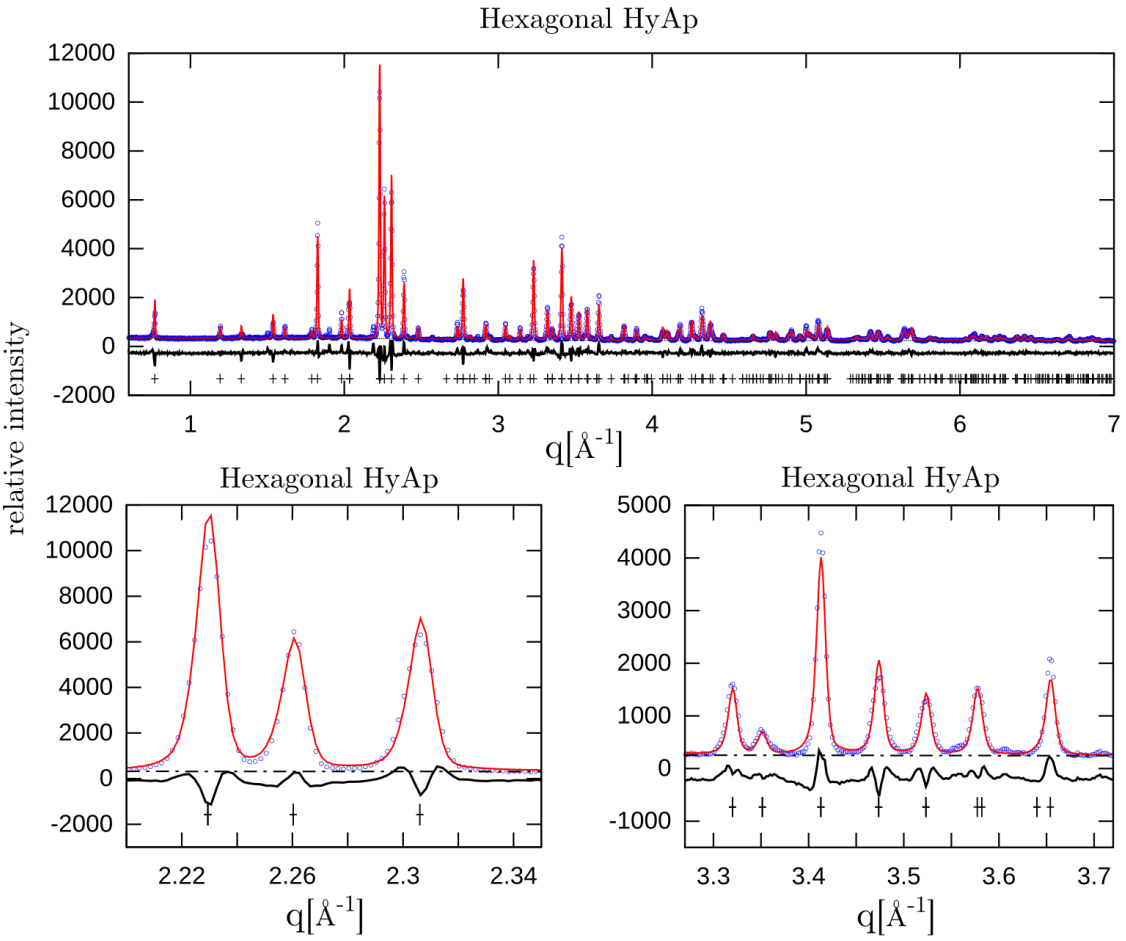

Figure 5.5: Rietveld refinement of the HyAp nominal hydroxylapatite sample with the hexagonal hydroxylapatite structure model with isotropic microstrain broadening parameter. Zoomed-in regions of the upper plot are shown in the lower section. Three diffraction peaks of the highest intensity (between 2.22-2.34$Å^{-1}$) region are showing inadequately modelled peak intensity as well as peak shape (lower left plot). The same appears on higher q regions of the diffraction pattern (lower right plot).

5.4.2 Single phase with monoclinic model

A monoclinic structure model has been also described in the literature for the calcium-phosphate apatite structure with a monoclinic angle is very close to the 120° of the hexagonal system. For the refinement a structure model of monoclinic ($P112_1/b$) pentacalcium-tris-(phosphate(V))-hydroxide was used in the refinement (Espanol et al., 2010). The fit shows a reasonably good match of the measured and modelled diffraction peaks (Fig.5.6).

The parameter of isotropic microstrain resulted in the values of 0.0978%, a much smaller value than in the case of the single phase refinement with the

hexagonal structure. This might be due to the fact that the lower symmetry structure has a more spread out distribution of the diffraction line positions, which can be observed in Fig.5.6, as the markers of the reflections cover several values of the q-space. As each reflection is modelled with it's own pseudo-Voigt distribution function, the sum of all corresponding reflections can better match the measured diffraction peak trace. A smaller value of a microstrain broadening parameter can in the case of a monoclinic structure produce a better peak profile fit.

However, due to the large number of structural parameters in the monoclinic cell, parameters such as the atomic position, thermal factors and site occupancy have not been refined. Whether the material is really monoclinic can only be decided by looking at the superlattice peaks, which are present for the monoclinic and absent for

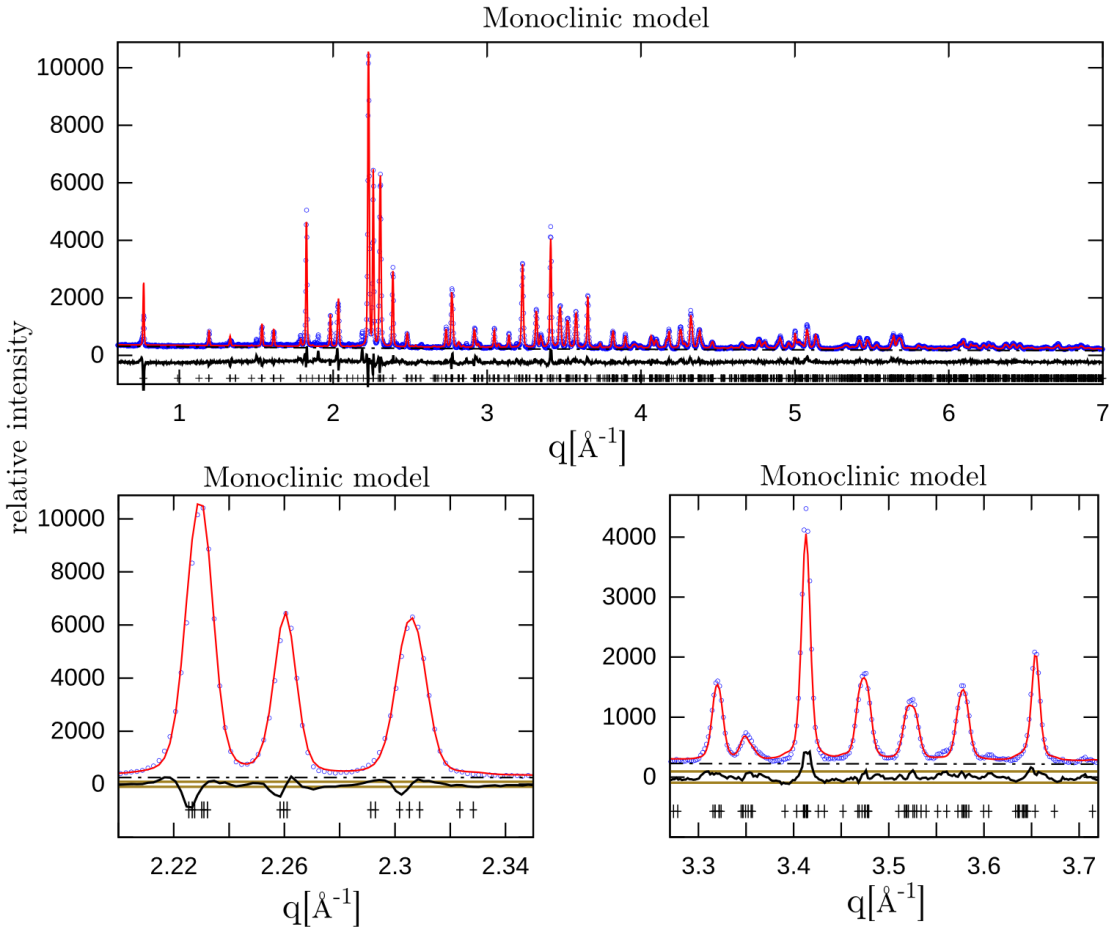

Figure 5.6: Rietveld refinement using a monoclinic unit cell model. The high intensity peaks are fitted reasonably good, shown on the lower plots. Due to the large number of structural parameters in the monoclinic cell, parameters such as the atomic position, thermal factors and site occupancies were not refined.

the hexagonal. Zoomed-in region in Fig.5.6 shows that this monoclinic model gives peaks near 3.4 $Å^{-1}$, and not precisely fir peaks existing peaks near 3.5 $Å^{-1}$ and 3.6 $Å^{-1}$.

5.4.3 Two-phase model refinement

A refinement model with a two-phases mixture of hydroxylapatite and fluorapatite was also examined for the HyAp nominal hydroxylapatite geological

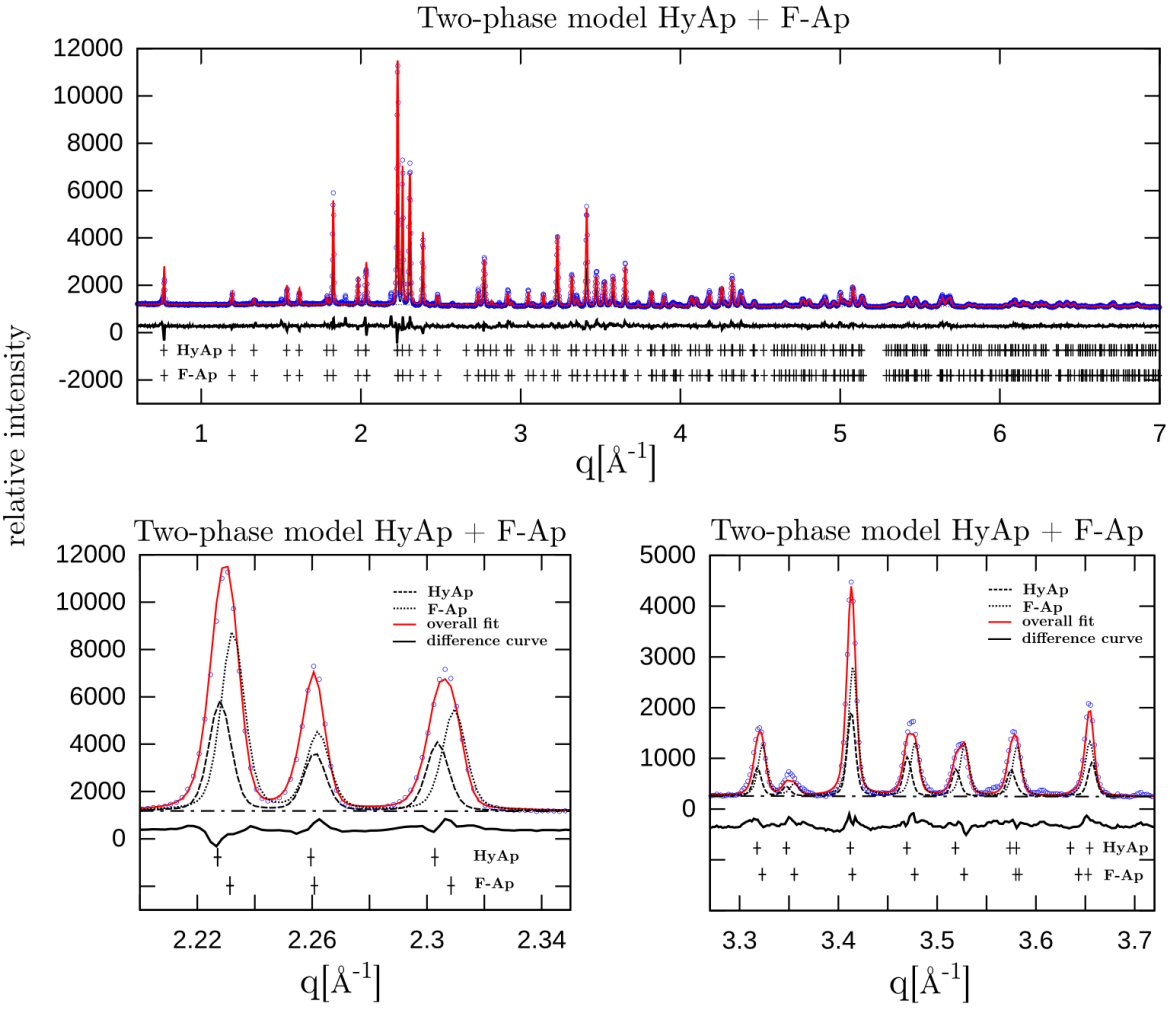

Figure 5.7: Rietveld refinement of the HyAp nominal hydroxylapatite sample using the two-phase mixture model of hexagonal hydroxylapatite (HyAp) and fluorapatite (F-Ap). The upper plot shows the overall matching of the model to the measured pattern. The lower plots show selected peaks with each phase's contribution to the peak profile (shape). The hydroxylapatite phase is marked with dotted line, while the fluorapatite with dashed line. The overall model (red line) models the data-points reasonable good (also see difference curve).

sample. Results of the refinement fit are shown in Fig.5.7, with the modelled diffraction pattern for each phase is plotted as well. The crystallographic structure of hydroxyl-, and fluorapatite differ by the z-position occupied by an atom of oxygen or fluorine, respectively, and also by the values of the lattice constant.

The obtained phase fractions are 43.7wt% and 56.3wt% for hydroxylapatite and fluorapatite, respectively, however, the refinement required a sequence of locking the phase fraction scale parameters. Reasonable phase fraction values were obtained by setting the initial phase ratio to 50:50wt% and by opening the scale parameters after other structural parameters were refined.

The broadening of the diffraction peaks was modelled by including an isotropic microstrain as well, and the obtained value was small, 0.01%. The refined values for the lattice constant of the phases are given in Table 5.6. For the hydroxylapatite phase the difference with respect to literature values is small, and more prominent for the flurapatite phase.

5.5 Electron-microprobe analysis

the measurements of electron-microprobe have been conducted with limited success due to the limited ability of the measurement technique to reliably quantify presence of carbon and carbon ions. Only the sample of nominal hydroxylapatite of geological origin (HyAp) was examined in greater detail and discussed in this section. The measurements were conducted as random point measurements over an area of 200x200µm-s on a broken fragment of the sample. No distinct regions of formations were observed on the back-scattered electron image, although the mineral has visible areas of different coloration. The WDX measurements show element concentration differences (see Table 5.7). The results of the point measurement indicate only a few locations with significantly higher fluorine content (rows highlighted in Table 5.7). For these point measurements the percentage of Ca and O appear to be lower than for the rest of the measured locations. At the points with the higher fluorine weigh percent values, the percentage of Cl is reduced relative to all other measured points.

This result indicates that the likelihood of a two-phase separate domain mixture is greater, at least in the case of the measured sample area. Moreover, the results indicate that chlorine is also present on domains where fluorine is not (apparent mutual exclusion).

Table 5.7: Electron-microprobe WDX point measurements showing the weight percent of element composition of the nominal HyAp sample. Point measurements indicate occasional higher F wt%.

	Ca	**P**	**F**	**O**	**Na**	**Mg**	**K**	**Cl**	**Al**	**Si**	**Fe**	**C**	**Tot**
1	39.35	18.41	0.26	40.52	0.04	0	0	0.24	0.03	0.11	0	1.53	100.48
2	39.04	18.69	0.18	40.52	0.06	0	0	0.52	0.02	0.04	0.06	0.68	99.74
3	39.53	18.81	0.23	40.7	0.04	0	0.03	0.32	0.04	0.04	0	0.79	100.53
4	38.99	18,42	0.23	40.35	0.05	0	0	0.32	0.04	0.05	0.13	0.92	99.49
5	39.17	18.18	0.23	40.89	0.02	0	0	0.73	0.03	0.03	0.02	0.98	100.28
6	39.25	18.46	0.25	40.58	0.04	0	0.02	0.5	0.03	0.03	0.06	0.96	100.18
7	41.84	18.82	3.91	38,31	0.09	0	0.01	0	0.01	0.01	0.01	0.25	103.24
8	41.27	18.01	3.58	38.29	0.14	0	0	0.07	0	0.02	0.45	0.89	102.72
9	0.21	0.08	0	52.15	0.03	0.22	0.18	0.03	18.99	21.78	1.98	0	95.65
10	16.85	7.56	0.8	43.66	0.26	1.0	2.67	0.04	5.76	13.56	5.52	1.92	99.61

5.6 Conclusion

In a multi-technique investigation of geological and synthetic hydroxylapatite, fluorapatite and carbonated-hydroxylapatite mineral samples different crystallographic models and phase mixtures were compared in order to evaluate isostructural apatites. In the case of the nominal hydroxylapatite HyAp sample the X-ray diffraction pattern was evaluated with assumptions of: 1.) single hydroxylapatite phase model with microstrain; 2.) monoclinic crystallographic structure model; 3.) two-phase mixture model. The results show that the best fit was obtained using a two-phase mixture model for the the special case of the nominal hydroxylapatite "Snarum" apatite.

FTIR spectroscopy results show diverse background hidden weak peak presence in the phosphate ν_4 vibrational region for the investigated samples. This could indicate a complex state of the phosphate bands and does not exclude the presence of different hydrogen-phosphate species, although, the measurements and analysis can not confirm this assumption. In the case of the samples such as the nominal hydroxylapatite HyAp spectroscopic peaks in the OH^- vibrational region hint toward a model of two-phase mixture, simultaneous presence of hydroxyl- and fluorapatite.

Evidence from the electron microprobe analysis led to the conclusion that in the case of the geological nominal hydroxylapatite sample (HyAp), it is indeed a two-phase mixture of hydroxylapatite and fluorapatite which is the most likely. The measurements also suggest that the presence of chlorine in the structure can not be

excluded either.

Geological minerals have been analysed in the attempt to use them as reference cases in the understanding of the appearance of ionic interchange that can potentially occur in the case of the carbonated calcium-phosphate apatite nano-crystallites in the bone composite material. From the presented investigation in this chapter, it can be concluded that geological samples are not adequate models for the case of bone sample, although the crystallographic structure appears to be very similar. The geological samples have their own complexity that is different from the complexity occurring in the bone samples. Primarily due to the size of the crystallites, which in the case of bones is on the size range of nanometers; secondarily the chemical environment during the nucleation and growth of the crystallites in the case of geological environment is much more unpredictable and versatile with respect to the physiological environment of the organism.

Chapter 6
Reference material 3. - Experimentally induced microstructural alterations in bone material

6.1 Context and aim

In Chapter 2 the extent of delicate differences between bone sample of different species and skeletal elements have been demonstrated, as well as the influence of cleaning and sample preparation. In Chapter 4 and Chapter 5 the influence of environment (soil conditions) and geological reference minerals have been investigated in order to explore the ionic flexibility of the carbonate calcium-phosphate apatite as an analogous materials to the bone apatite nanocrystallites. An alternative approach to examine the nature of the bone apatite crystalline material is to induce alteration to the natural (nucleated and grown in biological-physiological conditions) calcium-phosphate apatite and interpret the response of the system to the alterations.

In this chapter results of experimental alterations to a selected bone sample and their effects on crystal growth are discussed. The starting bone material is assumed to be in the state as in-vivo, with conserved properties after a preparation method consisting of mechanical cleaning from residual non-bone tissue and washing with de-ionised water without any additional chemical treatment.

Two experiments will be presented in this chapter. The first set of experiments (section 6.2) was designed with the aim to study the growth of the crystallites under wet (hydrothermal) conditions in a closed compartment (isolated system). The temperature is raised well above protein denaturation temperatures* (set to 130°C) in order to accelerate any crystallite growth reaction. The second set of experiments (section 6.3) was targeted at the crystallite growth in dry conditions induced by heat energy as the only assumed external control factor (annealing).

The hydrothermally induced crystallite growth experiments were motivated by two major issues that emerged during the research of environmentally altered bone

*protein denaturates already at temperatures around 41°C (Bächinger et al., 1993)

material (Chapter 4). Firstly, results of diffraction studies of archaeological bone material show no clear dependence between sample crystallite size and the estimated age of the samples. The observed large variance in the relation of age and microstructural effects can be due difference in ageing conditions or intrinsic differences between the samples. Hydrothermal alteration experiments were aimed to investigate the ageing effect on the crystallites. Secondly, the effect of water on the crystallite growth was investigated by the comparison of the nanocrystallite growth in wet and dry conditions. The wet conditions apply for the hydrothermal treatment, and the dry conditions correspond to the combustion of the bone material (annealing).

6.2 Hydrothermally induced crystallite growth in bone material

Hydrothermally induced crystallite growth was studied in crushed powders of *bos taurus* femur skeletal element bone material. The powdered samples were exposed to water at elevated temperatures of 130°C. At this temperature the closed compartment of the autoclave produced a calculated pressure of about 0.23MPa[*]. A sequence of microstructural differentiation was achieved as a time series of treatment duration. With increasing time duration of the ageing treatment the sharpening of diffraction and spectroscopic peaks is observable. Microstructural changes were monitored using X-ray powder diffraction Rietveld refinement and peak fitting of FTIR vibrational spectroscopy. The goal of the experiments was to measure the extent of the long range order increase (as crystallite growth) under experimental conditions.

The sequence of microstructural transformation is mapped in order to examine whether the increase of the long range order first undergoes through a reduction of strain that is followed by the increase of the bulk volume of the crystallites, or whether the increase of the long range order is primarily and only due to the increase of the bulk volume of the crystallites. In the second case the sources of microstrain are treated as redundant with the progression of the transformation.

Similar experiments of hydrothermal treatment of bone material have been previously conducted by Turner-Walker et al. (Turner-Walker, 2011) focusing on the changes of the mechanical properties with the duration of the hydrothermal treatment. By observing the materials strength with treatment duration the integrity of the structure was probed. However, Turner-Walker et al. haven't investigated the alterations of the nanocrystallites, only the effect on the collagen-crystallite interface as his experiments were focused on the collagen-nanocrystallite bonding.

* Pressure calculated: $p = e^{20.386 - \frac{5132}{T + 273.15K}} \cdot 133.322 \times 10^{-6}[MPa]$ from the vapour pressure curve

Experiments of hydrothermal ageing on synthetic HAP had been conducted by Kothapalli et al. as well (Kothapalli et al., 2005). However, their reported research does not provide a thorough microstructural analysis of the crystallites and therefore the synthetic analogous model proposed by the authors can not be considered as an adequate model for experimentally or naturally altered bone material.

Hydrothermal ageing experiments can also be considered to resemble maturation experiments (ageing in solution), since both experimental methods are probing the crystallite volume increase (decrease) in aqueous medium. Thermodynamic aspects of maturation processes and an increase of crystallite size of synthetic hydroxylapatite nanocrystallites has been analysed in depth by Rollin-Martinet et al. (Rollin-Martinet et al., 2013). Their maturation experiments time-lengths range from days to weeks and resulted in nanometer-sized (12-27nm) hydroxylapatite crystallites. The diffraction pattern of their synthesis products remained in all cases poorly developed and severely overlapped.

Similar experiments by Pang and Bao (2003) describe the crystal growth process dependant of "ripening time", where the growth was terminated by removing the crystalline material from the solution. The reaction products have been analysed by comparison of empirical diffraction peak height and width ratios in the XRPD patterns. The authors provided an experimental series relating "crystallinity" and crystal size depending on the ripening time.

The hydrothermal alteration experiments on powdered bone material presented in this section of the thesis can be considered as the combination of the influence of heat energy, maturation and ripening. The bone material was exposed to water at an elevated temperature in a closed compartment, which can be conceptually considered as ageing in a solution. The effect of the experimental conditions is investigated in a series of ripening time intervals, as each consecutive sample was exposed to the alteration factors for an increasingly longer period of time. As the results show, in the altered materials the XRPD Bragg peaks are more developed, more distinct and pronounced compared to the state of the original inorganic nanocrystallites of the bone material. It is inferred that the increase of crystallite size is the cause of the observed diffraction pattern sharpening.

According to J. Christoffersen and Christoffersen (1992) and M. R. Christoffersen and Christoffersen (1992) the crystallite size or shape is considered independent of the surface free energy. Comparison of growth rate calculations based on the relationship of surface free energy and solubility show that there are discrepancies between calculated and measured rate values. The authors argue that these are due to presumable surface imperfections that are not adequately calculated.

Kaptay (Kaptay, 2012, 2011) discusses further the meaning of the Gibbs-free energy with respect to the shape of a dissolving particle, and concludes that the surface area is more meaningful than the radius of an approximated spherical

particle. His work disentangles the surface of a particle (crystallite) from an ideal shape (sphere) and states that particles with complex surface can not be approximated with ideal spheres.

In case with a given particle size distribution, a process that resembles the Ostwald ripening (Ostwald, 1900) (later as Ostwald-Freundlich relation) could also be plausible. According to this theoretical approach the bigger crystallites grow at the expense of the smaller ones. However, the influence of anisotropic size on Ostwald ripening is unclear, due to the theoretical limitation of the approximation that this process is based on, namely the authors devised the ripening effect for the spherical particle case only. Moreover, Wu and Nacollas (Wu and Nancollas, 1998) argue that the Ostwald ripening and the Ostwald-Freundlich equation is not adequate to model the interfacial tension between solid and solution.

In the following section of this thesis an empirical description of the crystallite growth will be given, relying on experimental observation of the nanocrystallites of bone material by the means of X-ray powder diffraction and vibrational spectroscopy (FTIR and Raman). The hydrothermal post-processing of bone material can be considered to provide better conditions for the interpretation of structural changes due to less overlapping X-ray diffraction and vibrational spectroscopic peaks.

6.2.1 Materials and methods

Bone material of *bos taurus* femur skeletal elements were physically cleaned and washed. The hard bone material was cut into smaller cubes and dried at room temperature and normal atmospheric conditions. The material was then hammered to chunks and grind in a ball mill. The powder was sieved (100μm mesh size). 0.74g of the finely ground bone powder was added into a Teflon crucible with 10ml of water in each autoclave. The sealed autoclaves were put into a preheated oven at 130°C. The samples were kept in the oven for a time interval in the range from 2 hours to 60 hours. After the set time duration the samples were pulled out, left to cool down, opened and the content was poured in a Petri-dish of 10cm diameter (area of about 157cm^2) to dry. After drying the powder was scrapped form the surface and measured. The total alteration impact is therefore a convolution of: starting conditions, wetting (water), temperature, pressure and drying. The closed compartment preserves the total amount of water. Any dissolution and growth processes during drying have an unknown impact factor.

The XRPD patterns were gathered at the DESY synchrotron facility in Hamburg. The material contained in 1mm diameter capillaries was irradiated with 60keV photons of 0.20727nm wavelength. The diffraction data were collected on Perkin-Elmer 2D detectors of 0.5x0.5m dimension and pixel size of 200microns (0.2x0.2mm). The measured diffraction pattern data for the set of hydrothermal

ageing duration sequence are shown in Fig.6.1, with an enlarged section of the data showing the first few reflections 010, 020, 110, 011 and 111 in Fig.6.2.

The FTIR spectra was measured on a Bruker Equinox spectrometer in transmission mode using the KBr pellet method. 200mg of KBr (kalium-bromid) powder was mixed with 1.4mg of bone powder with maximum grain size of 100μm. The spectrum was gathered in the range of 400-4000cm^{-1} with 4cm^{-1} resolution and 128 scans.

Raman spectra were collected on a Keiser Optics Raman microscope. The data was collected with 32 summed scans, each exposure lasting for 4s. Objective of 80x magnification was used, laser power was 14mW.

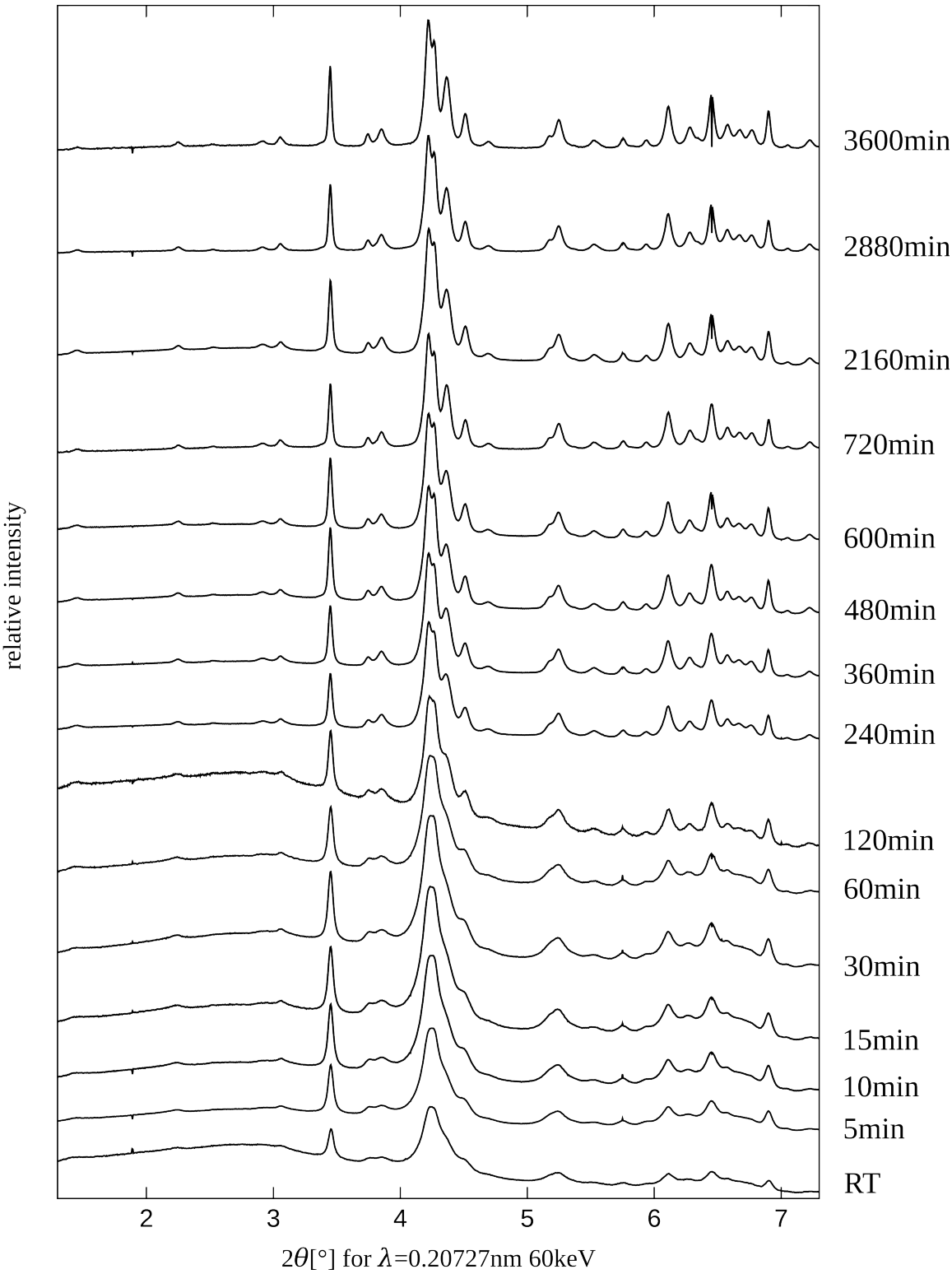

Figure 6.1: Section of the XRPD synchrotron diffraction pattern data of the hydrothermally processed bone material time series of *bos taurus* femur bone. The figure show the differentiation of the Bragg peaks as they are broad for the control reference sample (RT) and reach significant differentiated state in the sample with long hydrothermal treatment duration (3600min = 60hours).

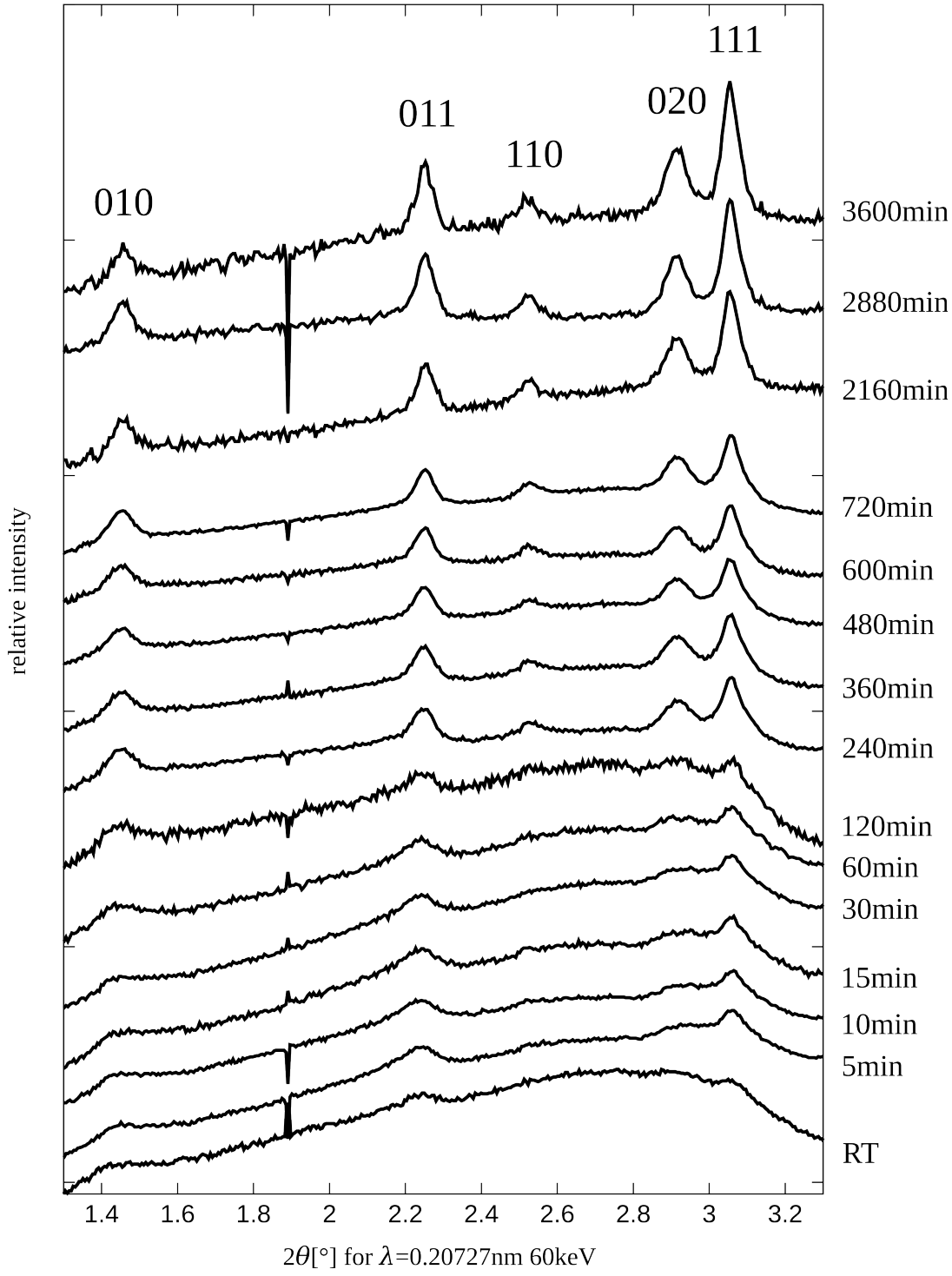

Figure 6.2: Magnified section of the XRPD synchrotron datasets from the Fig.6.1, where the Bragg peaks of reflections 010, 020, 110, 011 and 111 are shown. The data is plotted by applying relative scaling. Artefacts of spikes are due to dead pixels from the detector and the masking procedure while transforming the 2D image to an intensity dataset.

6.2.2 XRPD results and discussion

The evolution of the line broadening with hydrothermal treatment time was followed by applying a full profile refinement with anisotropic size model. The plot of the obtained result of the Rietveld refinements line broadening microstructure analysis with apparent crystallite sizes and microstrain parameters as the function of hydrothermal treatment duration is shown in Fig.6.3. Applying only size terms (anisotropic size model) for the evaluation of the diffraction peak broadening, an increase can be seen in the apparent crystallite size values with increasing treatment duration time (left plot in Fig.6.3). In comparison, results of the refinements with anisotropic size together with isotropic strain broadening contribution are shown on the right plot of Fig.6.3. According to the results of the refinements (see all parameters in appendix A6) using this mode the microstrain parameter values are decreasing with the increase of the hydro-thermal treatment duration time. The apparent size values, however, show uninter-pretable behaviour in the short treatment duration time interval (the line for 00l reflections in Fig.6.3.).

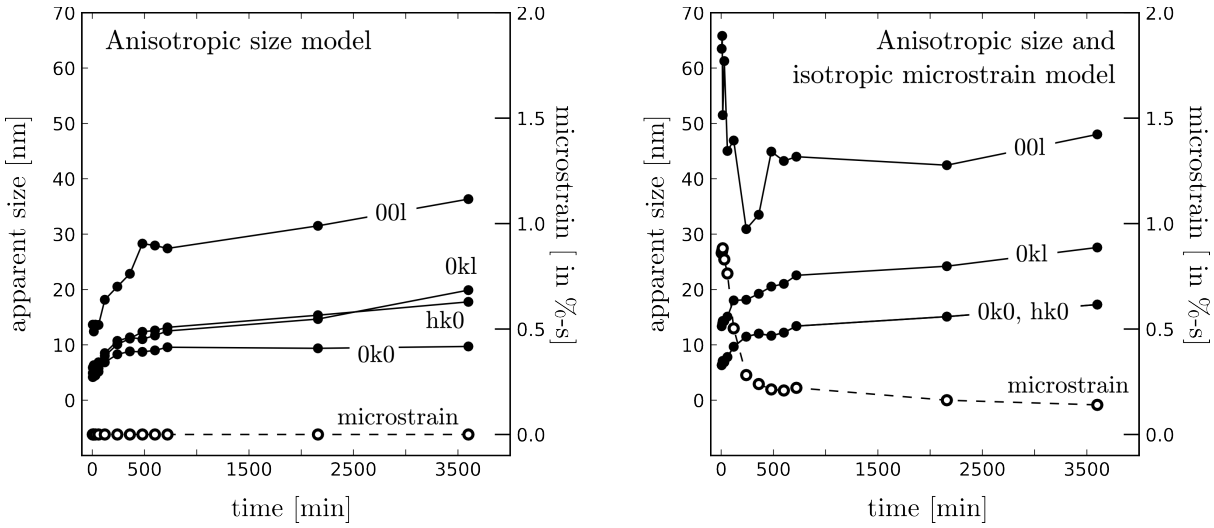

Figure 6.3: Comparison of the Rietveld refinement results for the hydrothermal treatment duration time series. Apparent crystallite size marked with full circles, while microstrain parameter marked with empty circles symbol. On the left side a model with only anisotropic size contribution to the Bragg peak broadening was modelled; on the right side a model with the combination of anisotropic size and isotropic strain included in the microstructure analysis model.

The results of the two approaches differ significantly. From the comparison it can be concluded that: (1). the two models differ significantly for the reference sample and the short treatment duration bone material. In the case of samples that have been treated for less then 500minutes, the incorporation of strain in the refinement produced large oscillations and an unrealistic trend (Fig.6.3. plot on the

right). (2.) according to theoretical arguments (Chapter 1 section 1.3.1) the major source for Bragg peak broadening is the finite size effect. In the case of the refinement with only size contribution to the broadening, the time series follows the expected trend of peak narrowing with increasing exposure time. Additional strain terms only result in uncontrolled parameter correlations. (3.) the high values of the microstrain can not be justified and it is highly likely that the obtained values have no physical meaning.

In order to explore the impact of the refinement parameter optimization sequence (refinement strategy), each dataset was analysed by a number of alternative strategies in automated refinement using the approach described in Chapter 3. In total 90 strategies have been generated by the combination of the parameter's introduction into the fit and fit sequence. Each strategy was used to refine the whole set of the hydrothermal duration sample sequence. Visualization of the refinement results for all the strategies and samples can be shown as a cumulative plot of all the obtained apparent size values (shown in Fig.6.4). The strategy that produced the best reliability factors (best diffraction profile matching) whilst obeying the set rules (inter-atomic distance limits for the phosphate tetrahedral unit P-O between 1.56Å-1.5Å, as described in Chapter 3 section 3.1.2) was chosen and further analysed. In Figure 6.4 this is marked with black circle symbols and correspond to the data-points plotted in Fig.6.3).

The lattice constant obtained from the automated refinement can also be visualized as a cumulative plot of all applied strategies (see Fig.6.5). The solution of the best matching refinement with parameter values satisfying the rules is also highlighted on the plot. It can be seen in the plot that the lattice constants of the c-axis oscillate between 6.886Å and 6.893Å (Δ=0.007Å, corresponds to 0.1% variance from the c-axis values). The a-axis lattice constant decreases with the treatment duration lime in the range between 9.420Å – 9.450Å (Δ=0.03Å, corresponds to 0.3% variance in the a-axis). From the plot it can be also inferred that in the case of short treatment times (up to 100min), all the strategies resulted in significantly different values for the lattice constants. With the increase of the hydrothermal treatment duration the results of the strategies tend to consolidate (left sub-plot in Fig.6.5).

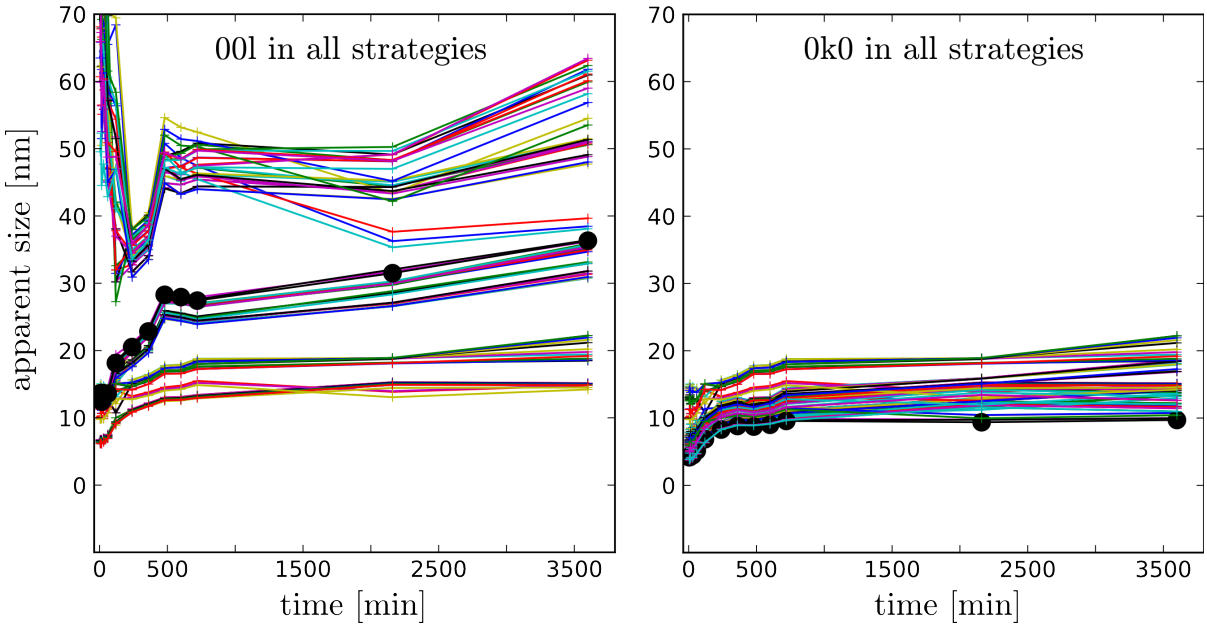

Figure 6.4: All strategies (n=90) in an overlay plot. Each strategy is shown as a color line. The solution satisfying all set criteria in the automated refinement is marked with black circle symbols – the model with only anisotropic size broadening. Results of the best matching refinement strategy are further analysed and separately plotted in Fig.6.3. The plot on the left shows the 00l reflection apparent size for all strategies. It appears that there are at least 3 clusters of similar solutions for the apparent size values for the 00l reflections. On the right hand side the 0k0 reflection apparent size for all strategies is plotted.

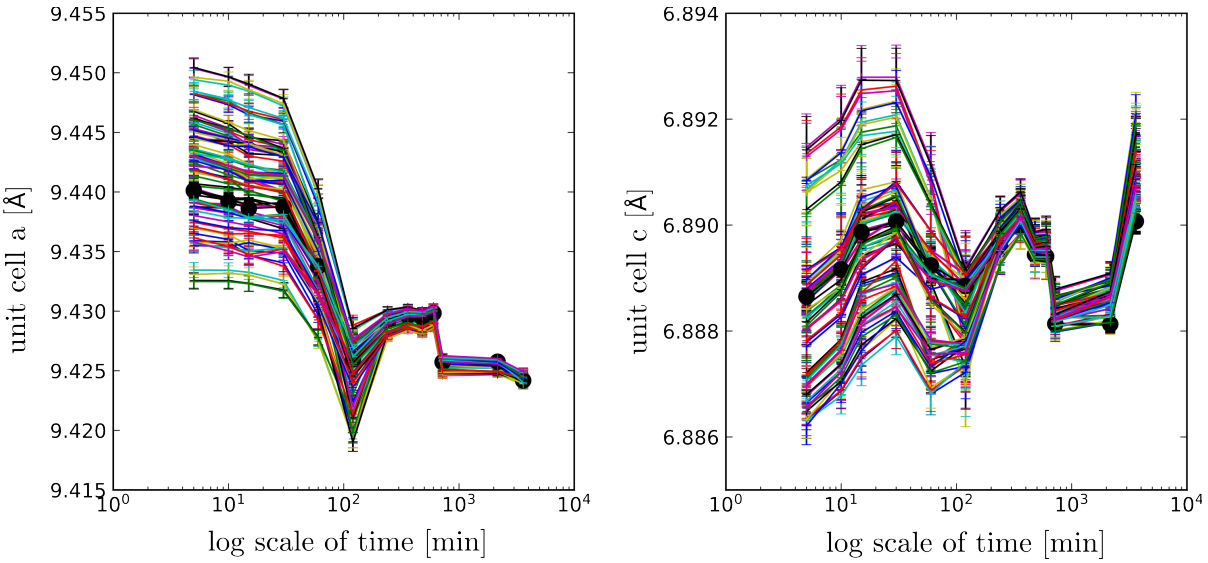

Figure 6.5: Lattice constants in the n=90 strategies each over all datasets of the treatment duration time-series. The horizontal axis of time is in log-scale. The black circles mark the highest ranking strategy with lowest reliability factors (best matching) satisfying all set rules. Left side plot shows the a(b) lattice constant, while the plot on the right shows the c-axis. Unit cell constants a-axis tend to merge for all strategies in the case of long duration times. Values for the unit cell c-axis oscillate, with variance of about 0.007Å.

Example of the Rietveld refinement for the shortest and the longest ageing duration samples applying the same refinement strategy are shown in Fig.6.6. Visual inspection of the model-to-data fit is in general satisfactory. The residual curve is inside two standard deviations from the mean of the residual curve. Nevertheless, there are a few problematic regions that show noticeable deviations of the model from the data. For example, the first peak (first reflection of the hexagonal structure) appears to model with higher intensity then the observed data, and also the shape of the peak is very broad. Moreover, the model does not cover correctly the peak just below 3.5[2ϑ°], as well as the peaks in the region between 4-4.5[2ϑ°]. The applied model and the various refinement strategies didn't manage to produce a better fit of these problematic regions with reasonable values for the fit parameters. This suggests that the model used in the refinement (hexagonal hydroxylapatite with space group $P6_3/m$ without carbonate in the structure) is not adequate in full extent for the Rietveld fit of the bone-, and the hydrothermally aged bone material.

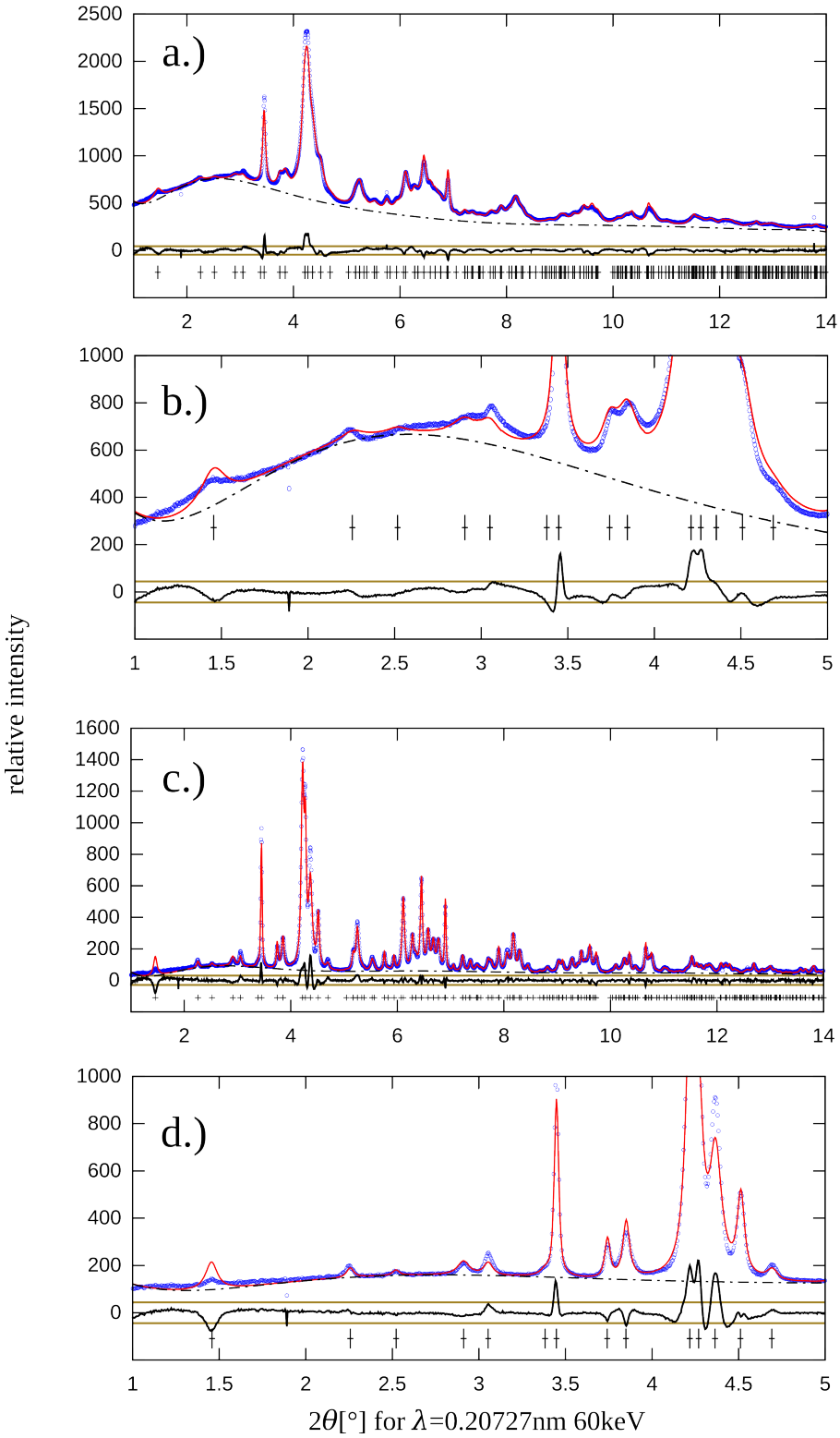

Figure 6.6: Rietveld refinement of hydrothermally aged samples: a.) sample treated for 5 minutes; b) magnification of the section on plot a. between 1-5 2ϑ[°]; c). sample aged for 3600 minutes; d.) magnified section of plot c. between 1-5 2ϑ[°].

6.2.3 FTIR measurements and spectral decomposition

Measured infrared spectra of the treatment time series are shown in Fig.6.7, with the magnified and scaled sections of selected spectral traces are shown in Fig.6.8 and 6.9.

The phosphate bands in the spectral trace show: (1.) the ν_2 P-O band near 470cm^{-1} (left sub-plot in Fig.6.8) displays an increase of the peak with treatment time and a clear separation from the background. This band has small intensity in comparison to other phosphate bands; (2.) the ν_1 P-O band near 960cm^{-1} (sub-plot on the right Fig.6.8) shows the same increase of the peak-features similarly to the ν_2 band; (3.) the strong peaks of the ν_4 vibration band region (400-650cm^{-1}) show differentiation, increase of the phosphate bands; (4.) in the same region (400-650cm^{-1}) the infrared spectral trace shows the decrease of the very broad bands usually assigned to apatitic (Vandecandelaere et al., 2012) and non-apatitic HPO_4^{2-} (Eichert et al., 2005) vibration modes in the background of the $\nu_4PO_4^{3-}$ region. Miller et al. reports the same state of the vibrational band of the P-O bonds (Miller et al., 2001).

A visual comparison of the spectral traces in the region between 400-800cm^{-1} suggests a gradual transformation of the P-O bands of the ν_4 mode from broad spectral features to pronounced peaks, while at the same time the HPO_4^{2-} bands (near 530cm^{-1} and 620cm^{-1}) show a decreasing tendency with treatment time. Furthermore, the band at lower wavenumber appears to be diminishing, while the band near 620cm^{-1} appears to be rising. In the spectral trace of the reference hydroxylapatite structure a characteristic OH^- libration mode is assigned to the spectral peak at 632cm^{-1} (González-Díaz and Hidalgo, 1976a).

The region of the water and OH^- vibrations, (sub-plot on the right side Fig.6.9) shows an appearance of the characteristic OH^- band of the hydroxylapatite reference structure, suggesting that a portion of the calcium-phosphate structure is progressively transforming to a HAP structure.

Carbonate vibrational bands near 870cm^{-1} show an apparent splitting with an increasing hydrothermal treatment time. Assignment of the split CO_3^{2-} band was investigated by Rey et al. (Rey et al., 1991b), although, a band in the close vicinity of the 870cm^{-1} assigned to HPO_4^{2-} has been reported as well (Young and Holcomb, 1984). The more characteristic carbonate bands $\nu_3CO_3^{2-}$ at 1415 and 1450cm^{-1}, similarly as the phosphate bands, gain in apparent peak differentiation from the spectral trace background with the increase of the ageing treatment time (Fig.6.9). The collagen vibrational band region in the immediate vicinity of the these carbonate bands tend to blend into an unresolvable cluster of peaks.

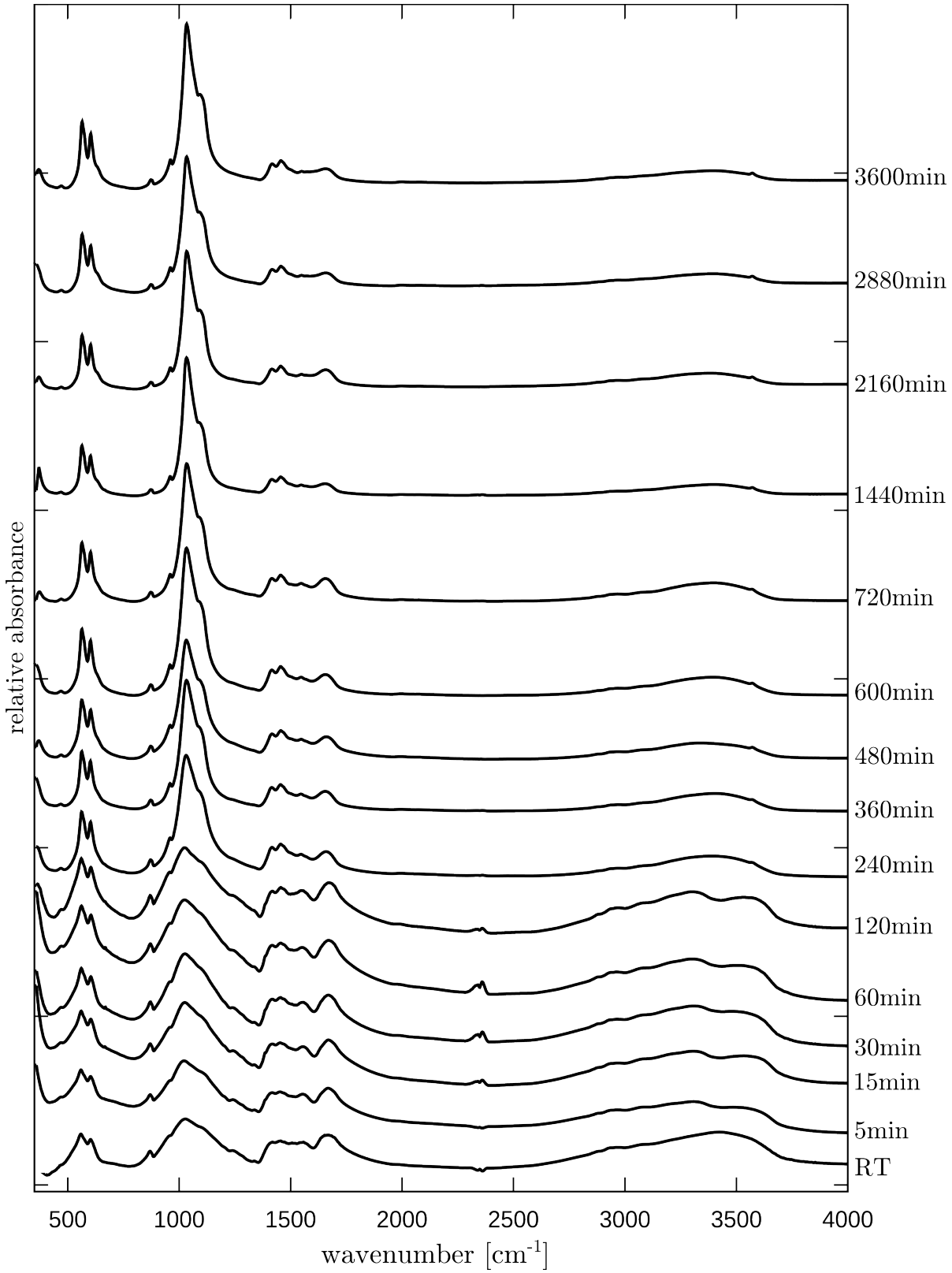

Figure 6.7: Measured FTIR spectra for the hydrothermal ageing time series of bone material. The spectral trace of each sample is arbitrary scaled for better visual comparison of peak features.

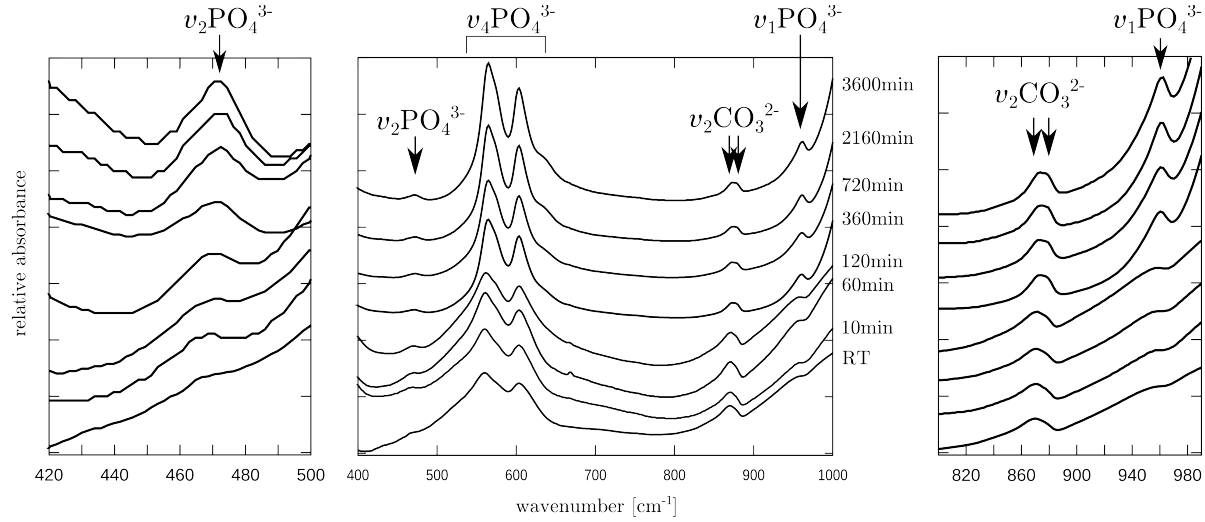

Figure 6.8: Selected FTIR spectra; plot on the left - a magnified section of the ν_2 P-O band is shown; middle plot shows part of the spectrum with the ν_2, ν_4, ν_1, and also the carbonate bands. Arrows point to peaks in the trace where band features appear to change with increasing hydrothermal treatment time duration. The left plot shows the ν_2 P-O totally symmetric mode appearing due to symmetry breaking with longer treatment duration time. The middle plot shows the relative intensities of the phosphate bands. On the right the magnification of the carbonate peak near 870cm^{-1} and the ν_1 P-O are shown. On all plots only selected samples are plotted for clarity.

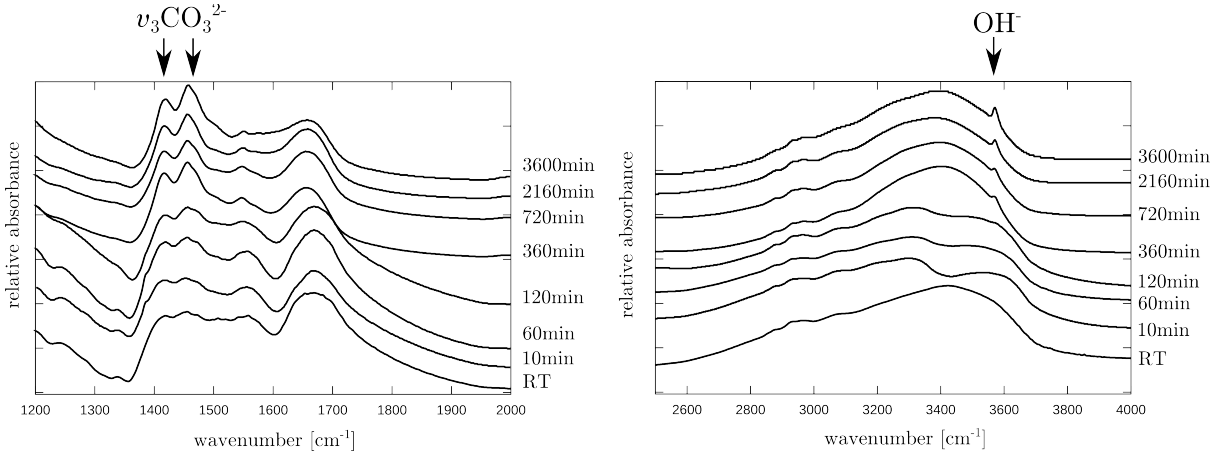

Figure 6.9: Section of the FTIR spectra showing the carbonate region (plot on the left) and hydroxyl-water bands (right) - arrows pointing to the peaks. Spectral trace of only a few selected samples are plotted for clarity of the visual comparison.

6.2.4 Analysis of the FITR $\nu_4PO_4^{3-}$ region

For further quantification the method of spectral decomposition was applied. Each spectral trace of the time series was fit with the same starting number of basis functions, allowing the same fitting starting conditions. In this section the analysis of

the spectral region between 450-800cm^{-1} is presented in greater detail. Hydrogen-phosphate bands are also included in the evaluation of the spectral trace. An example of the band assignment is shown in Fig.6.10. Figure 6.10 shows the sample of the longest hydrothermal ageing time plotted together with the second derivative* of the data. Minima in the second derivative plot hints to the peak positions. According to the second derivative plot the bands are assigned to: p1 peak – $\nu_2PO_4^{2-}$, p2 peak – HPO_4^{2-}, p3-p5 – $\nu_4PO_4^{2-}$, and p7 to an additional peak that is only necessary for the fit, but has no physical meaning. The presence of the HPO_4^{2-} have been inferred from the plot. However, the second derivative plot can not be considered unambiguous. Slight deviations of peak placements have been made during the spectral deconvolution. For example, for the peak p2 in Fig.6.10 the second derivative does not give a clear minimum, however, by observing the spectral trace it appears as if the band p2 is is required at 550cm^{-1} to compensate for the spectral trace curvature. The same issue appears for the p7 peak as well, where the background appears to be correlating with the spectral trace and introduces difficulties of background separation.

An example result of the non-linear least squares fit of the spectral region 450-800cm^{-1} is shown in Fig.6.11. The fit is adequate, without regarding the adjusted r^2 values (r^2 =0.99973 for the sample of 3600min hydrothermal ageing duration).

For the validity of the fit the stabilized normality plot was monitored after each iteration bunch. The fit-stopping criterion was based on the normality of errors. The fit residuals have been monitored and when all residual data points were inside the 95% confidence bound on the stabilized normality plot (lower plot Fig.6.11) the fit was terminated and the results extracted. The statistics of the fit parameters (standard errors of peak position, width, amplitude and shape) are considered valid only in case that the standard errors of the residual curve are inside adequate confidence intervals. The concept of the stabilized normality plot is used according to Michael (1983). It represents a statistical test, where a distribution is evaluated against the normal distribution (probability-probability or P-P-plot) resulting in a linear slope (45°angle) if the tested distribution matches the reference distribution. The plot in Fig.6.11 is modified according to Michael (1983) by adequate coordinate transformations in order to present a horizontal line. The confidence limits are based on the Kolmogorov-Smirnov statistic. All the sample of the hydrothermal ageing time series have been evaluated using the described approach. The result of fit parameters for the hydrothermally treated samples is plotted in a matrix-plot as a function of the treatment time in Fig.6.12.

*second derivative was obtained as a polynomial fit of the data, and taking the derivative of the polynomial fit function. Smoothing was applied, moreover, the result heavily depends on the smoothing coefficient.

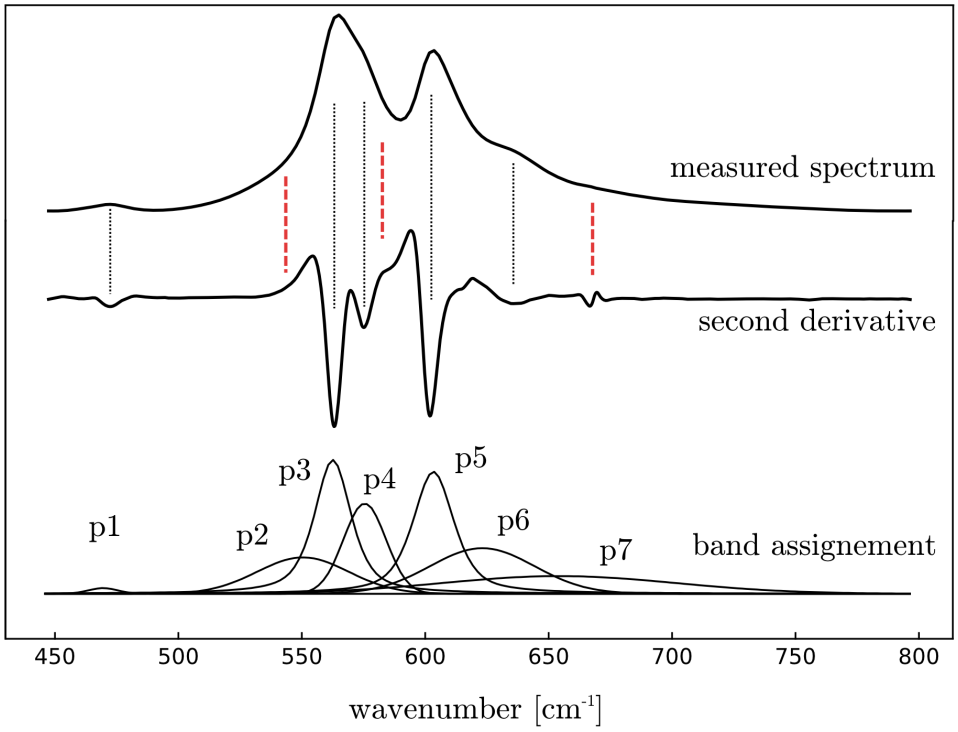

Figure 6.10: Plot of a ν_4PO_4 section of the longest hydrothermal ageing sample (3600 minutes). The $\nu_2 PO_4$ mode is also included (p1 peak on the far left).
Top plot shows the measured data; middle plot shows the second derivative; bottom plot shows the positioning of the bands. The minima of the second derivative curve indicates the location of peaks. Although, this method is usually applied in resolving hidden peak issues, the second derivative curve of the data is highly dependent on the smoothing (Savitzky-Golay). The bands are assigned to: p1 peak – $\nu_2PO_4^{2-}$, p2 peak – HPO_4^{2-}, p3-p5 – $\nu_4PO_4^{2-}$, p7 – additional peak necessary for the fit, but no physical meaning.

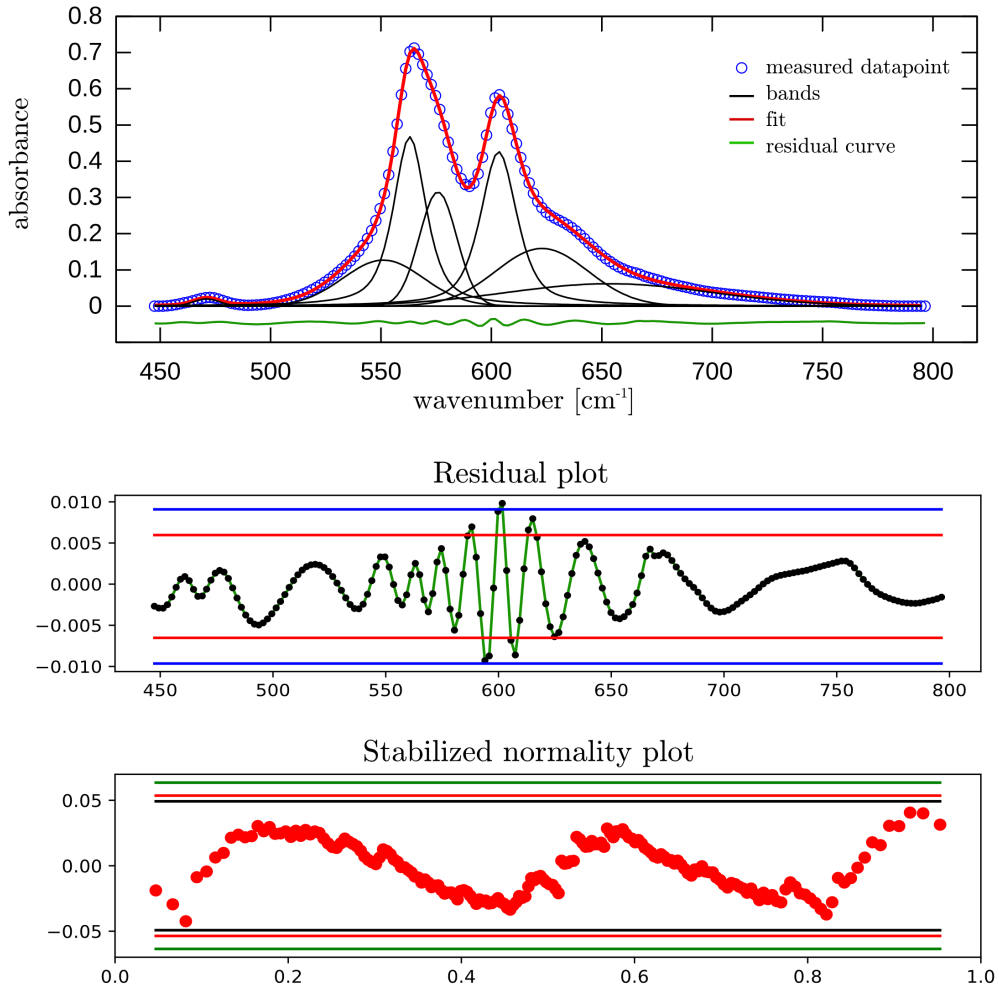

Figure 6.11: Spectral decomposition and fit analysis of the 3600minutes long treatment. The top plot shows the band assignment with highlighted peaks of the ν_2PO_4 near 472cm^{-1} and the very broad at near 660cm^{-1}. This later band is necessary to be included for the fit.; The middle plot shows the enlarged residual curve. The red horizontal lines represent the 2σ limits above and below the mean value of the residuals. The blue line is the 3σ limit. On this sub-plot it can be inferred that about all data points are inside 3 standard deviations; The bottom plot shows the standard deviation normality check. The green line is the 99% confidence limit, red is the 95% and the black is the 90% confidence limit. It represents the check of the distribution of the errors vs. the normal distribution. This plot is a modified probability-probability plot. From the plot it can be inferred that the residuals are distributed in alliance with the normal distribution, meaning that the obtained standard deviation on the fit parameters satisfy the central limit theorem (are normally distributed).

The first column of the plot matrix in Fig.6.12 represents the peak amplitude ratios for p1/p3, p2/p3, p2/p5, p3/p6 and p5/p6 peaks. The peak notation numbering follows the notation used in Fig.6.10. The values for the propagated standard error of the peak amplitude obtained from the fit are apparently too high for some of the samples. This leads to the conclusion that there is no significant variation of the peak amplitude parameter values dependant on the ageing time, expect for the ratio of the p1/p3 and p2/p5. The p1 peak is the symmetric stretch mode of the P-O ($\nu_2PO_4^{3-}$) while the p3 peak is the asymmetric stretching ($\nu_4PO_4^{3-}$). With the increase of the hydrothermal ageing time all the peaks in the spectral trace in the region 450-800cm^{-1} increase in amplitude due to the presumable increase of the long range order in the crystalline domains. The p3 peak ($\nu_4PO_4^{3-}$) apparently gains more amplitude than the p1 peak ($\nu_2PO_4^{3-}$), although the amplitude of the p1 peak increases as well. Peak amplitude ratios (p2/p3 and p2/p5) with the HPO_4^{2-} band (p2 peak) appear with high standard error values and although a trend is visually apparent, practically it is not significant enough with respect to the precision of the evaluation.

The second column of plots in Fig.6.12 represents the behaviour of the peak shifts. Due to the high standard errors, no significant change relative to the increase of hydrothermal ageing time can be inferred from the result. Peaks for p1, p3, p5 were kept fixed during the fit as constrained to a theoretical value in order to observe the HPO_4^{2-} peaks, without the fit correlations. However, the standard errors of the peak profile function parameters remained high.

The third column of plots in Fig.6.12 shows the FWHM parameter of the basis functions as ratios between modes (p1/p3, p2/p3, p2/p5, p3/p6 and p5/p6 peaks). A significant trend appears in the intensity ratios of the peak p1 and p3 (phosphate bands ratios ν_2 / ν_4), where the decrease of the ratio values might be due to the narrowing of the p3 peak (the ν_4 band near 563cm^{-1}). The FWHM ratios with the HPO_4^{2-} (referred to as the non-apatitic hydrogen-phosphate) p3/p6 and p5/p6 show a decrease as well. In this case the decrease of the ratio might be controlled by the decrease of the p3 and p5 P-O mode widths.

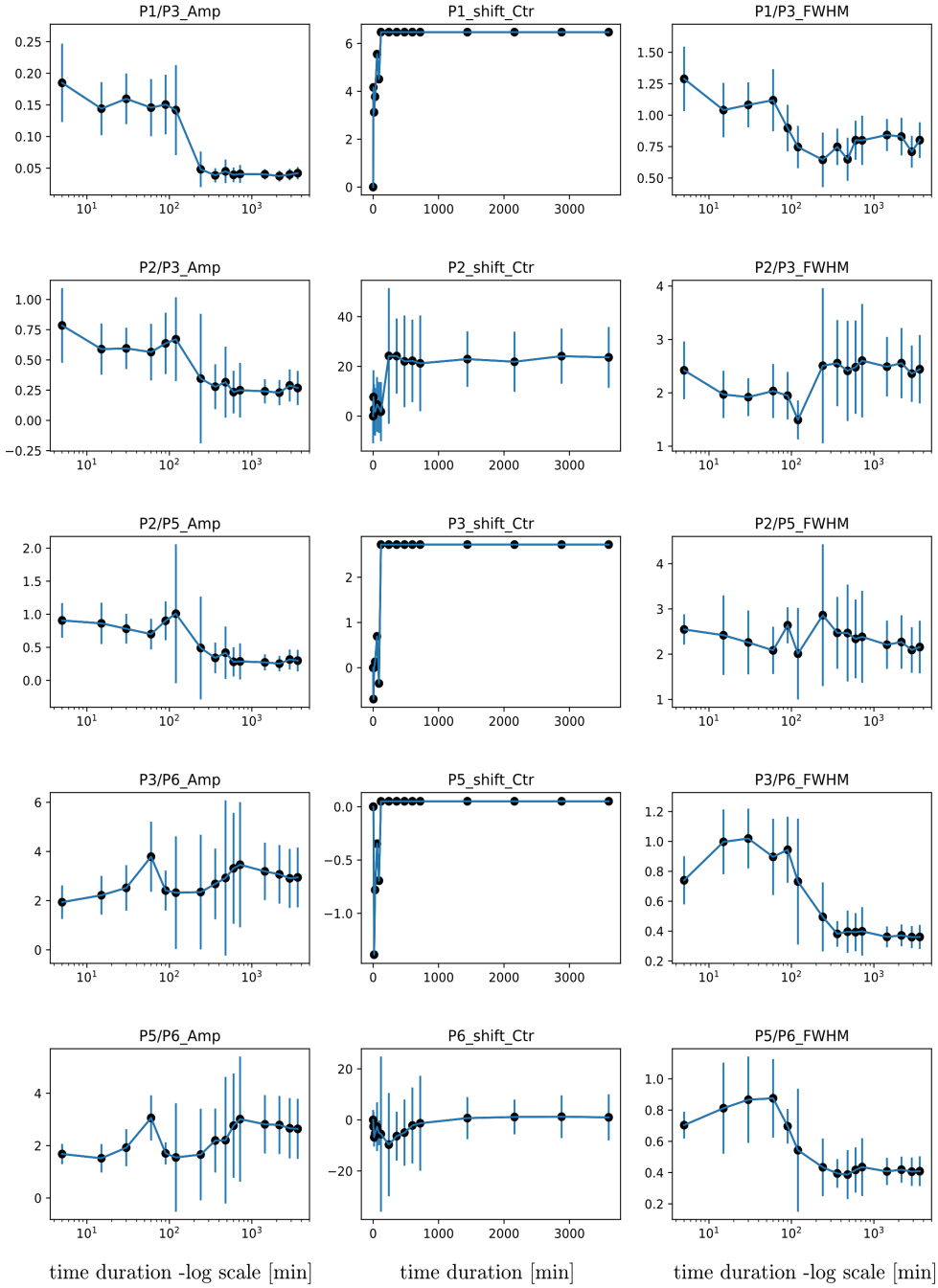

Figure 6.12: Spectral decomposition parameters and ratios of the hydrothermal ageing time series. First column shows the amplitude peak parameter ratios of bands p1/p3, p2/p3, p2/p5, p3/p6; Middle column shows the peak position parameter (P1_shift_Ctr - P6_shift_Ctr) expressed as shifts from the reference peak position. (peak positions for p1, p3 and p5 were kept fixed in the fit, hence no standard error for the data points). The y-axis is the center position wavenumber difference; Third column on the right shows the peak breadth (FWHM) ratios of bands. The band assignment and peak notation is shown in Fig.6.10.

6.2.5 Raman band position shift and band width narrowing

A similar approach was taken for the evaluation of the measured Raman spectra of the hydrothermal ageing time series. A dominant spectral feature of the samples (and for the reference structure of hydroxylapatite) is the ν_1PO_4 band near 960Δcm^{-1}. Band position and band width analysis of the ν_1PO_4 band near 960Δcm^{-1} in all the hydrothermally treated samples resulted in a correlation plot shown in Fig.6.13. For each sample the obtained center position of the peak from the fit is shown on the x-axis (ν_1 peak position), while the y-axis shows the corresponding FWHM parameters of the peak.

The FWHM and peak position values on the axis are sorted by ascending values. The trend of the treatment duration time (marked with red annotations of time in Fig.6.13) is following the expected sequence as an emerging consequence.

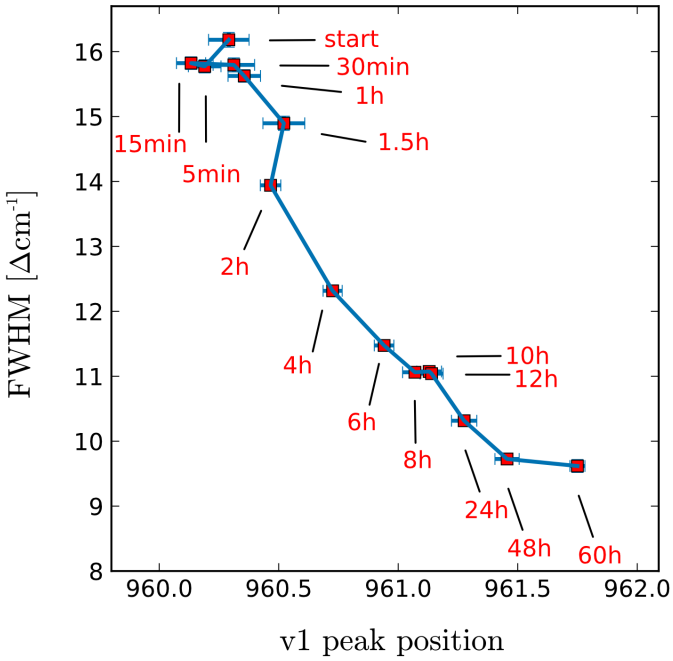

Figure 6.13: Raman peak broadening and peak position correlation for the time series of hydrothermal ageing of bone samples. Peak parameter (position and FWHM) correlation of the ν_1 P-O symmetric stretch Raman band. The band's center position and its width were obtained by peak fitting the region from 920-1000Δcm^{-1}. The peak center position and the FWHM is sorted in ascending order on the abscissa and the ordinate. The treatment duration time almost in every case follows the expected trend of increased narrowing and blue-shift with time. However, bone samples treated for 10 and 8 hours switch in this trend sequence, namely the sample treated for 8h is interpreted as more altered as the 10h duration sample. This is assigned to systematic errors in the evaluation.

Samples that were in contact with water for short times have higher values of FWHM and are red-shifted, while samples that have been exposed to water and heat for long times have resulted in band profile narrowing and blue-shift of the peak position wave number. Moreover, the trend in data point scatter (blue line in Fig.6.13) suggests a non-linear underlying correlation, although a fit of the resulted data points was not attempted. Such trend indicates a complex relation of structural changes during a hydrothermal ageing experiment, despite the seemingly evident correlation.

For the acquisition of the Raman spectra several point measurements were taken for each sample. Only those acquisitions were further analysed where the fluorescence effect was negligible. Averaging the datasets was not applied, instead, spectra was selected based on lowest background, absence of fluorescence, and highest signal-to-noise ratio. Sample selection bias is bridged with the argument that in order to get details of the spectroscopic features an interpretable measurement is mandatory.

6.2.6 Discussion on the hydrothermally induced crystal growth in bone material

Rietveld refinement of the X-ray powder diffraction patterns of the hydrothermally treated powdered bone material led to conclusion that there is no simple solution for satisfactory modelling of the measured data. The structural complexity in the hydrothermally aged sample series could not be adequately approximated by a single phase with a unique unit cell model that satisfies translational periodicity and long range order. Optimising a hypothetical highly regular unit cell via (in this case) the Rietveld refinement method is seemingly converging to a solution that is not describing the measured data without further questions.

Due to the non-linear correlation of the ν_1PO_4 band width (FWHM of the peak at $960\Delta cm^{-1}$) and center position in the Raman spectra of the time duration sequence of the hydrothermal treatment of bone material a two stage transformation regime is hypothesized. From the correlation plot in Fig.6.13 it can be inferred that in the first section (lower wavenumbers) the major type of the peak change is the reduction of width. As the treatment duration is increasing (after about 2 hours treatment time) the change of the peak width values becomes less dominant, while the shift of the peaks increases. It is therefore hypothesized that the breadth of the spectroscopic band is influenced by the distribution of the bond lengths present in the structure. Furthermore, the median of a hypothetical bond length distribution could affect the center position of the spectroscopic band. In the theoretical frame of phonon-confinement model, the source for the broadening can be various combinations of

effects including finite crystallite size, chemical disorder (substitution), dislocations, presence of grain boundaries, etc. (Gouadec and Colomban, 2007; Gupta and Jha, 2009).

The interpretation of the obtained FTIR spectra for the hydrothermal treatment time series can be approached in two ways, (1) interpret the data using ideal crystallographic models, or (2) statistical evaluation of the complex spectral pattern. In the first case, the approach is that the material is (hydroxyl)-apatite and that this crystallographic description fully describes the observed spectral trace (the model is considered according to literature references and applied to the data). Slight variations and peak deviations form the model remain unanswered and left out of interpretations. In the second case peak shifts, shouldering of peaks, or peak splitting are included into the interpretation of the data even if more complex scenarios are needed to be considered (hypothesis tests) for the understanding of the crystalline structure of the bone material. This would suggest that the complexity of the system can not be resolved with standard crystallographic methods. The problem of the interpretation would require computational tools with extensive automated statistical evaluation.

All parameters in the band assignment bring additional information about the reality of the structures state. Therefore the structure of the hydrothermally aged bone material and bone material in general could be understood only if all the fit parameters are modelled with reasonable and explainable values. Incorporation of many parameters in an unconstrained (and partially constrained) optimization algorithm did not result in reliable, reproducible, and therefore true values. An approach that evaluates and compares multiple hypothesis of the physical description of the apatite structure present in the altered bone material would be required. This requires not only advanced computational experimental methods of data evaluation and modelling but also theoretical ab-initio calculations as well.

In the process of spectral decomposition of the vibrational spectroscopic data (FTIR and Raman) the problem of a unique basis function set definition arises. It is practically impossible to maintain the same initial starting condition of the fit for all samples of the time series due to intensity variations and trace curvature differences (for example Fig.6.7 and Fig.6.8). The initial conditions need to be defined for each subsequent sample (peak width, amplitude, shape). Unconstrained fit affects broad peaks the most, as the optimization algorithm tends to flatten those out more rapidly during the fit, hence rendering reliable retrieval of quantitative information difficult or impossible. Limiting parameter value variability is one measure to control the fit, but that evidently introduces bias. The control of the non-linear least squares optimization algorithm appears to be a crucial factor for any meaningful evaluation attempt. Parameter constraints were applied in the fitting procedures of the presented evaluation. However, this was conducted manually which may contain

systematic unsupervised errors against all attempts to eliminate them.

In the presented fit Gaussian-Lorentzian sum functions were used to model the basis functions peak shape. Usually, values of peak shape parameter are fixed to 0.7, signifying a 70:30% ratio of Gaussian to Lorentzian contribution to the band's peak shape. However, in case when this parameters were also included in the unconstrained fit, the mixing coefficient often took unrealistic values. The peak shape parameters affect the values of the other parameters with unpredictable scale of impact.

Another problematic aspect is the identification of the hidden peaks in the vibrational spectroscopic trace (measured data). The second derivative approach for identifying hidden peak is dependent on the method of obtaining the derivative of the measured dataset resulting in a bias due to smoothing. The amount of the present noise in the data affect the outcome greatly.

In the reflection of the peak fitting limitations it can be considered that fitting spectra using parameter constraints should be addressed as hypothesis testing. An efficient automatized evaluation approach would be required to test all hypotheses about the crystallographic structure that gives the observed complexity in the spectral pattern.

6.3 Induced crystallite growth by annealing of bone material at normal atmospheric condition – formation of secondary phases

In order to study the crystallite growth process in dry conditions a sequence of annealed samples was prepared and analysed. Similar studies have been reported by Rogers and Daniels, where the authors have been focusing of the change of lattice constants as the effect of exposure to heat energy in the form of annealing (Rogers and Daniels, 2002). In addition the same research group investigated the impact of annealing on bone samples of various animal species (Beckett, 2011; Beckett et al., 2011). In this section it was attempted to extend the work done by the cited research group of Rogers with the contribution of the analysis of the secondary phases appearing at high annealing temperatures.

6.3.1 Materials and methods

Bone material of *bos taurus* femur skeletal elements was physically cleaned and washed. The hard bone material was cut into smaller cubes and dried at room temperature and normal atmospheric conditions. The material was then hammered to chunks and grind in a ball mill. The powder was sieved with a 100μm mesh size grid. The samples were kept in the oven for one hour in the range of set temperature

up to 1000°C. After the set time duration the samples were left to cool down by natural heat exchange at ambient temperature.

The XRD patterns were gathered at the DESY synchrotron facility in Hamburg. The material contained in 1mm diameter capillaries was irradiated with 60keV photons of 0.20727nm wavelength. The diffraction data were collected on Perkin-Elmer 2D detectors of 0.5x0.5m dimension and pixel size of 200microns (0.2x0.2mm).

The FTIR spectrum was measured on a Bruker Equinox spectrometer in transmission mode using the KBr pellet method. 200mg of KBr (kalium-bromid) powder was mixed with 1.4mg of bone powder with maximum grain size of 100μm. The spectrum was gathered in the range of 400-4000cm^{-1} with 4cm^{-1} resolution and 128 scans.

6.3.2 XRPD results and interpretation

A series of bone samples have been exposed to annealing conditions for 1 hour long time interval. The diffraction patterns were gathered after the cooling of the material. The examination of the Rietveld refinement fit results of the sample series shows that up to 400°C the width of the peaks remains practically unchanged while the lattice constants show variation (Fig.6.14). The values for the unit cell dimensions in the temperature region from 400°C to 600°C shows an opposite trend to lower temperatures. Above 600°C the diffraction peaks are significantly sharper, which in the first approximation indicates increase of the crystallite size. The obtained values from the refinement using anisotropic crystallite size model confirm the crystallite size increase from values of 20nm to 120nm for the *h00* reflection (along a-axis). Small difference of about 10-15nm can be inferred for the reflections along *00l* (along c-axis). For the refinement of this data set the unit cell of hydroxylapatite was taken as the reference structure for the main phase. Isotropic microstrain was not included into the model.

Detectable secondary phases appear in the diffraction patterns of high annealing temperature sample. Section of the diffraction patterns of the bone mineral demonstrating the appearing reflections as a function of annealing temperature is shown in Fig.6.15. Above 700°C reflection peaks for calcium-oxide CaO and buchwaldite ($CaNaPO_4$) appear and the relative peak amplitude is increasing with the increasing annealing temperature (800°C-1000°C). Diffraction pattern peaks at 3.1[2ϑ°] and 4.4[2ϑ°] assigned to sodium bearing phosphate phase buchwaldite ($CaNaPO_4$) and calcium-oxide phase appear clearly first at the sample annealed at 900°C (marked with black and green lines in Fig.6.15.). However, there is an unassigned diffraction peak at 4.1[2ϑ°], suggesting that there might be another phase present in the sample. Despite all efforts, this phase could not be identified.

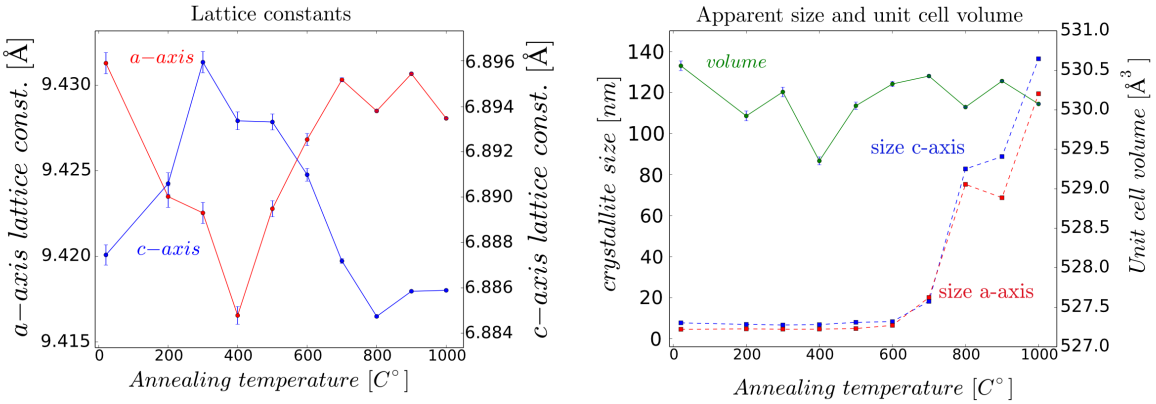

Figure 6.14: Lattice constants and apparent size change upon heating. The left side plot shows the temperature dependence of the lattice constants; The right side plot shows the temperature dependence of the apparent size and the unit cell volume.

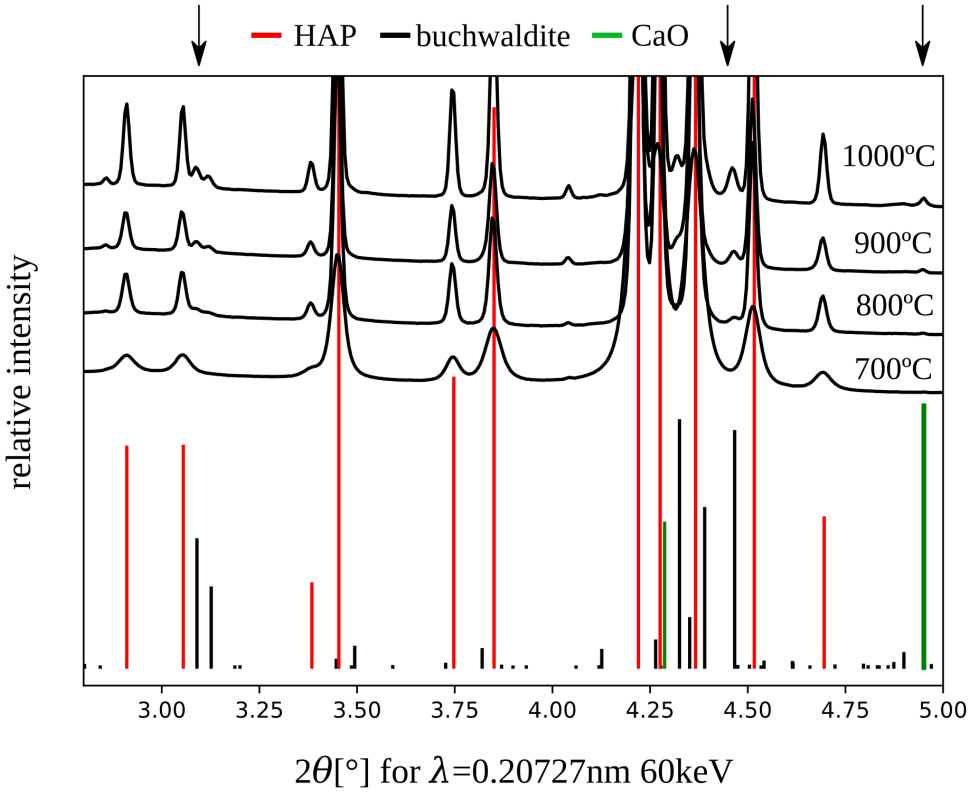

Figure 6.15: Section of measured XRD patterns of powdered bone material annealed at high temperatures. Relative intensities for the HAP phase (red line markers), buchwaldite (black line markers) and CaO (green line markers) are plotted. The relative intensity markers are scaled so that the smallest intensity reflection of the HAP could be seen. The buchwaldite phase can be inferred already at 800ºC, while CaO is resolvable first in sample annealed at 900ºC.

The annealing experiment data presented here confirms the sodium-bearing phase (buchwaldite), however, similar annealing experiments of Rogers et al. (Rogers and Daniels, 2002) failed to identify this phase. In their publication the authors provided diffractograms of the measured data, where it is possible to infer that characteristic peaks of the sodium-bearing phosphate phase are present, however, that detail was not reported in their publication, probably due to lack of angular resolution and high noise levels in the measurement.

6.3.3 FTIR measurements and interpretation of spectral features

The exposure of the bone material samples to high temperatures leads to increased crystallite size (from the XRPD results in the previous section). It is therefore, hypothesised that with increasing annealing temperatures the structure of the apatite transforms into a state with higher degree of long range order, and it approaches the stoichiometric values of the reference (ideal) hydroxylapatite deduced from the appearance of the characteristic OH^- vibration modes. The mode near the $632cm^{-1}$ is attributed to OH^- libration (Santos and Gonzalez-Diaz, 1977; Gonzalez-Diaz and Santos, 1979; Vandecandelaere et al., 2012). Development of the OH^- stretching vibration at 3568 cm^{-1} and the OH^- libration near $632cm^{-1}$ as a function of heat treatment indicates that the structure in transitioning to a hydroxylapatite phase. Water bands are reduced with increasing temperature and are practically absent in the sample treated at 1000°C.

The results of infrared spectra analysis of the annealed bone material show an increase of the spectral trace features with increasing temperature (Fig.6.16). At low temperatures of annealing up to 400°C the FTIR spectral peaks are poorly developed and show large overlap of broad bands. Sample annealed at 600°C and higher temperatures show increase in spectral trace peak sharpening and the appearance of additional peaks. The high temperature annealed samples in general show more resolved bands. This is is shown in the case of the $\nu_4PO_4^{3-}$ spectral regions section in Fig.6.16.

Spectral decomposition of the ν_4 phosphate group conducted in the spectral region of $400\text{-}800cm^{-1}$ was modelled with 7 basis functions during the band assignment. Parameters for the modelling peaks have been obtained using the same method and approach described in the previous sections. From the evaluation of all the fit results in the annealing series, the most robust band parameter appears to be the width (FWHM) of the P-O band near $603cm^{-1}$. This parameter displays an evident correlation with the annealing temperature (Fig.6.17.). Evaluation the obtained width parameter (FWHM) in the spectral decomposition of the phosphate band at $603cm^{-1}$ in all of the samples resulted in a linear calibration equation:

$$FWHM = k[\frac{cm^{-1}}{^{\circ}C}] \cdot T[^{\circ}C] + b[cm^{-1}] \qquad \text{(Equation 6.1)}$$

where T is the annealing temperature in °C. The values of the slope (k) and intercept (b) are -0.023(3) and 37.9(1.6), respectively. However, this is valid only for the case of a non-weighted fit.

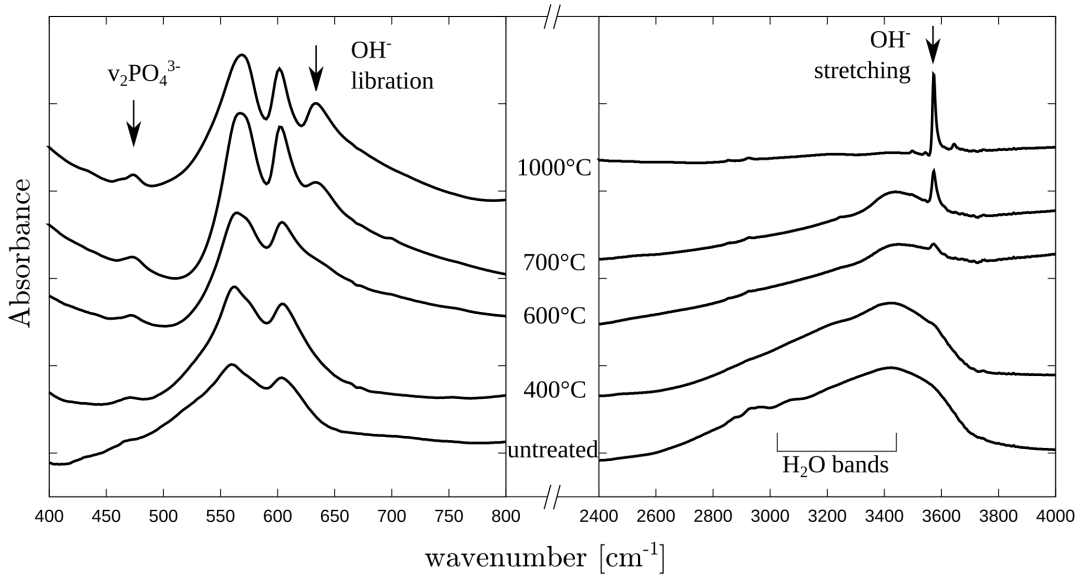

Figure 6.16: FTIR spectra of *bos taurus* femur bone sample annealed up to 1000°C. The left side plot shows the ν_4 phosphate vibrational region. The sample label "untreated" refers to the starting material without any exposure to elevated temperatures. In addition the OH^- libration mode is shown as it emerges from the background signal; The right side plot shows the characteristic OH^- stretching mode and the bands assigned to water. Only selected spectra are shown for clarity.

On the right side plot in Fig.6.17, the standard errors of the FWHM parameter estimation are shown. The standard errors gradually decrease with increasing annealing temperatures. The cause of this can be that the spectral trace of the phosphate region is more developed, the peak are less overlapping and the fit can achieve greater precision and accuracy. The FWHM value of the starting sample (not annealed reference material) is very large (very broad peak), while the high temperature annealed samples have very small errors, and are therefore considered more precise. Additionally, based on observation of the results the values of the standard error can be grouped into three categories: the first group can be set for the low temperature region up to 300°C, the second region can be set between 300°C and 600°C where there are not significant changes in the band width values, and thirdly the high temperature region where the width remains steady again. Such a multi-

stage transformation process would require additional examination and more denser temperature step sampling. Nevertheless, the results suggest that a linear model for the structural transformation based on one P-O band is not an adequate model since it under-fits details of the parameter behaviour. Moreover, the evaluation highlights the importance of the obtainable precision of the parameters from the peak-fitting in the spectral decomposition method.

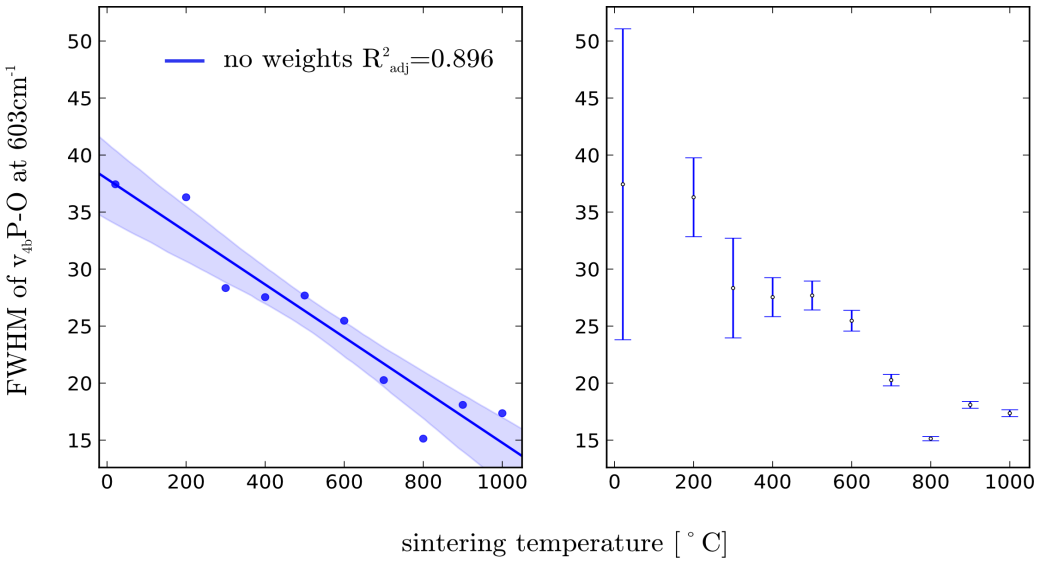

Figure 6.17: Calibration curve for temperature from the width of the P-O band at 603cm^{-1}. On the left a non weighted regression curve is shown with 95% confidence bounds. On the right side plot standard errors are shown for each observation as obtained from the spectral decomposition. The full-width-at-half-maximum of the P-O symmetric stretching band at 603cm^{-1} shows no significant change until 600°C, after which the FWHM is derivable with much more precision. From 700°C onward the bands do not change their width in great steps.

6.3.4 *Discussion on the results of the annealing experiments*

The transformation of the bone material calcium-phosphate-apatite under annealing conditions appears to be a complex process. Exposing the bone material as a composite to heat energy in normal atmospheric conditions results in thermal degradation, chemical transformation towards hydroxylapatite, and increasing crystalline state (long range order). As the water and carbonate leave the system the pathway of the alteration is not fully determined by the heat energy input. The separation of water and carbonates up to 400°C alters the structure of the apatite, but at high temperatures the chemical environment might be significantly different

than at low temperatures giving rise to new conditions for the structural change.

Nevertheless, the results of the annealing experiments can be still used as a proxy for the determination of the extent of cremation of bone samples in anthropological context. The use of calibration curves such as presented here (section 6.3.3), however, requires intensive tinkering with the peak fitting procedures. This fact might set a limit on its usability.

Raman spectroscopy measurement on the annealed bone samples were inhibited due to very strong fluorescence signal. Samples up to 800°C treatment temperature appear to have a char-resembling coating of the sample surface when inspected with optical light-microscope. It appears that residues of the burned organic material accumulate on the surface of the particles blocking any Raman signal from the inner part of the material.

6.4 Concluding remarks on the experimentally induced alteration in bone material

In this chapter the results of bone material alteration under wet and dry influence factors have been explored. Although, the results of the two experiments can not be directly compared due to the significant difference in the influencing conditions, it can be deduced that the structural changes in both cases appear and are directed toward a state with more developed long range order and crystallite growth (domain volume-size increase). From the observed trends it is possible to back-extrapolate and infer about the structure of the original bone material. It can be concluded that the original crystalline state is more complex before the alteration experiment and the long range order emerges due to the influence factors. It appears that the structure undergoes a transition from a state that includes ionic substitution, underdeveloped long rage order, and diverse phosphate ionic environments to an ordered and defined hydroxylapatite alike state. According to the evaluation shown in this chapter it appears that existing crystallographic models are not fully adequate in describing the true state of the inorganic part of the bone material as carbonated-hydroxyl-apatite nanocrystallites. This is in contrast to many literature references, where often only hydroxylapatite is used to describe biological calcium-phosphate nanocrystallites of the bone material.

If the annealed bone material develops a sodium containing separate phase, the Na^+ ions have to be present in the original material as well. As the bone material is annealed as a composite, the sodium can also come from the remnants of the organic collagen, proteins or remnants of other tissue. As organic molecules decompose at elevated temperatures, it can be speculated that the newly available sodium forms the calcium-sodium-phosphate (buchwaldite – $CaNaPO_4$) phase.

Growth of the nanocrystalline phase in the composite material of bone during the induced crystallite growth experiments in dry and wet conditions suggest that a simple model for the inorganic phase domain growth can not be easily derived. The denaturation process and the separation of the nanocrystallites from the collagen might play a role as an inhibiting factor on the growth of the nanocrystallites. In aqueous medium the potential dissolution of the interfibrilar calcium-phosphate material can be speculatively achieved by the separation from the collagen bonding. This can arguable be the source of calcium and phosphate ions that then enable the growth of the existing nanocrystallites in bone material.

During the annealing process the heat energy induces thermal decomposition of the material. Water is among the first components that leave the system resulting in a disability of any dissolution reaction. As the temperature increases at a critical point (near or above 600°C) the heat energy is sufficient to induce spontaneous ordering and rearrangement of atoms so that the apparent domain size increases in the process of recrystallization.

Chapter 7
Reference material 4. - Synthetic bone-analogous materials

7.1 Context and aim

"Perhaps one of the greatest challenges, at least from a biological standpoint, will be to understand the factors that control the nucleation, growth, and growth inhibition of the biological apatites at the molecular level." states Elliott (Kohn et al., 2002 p448) hinting at the unsolved problems in bone material research. Nano-particulate carbonated calcium-phosphate apatite forms the inorganic part of bone material (Legeros et al., 1967; Fratzl et al., 1996; Currey, 2001; Fleet and Liu, 2007; Fleet, 2014; Wegst et al., 2015), therefore understanding the nucleation and growth of the calcium deficient carbonated hydroxylapatite is of a great relevance. Precise determination of the early stages of the nanocrystallite phase formation of synthetic bone-apatite analogous are of great importance in the biomedical and pharmaceutical field. The synthesis process control of bone and tooth replacement materials, as well as of coatings of metal implants can have huge influence on the end-products bio-compatibility, strength and durability (Chu et al., 2009; Zhou and Lee, 2011). The desired state of synthetic bone-analogous material is the nanocrystalline apatite that resembles the natural state found in the bones of humans. However, it is not straightforward to assume that any process of obtaining synthesised bone-apatite analogous nanocrystalline phase does not have an amorphous part, or other non-apatitic or apatite secondary phase. The relevance of amorphous phase fraction determination or the incorporation of various ionic species into a nanocrystalline phase is therefore important for the application of ACP or its nanocrystalline-, and crystalline derivatives for pharmaceutical or biomedical purposes.

Bone-apatite analogous materials can be obtained in a multitude of ways. Synthesis routes of HAP and ACP have been extensively explored and at the current state-of-art any desired phase (such as HAP) and crystallite morphology (sphere, platelets, dendritic) is possible to achieve by following chemical procedures as recipes (Sadat-Shojai et al., 2013 and references therein). It had been observed that differences in the synthesis condition lead to specific variations in the calcium-phosphate stoichiometry (Termine and Eanes, 1972; Sun et al., 2010). In the case of the aqueous synthesis route, the pH and temperature, as well as experimental conditions such as stirring affect the final product phase (Vandecandelaere et al., 2012), coexistence of

phases, and the morphology of the crystallites.

The nanocrystalline phase formation mechanism in living tissue is described by Xie et al. (Xie et al., 2014) thusly: "...hydroxyapatite (HAP) participates in vertebral bone and tooth formation by a non-classical hitherto unknown nucleation mechanism, in which amorphous precursors form and transform during long induction periods." It is also unclear what is the exact role and mechanism of protein interaction in the formation of the nanocrystalline biomineral. Ibsen and Birkedal highlights the importance of organic molecule, proteins or any additives influence on the crystallization process as: "...specific interactions between the additives and the growing mineral are in general unknown" (Ibsen and Birkedal, 2012). Nevertheless, ACP alone is considered as precursor for the formation of the nano-crystalline apatite state (Johnsson and Nancollas, 1992; Xie et al., 2014).

In the previous chapters the growth of the existing nanocrystalline bone-apatite phase was discussed (Chapter 6). In this chapter the earliest stages of the formation and growth of bone-apatite analogous material are in the focus. Capturing the early stages of nanocrystallite formation the evolution of the long range order is targeted. The aim of the research work presented in this sections of the thesis is to explore the formation of end-products of nanocrystalline carbonate-, or hydroxyl-apatite formation from the amorphous-calcium-phosphate APC starting phase.

7.1.1 Description of the amorphous-calcium-phosphate (ACP) and concepts of clustering

Synthetic and naturally occurring ACP has been in the center of many studies aimed to understand the formation and structure of a nanocrystalline phase (Betts et al., 1975; Harries et al., 1987). It has been proposed that ACP could be the precursor phases for crystalline HAP formation (Gower, 2008; Mahamid et al., 2008). Wang and G.H.Nancollas summarises that the formation of the HAP phase from the ACP is likely to form through a dissolution-reprecipitation pathway (Wang and Nancollas, 2008).

In 1980 Posner proposed a possible structuring concept of the amorphous calcium phosphate as agglomerate of phosphate tetrahedra surrounding Ca^{2+} ions forming spherical units (Posner et al., 1980). Conclusions about the short-range order present in the ACP were derived in great extent from the pair distribution function analysis (also radial distribution function) as it yields the frequency of occurrence of the inter-atomic distances. Diffraction experiments based on the pair distribution function analysis led Posner to the conclusion that the amorphous state is constituted of clusters of calcium atoms coordinated and surrounded by phosphate tetrahedral units. Earlier work of Posner and Betts aimed to understand the structuring of calcium-phosphate formations extends to the investigation of the

potential presence of ACP in bone material (Posner and Betts, 1975). In their report, Posner and Betts conclude that the ACP cluster size is estimated to be 9.5Å long and the inter-atomic Ca-P distance was estimated in the range of 3-6Å. Originally, the Posner cluster was described without presence of water molecules in the calcium-phosphate formation of ACP. Holt and Hukings, however, observed and retrieved water-calcium distances (2.3Å) in the amorphous phase using the pair distribution function (Holt and Hukins, 1991). They describes an HPO_4^{-2} ("acidic") environment for the amorphous calcium-phosphate suggesting that hydrogen-phosphate ions can also be incorporated in the ACP cluster.

The definition of the Posner-cluster type formation remains actual in recent time as well. Recent results of Wang et al. tend to confirm the Posner cluster as it nucleates and grows (Wang et al., 2012). Aspects of the clustering structure has been investigated by Du et al. (Du et al., 2013). Dey at el. discus the pre-nucleation clustering events and its influence on the further crystallization processes (Dey et al., 2010), while Kim et al. discuss the internal rearrangement model for the ACP formation (Kim et al., 2005).

7.1.2 Stability and solubility of the amorphous calcium phosphate

The stability of the amorphous phase might be a crucial factor when ACP is considered as a potential precursor for the apatite phase formation. Efforts to understand ACP's stability are stretching from theoretical studies, such as of Yin and Scott with focus on ab-initio calculations of the ACP's stability (Yin and Stott, 2003), to studies of the chemical aspects of apatite formation (Omelon and Grynpas, 2008). Lifelong research of G.H.Nancollas produced an extensive record on the chemical conditions of nucleation and crystal growth in the calcium-phosphate system (Nancollas and Koutsoukos, 1980; Xie et al., 2014). Furthermore, G.H.Nancollas explored the relation of the particle size consideration with respect to the Gibbs surface energy (Wu and Nancollas, 1998), morphology, and size controlling factors (Xie and Nancollas, 2010).

The time resolved XRPD study by (Borkiewicz et al., 2010) focuses on the issue of the hydroxylapatite phase stability in aqueous precipitation reactions. The formation of monetite is discussed by Borkiewicz et al., as it appears in the reaction product depending on the synthesis conditions. The condition of calcium-phosphate and apatite polymorph formation with respect to synthesis routes are also discussed by Sadat-Shojai et al. (Sadat-Shojai et al., 2012, 2013). Formation of various polymorph-types is recognized as a function of pH value and temperature. In an earlier paper Johnsson and Nancollas discuss the role of various polymorphs as a precursor for the formation of the apatite (HAP) phase (Johnsson and Nancollas, 1992).

Water plays a crucial role of the solvent and medium for ion diffusion in the ACP formation in the transformation of ACP to nanocrystalline carbonated-, or hydroxyl-apatite in aqueous synthesis routes. The solid-liquid interface plays an important influencing factor in the growth of a crystalline phase. Dissolution of the ACP can be coupled with the growth of the nanocrystalline carbonated-, or hydorxyl-apatite phase (also pH dependent). Wu and Nancollas argues that the interpretation of Gibbs free energy should be reconsidered in the case of solid-liquid interface (Wu and Nancollas, 1998). A domain shape and size influence on the solubility has been theoretically accessed by Kaptay (Kaptay, 2012).

Considering the timespan of the research done in the investigation of the amorphous phase, Pan et al. writes in a recent paper that the ACP transformation process is still remaining a "mystery" despite of tremendous amount of research covering many aspects of this topic (Pan et al., 2010).

The ACP has a wide application field in medicine. Its potential in tooth and bone replacement has been emphasized in an article by Zhao et al. and Dorozhkin (Zhao et al., 2012; Dorozhkin, 2012).

7.1.3 Description of the phase transformation experiment of ACP

The aim of the experiments was to observe the formation of the nanocrystalline apatite phase from the amorphous precursor (ACP) phase in aqueous medium. The experiments were designed as a two-stage synthesis process. The end-product of the second synthesis stage was targeted towards achieving structural properties of the material that resembles the structural properties of original bone material. In the first stage the aqueous synthesis route for ACP was chosen. In the second stage the obtained synthesis product of the first stage was used as a starting material for various post-processing experiments. These experiments were conducted based on the assumption that the nanocrystalline bone-apatite-analogous material can be synthesised from dry ACP powder under wet conditions. In this stage the previously obtained ACP was exposed to water in a sequence of samples with increasing time of exposure in water.

In order to investigate a bone-analogous system and to evaluate its formation the two-stage experiment was conducted in the following stages:

1. controlled synthesis of ACP via the aqueous route by the reaction of diammonium-hydrogenphosphate $(NH_4)_2HPO_4$ and calcium-nitrate-tetrahydrate $Ca(NO_3)_2{\cdot}4H_2O$ at pH 10 stabilized by ammonium-hydroxide buffer solution (described in section 7.2).
2. post-processing in water at 37°C by making a 0.02M (calculated value using the HAP formula) solution of ACP powder. Treatment of samples with duration time-series were made ranging from instantaneous wetting-and-

drying, to 9 hour long treatments. After the reaction time the samples were vacuum dried. No stirring was applied during the treatment (described in section 7.3).

7.2 ACP synthesis route and characterization

7.2.1 Materials and methods

In the first stage of the experiment amorphous calcium-phosphate was synthesized via an aqueous route according to (Tadic et al., 2002; Drouet et al., 2009), as a controlled synthesis reaction of (0.024M) diammonium-hydrogen-phosphate $(NH_4)_2HPO_4$ and (0.01M) calcium-nitrate-tetrahydrate $Ca(NO_3)_2{\cdot}4H_2O$ stabilized by ammonium-hydroxide buffer solution. The phosphate solution was titrated into the calcium solution while the pH was continually adjusted (manually) to 10 during the reaction by adding a small amount of ammonium-hydroxide buffer solution when the pH started to drop below 10. Immediately after the titrant (phosphate solution) was depleted, the precipitates was collected by vacuum filtration using a 0.2μm mash-size filter. The filtrate was then air dried. The dry ACP flakes were collected and ground to fine powder. The precipitated reaction product was used as the starting material for the second stage of the experiment (post-processing described in section 7.3).

The XRPD patterns were gathered with a laboratory X-ray source General Electric powder diffractometer in transmission mode with MoK_{alpha1} radiation using the Ge-111 monochromator with a Soller slit and a divergence slit of 1mm opening. 1D-stripe detector Metero1D was used with an angle coverage of 6°.

The FTIR spectrum was measured on a Bruker Equinox spectrometer in transmission mode using the KBr pellet method. 200mg of KBr (kalium-bromid) powder was mixed with 1.4mg of bone powder with maximum grain size of 100μm. The spectrum was gathered in the range of 400-4000cm^{-1} with 4cm^{-1} resolution and 128 scans.

7.2.2 Diffraction and spectroscopic characterization of the ACP

In the first stage of the experiments the synthesized ACP was evaluated using laboratory X-ray sources. Angle resolved powder diffraction patterns and the corresponding transformation to the Pair Distribution Functions (PDF) (described in section 2.1.3) is shown in Fig.7.1. In the figure 7.1 next to the ACP samples showing phase mixture of nano and ACP, as well as a pure HAP sample as a reference are displayed. The pure ACP samples doesn't show Bragg peaks. In case of a phase mixture of ACP and a proto-nanocrystalline phase few broad Bragg peaks are possible to infer from the diffraction pattern.

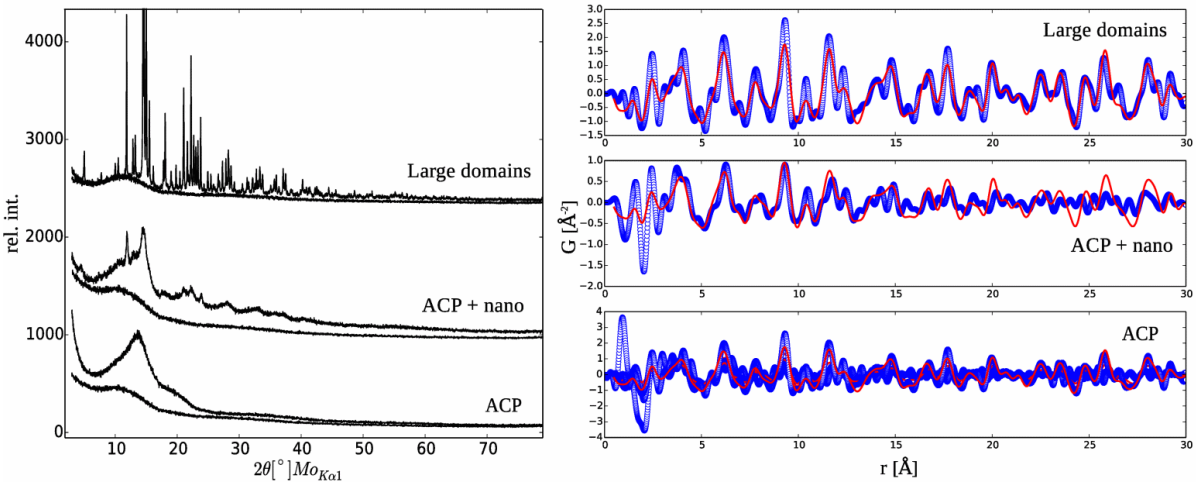

Figure 7.1: XRDP measurements of three stages of end-products
The left side plot shows the diffraction patterns of different stages of ACP and nano phase mixtures measured with laboratory X-ray source with molybdenum radiation source. Under each diffraction pattern the empty glass capillary measurement is shown for scale. This was subtracted in the "Pdfgetx3" code's procedure of the data transformation (see Chapter 2 section 2.1.3); The right side plot shows the obtained PDF fit. The PDF pattern lacks resolution and it is shown here as a comparison to the PDF function patterns obtained from a synchrotron source in section 7.3.3.

The corresponding PDF function plot (right side in Fig.7.1) illustrates the difficulties of the transformation of the dataset in the case of noisy and low q-space resolution diffraction patterns of a laboratory molybdenum X-ray source. Analysis of diffraction patterns of the ACP samples using synchrotron radiation source are in detail examined in the following section 7.3.3.

The absence of crystalline HAP in the ACP powder was confirmed with infrared spectroscopy as well (Fig.7.2). FTIR spectra of ACP show broad bands without peak separation and shoulder formation of the characteristic vibrational band regions of the reference HAP structure. Vibrational modes induced by the distortion of the phosphate tetrahedra due to calcium cation neighbours (Adler, 1964) are missing from the ACP spectrum (Fig.7.2), in agreement with similar studies (Sun et al., 2010).

The inter-atomic distance between P-O in a symmetric tetrahedron in the structure of a crystalline material is 1.537Å, as a mean value according to Baur (Baur, 1974). In the reference HAP structure the phosphate tetrahedra are distorted, resulting in three different P-O distances (in the structure with space group $P6_3/m$). In the amorphous state, however, these distances and variation of P-O bond length aren't necessarily kept.

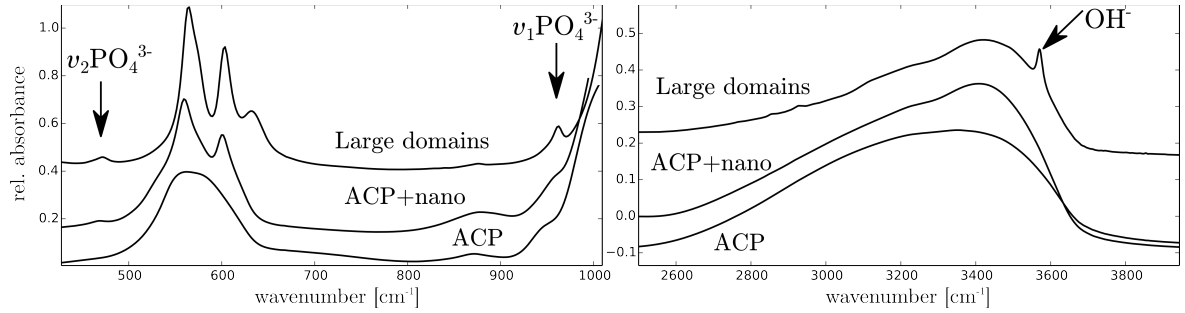

Figure 7.2: FTIR spectra of three stages of end-products. Left side plot shows the FTIR of the ν_2, ν_4 and ν_1 PO_4^{3-} vibration region. Arrows point to the modes induced by the distortion of the phosphate tetrahedra ν_2 and ν_1; Right side plot shows the characteristic OH^- stretching mode is shown for a nano-crystalline hydroxylapatite (arrow) on top of the water vibrational band which is present in all samples.

In the FTIR spectra of totally symmetric phosphate tetrahedra, the ν_1 and ν_2 modes are absent. The appearance of a FTIR mode is activated by the distortion of the P-O tetrahedra due to the symmetry break in the rigid body unit lowering from C^2_{6h} to C_{3h} (Adler, 1964; Antonakos et al., 2007). The FTIR measurements suggest that this distortion increases as the ACP transforms to nanocrystalline (and later to crystalline) HAP. As it can be seen in Fig.7.2, the FTIR spectrum of the amorphous phase does not show developed peaks at wavenumbers where a reference apatite P-O induced modes would appear (460-470cm^{-1} in Table.1.1 in Chapter 1 section 1.3.3).

In the next section the relation of the coherently scattering domain size increase and the emergence of the long range order will be examined. Amorphous materials form a network type structure with only short range order (SRO) present and no translational symmetry. The nanocrystalline state on contrary should be considered as a very small domain but with a long-range order (LRO) and translational periodicity. To follow up the early stages of crystallite domain formation higher quality measurements have been conducted at a synchrotron facility to determine the extent of the ordering (SRO-to-LRO) and atomic structure from the PDF analysis. It needs to be added that previous detailed studies have been described the local atomic structure using the pair distribution function of the nano crystalline Ca-phosphates as well as the amorphous phases (Betts et al., 1975; Betts and Posner, 1974; Harries et al., 1987), the latter synthesised at pH 10.

7.3 Nucleation and growth of nano-crystalline carbonated calcium deficient hydroxylapatite from the amorphous phase

The appearance and growth of a crystalline phase from the amorphous phase was examined by exposing the ACP powder to water at 37°C[*]. This temperature was chosen for the reason that it is near the human body temperature and so simulating the conditions for medical usage of the ACP under normal human body conditions[**]. The results show a transformation from an amorphous to a crystalline state. The amorphous phase decreases with treatment duration, while the nano-crystalline fraction increases. From the combination of FTIR and Raman spectroscopy it is concluded that the crystallization process starts from the surface of the amorphous agglomerates and forms a nanocrystalline carbonated-hydroxylapatite phase. Micro-structural analysis via Rietveld refinement shows anisotropy of the coherently diffracting domain lengths. Analysis of the atomic pair distribution function (PDF) of the transformation yields the description of the inter-atomic distances, hence describes the structural changes on the atomic level. SEM imaging shows that with increasing treatment duration the surface features transition from spherical agglomerates to a surface that appears as a network of pillar-like formations.

7.3.1 Nucleation and growth mechanism

A recent in-situ synchrotron study by Ibsen and Birkedal (Ibsen et al., 2016) (conducted at pH values of 10 to 12) shows an almost instantaneous nucleation of the nanocrystalline hydroxylapatite phase from the reaction of calcium and phosphate aqueous solutions. Their result shows that the measurable effect of nucleation and growth of the HAP phase becomes significant almost instantaneously in contrast to maturation experiments, where the time intervals of nanocrystalline HAP formation is in the order of days and weeks (Rollin-Martinet et al., 2013).

Although Dorozhkin (2010) states that "...the amorphous-to-crystalline transfor-mation mechanisms of ACPs have not been well elucidated...", there have been several pathways hypothesised:
(1.) dissolution of ACP and re-precipitation of the crystalline phases (Boskey and Posner, 1973; Tung and Brown, 1983; Somrani et al., 2005),
(2.) internal structural rearrangements (Onuma and Ito, 1998; Kim et al., 2005; Somrani et al., 2005),
(3.) development of long-range-order without changing the immediate environment of

* actual temperature at experiment was 1°C - 4°C below 37°C±1°C

** normal human body conditions with respect to temperature only – the temperature degree choice also means that no hydrothermal or other elevated temperature reaction experiment has been conducted in the context of research presented in this section

calcium atoms (Harries et al., 1987),
(4.) formation of crystalline phases directly within the ACP phases (Wang et al., 2009),
(5.) self-aggregation and surface-mediated transformation (Combes and Rey 2010).

According to Onuma (Onuma, 2006) when the ACP density reaches a critical value, the random arrangement of ACP units becomes disadvantageous in terms of total free energy, resulting in a sudden regularization of the structure that forms hydroxylapatite. Yin and Stott (Yin and Stott, 2003) argue that, in the transformation from ACP to calcium deficient hydroxylapatite (or carbonated calcium-phosphate apatite) the amorphous phase needs only to dissociate into clusters instead of complete ionic solvatation* (the dissolved ions get surrounded by the solute molecules making complexes). This would mean that the ACP doesn't need to be dissolved completely. Dorozhkin (Dorozhkin, 2013, 2010) states that the solubility of the ACP can not be determined precisely due to possible variations of the chemical composition. This result highlights the importance of in-detail characterisation of the synthesis products that are derived from the ACP. For this reason in the context of this thesis the microstructural parameters, such as the anisotropicity of the crystallites, as well as the inter-atomic distances are evaluated using total scattering methods in parallel with the Rietveld refinement. Vibrational bands are examined with FTIR and Raman spectroscopy, while the surface of the particles was imaged with SEM techniques.

7.3.2 Materials and methods of ACP Post-processing

A series of 11 samples with various treatment times have been prepared each with 0.424g of ACP powder dispersed in 20ml of preheated water in preheated glassware. The dry powder of ACP was used as a starting material in the reaction with water at the target temperature of 37°C, however the handling of the equipment and glassware together with the interaction between the thermometer and the solutions liquid resulted in measured temperatures different from the set value (see Table 7.1). The pH was measured before and also after the reaction.

Diffraction patterns were measured at the DESY PETRA3 synchrotron facility at the P02.1 beamline. 60keV radiation was used (λ=0.20727Å). Beam spot-size was 0.5x0.5mm on a 1mm diameter Kapton-capillary. A 2D detector was used and the data were integrated using the "fit2d" software (Hammersley et al., 1996), and the atomic pair distribution function was evaluated using the "pdfgetx3" (Juhás

* solvation – solvatation - (IUPAC definition) any stabilizing interaction of a solute and the solvent or a similar interaction of solvent with groups of an insoluble material (i.e. the ionic groups of an ion-exchange resin).

et al., 2013) and "pdfgetx2" (Qiu et al., 2004) software. The diffraction patterns were evaluated using "Fullprof" Rietveld refinement code (Rodríguez-Carvajal, 1993; Rodríquez-Carvajal and Roisnel, 2004). Fitting of the PDF was done in "pdfgui" software (Farrow et al., 2007). The instrumental resolution was obtained from measurement and refinement of the NIST LaB_6 standard material. This experimental resolution function was used in all further refinements of the ACP and HAP data.

Table 7.1: Series of post-processing of ACP. The dry ACP powder reaction with water and maturation time t. Deviation of temperature from the targeted values varied between 1°C – 4°C. The table contains actual measured temperature values.

Sample	pH_{init}	T_{pHinit} (°C)	$pH_{set\text{-}start}$	**t**	pH_{end}	$T_{pH\text{-}end}$ (°C)
1	(5.85-6.6)*	33.6	-	**0 (in 20sec)**	(6.8)*	33.3
2	6.68	32.3	9.1	**2 min**	8.94	33
3	7.7	32.7	9.15	**5 min**	8.88	31.9
4	7.7	32.9	9.07	**15 min**	8.87	32.5
5	7.63	33.3	9.07	**30 min**	8.84	34.2
6	7.04	35.4	9.13	**60 min**	8.81	35.5
7	8.04	34	9.13	**90 min**	8.57	36.1
8	7.2	34.9	9.08	**120 (2h)**	8.21	36
9	7.8	33.6	9.13	**150 (2.5h)**	7.63	36.4
10	6.8-7.2	32.9	9.04	**180 (3h)**	7.48	36.1
11	7.82	32.8	9.13	**9h**	6.69	35.6

* instantaneous measurement, but with respect to the readout inertness of the pH meter

The FTIR spectrum was measured on a Bruker Equinox spectrometer in transmission mode using the KBr pellet method. 200mg of KBr (potassium-bromid) powder was mixed with 1.4mg of sample powder with maximum grain size of 100μm. The spectrum was gathered in the range of 400-4000cm^{-1} with 4cm^{-1} resolution and 128 scans.

Raman spectra were measured on a Horiba XploRa Raman microscope. The 532nm green laser was used with a spot size* of 811nm. The power of laser used was 10mW. Settings of the grating filter and collimator were set to give maximum measurable intensity.

Spectroscopic data were evaluated using the "PeakFit" software. The least-squares fit procedure was continued until the normality of standard deviations was reached (the procedure is in details described in Chapter 6 section 6.2.4). When all data-points in the measured spectra were inside the 95% confidence bound, the fit was terminated and the obtained spectral band parameters were extracted for further

* spot size diameter is calculates as $d = 1.22 \lambda / 0.8$, while using the x80 objective

analysis. In case that this criterion was not met, the peak position, number of peaks, the background subtraction or the fit region were altered and a new fit was attempted. The background subtraction parameters were not included into the least-squares fit, as it can give unpredictable correlations with the profile function parameters of the spectral bands. Instead, several options were tested to model the background (with linear, constant, cubic, quadratic, etc. function) which was subtracted from the data before the fit.

7.3.3 Diffraction and total scattering measurement

The starting material of ACP powder (obtained as described in section 7.2) is assumed to be free of any nuclei of a crystalline phase, and also that the appearing and emerging nano-phase has nucleated due to the applied treatment of the post-processing in water. Based on these assumptions the experiment allows to quantify the reduction of the amorphous phase with the increase of the long range order of a carbonated-nano-apatite phase. The amorphous phase transforms to nanocrystalline apatite during which the phase fraction of the nanocrystalline apatite increases with the depletion of the ACP. At the same time the Bragg-peak intensity increases as the result of an increased long range order in the growing domains and the increase of the domain lengths (apparent crystallite size).

The measured diffraction patterns and the obtained pair distribution functions are shown in Fig.7.3 and Fig.7.4. All diffraction pattern data have been obtained after the 2D image transformation in “fit2D”. Rietveld analysis was conducted in the reciprocal space on a low Q-space measurement (with high diffraction angle resolution). The process of acquiring the PDF G(r) function was analogous to the approach described in section 2.1.

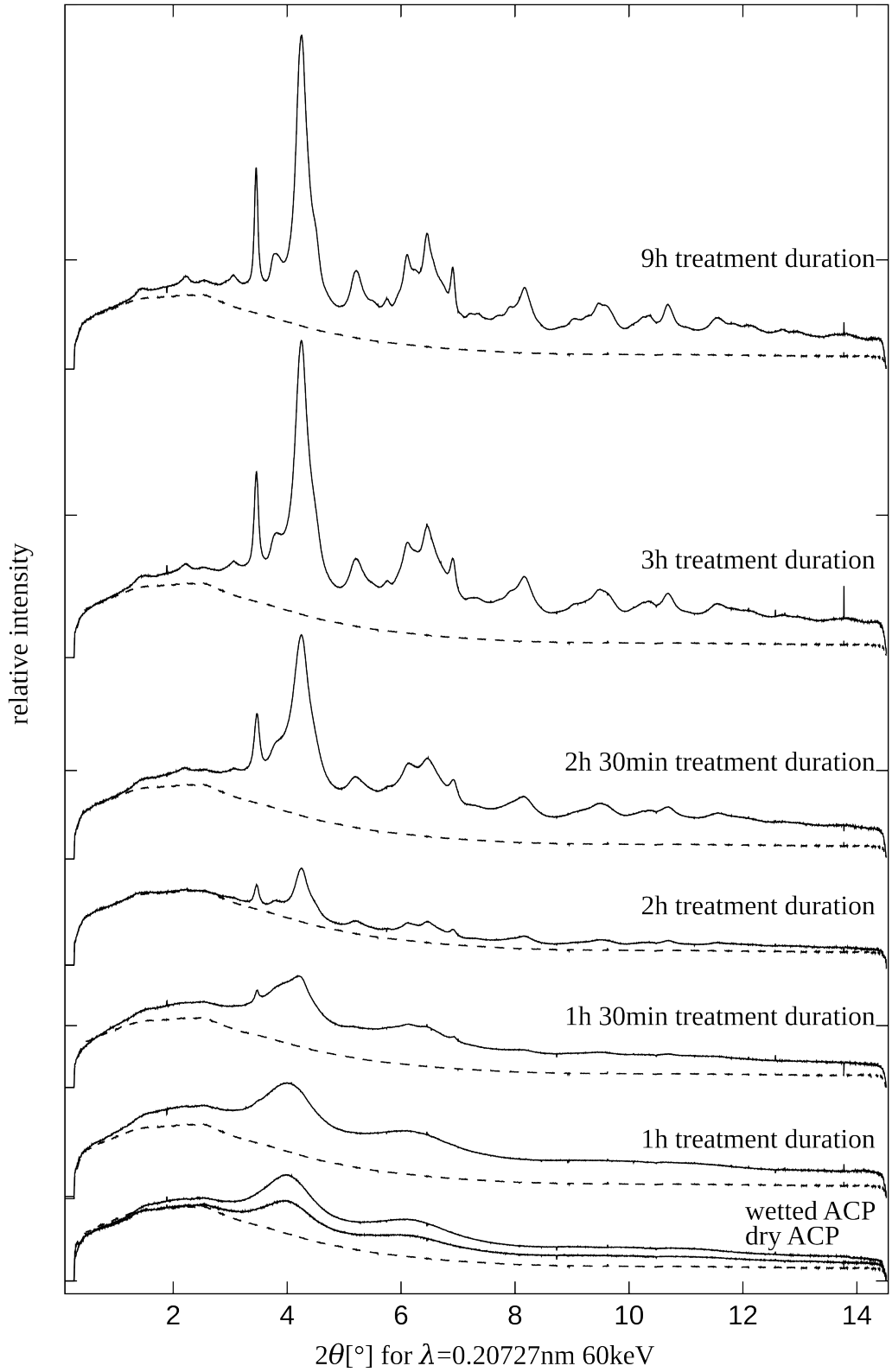

Figure 7.3: Measured diffraction pattern of the amorphous-to-nanocrystalline calcium-phosphate transformation. The dashed line is the measured empty kapton capillary sample holder.

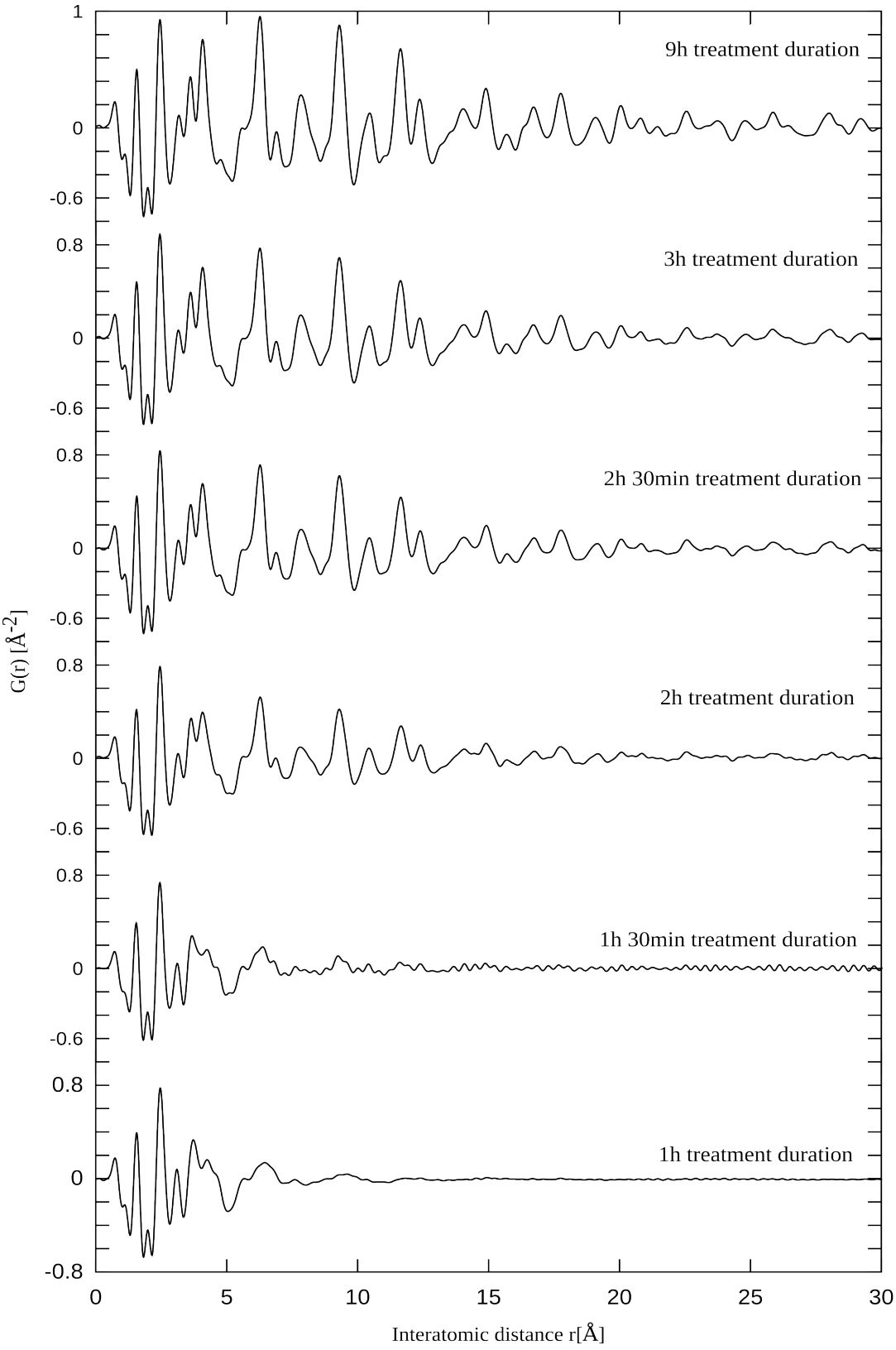

Figure 7.4: Pair distribution function G(r) of the amorphous-to-nano HAP phase The measured data was transformed with Q_{max} of 18Å.

Rietveld analysis

The results of the Rietveld refinements are given in Table 7.2. The Rietveld refinements of the diffraction patterns have been conducted in two stages. Firstly, fit of the "XRD-amorphous" diffraction pattern have been attempted, where no apparent Bragg peaks are present (Fig.7.5). The measured diffraction pattern is assumed to be generated by the presence of a short range order structure, rather than the long range order domains. Applying the Rietveld refinement of "XRD-amorphous" material stretches the applicability of the method, as it is no longer based on the ideal crystallographic structure approximation.

After the nucleation event has occurred and the crystallites are growing Bragg peaks are apparent in the diffraction pattern. In this second stage the Rietveld refinement was attempted with a two phase model, where the first phase is modelled with the resulting parameters of the XRD amorphous phase, and the second as a nanocrystalline apatite phase (Fig.7.6). The chemical formula of the crystallographic models was considered the same for both phases.

Table 7.2: Results of Rietveld refinement microstructural analysis with anisotropic size

t	a	c	Size along reflections [Å] [*1]					wt% of ACP
			010	011	110	002	112	
dry	[*2]10.37(9)	[*2]6.88(2)	-	-	-	-	-	100
0min	[*2]10.29(9)	[*2]6.90(1)	-	-	-	-	-	100
15min	[*2]10.34(1)	[*2]7.06(1)	-	-	-	-	-	100
[*3]1h	[*3]10.35(6)	[*3]6.91(1)	-	-	-	-	-	[*3]100
[*4]1p5h	9.431(8)	6.859(4)	14	25	27	55	41	87(3)
[*4]2h	9.474(2)	6.8686(8)	23	35	28	56	42	49(2)
[*4]3h	9.4622(8)	6.8783(4)	27	43	36	70	52	30.4(1.6)
[*4]9h	9.4568(6)	6.8802(3)	32	52	42	91	66	19.3(1.6)

[*1] - apparent coherently diffracting domain length refers to size along a reflection in the anisotropic refinement; it is calculated using Scherrer's formula

[*2] - lattice parameters are given only for orientation value, the estimated uncertainties refer to the constrained fit and their practical physical meaning does not apply for the amorphous case

[*3] - even though a weak indication of very small Bragg peaks can be inferred from the diffraction pattern, the refinement was carried out disregarding a potential very small amount of crystalline phase, so the 100% amorphous fraction might be incorrect.

[*4] - samples were refined as a two phase mixture of amorphous and nano-crystalline

XRD amorphous pattern

In Rietveld refinement only the coherent scattering is analysed as it is the source for Bragg peaks. "XRD-amorphous" patterns can be analysed using the Debye equation (as implemented in GSASII as a contribution to the background modelling). However, in this case a crystallographic model was used with the assumption that the long range order covers only just about the size of the unit cell. The diffraction pattern was analysed by very large broadening terms values in the model. In Fig.7.5 the result of such a Rietveld refinement is shown on an ACP sample.

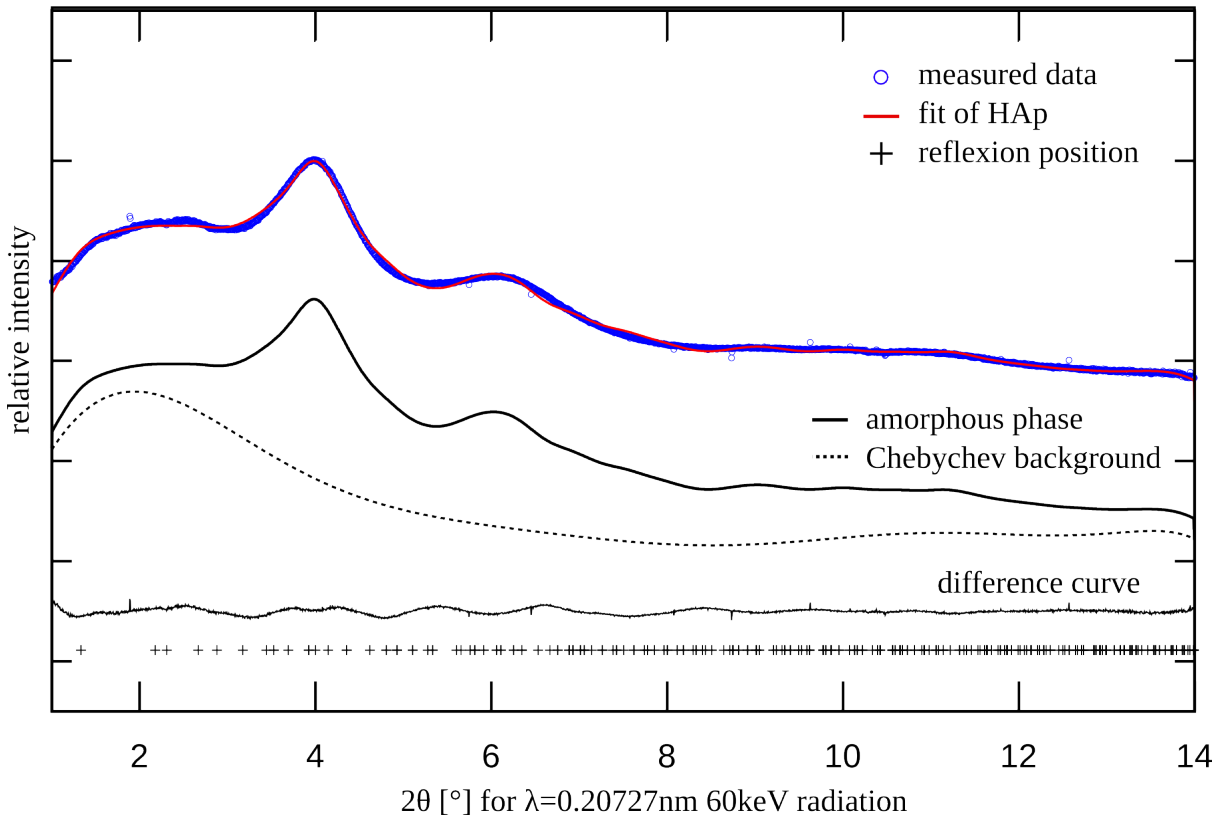

Figure 7.5: Rietveld refinement of the amorphous phase.
The fit of the hydroxylapatite crystallographic model to the measured data is shown in the upper section of the plot. The model of the phase is plotted in the middle. The difference curve shown on the bottom. The "+" sign signifies the position of the Bragg peaks of the reference hydroxylapatite structure.

The initial crystallographic parameters were set according to the reference structure of Sudarsanan and Young (Sudarsanan and Young, 1969). Only the lattice constants have been refined leaving other structural parameters locked. The scaling factor and a generalized size broadening term were also included as fit parameters. The obtained lattice constants and the apparent size of several reflections are given in Table 7.2. The starting crystallographic model can be also subjected to discussion, as it was shown in section 3.4. However, in order to reduce the complexity in the

evaluation, in the first approximation, the hydroxylapatite model was used. Presence of carbonate is evident in the FTIR measurement but is neglected in this model.

XRD amorphous and nanocrystalline phase mixture samples

With longer maturation time the peaks in the diffraction pattern tend to get more differentiated (Fig.7.3). For these measurements a two phase refinement model was utilised, since a two phase model outperforms a single-phase nano-crystalline model refinement. In Fig.7.6 the 3 hours long treatment time sample refinement diffraction pattern is shown. In the case of the two-phase mixture model both phases used the same initial structural model (Sudarsanan and Young, 1969). For modelling of the amorphous phase the obtained structural parameters of the single amorphous phase refinement (described in the previous section) were used as one of the two-phases in the model.

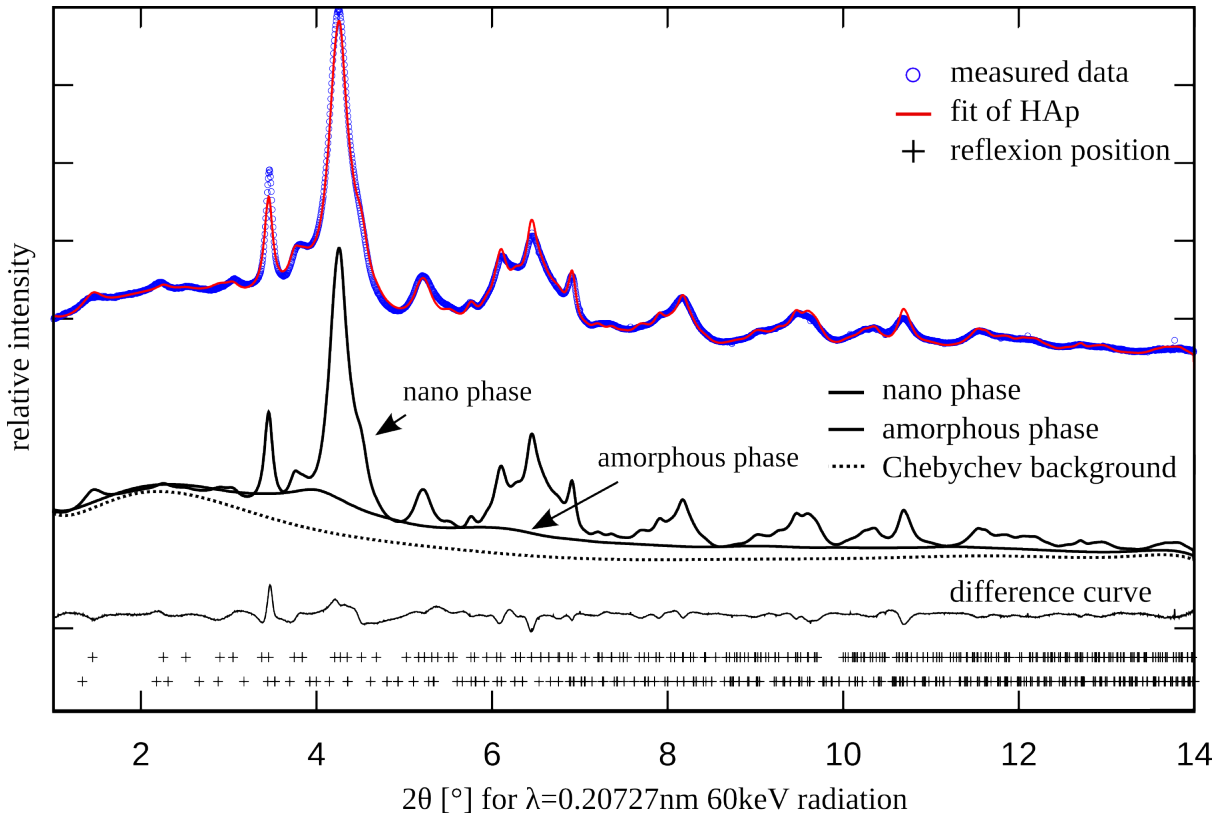

Figure 7.6: Rietveld refinement with a nano-crystalline and amorphous phase. The fit of the hydroxylapatite crystallographic model to the measured data is shown in the upper section of the plot. The nanocrystalline and the amorphous phase are plotted up to scales, but shifted on the relative intensity scale for clarity. The difference curve shows the model to data difference. The "+" sign signifies the position of the Bragg peaks. For the amorphous phase only the scale was refined and the lattice constants and broadening parameters were obtained from the Rietveld refinement on the amorphous phase alone.

All structural and profile parameters were kept fixed (except the scale factor). The Bragg peaks were fit with a secondary HAP phase with different broadening parameters.

The estimation of the amorphous content was done in the full-profile refinement. In his report Madsen refers to this methodology as "full structure method" (Madsen et al., 2011), where one of the phases is actually in amorphous state. According to the "full structure method" a crystallographic structure is used to model the diffraction pattern of the amorphous component with large values for the broadening parameters. The phase fraction of the amorphous phase is obtained as any crystalline phase in a multiphase refinement as:

$$W_\alpha = \frac{S_\alpha (Z \cdot M \cdot V)_\alpha}{\sum_{j=1}^{n} S_j (Z \cdot M \cdot V)_j} \qquad \text{(Equation 7.1)}$$

where the phase weight fraction is W_α, S_α is the phase scale factor in the Rietveld refinement, Z_j number of formula units per unit cell for phase j, M and V are the mass of the formula unit and unit cell volume, respectively. The result of the refinement from Table7.2 are plotted in Fig.7.7.

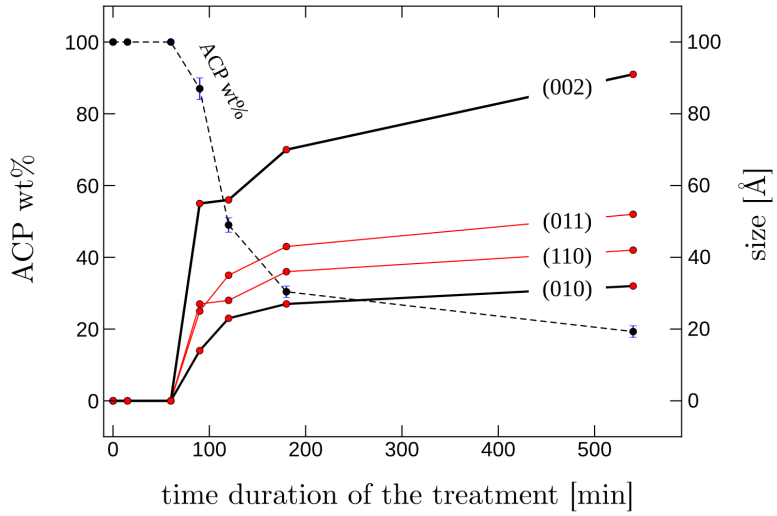

Figure 7.7: Weight fraction of ACP and the apparent size of the crystallites in the anisotropic model. Only selected reflections are plotted, directions along a-axis (reflection 010) and along c-axis (reflection 002) are highlighted. Rietveld refinement using a two-phase fit model shows gradual decrease of the ACP phase weight percentage.

Pair distribution function (PDF) analysis

In the Rietveld analysis structural parameters such as the atomic positions, occupancy values, mean-atomic displacement parameters have been left with the values of the reference HAP structure model. The reason not to refine these parameters was that in the case of unconstrained Rietveld refinement the values for those parameters converge to physically implausible values. Access to the atomic parameters is in general difficult if not impossible in the case of nanocrystalline materials and broad powder diffraction Bragg peaks. On the other hand as an attempt to access atomic positional parameters for these kind on nano-scale domains the PDF analysis was used. In the series of the amorphous to crystalline phase transformation the PDF function shows slight variations notifying structural changes (Fig.7.8).

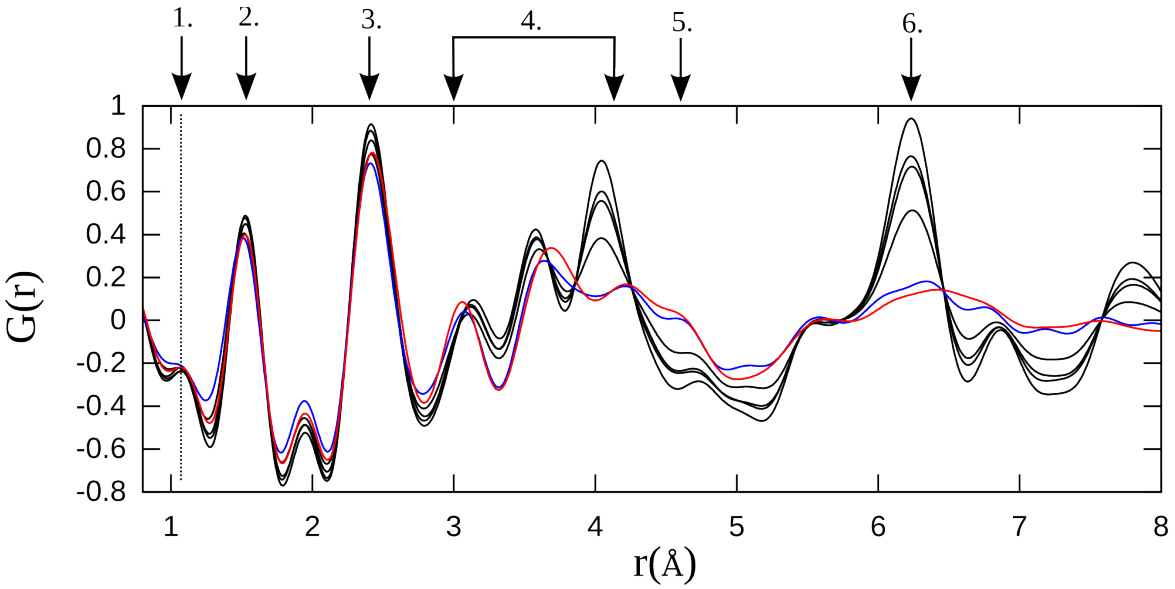

Figure 7.8: Overlay of the G(r) data from shown in Fig.7.4 for the amorphous-to-nanocrystalline carbonated apatite transformation. Arrow 1 points to the very first peak, that is arguable on the limit of resolution, however, the H-O distance in a water molecule is about 0.99-1.1Å. It is highly arguable if this peak is a data transformation artefact. Arrow 2 points to the P-O peak at 1.5Å, the distance of P-O in the phosphate tetrahedra. Arrows 3-6 point to the sum of Ca-O, Ca-Ca, Ca-P distance peaks and also cumulative contribution of several inter-atomic distances to the G(r) function. The peaks under arrow 4 show greater shift relative to the peaks at arrow 2 and 3. Above 4Å as the phase transformation progresses (with increased exposure to water) the increase in G(r) amplitude is more rapid relative to the other peaks – especially for the peak marked with arrow 6.

On the overlay plot of the G(r) functions of all the samples of the amorphous-to-nanocrystalline carbonated-apatite transformation it can be seen that the position,

amplitude and the width of the first few peaks match. With the increase of the post-processing time (exposure of the ACP powder to water) peaks at longer distances in the G(r) increas in amplitude and become more featured.

From the fadeout of the structural signal in the PDF function of each sample (see Fig.7.4 as the signal oscillates with ever smaller amplitude around zero) it is possible to retrieve the extent of the long range order in the form of a spherical particle diameter as implemented in the "PDFGui" software (Farrow et al., 2007). The shifts of the pair distribution function peaks G(r) are interpreted as an indication of changes in the distribution of the bond lengths. The width of the peaks in the PDF function bear information about both static (different ionic environments) and dynamic disorder. Examples of the "PDFGui" fit are given in Fig.7.9. Representative results of the G(r) function fitting for all samples are listed in Table 7.3. In the Table 7.3 the calculated percentage of the amorphous phase estimate is also shown. This value was derived from the ratio of the scale factors of the two-phase fit as $scale_{nano}$=1-$scale_{ACP}$. This is arguably possible due to the assumed same chemical composition of the two phases, which results the same weighting of the scale factors, therefore a ratio of the scale factors can be an estimator of the amount of phase. This approach to estimate the amorphous content from the PDF function can be seen in Proffen et al, (2005).

Table 7.3: PDF analysis and the obtained P-O distances, lattice constants, broadening parameter coefficient ("delta1"), diameter of a spherical particle ("spdaim" estimating the length of the long-range order) and the scale factor. The meaning of parameters in details is given in section 1.3.2. As the scale factor is normalized to unity, a two-phase fit of the PDF can be constrained as $scale_{nano}$=1-$scale_{ACP}$. The amorphous phase content is estimated from the scale factors.

	P-O [Å]	a [Å]	c [Å]	delta1 [Å]	"spdiam" [Å]	Scale factor of the nano phase	Estim. ACP wt%
1h	1.52-1.53	9.4567	6.8506	1.33	9.2	(only ACP)	100
1h30min	1.48-1.51	9.5389	6.8063	1.36	22	0.22	78
2h	1.40-1.52	9.4560	6.8681	1.36	31	0.49	51
2h30min	1.49-1.54	9.4475	6.8676	1.35	33.5	0.68	32
3min	1.48-1.52	9.4448	6.8637	1.33	35	0.70	30
9h	1.49-1.55	9.4437	6.8655	1.34	38	0.83	17

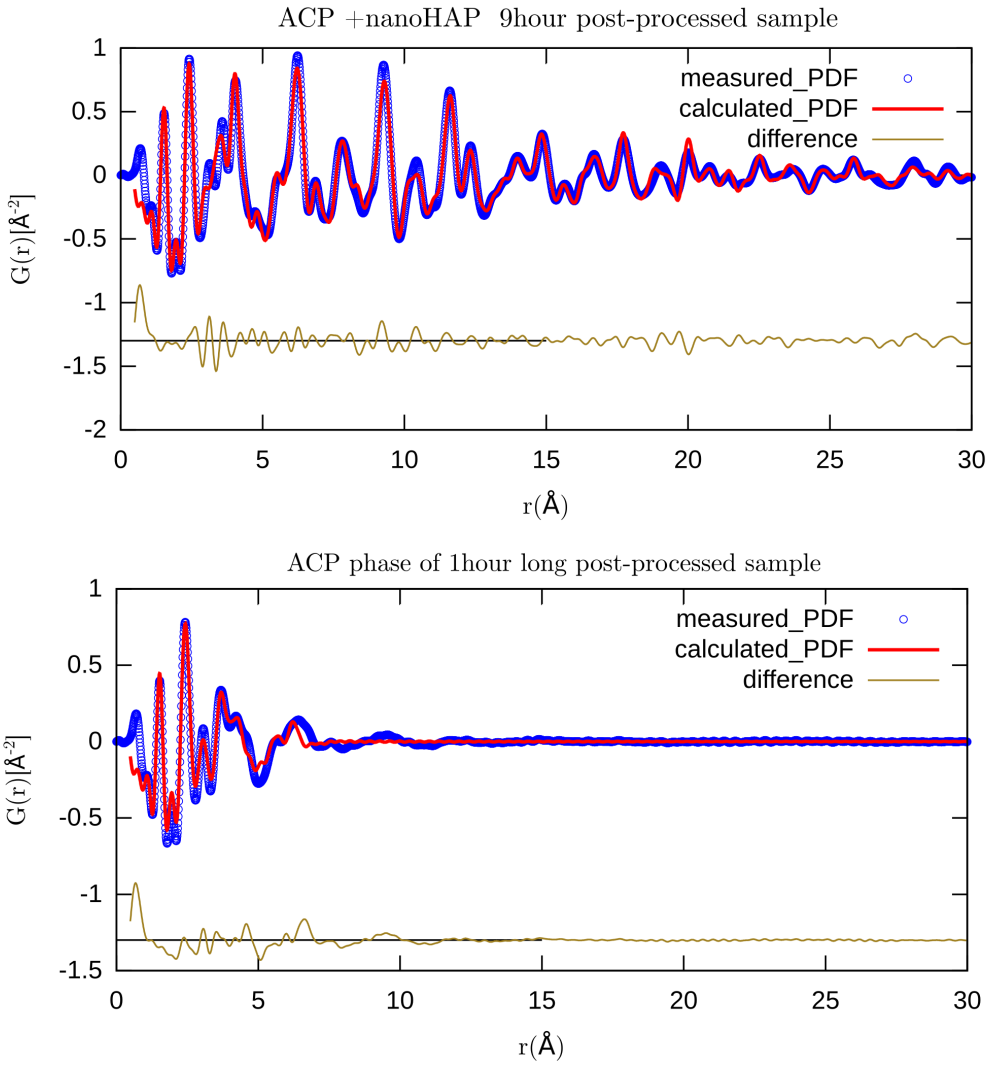

Figure 7.9: Atomic pair distribution function fit in "PDFGui" for the end-members of the ACP-to-nanocrystalline carbonate-calcium-phosphate transformation. Upper sub-plot shows the PDF fit for the sample with assumed phase mixture of nanocrystalline and amorphous phases (9 hours long treatment), while the lower sub-plot show the PDF fit for the sample of the amorphous phase (1 hour long treatment). The integration limit of the data transformation was Q_{max}=18Å^{-1}. The difference curve show in both cases good match for the peaks in the range above 1Å^{-1}.

The initial atomic positions in the unit cell was according to the hexagonal HAP structural model of apatite given by Sudarsanan and Young (1969). According to the PDF fit method applied (implementation of "PDFGui"), the atomic positions of the initial structure are fit in the least-squares optimization over the asymmetric unit cell (P1), where each individual atom in the unit cell can shift its position as free parameters. However, constraints regarding symmetry can be imposed as well,

together with constraints over the atomic displacement factors, which were kept at initial values and were not refined as a free parameter. In the evaluation of patterns and the results presented here, some constraints have been applied to the fit, such as the position of the P-O keeping to phosphate tetrahedra as a rigid body unit. Other crystallographic structure models (listed in section 3.4) have been tested as well for the PDF fit, however, a comprehensive and exhaustive comparison of the results with all possible crystallographic model was not conducted.

FTIR measurements show carbonate presence in the structure Fig.7.11. However including carbon atoms the model and PDF fit resulted in no interpretable change of the inter-atomic distances and had no effect in improving the fit. One of the primal causes for this can be found in the data transformation, were the used software "fit2D" does not calculate standard errors of the measured intensities from the 2D diffraction pattern conversion. In such cases the PDF evaluation software uses dummy values for the standard errors of the intensities, therefore rendering the calculation of small differences practically unreliable.

Inter-atomic distances were obtained from the fit as follows: 1. all bond lengths were gathered in an inter-atomic distance interval (1-2.8Å and 3-6Å); 2. in a distance range sort the distances out by atom pairs (P-O, Ca-O, etc.); 3. sum the unique values up and obtain the frequency of occurrences of each calculated inter-atomic distance. Results obtained by this approach for the amorphous phase as well as the phase mixture models are given in Tables 7.4 and 7.5-7.6, respectively. The extracted P-O bond distances of the PDF analysis for the amorphous and the nanocrystalline HAP samples are visually compared in Fig.7.10. In the two-phase fit model the nanocrystalline HAP phase results in three distinct P-O distances in the phosphate tetrahdra, in accordance to the initial HAP structure. Fit of the amorphous phase yields three P-O distances that are almost identical, which approximates to the totally symmetric description of the phosphate tetrahedra.

In the sub-plot of Fig.7.10, the FTIR data is displayed as a comparison to illustrate the phosphate tetrahedra and the relative displacement of phosphor and oxygen atoms. From the spectral trace comparison it is evident that a peak at 470 cm^{-1} is appearing with increasing maturation time. The appearance of a peak in the spectral trace correlates with the post-processing time duration indicating that a symmetry break occurred, as described in section 7.2. Therefore, it was anticipated that the results of the bond distance deviations should follow a trend of increasing difference between P-O distance values of each vertices as the phosphate tetrahedra becomes more distorted (highlighted area in Fig.7.10). However, the results of the PDF fit could not fully confirm this assumption, presumably due to the fit procedure and parameter correlations.

Table 7.4: Inter-atomic distances from the PDF fit of the amorphous phase (using the hydroxylapatite as a starting model). The P-O, O-O and Ca-O distances have been extracted from the fit results and evaluated in the ranges 1-2.8Å and 3-6Å. Unique distance values for each atom pair occur multiple times in the data here denoted as f.o. - frequency of occurrence of a distance value. The mean distance for an atom pair is also given with the standard deviation. In the range 3-6Å P-O, Ca-P, Ca-Ca, and P-P distances are evaluated. The mean value was not calculated in this cases due to the big value range of the atom pair inter-atomic distances.

Region [Å]	pair	inter-atomic distances						
1 – 2.8	P-O	unique values [Å]	1.524		1.527		1.532	
		f.o.	24		12		12	
		mean [Å]	1.527(3)					
	O-O	unique values [Å]	1.078	2.353	2.358	2.361	2.362	2.409
		f.o.	12	24	24	4	12	12
		mean [Å]	2.3(3)					
	Ca-O	unique values [Å]	2.376	2.399	2.445	2.461	2.487	
		f.o.	24	12	24	24	24	
		mean [Å]	2.44(4)					
3 – 6	P-O	unique values [Å]	3.645 3.681 3.754 3.822 3.865 3.967 4.006 4.285 4.591 4.69 4.692 4.752 4.864 4.985 5.414 5.455 5.489 5.495 5.545 5.631 5.637 5.722 5.767 5.771 5.779 5.932					
	Ca-P	unique values [Å]	3.067 3.136 3.173 3.58 3.623 3.753 5.451 5.694 5.951					
	Ca-Ca	unique values [Å]	3.623 3.889 4.074 4.324 4.568 5.424 5.478 5.724					
	P-P	unique values [Å]	4.107 4.119 5.104 5.971					

Table 7.5: Part 1. Inter-atomic distances from the PDF in the region of 1-2.8Å in the two-phase fit (ACP + nanocrystalline apatite). Values for the ACP phase were obtained from the fit of pure amorphous phase and were kept unchanged. The nanocrystalline phase in the two-phase fit resulted with the listed inter-atomic distances and spherical diameter parameter given in the first column. Unique distance values for each atom pair occur multiple times in the data here denoted as f.o. - frequency of occurrence of a distance value. The mean distance for an atom pair is also given with the standard deviation.

Phase	pair	inter-atomic distances						
Sample **ACP phase** with domain size **9.2 Å**	P-O	unique values [Å]	1.524		1.527		1.532	
		f.o.	24		12		12	
		mean [Å]	1.527(3)					
	O-O	unique values [Å]	1.078	2.353	2.358	2.361	2.362	2.409
		f.o.	12	24	24	4	12	12
		mean [Å]	2.3(3)					
	Ca-O	unique values [Å]	2.376	2.399	2.445	2.461	2.487	
		f.o.	24	12	24	24	24	
		mean [Å]	2.44(4)					
Sample treatment duration **1h30min** Nano phase with domain size **22 Å**	P-O	unique values [Å]	1.484		1.488		1.517	
		f.o.	24		12		12	
		mean [Å]	1.494(14)					
	O-O	unique values [Å]	1.9782	2.24015	2.24734	2.32221		
		f.o.	12	12	24	24		
		mean [Å]	2.23(12)					
	Ca-O	unique values [Å]	2.384	2.402	2.41	2.431	2.483	2.578
		f.o.	24	24	24	24	12	24
		mean [Å]	2.45(7)					
Sample treatment duration **2h** Nano phase with domain size **31 Å**	P-O	unique values [Å]	1.41		1.527		1.528	
		f.o.	12		12		24	
		mean [Å]	1.50(5)					
	O-O	unique values [Å]	1.252	2.182	2.421	2.439	2.448	2.493
		f.o.	4	4	24	12	24	12
		mean [Å]	mean not calculated – broad value range					
	Ca-O	unique values [Å]	2.333	2.395	2.413	2.449	2.487	2.507
		f.o.	24	12	24	24	24	24
		mean [Å]	2.43(6)					

Table 7.6: Part 2. Continuation of the table 7.5.

Phase	pair	statistics						
Sample treatment duration **2h30min** Nano phase with domain size **33.5 Å**	P-O	unique values [Å]	1.493		1.523		1.548	
		f.o.	12		24		12	
		mean [Å]	1.522(19)					
	O-O	unique values [Å]	1.362	2.072	2.469	2.478	2.504	2.508
		f.o.	4	4	24	24	12	12
		mean [Å]	2.4(3)					
	Ca-O	unique values [Å]	2.328	2.371	2.382	2.453	2.492	2.503	2.792
		f.o.	24	12	24	24	24	24	12
		mean [Å]	2.46(12)						
Sample treatment duration **3h** Nano phase with domain size **35 Å**	P-O	unique values [Å]	1.482		1.521		1.524	
		f.o.	12		12		24	
		mean [Å]	1.513(18)					
	O-O	unique values [Å]	1.013	2.418	2.438	2.463	2.491	2.492
		f.o.	4	4	24	12	12	24
		mean [Å]	mean not calculated – broad value range 2.4(3)					
	Ca-O	unique values [Å]	2.341	2.371	2.380	2.421	2.481	2.497
		f.o.	24	12	24	24	24	24
		mean [Å]	2.42(6)					
Sample treatment duration **9h** Nano phase with domain size **38 Å**	P-O	unique values [Å]	1.499		1.526		1.555	
		f.o.	12		24		12	
		mean [Å]	1.527(20)					
	O-O	unique values [Å]	2.471	2.479	2.503	2.512	2.712	
		f.o.	24	12	12	24	4	
		mean [Å]	2.5(5)					
	Ca-O	unique values [Å]	2.342	2.345	2.382	2.397	2.481	2.482	2.795
		f.o.	24	12	24	24	24	24	12
		mean [Å]	2.44(12)						

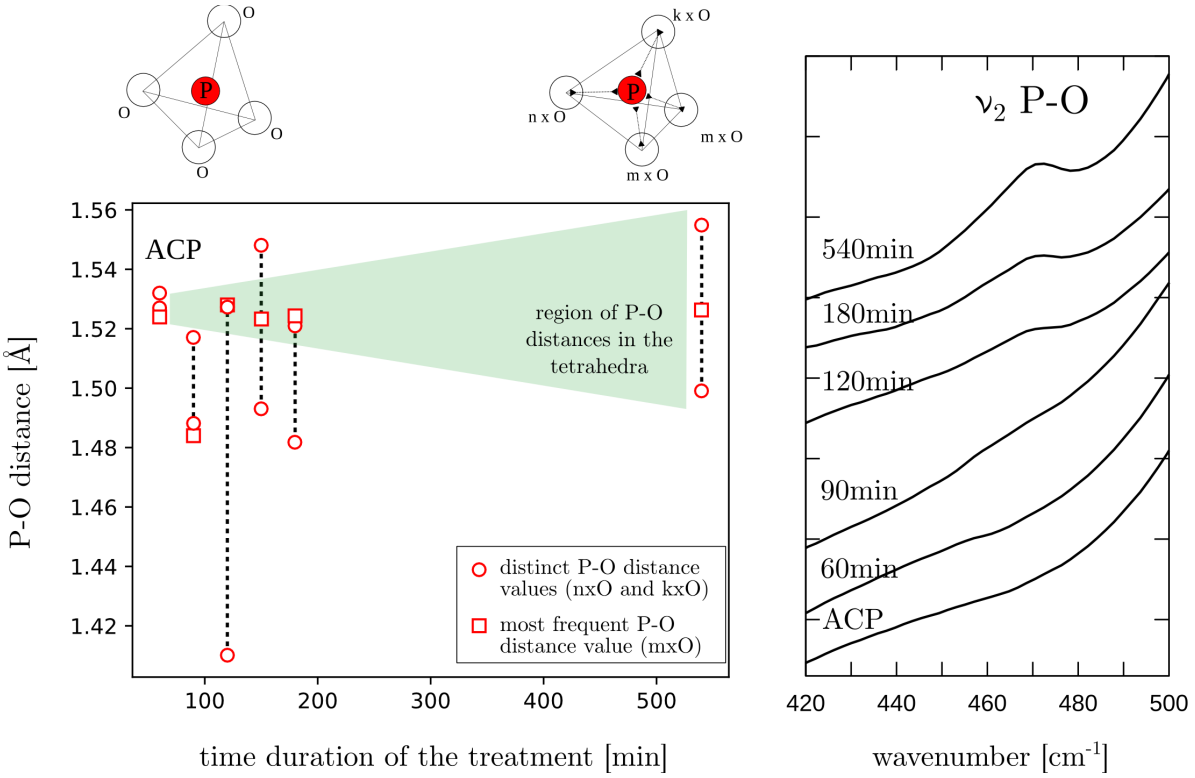

Figure 7.10: Unique values of the P-O distances in the phosphate tetrahedra obtained from the PDF fit as a function of post-processing treatment time. The highlighted area represents the expected region of the P-O distances. P-O distances in the tetrahedra are near equal for the ACP and are differentiating as the function of structural transformation due to post-processing time; Right side plot shows the corresponding FTIR dataset showing the magnified ν_2 P-O band region, where the distortion induced IR mode emerges in the spectra as the post-processing time duration increases.

7.3.4 Vibrational spectroscopy

FTIR and Raman spectra for the transformation steps in the amorphous ACP to nanocrystalline carbonated-HAP are shown in Fig.7.11. The measurements show a strong differentiation of the phosphate bands as the maturation treatment time increases. From the FTIR spectral trace the presence of carbonate bands in the amorphous phase can be inferred. Moreover, the vibration modes centred at 1415cm^{-1} and 1450cm^{-1} of the FTIR spectra assigned to carbonate $\nu_3CO_3^{2-}$ bands suggest that both the amorphous and the nanocrystalline apatite phases incorporate some amount of carbonate (Fig.7.11a). Satisfactory spectral decomposition of the carbonate vibrational region $\nu_3CO_3^{2-}$ was not obtained due to difficulties in the definition of the background contribution and spectral region limits in the process of spectral decomposition. Additionally small peak features appear in the spectral trace of the nanocrystalline sample in the region of the $\nu_3CO_3^{2-}$ vibrational bands (Fig.7.11a).

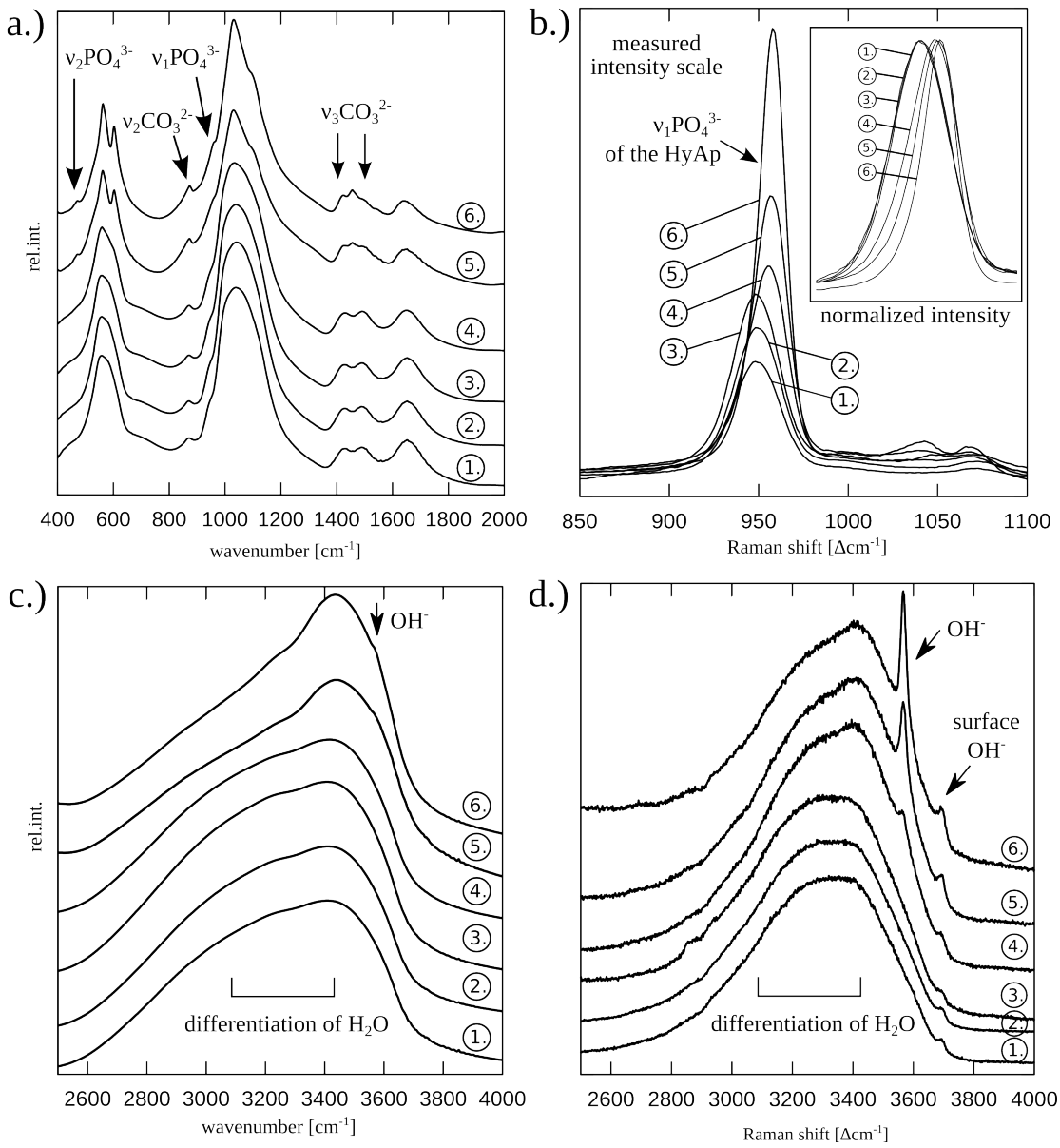

Figure 7.11: Comparison of the FTIR (a,c) and Raman (b,d) spectra for the amorphous-to-nanocrystalline transformation.

The notation of samples in the spectral traces is: ①- sample of the amorphous phase; ②- sample treated for 15min; ③- sample treated for 1hour and 30min; ④- sample treated for 2 hours – in the Raman spectra the OH^- appear; ⑤- sample treated for 3 hours; ⑥-sample treated for 9 hours.

a.) section of the FTIR spectra showing the phosphate and carbonate vibration regions; b.) shows the Raman spectra of the main ν_1 vibrational region while the inset plot shows the normalized comparison of the spectra. c.) OH^- and water vibrational region as measured with FTIR d.) the water and OH^- bands measured with Raman spectroscopy.

The OH^- stretching mode is not resolvable from the FTIR spectra despite the very small and broad shouldering in the nanocrystalline sample (Fig7.11c.). Moreover, samples that have significant amounts of the nanocrystalline phase do show its presence (Fig.7.2). In the Raman spectra, however, the distinct OH^- stretching mode becomes evident (Fig.7.11d.).

The difference of the vibrational spectroscopy results on the case of the OH^- stretching vibrational mode can be speculatively attributed to surface effect induced by the heat transfer from the Raman laser. Measurement influencing observations of surface related spectroscopic artefacts induced in the sample are further discussed in the section 8.1 of Chapter 8.

A quantitative description of the appearance of the IR-inactive phosphate modes of the totally symmetric phosphate tetrahedron was also attempted. In the spectrum of crystalline calcium-phosphate apatite bands at $471cm^{-1}$ (ν_2) and $960cm^{-1}$ (ν_1) appear as the result of the symmetry break in the phosphate tetrahedra (Adler, 1964; DeAngelis et al., 1972). These modes are activated by the distortion of the phosphate tetrahedra. The manifestation of the symmetry break appears as emerging peaks in the spectral trace with increasing processing treatment time shown in Fig.7.2 and Fig.7.11a. In the previous section, the FTIR spectral trace was compared with the results of the PDF analysis (Fig.7.10). The effort made to quantitatively determine the magnitude of the transformation of the phosphate tetrahedra using the spectral decomposition and fit method are graphically presented in the case of one sample (sample of 3 hour long maturation time in Fig.7.12).

The weak band at $471cm^{-1}$ (ν_2) was included in the evaluation of the whole $\nu_4PO_4^{3-}$ spectral region. From the fit of the FTIR spectral region between 400-$800cm^{-1}$ it can be seen that the overall fit of the spectral trace is good. However, adequate quantitative description of the shouldering at the $\nu_2PO_4^{-3}$ was not achieved. This is also due to the fact that this band appears first in samples that have reasonable fraction of the nanocrystalline apatite phase.

Phase fraction estimate from Raman spectroscopy

Samples of the amorphous-to-nanocrystalline apatite transformation have been compared using detailed evaluation of the strongest Raman shift peak in the spectral trace, which corresponds to the strongest phosphate peak ν_1 at $960\Delta cm^{-1}$ of the reference hexagonal hydroxylapatite structure. The ν_1 peak's shift and broadening have been also included in the spectral decomposition examination. The position and breadth of the ν_1 peak show large change between the samples of amorphous state (Fig.7.13a peak highlighted with green) and the samples that have nanocrystalline apatite phase (Fig.7.13a peak highlighted with blue colour). The transformation of ACP is illustrated also by the normalized peak intensity comparison, from which the complete peak alteration can be seen (Fig.7.13a inset plots).

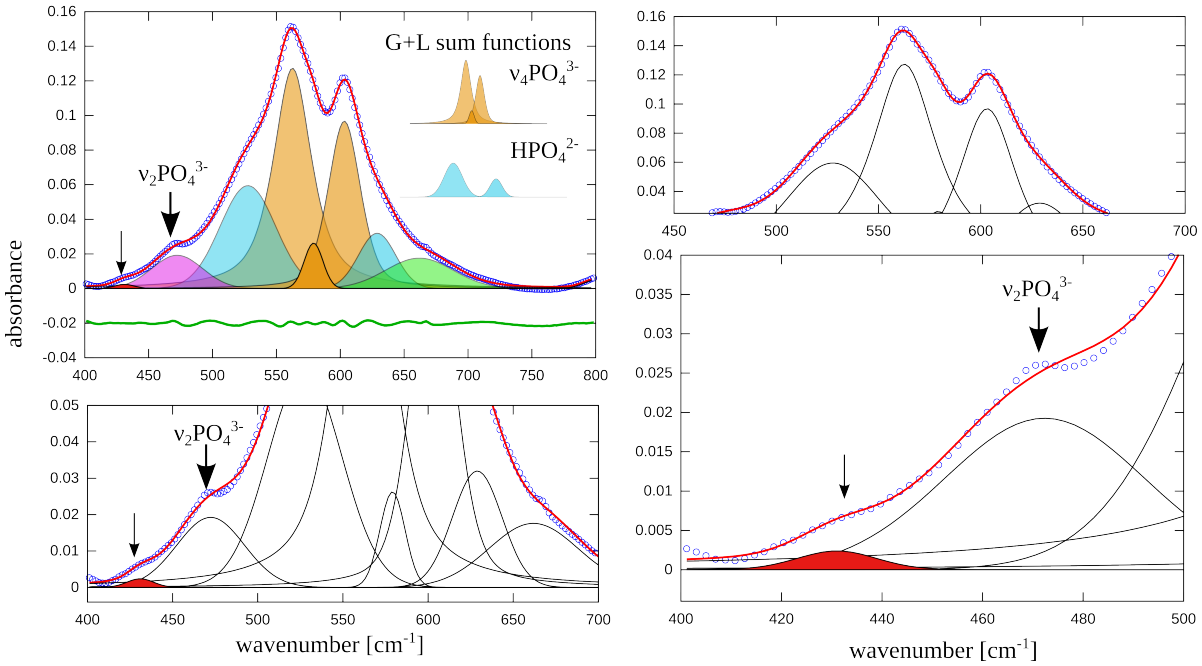

Figure 7.12: Spectral decomposition of the $\nu_4PO_4^{3-}$ region of the FTIR spectra of a nanocrystalline carbonated apatite of the 3 hour long treatment duration sample. Colours highlight the band assignment: in orange $\nu_4PO_4^{3-}$ asymmetric bending, in blue the HPO_4^{2-}, in purple $\nu_2PO_4^{3-}$, in red and green are bands that are required for the fit of the region. Critical regions of the fit are shown in magnification. Arrows point to an unidentified band (peak area marked in red colour), while the distortion induced phosphate band is denoted ($\nu_4PO_4^{3-}$)

Peak fitting of the strongest phosphate band in the Raman spectra was carried out in two stages. In the first stage the sample of pure amorphous phase was modelled with only one peak of a Gaussian shape. An example fit with the peak placement for the ACP sample is show in Fig7.13b. In the second stage all consecutive samples in the post-processing treatment duration sequence showing a phase mixture (longer than 90minutes post-processing exposure time duration) were fit with two bands. One band was fixed by its center position to the position obtained from the fit of the amorphous phase, while a second peak was added with a free parameter of position. An example fit with the peak placement is shown in Fig.7.13c. For each, the basis function of a Gaussian-Lorentzian sum functions were used with a free amplitude parameter. The obtained band peak parameters from three different point measurements for each of the sample are listed in Table7.7. The amorphous phase fraction was then calculated as the peak amplitude ratio of the ACP at 949.85Δcm^{-1} and the amplitude of the peak near 958Δcm^{-1} for each measurement A_{ACP}*100/(A_{ACP}+A_{nano}) (expressed as percentage of ACP). The amplitude ratios show high match with the amorphous phase fraction obtained with Rietveld refinement (Table7.2).

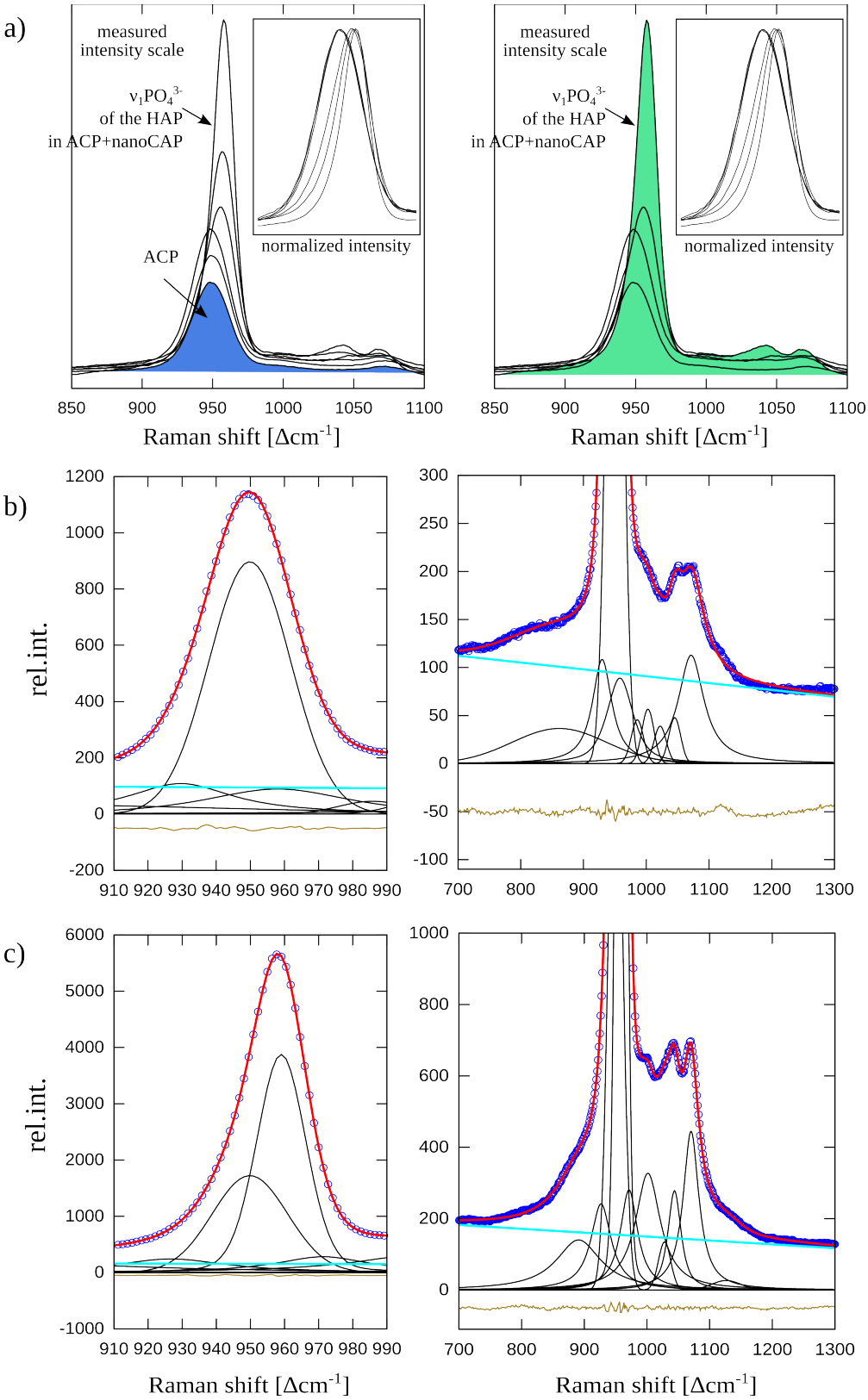

Figure 7.13: Raman spectra of the amorphous-to-nanocrystalline carbonated calcium-phosphate apatite a) plot of the ν_1 region with relative intensities b.) spectral decomposition of the ACP sample, c.) two-phase spectral decomposition of the sample altered for 9 hours.

Table 7.7: Raman spectral peak fit results

sample	point	ACP peak at 949.85 Δcm^{-1} (100% Gauss)			Apatite peak 958Δcm^{-1}				Amp^{948}/Amp^{958} *1
		Peak Center [cm^{-1}]	Peak FWHM [cm^{-1}]	Peak Amplitude [rel.int.]	Peak Center [cm^{-1}]	Peak FWHM [cm^{-1}]	Peak Amplitude [rel.int.]	%Gauss	[as % ACP]
0min	1	949.4(1)	30.3(5)	/	-	-	-	-	100
	2	948.8(3)	31(1)	/	-	-	-	-	100
	3	949.1(1)	29.9(5)	/	-	-	-	-	100
1h	1	949.7(1)	29.6(4)	/	-	-	-	-	100
	2	948.82(9)	30.0(4)	/	-	-	-	-	100
	3	949.7(1)	29.5(4)	/	-	-	-	-	100
1.5h	1	948.9(2)	29.4(6)	/	-	-	-	-	100*2
	2	950.4(7)	30(2)	/	-	-	-	-	100*2
	3	949.85(9)	29.7(4)	/	-	-	-	-	100*2
2h	1	949.85	32(3)	796(88)	957.8(5)	20.3(7)	857(134)	0.98(11)	48(10)
	2	949.85	30(2)	808(140)	957.6(1)	18.4(6)	781(34)	0.56(1)	50(9)
	3	949.85	31(4)	787(60)	958.3(4)	20(1)	874(216)	1.0(1)	47(14)
3h	1	949.85	26(7)	706(67)	958.2(6)	18.4(6)	1364(49)	1.0(1)	34(7)
	2	949.85	30(5)	753(137)	957.9(2)	18.3(4)	1724(47)	0.87(9)	30(13)
	3	949.85	26(3)	1722(305)	959.05(9)	17.1(4)	3875(127)	0.80(5)	30(13)
9h	1	949.85	22(2)	893(39)	958.78(11)	14.9(4)	2558(40)	0.91(7)	26(3)
	2	949.85	25(5)	1058(155)	958.9(2)	17.1(3)	3094(73)	1.00(7)	26(11)
	3	949.85	23(4)	990(102)	958.1(1)	15.2(3)	2466(50)	1.00(6)	28.6(7.5)

*1 $A^{949}*100/(A^{949}+A^{958})$

*2 – XRD results show a small fraction of nanocrystalline phase present in the sample. However, the fitting of Raman spectra with the apatite peak did not converge to produce a satisfactory fit, so only a single amorphous phase was fit.

7.3.5 Electron microscope imaging

SEM secondary electron images show different stages of the amorphous-to-nanocrystalline carbonated apatite phase transformation (Fig.7.14). The surface of the sample of the amorphous phase show formations of agglomerates with apparent spherical particles or grains (Fig. 7.14a). The surface of the sample treated for time duration of 90minutes shows slightly modified surface features with respect to the amorphous sample (Fig.7.14b). For this sample the Rietveld analysis provides an estimate of 87% amorphous phase fraction. More developed topology of the surface is visible on samples with longer exposure to water (Fig.7.14 c and d). In these sample it appears that a network of pillar-like structures has been formed. Repeated point scans on multiple spots, however, do show surface feature variations with more and less pillar-network like character.

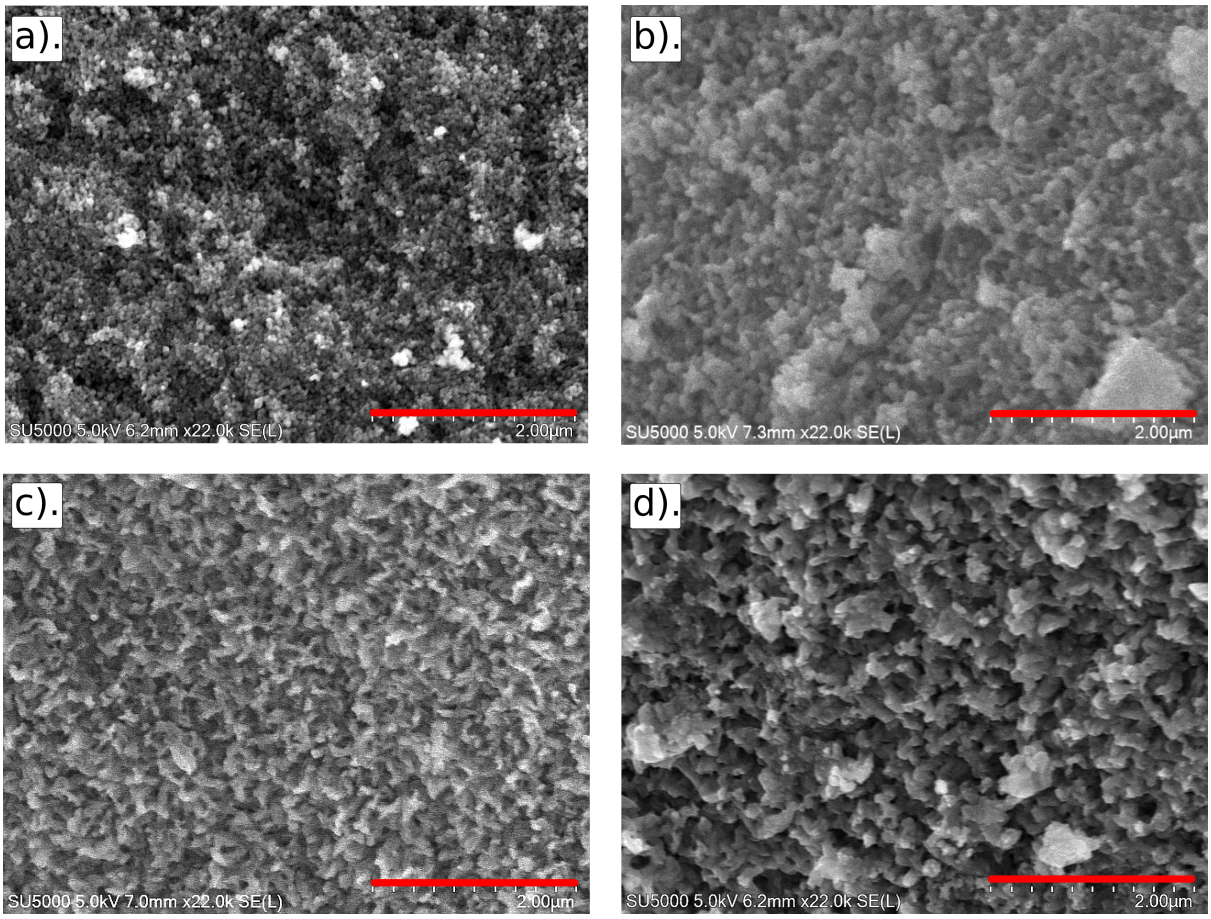

Figure 7.14: Back-scattered electron SEM images of the amorphous-to-nanocrystalline carbonated apatite transformation. a.) Dry ACP starting material; b.) sample of 90 minutes long treatment duration; c.) 2 hours long sample treatment time duration; d.) 9 hour long sample treatment time duration. Carbon coating was used for all samples. All images were taken with the same magnification, enabling direct visual comparison of sizes.

7.4 Conclusion

From the presented results of the diffraction and spectroscopic studies it can be concluded that the obtained product of the post-processing of ACP at approximated body temperature and water medium shows a gradual transformation of the initial amorphous state into a nanocrystalline carbonated calcium-phosphate apatite structure. The presence of the hydroxyl group can be identified, but only in samples that have substantial amount of the nanocrystalline phase. An approach with multiphase model was used in the refinements and fit, where the fraction of ACP was determined using multiple analytic techniques. The ACP and nanocrystalline carbonated apatite phase fractions obtained in the sequence of post-processing time of the ACP powder are compared in Table7.8.

Table 7.8: Comparison of ACP fraction of result obtained with various measurement techniques and evaluation methods

Sample	XRPD [wt% of ACP]	PDF [scale ratio % of ACP]	Raman [Amp^{948}/Amp^{95}]
0min	100	100	100
1h	100	100	100
1.5h	87(3)	78	100
2h	49(2)	51	47(14) – 50(9)
3h	30.4(1.6)	30	30(13) – 34(7)
9h	19.3(1.6)	17	26(3)– 28.6(7.5)

Discussion on the applied diffraction methods

Analysis of the "XRD-amorphous" diffraction patterns is not the typical application for the Rietveld method as it yields information about the average state of crystalline materials. In the evaluation of the diffraction patterns an assumption was made that the short range order of the ACP does not change, furthermore, it was approximated that this short range order can be modelled with the unit cell structure of the HAP. These approximations allowed in all the used analytic techniques to obtain a quantitative estimate for the phase fraction of ACP in the series of amorphous-to-nanocrystalline apatite transformation. However, questions regarding the simultaneous occurrence of the crystalline domain growth and speculated internal rearrangement of atoms that results in a structural change from short-to-long range order remains unsolved in this case.

During the amorphous-to-nanocrystalline apatite transformation the presence of coherently diffracting crystalline domains increases. Moreover, in addition to the growing number of domains the long range order inside the domains increases. The first appearance of the crystallization nuclei (coherently diffracting domains) should be, in principle, measurable given that there is a significant number of domains, enough to produce signal that overcomes the noise level of the detection. It is also conceivable that the amorphous phase undergoes a transformation itself before the first nucleation event becomes energetically favourable (even in heterogeneous nucleation case). Although, only coherently scattering domains can yield Bragg peaks, domains in the size range comparable to the unit cell (reference unit cell of HAP), should not be excluded from the hypothesis about the early stages of the crystallization process.

The Rietveld refinement optimizes the crystallographic structure of a given crystallographic model. Diffuse scattering that comes form the short range order such

as the ACP for example is treated as signal that contributes to the background signal and it is in general not interpreted for structural information. In Rietveld refinement code such as the GSAS, it is possible to handle amorphous phase contribution as part of background signal using the Debye equation. This allows a more meaningful treatment of cases where, for example, the signal from a glass capillary sample container needs to be exactly addressed. In the case of the calcium-phosphate a significant number of inter-atomic distances would be needed to accurately model contribution from an amorphous phase.

In the case of the samples that clearly show broad Bragg peaks a single phase model did not give a satisfactory agreement with the observed diffraction and PDF patterns. One-phase refinements have been unable to yield better refinement in comparison to two-phase fit. On the other hand, the two-phase refinement approach reveals the amorphous phase fraction trend in the data. In addition, the Rietveld method yielded reasonable values for anisotropic crystallite sizes of the nanocrystalline phase allowing the description of the domain growth induced by the increasing treatment time. In the presented case the Rietveld method can not give accurate atomic positions, Debye-Waller factors, and occupancy values of the nanocrystalline calcium-phosphate, nor in general for nanocrystalline materials with high number of structural degrees of freedom, as the Bragg peaks are severely broadened and overlapping. These same considerations limit the high quality data obtained from a synchrotron source as well. Given adequate capabilities in instrumental measurement and data transformation, the PDF analysis can yield information about inter-atomic distances. Interpretation of the PDF function, however, demonstrates the complexity of the ACP-to-nanocrystalline carbonated-apatite transformation. The shortcomings of the applied method are that anisotropic size interpretation is not included in the "PDFGui", as it only incorporates a spherical domain diameter parameter (according to the theoretical framework of the applied software approach).

On a summary plot (in Fig.7.15), diffraction patterns illustrate the transition from the amorphous to the long-range ordered apatite phase. Fit of the PDF and diffraction pattern show the validity of the HAP and also the two-phase model in the synthetic bone analogous materials following the presented synthesis route.

Considering the evidence of the amorphous phase fraction depletion and the growth of the nanocrystallites during the amorphous-to-nano-crystalline carbonated apatite transformation, it is concluded that the experiment resulted in favour of a dissolution-reprecipitation mechanism.

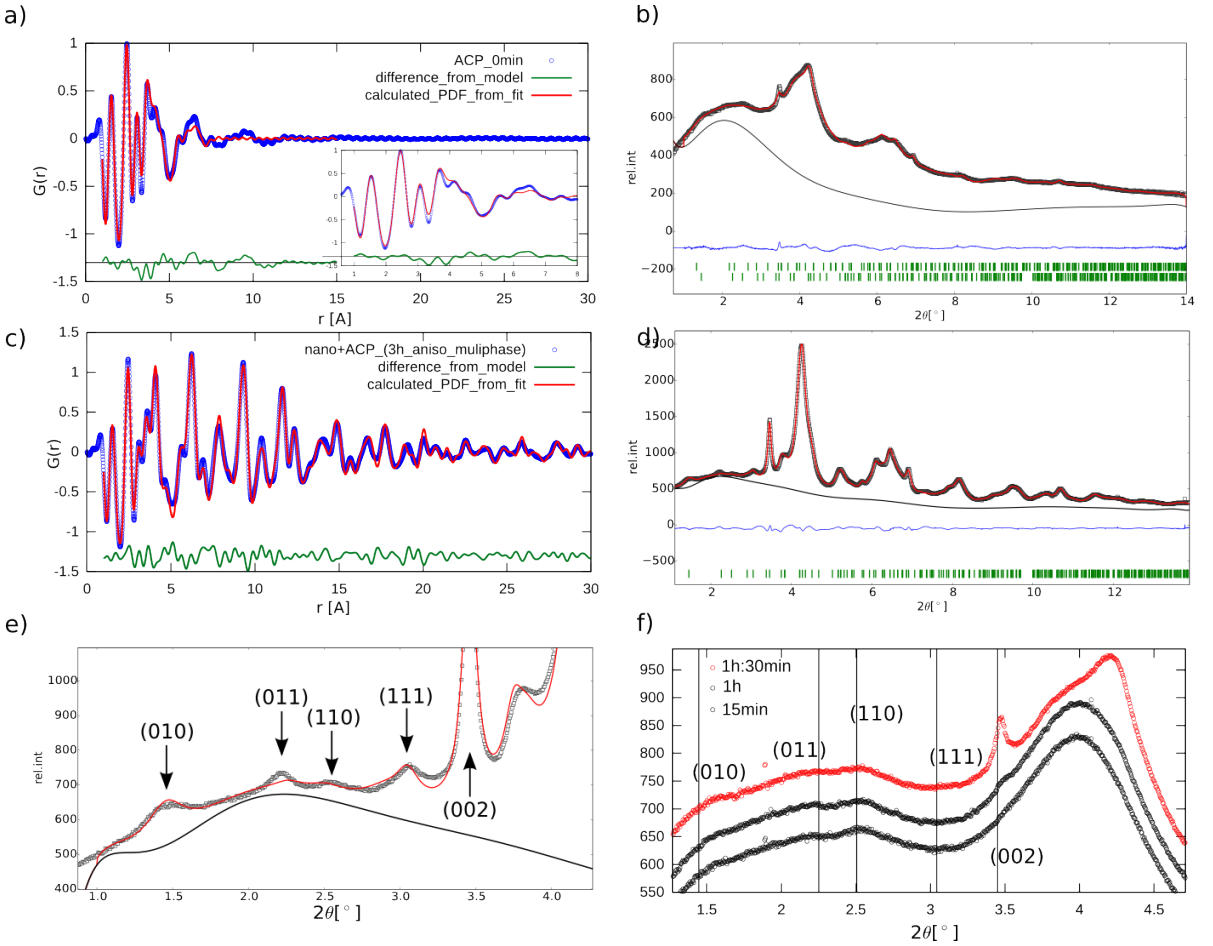

Figure 7.15: Diffraction data analysis with PDF fit and Rietveld refinement a.) PDF plot of the amorphous phase and fit; the inset plot show the region of 1-8Å where it is shown that the first peaks are fit fully, while the rest of the peaks are not matched with the same accuracy. b.) Rietveld refinement of the sample with 1hr. 30minutes treatment duration, where the major phase is amorphous. Bragg peaks appear for the nanocrystalline phase, c.) PDF fit of the nanocrystalline phase (sample with 3h treatment duration) and the corresponding Rietveld refinement on plot d. e.) magnification of the Rietveld refinement region showing the first Bragg reflections. f.) comparison of samples containing the amorphous phase. Positions of Bragg reflections of the hexagonal apatite structure are marked. The pattern on top corresponds to the sample of 1hr. 30minutes treatment duration; the bottom patterns show the pure amorphous phase, for which the PDF is shown on plot a.

Mechanism ACP-to-nanocrystalline carbonated apatite transformation

The results suggest that in the presented experimental design, it is reasonable to deduce that the nucleation takes place on the surface of the initial ACP flakes and the mechanism for the crystallite growth is according to the model of dissolution and precipitation. The measurable crystallization process occurs after a specific time upon

the contact with water (in the case of dry ACP powder starting material).

However, fit of the G(r) function shows the distortion of the phosphate tetrahedra, as well as the significant alteration of inter-atomic distances in the 5-6Å range (Fig.7.8). Ca-Ca bond lengths are in this inter-atomic distance region. The PDF analysis results show appearance and increasing G(r) peaks growing in relative amplitude in the region between 5Å and 6Å. Although quantitative examination of these longer inter-atomic distances is problematic, it can be still inferred that during the amorphous-to-nanocrystalline transformation the nanocrystalline carbonated-apatite phase might have a different structure shortly after the nucleation, and at longer exposure times to water medium. This observation leads to the conclusion that there might be more than one mechanism acting during the phase transformation in the presented post-processing experiment (both a dissolution-reprecipitation and internal rearrangement mechanism).

P-O distances

The fit of the G(r) function as well as the FTIR data shows that the phosphate tetrahedra appears to be more symmetric in the amorphous phase. The result show that the center-to-vertice distances in the phosphate tetrahedra become increasingly different for each P-O distance as the phosphate tetrahedra becomes more distorted (Fig.7.10). Quantitative results from the PDF fit could not fully confirm the expected structural symmetry break of the phosphate tetrahedra. On the other hand, FTIR shows that the ν_1 and ν_2 IR-inactive bands in the totally symmetric tetrahedra appeare in the spectra as a result of the lowering of the point symmetry due to the development of the nanocrystalline domains. Causes of the tetrahedral distortion are primarily the Ca^{+} ion vicinity, as the increase of the long range order seemingly favours the distortion of the tetrahedral unit. This conclusion allows the claim that the long range order grows on the expense of the local point group symmetry of the phosphate rigid-body unit.

Presence of structural carbonate

FTIR spectra of all samples of the amorphous-to-nanocrystalline apatite phase transformation show peaks that are usually assigned to carbonate in the apatite structure (Table1.1 Fig.7.11). For a low percentage of carbonate, which can occupy both the PO_4^{3-} site as well as the OH^{-} site the in the structure is difficult to identify by diffraction methods (Rietveld and PDF analysis) even in cases of favourable crystallite size and high quality diffraction measurements (high photon flux of a synchrotron facility) primarily due to the low scattering power of carbon atoms.

The incorporated structural carbonate measured in these experiments originates presumably from the water used in the synthesis process, which is considered equilibrated with the atmosphere. The dissolved carbonate in water is

assumed to be the most likely source of the carbonate that is incorporated in the apatite structure, as it was identified already at the early stage of the nanocrystalline phase formation. From the FTIR spectra the incorporation of carbonate in the synthetic ACP appears to be significant even though it is expected that the carbonate of the de-ionized water is low. It is speculated that the synthesis process that circulates larger amount of water would lead to concentrating effect of the carbonate amount in the final product. Uptake of carbonate from the air is plausible and in any case rises the question if carbonate free ACP and nanocrystalline calcium-phosphate apatite structure is even possible.

Hydroxylation

Vibrational spectroscopy results reveal an apparent contradiction in the measurements for the bands of the OH^- stretching modes. The characteristic bands of the hydroxylapatite structure are absent in the FTIR spectra of the nanocrystalline apatite containing sample, while Raman spectra shows clear presence of this band in the same samples. In Raman spectra the OH^- band is clearly distinguishable, and it appears already in the sample treated for 2 hours duration, and increases with treatment duration time. In the FTIR spectra the band is practically absent (Fig.7.11 c. and d.). Only in the case of the longest treatment duration (9 hours) the FTIR spectrum show only a very weak hint to an OH^- band.

In the case of the Raman measurements certain degree of induced structural changes of the material might be present presumably due to Raman laser light interaction with the sample during measurement. The apparent OH^- stretching modes in the Raman spectra could also be assigned to artefacts of the measurement rather than to intrinsic property of the material. The FTIR does not show neither the OH^- stretching nor the OH^- librational band. However, the FTIR does have a broad band about the same position where an OH^- libration should be centred. According to literature this broad band is assigned to HPO_4^{2-}.

It is speculated that this difference in the resolvability of the OH^- peak between the two spectroscopic techniques lies in the fact that FTIR yields information about the bulk properties of the material (via absorbance), while the Raman microscopy can be considered more bound to the surface of the sample, as the penetration of exciting photons is limited by the attenuation.

Based on the outlined considerations it can be hypothesised that the amorphous-to-nanocrystalline apatite transition starts on the surface of the amorphous agglomerates of the ACP, and progresses towards the inner region. The surface layer of the nanocrystalline domains is more hydroxylapatite alike, as the Raman signal shows clearly stronger OH^- band, while the bulk of the samples is more amorphous, as the FTIR shows the average of both the amorphous and nano-phase.

In other systems the influence of the laser can also be recognized as a source

for photo-catalytic reactions. It is also possible that the laser energy transforms the structural water by splitting the water molecules and inducing OH^- ion formation that is then measurable by Raman. Test measurement on the impact of exposure to the Raman laser have been made, but this effect has not been studied systematically. Leaving the material under the Raman laser light for several minutes before the acquisition increases the measured OH^- band signal. The state of measured spectrum returns to its initial state after the laser was turned off and the material was left not irradiated for a while. It is also known that the heat generated by the laser can affect the surface of heat-sensitive materials, which can induce retrievable, or permanent alteration at the measured spot under Raman microscopy. Whether the heat transfer or some photo-catalytic reaction induces the observed peak appearance remains unexplored in the frame of this thesis.

Scanning electron microscopy images

Imaging of the samples using back-scattered electron scanning electron microscopy shows a gradual change in the surface features of the samples. Samples of with the ACP material appear as agglomerates resembling spherical formations, while the longer post-processed samples with nanocrystalline apatite phase show more feature rich surface apparently shaped as a network of pillar-like agglomerates. The SEM images can confirm the overall differentiation of the surface and surface feature size increase. This is in concordance with the proposed phase transformation mechanism.

Synthesis parameters

Synthesis-, and post-processing parameters such as the physical mixing and stirring, drying method and water removal speed clearly have an influence on the end-product. Stirring leads to increased mobility of ions and increased mass transport from the dissolving and unto the growing surface. The turbulent environment may lead to crystallite morphology preference of isotropic over irregular crystallite shapes. During the drying process the concentration of the dissolved atoms is constantly changing as the water amount is decreasing. The dilution of the ACP powder in water during the post-processing may be a factor that can influence the amorphous-to-nanocrystalline apatite transformation and crystallite morphology of the end product.

Influence of the mentioned synthesis parameters was not explored in the experiments conducted in the frame of the thesis due to time and materials reasons. Further in-situ synchrotron measurement with several dilution stages would give insight into the extent of the kinetics of the transformation.

Outlook

Studies that incorporate theoretical description for the crystallite size distribution in combination with microstructural analysis using the pair distribution function (G(r)) are currently missing in the literature of calcium-phosphate apatite. Structural-chemical complexity and microstructural diversity (crystallite size and shape distribution) are not yet adequately explored from a theoretical modelling point of view, specially in the case of the calcium-phosphate apatite systems. Extension of the current understanding of the calcium-phosphate system with broader theoretical concepts is required, as the interpretation of the measured diffraction and spectroscopic data, as well as ab-initio calculations tend to provide limited explanations. Furthermore, the interpretation of the crystallographic microstrain with regard to the nano sized crystallites of calcium-phosphate apatite, where the surface-to-bulk ratio is near one, could represent the next research challenge.

Chapter 8 Conclusion and Outlook

8.1 Summary of results

The scope of the presented work in this thesis covers the system of carbonated calcium-phosphate apatite in the context of biological mineral formation in the bone material. Investigated topics range from observation of natural occurrence of nanocrystalline formations in bone samples, bone material alteration experiments, geological reference samples, as well as synthetic calcium-phosphate apatite obtained by phase transformation of the amorphous state ACP. A research focus also aimed at environmentally altered bone material by the soil conditions. In order to understand the alterations, natural bone has been included into the research as the starting reference material for the laboratory experiments. Controlled alteration experiments on the bone material were designed in order to compare structural modifications with the bone material that was exposed to geological and soil conditions. This research thread required to include geological hydroxylapatite and other geological samples next to the biomineralized sample of bone material in the comparison. As an ultimate task, a complete recreation of the various states of the apatite (chemical-structural and crystallographic) was attempted in the synthesis experiment, that had the aim to address questions of the nanocrystalline apatite formation under controlled laboratory conditions and its quantitative characterization.

In the previous chapters, details of the characterization of nano-crystalline calcium-phosphate of the bone and bone-analogous materials have been outlined by applying multiple characterization techniques and methods (diffraction analysis with Rietveld, PDF, WPPM methods, vibrational spectroscopy evaluation, electron microscopy).

Microstructural analysis of the diffraction profile of bone sample measurements using the Rietveld method have been tackled with the anisotropic size model, which gave good refinement fits and reasonable values for crystallite size (Chapter 2 and Chapter 3). Furthermore, when microstrain is included in the evaluation, the results show that there is no or only very minor microstrain component contributing to the diffraction profile peak broadening. The origin or the cause for low microstrain in some samples can be due to the incorporation of carbonate anions of both A-, and B-type, as well as the presence of OH^- in the the samples that resemble hydroxylapatite.

In Chapter 3 the automation code for the Rietveld refinement was described and the application was demonstrated on samples of bone material using several crystallographic models of calcium-phosphate apatites (hexagonal and monoclinic

structure). Refinement strategies and parameter sequence for each crystallographic model have been systematically compared using the "AlgoRun" code. The capabilities of automated Rietveld refinement were demonstrated not only on comparison of crystallographic structure hypotheses and refinement strategy optimization, but also on multiple samples of nanocrystalline bone material.

In Chapter 4 bone material altered by environmental soil conditions was investigated in the frame of archaeological context. Only apatite and calcite were identified in bones that were selected and cleaned according to described protocols. Sources of calcite can be from the soil or resulting from diverse soil conditions. Evidence for this can be the sub-micron size of the calcite crystallites and their rhombohedral morphology in SEM. In the investigated bone samples in the archaeological context there was no evidence found for other phosphate minerals such as brushite or whitlockite. Furthermore, the samples have been evaluated against correlation between structural parameters as well. Weak correlations have been identified, however, causality between parameters and archaeological context could not be proved in the scope of the research effort.

Diffraction and spectroscopic evaluation of various geological apatite and non-apatite samples (in Chapter 5) reveals that hydroxylapatite or fluorapatite of geological origin can not be used as analogues for the biologically generated nanocrystalline carbonated-apatite. Firstly, due to the difference in crystalline state (nanocrystalline bone and crystalline geological minerals), secondly due to the anion incorporation state in the anionic column (A-B-type CO_3^{2-} in bone and F^-,Cl^-, OH^- balance in geological mineral samples).

Moreover, according to the evaluation of natural bone samples, altered bone samples, geological and synthetic carbonate-apatite, it is evident that the bone apatite is not hydroxylapatite, but rather carbonated calcium-phosphate apatite and not carbonated hydroxylapatite. This conclusion is drawn from the fact that in the natural bone the FTIR spectra do not show the characteristic OH^- band, while experimentally altered bone material by annealing at high temperature does produce proper hydroxylapatite.

Experimentally altered bone material

In the bone material alteration experiments (Chapter 6), the crystal-chemical structural changes have been examined under annealing (induced by heat treatment), and hydrothermal conditions.

In experiments of bone material annealing a simple linear model was derived that can be used to predict annealing (cremation) temperature from the crystallographic para-meters obtained from Rietveld refinement. This result can have an application in archaeological or forensic fields, where the burning degree of bone material needs to be estimated. From the state of the burned bone material the

archaeological material context can be estimated.

The aim of the hydrothermal bone alteration experiment series was to observe the changes due to ageing of the material in wet condition. The results show that even under moderate temperatures (130°C) the material does change to hydroxylapatite. This reveals that the heat energy itself is not the source, or the cause, of the transformation of the bone material carbonate-apatite into hydroxylapatite.

Synthetic bone material analogues

Results of the synthetic amorphous-to-nanocrystalline carbonate-apatite transformation experiments show a gradual change of the short range order toward long range order. The appearance of the Bragg peaks and the growth of the nanocrystalline apatite phase was tracked by microstructural analysis in the Rietveld method. The PDF analysis show the change of the P-O inter-atomic distances and the morphing of the phosphate tetrahedra (center-to-vertex distance variation). However, results consistent with expected behaviour show disagreement (see Fig.7.10).

Vibrational spectroscopy measurements of the synthetic apatite samples obtained from the transformation of the ACP show presence of carbonate in the apatite structure. Carbonate bands have been identified using FTIR spectroscopy. It is speculated that the used ACP synthesis process can act as a trap for atmospheric CO_2 which is consequently incorporated into the carbonate-calcium-phosphate apatite structure.

Furthermore, as expected, samples of nanocrystalline carbonated-apatite do not show FTIR characteristic fingerprint bands for the OH^-, however, the spectral traces of Raman measurements clearly show the characteristic OH^- bands. It was discussed in section 7.3.5, that the cause of the disagreement between the results of the two applied vibrational spectroscopy techniques might be related to measurement artefacts. The influence of the laser power and the sample material interaction was not studied systematically in the scope of this thesis. However, an illustration of the effect is given in Fig.8.1 on the sample of annealed bone material, where the sample treatment altered the colour of the sample surface to black, so the laser interaction with the sample became optically visible.

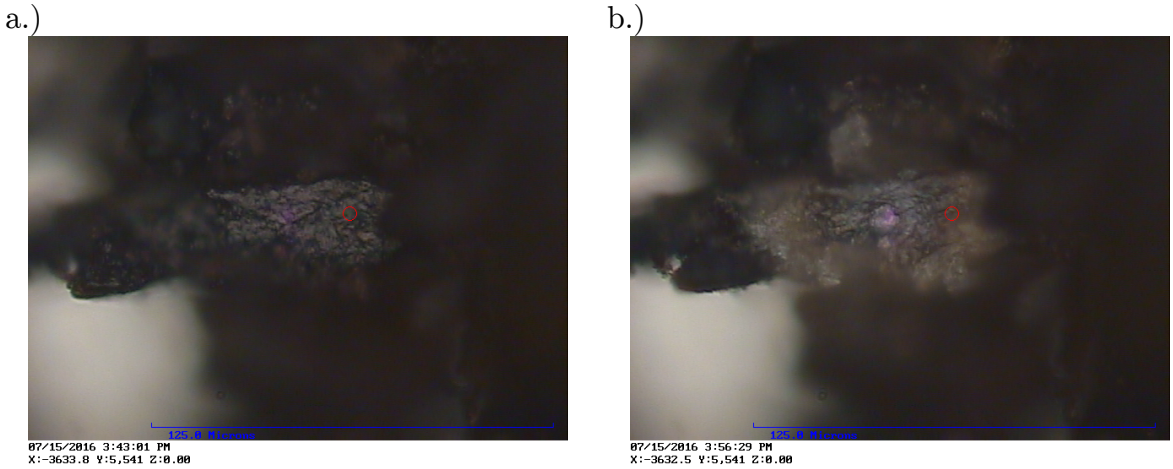

Figure 8.1: Optical microscope image of the Raman laser sample surface impact demonstrated on a sample of annealed bone material treated at 400°C, hence the black colour of the samples surface. a.) the sample surface before the Raman measurement; b.) after the Raman spectra acquisition. The impact of the laser spot is visible as the white ring.

Crystallite size anisotropy and microstrain

Some of the limitation of microstructural analysis using diffraction methods for the particular case of bone nanocrystallites have been addressed by author Kohn et al. arguing that the anisotropic crystal morphology can cause that the smaller domains have dominant influence on the broadening of the diffraction patterns shadowing the contribution of bigger (or even a distribution of) domains, making the evaluation intrinsically flawed (Kohn et al., 2002 p433).

In Chapter 6, the Rietveld refinement results suggest that only the size broadening can be interpreted meaningfully. The strain contribution does not fulfil the theoretical description and it is not valid in the examined cases. However, this limitation does not mean that there are no microstrain causing sources present in the system. It is only a sign that current interpretations are unable to fully explain the observations.

The meaning of microstrain in the context of the bone biomineral diffraction pattern evaluation remains unclear. In the evaluation of diffraction patterns using the Rietveld method the microstrain is included to contribute to the Bragg-peak broadening factor, as a function of the scattering vector. In the case of the nanocrystallites, where the finite size effect has to be included as a major source of broadening, the incorporation of microstrain as an isotropic model yields uncontrolled and non-physical values (as in the case of the hydrothermal bone alteration experiment series – see Fig.6.3). Constrained refinement of the microstrain

with the apparent crystallite size would require theoretical justification.

In Chapter 7 the transformation of ACP to nanocrystalline HAP showed that even small amounts of amorphous weight fractions can be identified. The phase fractions have been cross-checked with a combination of evaluation methods and measuring techniques. It appears that carbonate incorporation can be shown already at the precursor level (ACP), although, this aspect was investigated by vibrational spectroscopy only. The nanocrystallites of carbonated calcium-phosphate apatite and natural bone material can appear remarkably similar (Fig.8.2). Spectroscopic comparison of the same samples is shown in Fig.8.3.

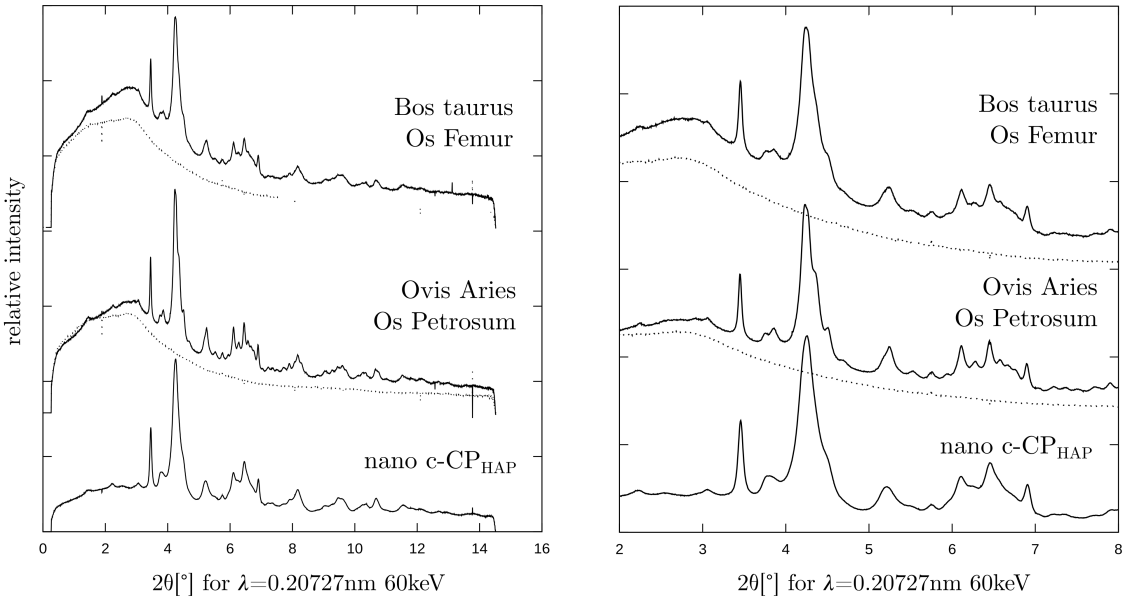

Figure 8.2: Comparison of powdered bone material of two species and skeletal elements (*bos taurus* – os femur, *ovis aries* – os petrosum) with the nanocrystalline carbonate-apatite synthesized as the post-processing of ACP in wet conditions. The synthetic sample that has undergone the transformation from ACP to nanocrystalline carbonated calcium-phosphate shows diffraction pattern features that resemble very closely the diffraction patterns of the natural bone samples. On the left, the whole region of the diffraction pattern are shown (0°-14°); on the right, magnified region from 2° - 8° degrees of 2theta.

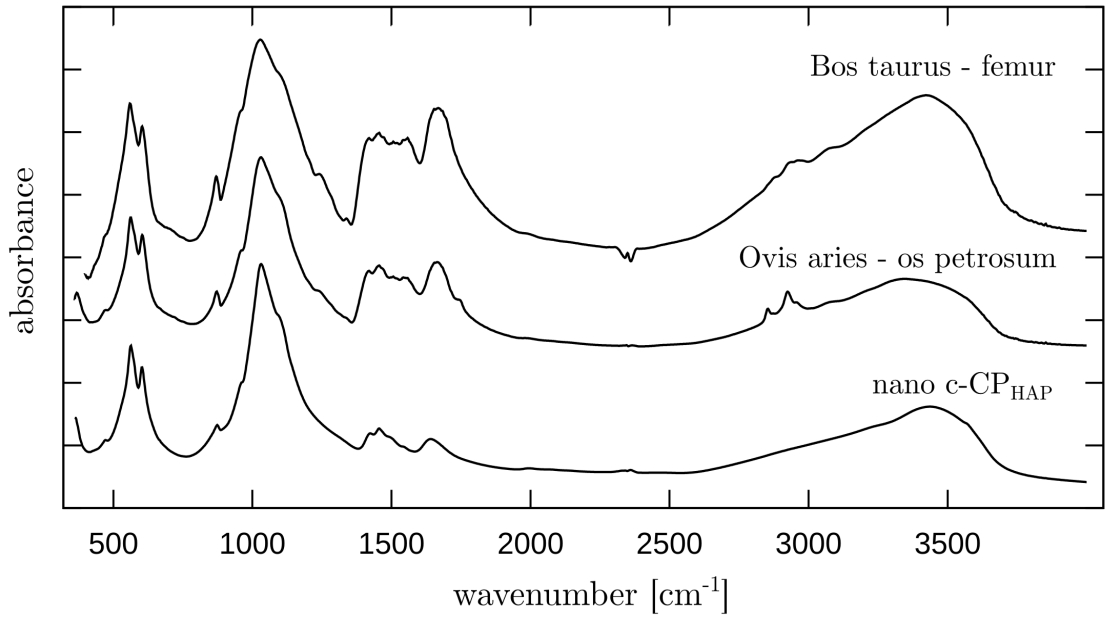

Figure 8.3: Comparison of FTIR spectra of bone material samples of two species (*bos taurus* - femur skeletal element and *ovis aries* – os petrosum skeletal element) with bone-analogous synthetic material of nanocrystalline carbonate-apatite obtained from post-processing of ACP as described in the experiment in Chapter 7. The overall spectral trace features of the three samples are very similar – there are no significant spectral trace (peak or shouldering) differences between natural and synthetic nano-crystalline carbonated apatite.

Sampling of bone material

Overall results confirm that in general the size of the crystallites depends both on species and on skeletal elements in question. Examination of powdered sample material suggests that the approach of mechanical averaging of the hierarchically structured material of bone might influence the outcome of the evaluation in the case when the whole skeletal element is completely crushed and pulverized. Extracting the material from its original environment may introduce alterations that can lead to significantly different understanding of the material. Sampling bone material of complete skeletal elements at different anatomical points can also have an influence on the interpretation of the measurement results. This might be due to structural differences between the segments of a single skeletal element as the bone material composition and state might vary due to differences in mechanical load bearing or other functionality variations in the skeletal system.

8.2 Concluding discussion

Even though theoretical concepts of size distribution, nanocrystallite shape anisotropy and microstrain integration in data evaluation software is in the constant research focus, a readily available solution for the analysis of the complex systems such as the biological nanaocrystalline calcium-phosphate in the bone material was not found during the research covered in this thesis. Although some solutions exist, such as the WPPM fitting in "pm2k" software (Appendix A3, p197) the obtained results are somewhat perplexing.

Further development of XRPD measurements evaluation software is necessary that can extend beyond the ideal crystallographic approximation. Summary of probabilistic statistical and maximum entropy methods in the evaluation of diffraction patterns have been discussed by Gilmore (Gilmore, 1996). An alternative evaluation approach to diffraction patterns based on Bayesian statistics has been described by Sivia and David, (1994), Armstrong et al., (2004) and Fancher et al., (2016).

The question of the relation between the nano-meter scale apatite crystallites and the metabolic (physiologic) processes remains unclear. From microscopy observations it is known that the crystallites are placed in-between the collagen fibrils in a steric model (Alexander et al., 2012). Cause-and-effect-relation between the type of the interwoven structure and the size of the crystallites is also put into question: are the nanocrystallites limited by the physical compartment that is between the fibrils (Boonrungsiman et al., 2012), or is there a physical-chemical limitation that does not allow the growth of the crystallites to larger sizes? The shape of the crystallite can also be influenced by protein interaction with the inorganic material due to electrostatic charge configurations. In the case when the unit cell in the nanocrystalline domain stack along the a preferred orientation along a(b) axis, plate-like crystallites are hypothesised. In this case the channel positions are exposed with more OH^- ions on the flat surface of the platelet. Protein interaction with the inorganic phase can be significantly different upon contact with such crystallite surfaces. The protein (and collagen) interaction might be substantially different in the case of needle-like crystalline domains, where unit cells are stacked along the c-axis.

The bone, as an organ, also serves as an ion reservoir that can dissolve Ca^+ in metabolic regulation processes, as well as to deposits other ions ("bone-seeking" elements) into the bone material. Through the process of constant bone-remodelling the nanocrystallites have to be in the state to easily dissolve and recrystallise in a dynamic manner. Therefore, a static and strictly deterministic structural interpretation might not be adequate to completely describe the structural stability

of the nanocrystalline phase inside the living organism. Understanding of the relation between the size of the calcium-phosphate apatite nanocrystallites in bone and the ionic substitutions in the crystallographic structure would imply a model for a design of nanocrystalline apatite material with tailored properties that can be potentially vital for biomedical applications. Insight on the contributing factors for dissolution rates in the mechanism of dissolution and re-precipitation could have high impact of the applicability of in calcium-phosphates carbonate-apatite.

Characterisation of isostructural, or phase mixture of nanocrystalline and amorphous phases with identical chemical composition can be challenging in the case of natural bone as well as in synthetic samples. Therefore, careful evaluation and characterisation of synthesis products is highly relevant for adequate interpretation of experimental results.

8.3 Outlook and future research perspectives

Data evaluation process automation

Desired rigour and systematic comparison of crystallographic models could be achieved through automation of the evaluation and hypothesis testing. Introduction of grid-search, hyperparameters and alternative structure optimization algorithms concurrent to the least-square method (Bayesian methods references above) could potentially reduce systematic errors.

Evaluation of spectroscopic measurements through the approach of peak fitting greatly depends on the applied restraints in the non-linear least squares data fitting process. Statistical evaluation of the spectral decomposition results requires methods that can compare and test various initial models and starting conditions. Estimation of the standard error of the fit parameters would be more meaningful following such an approach. Furthermore, such a computational infrastructure could potentially facilitate implementation of Bayesian statistics enhancing the data evaluation quality.

Conducting research in a concise way with interconnected tools that can interact with each other had been proposed by Juhás and Billinge. Their software framework offers a solution that combines experimental techniques with theoretical modelling methods enabling multifaceted investigation (Juhás et al., 2015). Other innovative use of existing method combinations have been also reported, such as the use of the pair distribution function analysis as a computer tomography based technique (Jacques et al., 2013). Previous efforts of the Billinge group to automatise the transformation of the data into the pair distribution function made possible its incorporation into other software solutions. Other PDF modelling solutions include

Monte Carlo simulation that incorporates actual measured data in an iterative process - EPSR (empirical potential structure refinement) ("ISIS Empirical Potential Structure Refinement"; Soper, 2005, 1996). In this case the material is modelled as an ensemble of different domain properties, and software package DISCUS (Neder and Proffen, 2008) for nano sized domain simulation with calculated pair distribution function.

References

Adler, H., 1964. Infrared spectra of phosphate minerals: Symmetry and substitutional effects in the pyromorphite series. Am. Mineral. 49.

Aizawa, M., Matsuura, T., Zhuang, Z., 2013. Syntheses of Single-Crystal Apatite Particles with Preferred Orientation to the a- and c-Axes as Models of Hard Tissue and Their Applications. Biol. Pharm. Bull. 36, 1654–1661. https://doi.org/10.1248/bpb.b13-00439

Alexander, B., Daulton, T.L., Genin, G.M., Lipner, J., Pasteris, J.D., Wopenka, B., Thomopoulos, S., 2012. The nanometre-scale physiology of bone: steric modelling and scanning transmission electron microscopy of collagen–mineral structure. J. R. Soc. Interface 9, 1774–1786. https://doi.org/10.1098/rsif.2011.0880

Antonakos, A., Liarokapis, E., Leventouri, T., 2007. Micro-Raman and FTIR studies of synthetic and natural apatites. Biomaterials 28, 3043–3054. https://doi.org/10.1016/j.biomaterials.2007.02.028

Arellano-Jiménez, M.J., García-García, R., Reyes-Gasga, J., 2009. Synthesis and hydrolysis of octacalcium phosphate and its characterization by electron microscopy and X-ray diffraction. J. Phys. Chem. Solids 70, 390–395. https://doi.org/10.1016/j.jpcs.2008.11.001

Armstrong, N., Kalceff, W., Cline, J.P., Bonevich, J., 2004. Bayesian Inference of Nanoparticle-Broadened X-Ray Line Profiles. J. Res. Natl. Inst. Stand. Technol. 109, 155–178.

Arora, A.K., Rajalakshmi, M., Ravindran, T.R., Sivasubramanian, V., 2007. Raman spectroscopy of optical phonon confinement in nanostructured materials. J. Raman Spectrosc. 38, 604–617. https://doi.org/10.1002/jrs.1684

Audebrand, N., Louër, D., 2004. The Microstructure of Nanocrystalline Powders from Line Profile Analysis. Mater. Sci. Forum 443–444, 71–76. https://doi.org/10.4028/www.scientific.net/MSF.443-444.71

Awonusi, A., Morris, M.D., Tecklenburg, M.M.J., 2007. Carbonate Assignment and Calibration in the Raman Spectrum of Apatite. Calcif. Tissue Int. 81, 46–52. https://doi.org/10.1007/s00223-007-9034-0

Bächinger, H.P., Morris, N.P., Davis, J.M., 1993. Thermal stability and folding of the collagen triple helix and the effects of mutations in osteogenesis imperfecta on the triple helix of type I collagen. Am. J. Med. Genet. 45, 152–162. https://doi.org/10.1002/ajmg.1320450204

Baig, A.A., Fox, J.L., Young, R.A., Wang, Z., Hsu, J., Higuchi, W.I., Chhettry, A., Zhuang, H., Otsuka, M., 1999. Relationships Among Carbonated Apatite Solubility, Crystallite Size, and Microstrain Parameters. Calcif. Tissue Int. 64, 437–449. https://doi.org/10.1007/PL00005826

Balan, E., Delattre, S., Roche, D., Segalen, L., Morin, G., Guillaumet, M., Blanchard, M., Lazzeri, M., Brouder, C., Salje, E.K.H., 2010. Line-broadening effects in the powder infrared spectrum of apatite. Phys. Chem. Miner. 38, 111–122. https://doi.org/10.1007/s00269-010-0388-x

Baur, W.H., 1974. The geometry of polyhedral distortions. Predictive relationships for the phosphate group. Acta Crystallogr. B 30, 1195–1215. https://doi.org/10.1107/S0567740874004560

Beckett, S., 2011. Inter-species variation in bone mineral [WWW Document]. URL https://dspace.lib.cranfield.ac.uk/handle/1826/4912 (accessed 3.7.17).

Beckett, S., Rogers, K.D., Clement, J.G., 2011. Inter-species variation in bone mineral behavior upon heating. J. Forensic Sci. 56, 571–579. https://doi.org/10.1111/j.1556-4029.2010.01690.x

Berry, E.E., 1967. The structure and composition of some calcium-deficient apatites. J. Inorg. Nucl. Chem. 29, 317–327. https://doi.org/10.1016/0022-1902(67)80033-2

Bertazzo, S., Bertran, C.A., 2006. Crystallites Size and Changes in Mineral Phase of Bone with Age and Type of Bone. Key Eng. Mater. 309–311, 7–10. https://doi.org/10.4028/www.scientific.net/KEM.309-311.7

Betts, F., Blumenthal, N.C., Posner, A.S., Becker, G.L., Lechninger, A.L., 1975. Atomic Structure of Intracellular Amorphous Calcium Phosphate Deposits. PNAS 72, 2088–2090.

Betts, F., Posner, A.S., 1974. An X-ray radial distribution study of amorphous calcium phosphate. Mater. Res. Bull. 9, 353–360. https://doi.org/10.1016/0025-5408(74)90087-7

Bhat, S.S., Waghmare, U.V., Ramamurty, U., 2014. First-Principles Study of Structure, Vibrational, and Elastic Properties of Stoichiometric and Calcium-Deficient Hydroxyapatite. Cryst. Growth Des. 14, 3131–3141. https://doi.org/10.1021/cg5004269

Bigi, A., Ripamonti, A., Cojazzi, G., Gazzano, M., Roveri, N., 1990. Thermal conversion of octacalcium phosphate into hydroxyapatite. J. Inorg. Biochem. 40, 293–299. https://doi.org/10.1016/0162-0134(90)80063-4

Bolis, V., Busco, C., Martra, G., Bertinetti, L., Sakhno, Y., Ugliengo, P., Chiatti, F., Corno, M., Roveri, N., 2012. Coordination chemistry of Ca sites at the surface of nanosized hydroxyapatite: interaction with H2O and CO. Philos. Trans. R. Soc. Lond. Math. Phys. Eng. Sci. 370, 1313–1336. https://doi.org/10.1098/rsta.2011.0273

Boonrungsiman, S., Gentleman, E., Carzaniga, R., Evans, N.D., McComb, D.W., Porter, A.E., Stevens, M.M., 2012. The role of intracellular calcium phosphate in osteoblast-mediated bone apatite formation. Proc. Natl. Acad. Sci. U. S. A. 109, 14170–14175. https://doi.org/10.1073/pnas.1208916109

Borkiewicz, O., Rakovan, J., Cahill, C.L., 2010. Time-resolved in situ studies of apatite formation in aqueous solutions. Am. Mineral. 95, 1224–1236. https://doi.org/10.2138/am.2010.3168

Boskey, A.L., Posner, A.S., 1973. Conversion of amorphous calcium phosphate to microcrystalline hydroxyapatite. A pH-dependent, solution-mediated, solid-solid conversion. J. Phys. Chem. 77, 2313–2317. https://doi.org/10.1021/j100638a011

Brittin, W.E., 1945. Valence angle of the tetrahedral carbon atom. J. Chem. Educ. 22, 145. https://doi.org/10.1021/ed022p145

Brown, I.D., Altermatt, D., 1985. Bond-valence parameters obtained from a systematic analysis of the Inorganic Crystal Structure Database. Acta Crystallogr. B 41, 244–247. https://doi.org/10.1107/S0108768185002063

Brown, W.E., 1962. Octacalcium Phosphate and Hydroxyapatite: Crystal Structure of Octacalcium Phosphate. Nature 196, 1048–1050. https://doi.org/10.1038/1961048b0

Brown, W.E., Smith, J.P., Lehr, J.R., Frazier, A.W., 1962. Octacalcium Phosphate and Hydroxyapatite: Crystallographic and Chemical Relations between Octacalcium Phosphate and Hydroxyapatite. Nature 196, 1050–1055. https://doi.org/10.1038/1961050a0

Caglioti, G., Paoletti, A., Ricci, F.P., 1958. Choice of collimators for a crystal spectrometer for neutron diffraction. Nucl. Instrum. 3, 223–228. https://doi.org/10.1016/0369-643X(58)90029-X

Cant, N.W., Bett, J.A.S., Wilson, G.R., Hall, W.K., 1971. The vibrational spectrum of hydroxyl groups in hydroxyapatites. Spectrochim. Acta Part Mol. Spectrosc. 27, 425–439. https://doi.org/10.1016/0584-8539(71)80050-8

Černý, R., Favre-Nicolin, V., 2007. Direct space methods of structure determination from powder diffraction: principles, guidelines and perspectives. Z. Für Krist. 222, 105–113.

Chen, F., Wang, Z.-C., Lin, C.-J., 2002. Preparation and characterization of nano-sized hydroxyapatite particles and hydroxyapatite/chitosan nano-composite for use in biomedical materials. Mater. Lett. 57, 858–861. https://doi.org/10.1016/S0167-577X(02)00885-6

Christoffersen, J., Christoffersen, M.R., 1992. A revised theory for the growth of crystals by surface nucleation. J. Cryst. Growth 121, 608–616. https://doi.org/10.1016/0022-0248(92)90568-4

Christoffersen, M.R., Christoffersen, J., 1992. Possible mechanisms for the growth of the biomaterial, calcium hydroxyapatite microcrystals. J. Cryst. Growth 121, 617–630. https://doi.org/10.1016/0022-0248(92)90569-5

Chu, C., Hu, T., Yin, L.H., Pu, Y.P., Dong, Y.S., Lin, P.H., Chung, C.Y., Yeung, K.W.K., Chu, P.K., 2009. Microstructural characteristics and biocompatibility of a Type-B carbonated hydroxyapatite coating deposited on NiTi shape memory alloy. Biomed. Mater. Eng. 19, 401–408. https://doi.org/10.3233/BME-2009-0605

Coelho, A., 2007. Topas Academic Version 4.1. Computer Software, Topas Academic, Coelho Software. Brisbane.

Corno, M., Busco, C., Civalleri, B., Ugliengo, P., 2006. Periodic ab initio study of structural and vibrational features of hexagonal hydroxyapatite Ca10(PO4)6(OH)2. Phys. Chem. Chem. Phys. 8, 2464–2472. https://doi.org/10.1039/B602419J

Corno, M., Rimola, A., Bolis, V., Ugliengo, P., 2010. Hydroxyapatite as a key biomaterial: quantum-mechanical simulation of its surfaces in interaction with biomolecules. Phys. Chem. Chem. Phys. 12, 6309–6329. https://doi.org/10.1039/C002146F

Cuisinier, F., Bres, E.F., Hemmerle, J., Voegel, J.-C., Frank, R.M., 1987. Transmission electron microscopy of lattice planes in human alveolar bone apatite crystals. Calcif. Tissue Int. 40, 332–338. https://doi.org/10.1007/BF02556695

Currey, J.D., 2001. Bone Strength: What are We Trying to Measure? Calcif. Tissue Int. 68, 205–210. https://doi.org/10.1007/s002230020040

Cuscó, R., Guitián, F., Aza, S. de, Artús, L., 1998. Differentiation between hydroxyapatite and β-tricalcium phosphate by means of μ-Raman spectroscopy. J. Eur. Ceram. Soc. 18, 1301–1305. https://doi.org/10.1016/S0955-2219(98)00057-0

de Keijser, T.H., Langford, J.I., Mittemeijer, E.J., Vogels, A.B.P., 1982. Use of the Voigt function in a single-line method for the analysis of X-ray diffraction line broadening. J. Appl. Crystallogr. 15, 308–314. https://doi.org/10.1107/S0021889882012035

DeAngelis, B.., Newnham, R.E., White, B.W., 1972. Factor Group Analysis of the vibrational spectra of crystals: A review and consolidation. Am. Mineral. 57, 255–268.

Delgado-López, J.M., Iafisco, M., Rodríguez, I., Tampieri, A., Prat, M., Gómez-Morales, J., 2012. Crystallization of bioinspired citrate-functionalized nanoapatite with tailored carbonate content. Acta Biomater. 8, 3491–3499. https://doi.org/10.1016/j.actbio.2012.04.046

Dey, A., Bomans, P.H.H., Müller, F.A., Will, J., Frederik, P.M., de With, G., Sommerdijk, N.A.J.M., 2010. The role of prenucleation clusters in surface-induced calcium phosphate crystallization. Nat. Mater. 9, 1010–1014. https://doi.org/10.1038/nmat2900

Dinnebier, R.E., 2008. Powder Diffraction: Theory and Practice. Royal Society of Chemistry.

Dong, Y.H., Scardi, P., 2000. MarqX: a new program for whole-powder-pattern fitting. J. Appl. Crystallogr. 33, 184–189. https://doi.org/10.1107/S002188989901434X

Dorozhkin, S.V., 2013. Nanodimensional and nanocrystalline calcium orthophosphates. Int. J. Chem. Mater. Sci. 1(6), 105–174.

Dorozhkin, S.V., 2010. Amorphous calcium (ortho)phosphates. Acta Biomater. 6, 4457–4475. https://doi.org/10.1016/j.actbio.2010.06.031

Drouet, C., Bosc, F., Banu, M., Largeot, C., Combes, C., Dechambre, G., Estournès, C., Raimbeaux, G., Rey, C., 2009. Nanocrystalline apatites: From powders to biomaterials. Powder Technol. 190, 118–122. https://doi.org/10.1016/j.powtec.2008.04.041

Du, L.-W., Bian, S., Gou, B.-D., Jiang, Y., Huang, J., Gao, Y.-X., Zhao, Y.-D., Wen, W., Zhang, T.-L., Wang, K., 2013. Structure of Clusters and Formation of Amorphous Calcium Phosphate and Hydroxyapatite: From the Perspective of Coordination Chemistry. Cryst. Growth Des. 13, 3103–3109. https://doi.org/10.1021/cg400498j

Dumont, M., Kostka, A., Sander, P.M., Borbely, A., Kaysser-Pyzalla, A., 2011. Size and size distribution of apatite crystals in sauropod fossil bones. Palaeogeogr. Palaeoclimatol. Palaeoecol., Special Issue: Fossil bones and teeth: preservation or alteration of biogenic compositions? 310, 108–116. https://doi.org/10.1016/j.palaeo.2011.06.021

Egami, T., Billinge, S.J.L. (Eds.), 2012. Underneath the Bragg Peaks Structural Analysis of Complex Materials. Pergamon Materials Series.

Egami, T., Billinge, S.J.L., 2003. Underneath the Bragg Peaks. Pergamon.

Eichert, D., Drouet, C., Rey, C., Sfihia, H., Combes, C., 2009. Nanocrystalline Apatite-Based Biomaterials. Nova Science Publishers.

Eichert, D., Salomé, M., Banu, M., Susini, J., Rey, C., 2005. Preliminary characterization of calcium chemical environment in apatitic and non-apatitic calcium phosphates of biological interest by X-ray absorption spectroscopy. Spectrochim. Acta Part B At. Spectrosc. 60, 850–858. https://doi.org/10.1016/j.sab.2005.05.012

Elliott, D.J.C., 1969. Recent progress in the chemistry, crystal chemistry and structure of the apatites. Calcif. Tissue Res. 3, 293–307. https://doi.org/10.1007/BF02058672

Elliott, J.C., Mackie, P.E., Young, R.A., 1973. Monoclinic Hydroxyapatite. Science 180, 1055–1057.

Espanol, M., Portillo, J., Manero, J.-M., Ginebra, M.-P., 2010. Investigation of the hydroxyapatite obtained as hydrolysis product of α-tricalcium phosphate by transmission electron microscopy. CrystEngComm 12, 3318–3326. https://doi.org/10.1039/C001754J

Fancher, C.M., Han, Z., Levin, I., Page, K., Reich, B.J., Smith, R.C., Wilson, A.G., Jones, J.L., 2016. Use of Bayesian Inference in Crystallographic Structure Refinement via Full Diffraction Profile Analysis. Sci. Rep. 6, 31625. https://doi.org/10.1038/srep31625

Farrow, C.L., Billinge, S.J.L., 2009. Relationship between the atomic pair distribution function and small-angle scattering: implications for modeling of nanoparticles. Acta Crystallogr. Sect. A 65, 232–239. https://doi.org/10.1107/S0108767309009714

Farrow, C.L., Juhas, P., Liu, J.W., Bryndin, D., Božin, E.S., Bloch, J., Proffen, T., Billinge, S.J.L., 2007. PDFfit2 and PDFgui: computer programs for studying nanostructure in crystals. J. Phys. Condens. Matter 19, 335219. https://doi.org/10.1088/0953-8984/19/33/335219

Fleet, M.E., 2014. Carbonated Hydroxyapatite: Materials, Synthesis, and Applications. CRC Press.

Fleet, M.E., Liu, X., 2007. Coupled substitution of type A and B carbonate in sodium-bearing apatite. Biomaterials 28, 916–926. https://doi.org/10.1016/j.biomaterials.2006.11.003

Fleet, M.E., Liu, X., 2004. Location of type B carbonate ion in type A–B carbonate apatite synthesized at high pressure. J. Solid State Chem. 177, 3174–3182. https://doi.org/10.1016/j.jssc.2004.04.002

Fleet, M.E., Liu, X.Y., King, P.L., 2004. Accommodation of the carbonate ion in apatite: An FTIR and X-ray structure study of crystals synthesized at 2–4 GPa 89, 1422–1432.

Fowler, B.O., 1974. Infrared studies of apatites. I. Vibrational assignments for calcium, strontium, and barium hydroxyapatites utilizing isotopic substitution. Inorg. Chem. 13, 194–207. https://doi.org/10.1021/ic50131a039

Fowler, B.O., Moreno, E.C., Brown, W.E., 1966. Infra-red spectra of hydroxyapatite, octacalcium phosphate and pyrolysed octacalcium phosphate. Arch. Oral Biol. 11, 477–492. https://doi.org/10.1016/0003-9969(66)90154-3

Frølich, S., Birkedal, H., 2015. MultiRef: software platform for Rietveld refinement of multiple powder diffractograms from in situ, scanning or diffraction tomography experiments. J. Appl. Crystallogr. 48, 2019–2025. https://doi.org/10.1107/S1600576715020099

Frølich, S., Leemreize, H., Jakus, A., Xiao, X., Shah, R., Birkedal, H., Almer, J.D., Stock, S.R., 2016. Diffraction tomography and Rietveld refinement of a hydroxyapatite bone phantom. J. Appl. Crystallogr. 49, 103–109. https://doi.org/10.1107/S1600576715022633

Gagin, A., Levin, I., 2015. Accounting for unknown systematic errors in Rietveld refinements: a Bayesian statistics approach. J. Appl. Crystallogr. 48, 1201–1211. https://doi.org/10.1107/S1600576715011322

Gans, P., Gill, J.B., 1980. Comments on the critical evaluation of curve fitting in infrared spectrometry. Anal. Chem. 52, 351–352. https://doi.org/10.1021/ac50052a035

Gilmore, C.J., 1996. Maximum Entropy and Bayesian Statistics in Crystallography: a Review of Practical Applications. Acta Crystallogr. Sect. A 52, 561–589. https://doi.org/10.1107/S0108767396001560

González-Díaz, P.F., Hidalgo, A., 1976a. Theoretical determination of the torsional frequencies in apatites. Spectrochim. Acta Part Mol. Spectrosc. 32, 1119–1124. https://doi.org/10.1016/0584-8539(76)80297-8

González-Díaz, P.F., Hidalgo, A., 1976b. Infrared spectra of calcium apatites. Spectrochim. Acta Part Mol. Spectrosc. 32, 631–635. https://doi.org/10.1016/0584-8539(76)80126-2

Gonzalez-Diaz, P.F., Santos, M., 1979. McConnell's model vs. the HPO4 .fwdarw. CO3 model for carbonate apatite. Inorg. Chem. 18, 899–900. https://doi.org/10.1021/ic50193a084

Gordon, L.M., Cohen, M.J., MacRenaris, K.W., Pasteris, J.D., Seda, T., Joester, D., 2015. Amorphous intergranular phases control the properties of rodent tooth enamel. Science 347, 746–750. https://doi.org/10.1126/science.1258950

Gouadec, G., Colomban, P., 2007. Raman Spectroscopy of Nanomaterials: How Spectra Relate to Disorder, Particle Size and Mechanical Properties. Prog. Cryst. Growth Charact. Mater. 53, 1–53.

Gower, L.B., 2008. Biomimetic Model Systems for Investigating the Amorphous Precursor Pathway and Its Role in Biomineralization. Chem. Rev. 108, 4551–4627. https://doi.org/10.1021/cr800443h

Grünewald, T.A., Rennhofer, H., Hesse, B., Burghammer, M., Stanzl-Tschegg, S.E., Cotte, M., Löffler, J.F., Weinberg, A.M., Lichtenegger, H.C., 2016. Magnesium from bioresorbable implants: Distribution and impact on the nano- and mineral structure of bone. Biomaterials 76, 250–260. https://doi.org/10.1016/j.biomaterials.2015.10.054

Gupta, S.K., Jha, P.K., 2009. Modified phonon confinement model for size dependent Raman shift and linewidth of silicon nanocrystals. Solid State Commun. 149, 1989–1992. https://doi.org/10.1016/j.ssc.2009.08.036

Hammersley, A.P., Svensson, S.O., Hanfland, M., Fitch, A.N., Hausermann, D., 1996. Two-Dimensional Detector Software: From Real Detector to Idealised Image or Two-Theta Scan. High Press. Res. 14, 235–248.

Handschin, R.G., Stern, W.B., 1995. X-ray diffraction studies on the lattice perfection of human bone apatite (Crista Iliaca). Bone 16, S355–S363. https://doi.org/10.1016/S8756-3282(95)80385-8

Harries, J.E., Hukins, D.W.L., Holt, C., Hasnain, S.S., 1987. Conversion of amorphous calcium phosphate into hydroxyapatite investigated by EXAFS spectroscopy. J. Cryst. Growth 84, 563–570. https://doi.org/10.1016/0022-0248(87)90046-7

Hirsch, A., Azuri, I., Addadi, L., Weiner, S., Yang, K., Curtarolo, S., Kronik, L., 2014. Infrared Absorption Spectrum of Brushite from First Principles. Chem. Mater. 26, 2934–2942. https://doi.org/10.1021/cm500650t

Holt, C., Hukins, D.W.L., 1991. Structural analysis of the environment of calcium ions in crystalline and amorphous calcium phosphates by X-ray absorption spectroscopy and a hypothesis concerning the biological function of the casein micelle. Int. Dairy J. 1, 151–165. https://doi.org/10.1016/0958-6946(91)90008-V

Hu, Y.-Y., Rawal, A., Schmidt-Rohr, K., 2010. Strongly bound citrate stabilizes the apatite nanocrystals in bone. Proc. Natl. Acad. Sci. U. S. A. 107, 22425–22429.

https://doi.org/10.1073/pnas.1009219107
Hughes, J.M., 2015. The many facets of apatite. Am. Mineral. 100, 1033–1039. https://doi.org/10.2138/am-2015-5193
Hughes, J.M., Cameron, M., Crowley, K.D., 1990. Crystal structures of natural ternary apatites: Solid solution in the Ca5(PO4)3X (X = F, OH, Cl) system. Am. Mineral. 75, 295–304.
Hughes, J.M., Cameron, M., Crowley, K.D., 1989. Structural variations in natural F, OH, and Cl apatites. Am. Mineral. 74, 870–876.
Ibsen, C.J.S., Birkedal, H., 2012. Influence of poly(acrylic acid) on apatite formation studied by in situ X-ray diffraction using an X-ray scattering reaction cell with high-precision temperature control. J. Appl. Crystallogr. 45, 976–981. https://doi.org/10.1107/S0021889812036576
Ibsen, C.J.S., Chernyshov, D., Birkedal, H., 2016. Apatite Formation from Amorphous Calcium Phosphate and Mixed Amorphous Calcium Phosphate/Amorphous Calcium Carbonate. Chem. – Eur. J. https://doi.org/10.1002/chem.201601280
Ikoma, T., Yamazaki, A., Nakamura, S., Akao, M., 1999. Preparation and Structure Refinement of Monoclinic Hydroxyapatite. J. Solid State Chem. 144, 272–276. https://doi.org/10.1006/jssc.1998.8120
ISIS Empirical Potential Structure Refinement [WWW Document], n.d. URL https://www.isis.stfc.ac.uk/Pages/Empirical-Potential-Structure-Refinement.aspx (accessed 8.1.18).
Jacques, S.D.M., Di Michiel, M., Kimber, S.A.J., Yang, X., Cernik, R.J., Beale, A.M., Billinge, S.J.L., 2013. Pair distribution function computed tomography. Nat. Commun. 4, 2536. https://doi.org/10.1038/ncomms3536
Jeanjean, J., McGrellis, S., Rouchaud, J.C., Fedoroff, M., Rondeau, A., Perocheau, S., Dubis, A., 1996. A Crystallographic Study of the Sorption of Cadmium on Calcium Hydroxyapatites: Incidence of Cationic Vacancies. J. Solid State Chem. 126, 195–201. https://doi.org/10.1006/jssc.1996.0329
Johnsson, M.S., Nancollas, G.H., 1992. The role of brushite and octacalcium phosphate in apatite formation. Crit. Rev. Oral Biol. Med. Off. Publ. Am. Assoc. Oral Biol. 3, 61–82.
Juhás, P., Davis, T., Farrow, C.L., Billinge, S.J.L., 2013. PDFgetX3 : a rapid and highly automatable program for processing powder diffraction data into total scattering pair distribution functions. J. Appl. Crystallogr. 46, 560–566. https://doi.org/10.1107/S0021889813005190
Juhás, P., Farrow, C.L., Yang, X., Knox, K.R., Billinge, S.J.L., 2015. Complex modeling: a strategy and software program for combining multiple information sources to solve ill posed structure and nanostructure inverse problems. Acta Crystallogr. Sect. Found. Adv. 71, 562–568. https://doi.org/10.1107/S2053273315014473
Kaptay, G., 2012. On the size and shape dependence of the solubility of nano-particles in solutions. Int. J. Pharm. 430, 253–257. https://doi.org/10.1016/j.ijpharm.2012.03.038
Kaptay, G., 2011. The Gibbs Equation versus the Kelvin and the Gibbs-Thomson Equations to Describe Nucleation and Equilibrium of Nano-Materials. J. Nanosci. Nanotechnol. 12, 1–9.
Kay, M.I., Young, R.A., Posner, A.S., 1964. Crystal Structure of Hydroxyapatite. Nature 204, 1050–1052. https://doi.org/10.1038/2041050a0
Kim, S., Ryu, H.-S., Shin, H., Jung, H.S., Hong, K.S., 2005. In situ observation of hydroxyapatite nanocrystal formation from amorphous calcium phosphate in calcium-rich solutions. Mater. Chem. Phys. 91, 500–506. https://doi.org/10.1016/j.matchemphys.2004.12.016
Klug, H.P., Alexander, L.E., 1974. X-Ray Diffraction Procedures: For Polycrystalline and Amorphous Materials, 2nd Edition, 2 edition. ed. Wiley-Interscience, New York.
Kohn, M., Rakovan, J., Hughes, J.M., 2002. Phosphates - Geochemical, Geobiological and Materials Importance, Reviews in Mineralogy and Geochemistry. The Mineralogical Society of America.

Kojdecki, M.A., 2004. Approximate Estimation of Contributions to Pure X-Ray Diffraction Line Profiles from Crystallite Shapes, Sizes and Strains by Analysing Peak Widths. Mater. Sci. Forum 443–444, 107–110. https://doi.org/10.4028/www.scientific.net/MSF.443-444.107

Kothapalli, C.R., Wei, M., Legeros, R.Z., Shaw, M.T., 2005. Influence of temperature and aging time on HA synthesized by the hydrothermal method. J. Mater. Sci. Mater. Med. 16, 441–446. https://doi.org/10.1007/s10856-005-6984-5

Kril, C.E., Birringer, R., 1998. Estimating grain-size distributions in nanocrystalline materials from X-ray diffraction profile analysis. Philos. Mag. A 77, 621–640. https://doi.org/10.1080/01418619808224072

Le Bail, A., Duroy, H., Fourquet, J.L., 1988. Ab-initio structure determination of LiSbWO6 by X-ray powder diffraction. Mater. Res. Bull. 23, 447–452. https://doi.org/10.1016/0025-5408(88)90019-0

Leemreize, H., Almer, J.D., Stock, S.R., Birkedal, H., 2013. Three-dimensional distribution of polymorphs and magnesium in a calcified underwater attachment system by diffraction tomography. J. R. Soc. Interface 10, 20130319. https://doi.org/10.1098/rsif.2013.0319

Leemreize, H., Eltzholtz, J.R., Birkedal, H., 2014. Lattice macro and microstrain fluctuations in the calcified byssus of Anomia simplex. Eur. J. Mineral. 26, 517–522. https://doi.org/10.1127/0935-1221/2014/0026-2391

LeGeros, R.Z., Trautz, O.R., Legeros, J.P., Klein, E., 1968. Carbonate substitution in the apatite structure. Bull. Soc. Chim. Fr. 1712–1718.

Legeros, R.Z., Trautz, O.R., Legeros, J.P., Klein, E., Shirra, W.P., 1967. Apatite Crystallites: Effects of Carbonate on Morphology. Science 155, 1409–1411. https://doi.org/10.1126/science.155.3768.1409

Leoni, M., Confente, T., Scardi, P., 2006. PM2K: a flexible program implementing Whole Powder Pattern Modelling. Z Krist. Suppl 23, 249–254.

Leoni, M., di Maggio, R., Polizzi, S., Scardi, P., 2004. X-ray Diffraction Methodology for the Microstructural Analysis of Nanocrystalline Powders: Application to Cerium Oxide. J. Am. Ceram. Soc. 87, 1133–1140.

Lesniewski, J.E., Disseler, S.M., Quintana, D.J., Kienzle, P.A., Ratcliff, W.D., 2016. Bayesian method for the analysis of diffraction patterns using BLAND. J. Appl. Crystallogr. 49, 2201–2209. https://doi.org/10.1107/S1600576716016423

Leventouri, T., Chakoumakos, B.C., Papanearchou, N., Perdikatsis, V., 2001. Comparison of crystal structure parameters of natural and synthetic apatites from neutron powder diffraction. J. Mater. Res. 16, 2600–2606. https://doi.org/10.1557/JMR.2001.0357

Li, Z., Pasteris, J.D., 2014. Tracing the pathway of compositional changes in bone mineral with age: Preliminary study of bioapatite aging in hypermineralized dolphin's bulla. Biochim. Biophys. Acta BBA - Gen. Subj. 1840, 2331–2339. https://doi.org/10.1016/j.bbagen.2014.03.012

Li, Z., Pasteris, J.D., Novack, D., 2013. Hypermineralized Whale Rostrum as the Exemplar for Bone Mineral. Connect. Tissue Res. 54, 167–175. https://doi.org/10.3109/03008207.2013.769973

Maddams, W.F., 1980. The Scope and Limitations of Curve Fitting. Appl. Spectrosc. 34, 245–267. https://doi.org/10.1366/0003702804730312

Madsen, I.C., Scarlett, N.V.Y., Kern, A., 2011. Description and survey of methodologies for the determination of amorphous content via X-ray powder diffraction. Z. Für Krist. Cryst. Mater. 226, 944–955. https://doi.org/10.1524/zkri.2011.1437

Mahamid, J., Sharir, A., Addadi, L., Weiner, S., 2008. Amorphous calcium phosphate is a major component of the forming fin bones of zebrafish: Indications for an amorphous precursor phase. Proc. Natl. Acad. Sci. U. S. A. 105, 12748–12753. https://doi.org/10.1073/pnas.0803354105

McCue, M., Malinowski, E.R., 1981. Target factor analysis of infrared spectra of multicomponent mixtures. Anal. Chim. Acta 133, 125–136. https://doi.org/10.1016/S0003-2670(01)93488-9

McNally, E., Nan, F., Botton, G.A., Schwarcz, H.P., 2013. Scanning transmission electron microscopic tomography of cortical bone using Z-contrast imaging. Micron 49, 46–53. https://doi.org/10.1016/j.micron.2013.03.002

Michael, J.R., 1983. The stabilized probability plot. Biometrika 70, 11–17. https://doi.org/10.1093/biomet/70.1.11

Miller, L.M., Vairavamurthy, V., Chance, M.R., Mendelsohn, R., Paschalis, E.P., Betts, F., Boskey, A.L., 2001. In situ analysis of mineral content and crystallinity in bone using infrared micro-spectroscopy of the nu(4) PO(4)(3-) vibration. Biochim. Biophys. Acta 1527, 11–19.

Mittemeijer, E.J., Scardi, P., 2004. Diffraction Analysis of the Microstructure of Materials. Springer Science & Business Media.

Mittemeijer, E.J., Welzel, U., 2008. The "state of the art" of the diffraction analysis of crystallite size and lattice strain. Z. Für Krist. Int. J. Struct. Phys. Chem. Asp. Cryst. Mater. 223, 552–560.

Monge, G., Carretero, M.I., Pozo, M., Barroso, C., 2014. Mineralogical changes in fossil bone from Cueva del Angel, Spain: archaeological implications and occurrence of whitlockite. J. Archaeol. Sci. 46, 6–15. https://doi.org/10.1016/j.jas.2014.02.033

Mul, F.F.M.D., Hottenhuis, M.H.J., Bouter, P., Greve, J., Arends, J., Bosch, J.J.T., 1986. Micro-Raman Line Broadening in Synthetic Carbonated Hydroxyapatite. J. Dent. Res. 65, 437–440. https://doi.org/10.1177/00220345860650031301

Mul, F.F.M. de, Otto, C., Greve, J., Arends, J., Ten Bosch, J.J., 1988. Calculation of the Raman line broadening on carbonation in synthetic hydroxyapatite. J. Raman Spectrosc. 19, 13–21. https://doi.org/10.1002/jrs.1250190104

Nancollas, G.H., Koutsoukos, P.G., 1980. Calcium Phosphate nucleation and growth in solution. Prog Cryst. Growth Charact 3, 77–102.

Neder, R.B., Proffen, T., 2008. Diffuse Scattering and Defect Structure Simulations: A cook book using the program DISCUS. OUP Oxford.

Omelon, S.J., Grynpas, M.D., 2008. Relationships between Polyphosphate Chemistry, Biochemistry and Apatite Biomineralization. Chem. Rev. 108, 4694–4715. https://doi.org/10.1021/cr0782527

Onuma, K., 2006. Recent research on pseudobiological hydroxyapatite crystal growth and phase transition mechanisms. Prog. Cryst. Growth Charact. Mater. 52, 223–245. https://doi.org/10.1016/j.pcrysgrow.2006.06.003

Onuma, K., Ito, A., 1998. Cluster Growth Model for Hydroxyapatite. Chem. Mater. 10, 3346–3351. https://doi.org/10.1021/cm980062c

Ostwald, W., 1900. Über die vermeintliche Isomerie des roten und gelben Quesck- silberoxyds und die Oberflachenspannung fester Körper. Z Phys Chem 34, 495–503.

Palmer, L.C., Newcomb, C.J., Kaltz, S.R., Spoerke, E.D., Stupp, S.I., 2008. Biomimetic Systems for Hydroxyapatite Mineralization Inspired By Bone and Enamel. Chem. Rev. 108, 4754–4783. https://doi.org/10.1021/cr8004422

Pan, H., Yang Liu, X., Tang, R., Yao Xu, H., 2010. Mystery of the transformation from amorphous calcium phosphate to hydroxyapatite. Chem. Commun. 46, 7415–7417. https://doi.org/10.1039/C0CC00971G

Pan, Y., Fleet, M.E., 2002. Compositions of the apatite-group minerals: substitution mechanisms and controlling factors, in: M.J. Kohn, J. Rakovan, J.M. Hughes (Eds.), Phosphates: Geochemical, Geobiolog- ical and Material Importance,. Rev. Mineral. Geo- Chem. Vol 48 Mineral. Soc. Am. Wash. DC Pp 13 – 50.

Panda, R.N., Hsieh, M.F., Chung, R.J., Chin, T.S., 2003. FTIR, XRD, SEM and solid state NMR

investigations of carbonate-containing hydroxyapatite nano-particles synthesized by hydroxide-gel technique. J. Phys. Chem. Solids 64, 193–199. https://doi.org/10.1016/S0022-3697(02)00257-3

Pang, Y.X., Bao, X., 2003. Influence of temperature, ripening time and calcination on the morphology and crystallinity of hydroxyapatite nanoparticles. J. Eur. Ceram. Soc. 23, 1697–1704. https://doi.org/10.1016/S0955-2219(02)00413-2

Pasteris, J.D., Yoder, C.H., Sternlieb, M.P., Liu, S., 2012. Effect of carbonate incorporation on the hydroxyl content of hydroxylapatite. Mineral. Mag. 76, 2741–2759. https://doi.org/10.1180/minmag.2012.076.7.08

Pawley, G.S., 1981. Unit-cell refinement from powder diffraction scans. J. Appl. Crystallogr. 14, 357–361. https://doi.org/10.1107/S0021889881009618

Pecharsky, V., Zavalij, P., 2009. Fundamentals of Powder Diffraction and Structural Characterization of Materials. Springer US, Boston, MA.

Pedone, A., Corno, M., Civalleri, B., Malavasi, G., Menziani, M.C., Segre, U., Ugliengo, P., 2007. An ab initio parameterized interatomic force field for hydroxyapatite. J. Mater. Chem. 17, 2061–2068. https://doi.org/10.1039/B617858H

Penel, G., Leroy, G., Rey, C., Bres, E., 1998. MicroRaman Spectral Study of the PO4 and CO3 Vibrational Modes in Synthetic and Biological Apatites. Calcif. Tissue Int. 63, 475–481. https://doi.org/10.1007/s002239900561

Peters, F., Schwarz, K., Epple, M., 2000. The structure of bone studied with synchrotron X-ray diffraction, X-ray absorption spectroscopy and thermal analysis. Thermochim. Acta 361, 131–138. https://doi.org/10.1016/S0040-6031(00)00554-2

Piga, G., Solinas, G., Thompson, T.J.U., Brunetti, A., Malgosa, A., Enzo, S., 2013. Is X-ray diffraction able to distinguish between animal and human bones? J. Archaeol. Sci. 40, 778–785. https://doi.org/10.1016/j.jas.2012.07.004

Posner, A.S., Betts, F., 1975. Synthetic amorphous calcium phosphate and its relation to bone mineral structure. Acc. Chem. Res. 8, 273–281. https://doi.org/10.1021/ar50092a003

Posner, A.S., Betts, F., Blumenthal, N.C., 1980. Formation and structure of synthetic and bone hydroxyapatites. Prog. Cryst. Growth Charact. 3, 49–64. https://doi.org/10.1016/0146-3535(80)90011-8

Posner, A.S., Eanes, E.D., Harper, R.A., Zipkin, I., 1963. X-ray diffraction analysis of the effect of fluoride on human bone apatite. Arch. Oral Biol. 8, 549–570. https://doi.org/10.1016/0003-9969(63)90071-2

Proffen, T., Page, K., McLain, S., Clausen, B., Darling, T.W., TenCate, J., Lee, S.-Y., Ustundag, E., 2005. Atomic pair distribution function analysis of materials containing crystalline and amorphous phases : Zeitschrift für Kristallographie - Crystalline Materials.

Qiu, X., Thompson, J.W., Billinge, S.J.L., 2004. PDFgetX2: a GUI-driven program to obtain the pair distribution function from X-ray powder diffraction data. J. Appl. Crystallogr. 37, 678–678. https://doi.org/10.1107/S0021889804011744

Rehman, I., Bonfield, W., 1997. Characterization of hydroxyapatite and carbonated apatite by photo acoustic FTIR spectroscopy. J. Mater. Sci. Mater. Med. 8, 1–4. https://doi.org/10.1023/A:1018570213546

Rey, C., Collins, B., Goehl, T., Dickson, I.R., Glimcher, M.J., 1989. The carbonate environment in bone mineral: A resolution-enhanced fourier transform infrared spectroscopy study. Calcif. Tissue Int. 45, 157–164. https://doi.org/10.1007/BF02556059

Rey, C., Renugopalakrishnan, V., Collins, B., Glimcher, M.J., 1991a. Fourier transform infrared spectroscopic study of the carbonate ions in bone mineral during aging. Calcif. Tissue Int. 49, 251–258.

Rey, C., Renugopalakrishnan, V., Shimizu, M., Collins, B., Glimcher, M.J., 1991b. A resolution-enhanced Fourier transform infrared spectroscopic study of the environment of the CO3(2-) ion in the mineral phase of enamel during its formation and maturation. Calcif. Tissue Int. 49, 259–268.

Rey, C., Shimizu, M., Collins, B., Glimcher, M.J., 1991c. Resolution-enhanced Fourier transform infrared spectroscopy study of the environment of phosphate ion in the early deposits of a solid phase of calcium phosphate in bone and enamel and their evolution with age: 2. Investigations in the nu3PO4 domain. Calcif. Tissue Int. 49, 383–388.

Rey, C., Shimizu, M., Collins, B., Glimcher, M.J., 1990. Resolution-enhanced fourier transform infrared spectroscopy study of the environment of phosphate ions in the early deposits of a solid phase of calcium-phosphate in bone and enamel, and their evolution with age. I: Investigations in thev 4 PO4 domain. Calcif. Tissue Int. 46, 384–394. https://doi.org/10.1007/BF02554969

Reznikov, N., Shahar, R., Weiner, S., 2014. Three-dimensional structure of human lamellar bone: The presence of two different materials and new insights into the hierarchical organization. Bone 59, 93–104. https://doi.org/10.1016/j.bone.2013.10.023

Rodríguez-Carvajal, J., 1993. Recent advances in magnetic structure determination by neutron powder diffraction. Phys. B Condens. Matter 192, 55–69. https://doi.org/10.1016/0921-4526(93)90108-I

Rodríquez-Carvajal, J., Roisnel, T., 2004. Line Broadening Analysis Using FullProf*: Determination of Microstructural Properties. Mater. Sci. Forum 443–444, 123–126. https://doi.org/10.4028/www.scientific.net/MSF.443-444.123

Rodríguez-Lorenzo, L.M., Hart, J.N., Gross, K.A., 2003. Influence of fluorine in the synthesis of apatites. Synthesis of solid solutions of hydroxy-fluorapatite. Biomaterials 24, 3777–3785. https://doi.org/10.1016/S0142-9612(03)00259-X

Rogers, K.D., Daniels, P., 2002. An X-ray diffraction study of the effects of heat treatment on bone mineral microstructure. Biomaterials 23, 2577–2585. https://doi.org/10.1016/S0142-9612(01)00395-7

Rogers, K.D., Zioupos, P., 1999. The Bone Tissue of the Rostrum of a Mesoplodon Densirostris Whale: a Mammalian Biomineral Demonstrating Extreme Texture. J. Mater. Sci. Lett. 18, 651–654. https://doi.org/10.1023/A:1006615422214

Rokita, E., Hermes, C., Nolting, H.-F., Ryczek, J., 1993. Substitution of calcium by strontium within selected calcium phosphates. J. Cryst. Growth 130, 543–552. https://doi.org/10.1016/0022-0248(93)90543-6

Rollin-Martinet, S., Navrotsky, A., Champion, E., Grossin, D., Drouet, C., 2013. Thermodynamic basis for evolution of apatite in calcified tissues. Am. Mineral. 98, 2037–2045. https://doi.org/10.2138/am.2013.4537

Root, M.J., 1990. Inhibition of the amorphous calcium phosphate phase transformation reaction by polyphosphates and metal ions. Calcif. Tissue Int. 47, 112–116. https://doi.org/10.1007/BF02555994

Rusu, V.M., Ng, C.-H., Wilke, M., Tiersch, B., Fratzl, P., Peter, M.G., 2005. Size-controlled hydroxyapatite nanoparticles as self-organized organic–inorganic composite materials. Biomaterials 26, 5414–5426. https://doi.org/10.1016/j.biomaterials.2005.01.051

Sadat-Shojai, M., Khorasani, M.-T., Dinpanah-Khoshdargi, E., Jamshidi, A., 2013. Synthesis methods for nanosized hydroxyapatite with diverse structures. Acta Biomater. 9, 7591–7621. https://doi.org/10.1016/j.actbio.2013.04.012

Sadat-Shojai, M., Khorasani, M.-T., Jamshidi, A., 2012. Hydrothermal processing of hydroxyapatite nanoparticles—A Taguchi experimental design approach. J. Cryst. Growth 361, 73–84.

https://doi.org/10.1016/j.jcrysgro.2012.09.010
Santos, M., Gonzalez-Diaz, P.F., 1977. A model for B carbonate apatite. Inorg. Chem. 16, 2131–2134. https://doi.org/10.1021/ic50174a067
Scardi, P., Leoni, M., 2006. Line profile analysis: pattern modelling versus profile fitting. J. Appl. Crystallogr. Wiley-Blackwell 39, 24–31. https://doi.org/10.1107/S0021889805032978
Scardi, P., Leoni, M., 2002. Whole powder pattern modelling. Acta Crystallogr. Sect. A 58, 190–200. https://doi.org/10.1107/S0108767301021298
Scardi, P., Leoni, M., 2001. Diffraction line profiles from polydisperse crystalline systems. Acta Crystallogr. A 57, 604–613. https://doi.org/10.1107/S0108767301008881
Scardi, P., Ortolani, M., Leoni, M., 2010. WPPM: Microstructural Analysis beyond the Rietveld Method. Mater. Sci. Forum 651, 155–171. https://doi.org/10.4028/www.scientific.net/MSF.651.155
Schwarcz, H.P., McNally, E.A., Botton, G.A., 2014. Dark-field transmission electron microscopy of cortical bone reveals details of extrafibrillar crystals. J. Struct. Biol. 188, 240–248. https://doi.org/10.1016/j.jsb.2014.10.005
Schwarzenbach, D., Abrahams, S.C., Flack, H.D., Gonschorek, W., Hahn, T., Huml, K., Marsh, R.E., Prince, E., Robertson, B.E., Rollett, J.S., Wilson, A.J.C., 1989. Statistical descriptors in crystallography: Report of the IUCr Subcommittee on Statistical Descriptors. Acta Crystallogr. Sect. A 45, 63–75. https://doi.org/10.1107/S0108767388009596
Sivia, D.S., David, W.I.F., 1994. A Bayesian approach to extracting structure-factor amplitudes from powder diffraction data. Acta Crystallogr. Sect. A 50, 703–714. https://doi.org/10.1107/S0108767394003235
Somrani, S., Banu, M., Jemal, M., Rey, C., 2005. Physico-chemical and thermochemical studies of the hydrolytic conversion of amorphous tricalcium phosphate into apatite. J. Solid State Chem. 178, 1337–1348. https://doi.org/10.1016/j.jssc.2004.11.029
Soper, A.K., 2005. Partial structure factors from disordered materials diffraction data: An approach using empirical potential structure refinement. Phys. Rev. B 72, 104204. https://doi.org/10.1103/PhysRevB.72.104204
Soper, A.K., 1996. Empirical potential Monte Carlo simulation of fluid structure. Chem. Phys. 202, 295–306. https://doi.org/10.1016/0301-0104(95)00357-6
Stathopoulou, E.T., Psycharis, V., Chryssikos, G.D., Gionis, V., Theodorou, G., 2008. Bone diagenesis: New data from infrared spectroscopy and X-ray diffraction. Palaeogeogr. Palaeoclimatol. Palaeoecol., Beyond documenting diagenesis: The fifth international bone diagenesis workshop 266, 168–174. https://doi.org/10.1016/j.palaeo.2008.03.022
Stock, S.R., 2015. The Mineral–Collagen Interface in Bone. Calcif. Tissue Int. 97, 262–280. https://doi.org/10.1007/s00223-015-9984-6
Stokes, A.R., Wilson, A.J.C., 1944. The diffraction of X rays by distorted crystal aggregates - I. Proc. Phys. Soc. 56, 174. https://doi.org/10.1088/0959-5309/56/3/303
Stork, L., Müller, P., Dronskowski, R., Ortlepp, J.R., 2005. Chemical analyses and X-ray diffraction investigations of human hydroxyapatite minerals from aortic valve stenoses. Z. Für Krist. - Cryst. Mater. 220. https://doi.org/10.1524/zkri.220.2.201.59118
Sudarsanan, K., Young, R.A., 1969. Significant precision in crystal structural details. Holly Springs hydroxyapatite. Acta Crystallogr. B 25, 1534–1543. https://doi.org/10.1107/S0567740869004298
Suetsugu, Y., Ikoma, T., Tanaka, M., 2001. Single Crystal Growth and Structure Analysis of Monoclinic Hydroxyapatite. Key Eng. Mater. 192–195, 287–290. https://doi.org/10.4028/www.scientific.net/KEM.192-195.287
Suetsugu, Y., Tanaka, J., 2002. Crystal growth and structure analysis of twin-free monoclinic

hydroxyapatite. J. Mater. Sci. Mater. Med. 13, 767–772. https://doi.org/10.1023/A:1016170924138

Sun, L., Chow, L.C., Frukhtbeyn, S.A., Bonevich, J.E., 2010. Preparation and properties of nanoparticles of calcium phosphates with various Ca/P ratios. J. Res. Natl. Inst. Stand. Technol. 115, 243. https://doi.org/10.6028/jres.115.018

Suzuki, O., 2010. Octacalcium phosphate: Osteoconductivity and crystal chemistry. Acta Biomater. 6, 3379–3387. https://doi.org/10.1016/j.actbio.2010.04.002

Tadic, D., Peters, F., Epple, M., 2002. Continuous synthesis of amorphous carbonated apatites. Biomaterials 23, 2553–2559. https://doi.org/10.1016/S0142-9612(01)00390-8

Tanaka, Y., Iwasaki, T., Katayama, K., Hojo, J., Yamashita, K., 2010. Effect of Ionic Polarization on Crystal Structure of Hydroxyapatite Ceramic with Hydroxide Nonstoichiometry. J. Jpn. Soc. Powder Powder Metall. 57, 520–528. https://doi.org/10.2497/jjspm.57.520

Taylor, T.G., Kirkley, J., 1967. The relation between the fluoride, citrate and carbonate contents of individual bones of the skeleton of the fowl. Calcif. Tissue Res. 1, 33–36.

Termine, J.D., Eanes, E.D., 1972. Comparative chemistry of amorphous and apatitic calcium phosphate preparations. Calcif. Tissue Res. 10, 171–197.

Thompson, P., Cox, D.E., Hastings, J.B., 1987. Rietveld refinement of Debye–Scherrer synchrotron X-ray data from Al $_2$ O $_3$. J. Appl. Crystallogr. 20, 79–83. https://doi.org/10.1107/S0021889887087090

Tian, H.H., Atzmon, M., 1999. Comparison of X-ray analysis methods used to determine the grain size and strain in nanocrystalline materials. Philos. Mag. A 79, 1769–1786. https://doi.org/10.1080/01418619908210391

Tian, P., Billinge, S., 2011. Testing different methods for estimating uncertainties on Rietveld refined parameters using SrRietveld. Z. Für Krist. Cryst. Mater. 226, 898–904. https://doi.org/10.1524/zkri.2011.1421

Tian, P., Zhou, W., Liu, J., Shang, Y., Farrow, C.L., Juhas, P., Billinge, S.J.L., 2010. SrRietveld: A program for automating Rietveld refinements for high throughput powder diffraction studies. ArXiv10060435 Cond-Mat.

Toby, B.H., Von Dreele, R.B., 2013. GSAS-II: the genesis of a modern open-source all purpose crystallography software package. J. Appl. Crystallogr. 46, 544–549. https://doi.org/10.1107/S0021889813003531

Tonegawa, T., Ikoma, T., Yoshioka, T., Hanagata, N., Tanaka, J., 2010. Crystal structure refinement of A-type carbonate apatite by X-ray powder diffraction. J. Mater. Sci. 45, 2419–2426. https://doi.org/10.1007/s10853-010-4209-x

Trueman, C.N., Kocsis, L., Palmer, M.R., Dewdney, C., 2011. Fractionation of rare earth elements within bone mineral: A natural cation exchange system. Palaeogeogr. Palaeoclimatol. Palaeoecol., Special Issue: Fossil bones and teeth: preservation or alteration of biogenic compositions? 310, 124–132. https://doi.org/10.1016/j.palaeo.2011.01.002

Trueman, C.N., Privat, K., Field, J., 2008. Why do crystallinity values fail to predict the extent of diagenetic alteration of bone mineral? Palaeogeogr. Palaeoclimatol. Palaeoecol., Beyond documenting diagenesis: The fifth international bone diagenesis workshop 266, 160–167. https://doi.org/10.1016/j.palaeo.2008.03.038

Trueman, C.N.G., Behrensmeyer, A.K., Tuross, N., Weiner, S., 2004. Mineralogical and compositional changes in bones exposed on soil surfaces in Amboseli National Park, Kenya: diagenetic mechanisms and the role of sediment pore fluids. J. Archaeol. Sci. 31, 721–739. https://doi.org/10.1016/j.jas.2003.11.003

Tung, M.S., Brown, W.E., 1983. An intermediate state in hydrolysis of amorphous calcium phosphate. Calcif. Tissue Int. 35, 783–790.

Turner-Walker, G., 2011. The mechanical properties of artificially aged bone: Probing the nature of the collagen–mineral bond. Palaeogeogr. Palaeoclimatol. Palaeoecol., Special Issue: Fossil bones and teeth: preservation or alteration of biogenic compositions? 310, 17–22. https://doi.org/10.1016/j.palaeo.2011.03.024

Tütken, T., Vennemann, T.W., 2011. Fossil bones and teeth: Preservation or alteration of biogenic compositions? Palaeogeogr. Palaeoclimatol. Palaeoecol., Special Issue: Fossil bones and teeth: preservation or alteration of biogenic compositions? 310, 1–8. https://doi.org/10.1016/j.palaeo.2011.06.020

Tütken, T., Vennemann, T.W., Pfretzschner, H.-U., 2008. Early diagenesis of bone and tooth apatite in fluvial and marine settings: Constraints from combined oxygen isotope, nitrogen and REE analysis. Palaeogeogr. Palaeoclimatol. Palaeoecol., Beyond documenting diagenesis: The fifth international bone diagenesis workshop 266, 254–268. https://doi.org/10.1016/j.palaeo.2008.03.037

Ungár, T., 2001. Dislocation densities, arrangements and character from X-ray diffraction experiments. Mater. Sci. Eng. A, Dislocations 2000: An International Conference on the Fundamentals of Plastic Deformation 309–310, 14–22. https://doi.org/10.1016/S0921-5093(00)01685-3

Ungár, T., Borbély, A., Goren-Muginstein, G.R., Berger, S., Rosen, A.R., 1999. Particle-size, size distribution and dislocations in nanocrystalline tungsten-carbide. Nanostructured Mater. 11, 103–113. https://doi.org/10.1016/S0965-9773(99)00023-9

V. Dorozhkin, S., 2012. Amorphous Calcium Orthophosphates: Nature, Chemistry and Biomedical Applications. Int. J. Mater. Chem. 2, 19–46. https://doi.org/10.5923/j.ijmc.20120201.04

van Berkum, J.G.M., Vermeulen, A.C., Delhez, R., de Keijser, T.H., Mittemeijer, E.J., 1994. Applicabilities of the Warren–Averbach analysis and an alternative analysis for separation of size and strain broadening. J. Appl. Crystallogr. 27, 345–357. https://doi.org/10.1107/S0021889893010568

Vandecandelaere, N., Rey, C., Drouet, C., 2012. Biomimetic apatite-based biomaterials: on the critical impact of synthesis and post-synthesis parameters. J. Mater. Sci. Mater. Med. 23, 2593–2606. https://doi.org/10.1007/s10856-012-4719-y

Vogel, S.C., 2011. gsaslanguage: a GSAS script language for automated Rietveld refinements of diffraction data. J. Appl. Crystallogr. 44, 873–877. https://doi.org/10.1107/S0021889811023181

von Gumbel, C.W., 1868. Geognostische Besckreibung des ostbayerischen Grenzgebirges oder des bayerischen und oberpfalzer Waldgebirges. Perthes, Gotha, p. 968.

Wagner, C.N.J., 1978. Direct methods for the determination of atomic-scale structure of amorphous solids (X-ray, electron, and neutron scattering). J. Non-Cryst. Solids, Proceedings of the Topical Conference on Atomic Scale Structure of Amorphous Solids 31, 1–40. https://doi.org/10.1016/0022-3093(78)90097-2

Wang, C.-G., Liao, J.-W., Gou, B.-D., Huang, J., Tang, R.-K., Tao, J.-H., Zhang, T.-L., Wang, K., 2009. Crystallization at Multiple Sites inside Particles of Amorphous Calcium Phosphate. Cryst. Growth Des. 9, 2620–2626. https://doi.org/10.1021/cg801069t

Wang, L., Li, S., Ruiz-Agudo, E., V. Putnis, C., Putnis, A., 2012. Posner's cluster revisited: direct imaging of nucleation and growth of nanoscale calcium phosphate clusters at the calcite -water interface. CrystEngComm 14, 6252–6256. https://doi.org/10.1039/C2CE25669J

Wang, L., Nancollas, G.H., 2008. Calcium Orthophosphates: Crystallization and Dissolution. Chem. Rev. 108, 4628–4669. https://doi.org/10.1021/cr0782574

Wang, Y., Von Euw, S., Fernandes, F.M., Cassaignon, S., Selmane, M., Laurent, G., Pehau-Arnaudet, G., Coelho, C., Bonhomme-Coury, L., Giraud-Guille, M.-M., Babonneau, F., Azaïs, T., Nassif, N., 2013. Water-mediated structuring of bone apatite. Nat. Mater. 12, 1144–1153.

https://doi.org/10.1038/nmat3787
Warren, B.E., Averbach, B.L., 1950. The Effect of Cold-Work Distortion on X-Ray Patterns. J. Appl. Phys. 21, 595–599. https://doi.org/10.1063/1.1699713
Weaver, J.C., Milliron, G.W., Miserez, A., Evans-Lutterodt, K., Herrera, S., Gallana, I., Mershon, W.J., Swanson, B., Zavattieri, P., DiMasi, E., Kisailus, D., 2012. The Stomatopod Dactyl Club: A Formidable Damage-Tolerant Biological Hammer. Science 336, 1275–1280. https://doi.org/10.1126/science.1218764
Wegst, U.G.K., Bai, H., Saiz, E., Tomsia, A.P., Ritchie, R.O., 2015. Bioinspired structural materials. Nat. Mater. 14, 23–36. https://doi.org/10.1038/nmat4089
Wiessner, M., Angerer, P., 2014. Bayesian approach applied to the Rietveld method. J. Appl. Crystallogr. 47, 1819–1825. https://doi.org/10.1107/S1600576714020196
Wilson, R.M., Dowker, S.E.P., Elliott, J.C., 2006. Rietveld refinements and spectroscopic structural studies of a Na-free carbonate apatite made by hydrolysis of monetite. Biomaterials 27, 4682–4692. https://doi.org/10.1016/j.biomaterials.2006.04.033
Wilson, R.M., Elliott, J.C., Dowker, S.E.P., 1999. Rietveld refinement of the crystallographic structure of human dental enamel apatites. Am. Mineral. 84, 1406–1414.
Wilson, R.M., Elliott, J.C., Dowker, S.E.P., Rodriguez-Lorenzo, L.M., 2005. Rietveld refinements and spectroscopic studies of the structure of Ca-deficient apatite. Biomaterials 26, 1317–1327. https://doi.org/10.1016/j.biomaterials.2004.04.038
Wopenka, B., Pasteris, J.D., 2005. A mineralogical perspective on the apatite in bone. Mater. Sci. Eng. C 25, 131–143. https://doi.org/10.1016/j.msec.2005.01.008
Wu, W., Nancollas, G.H., 1998. A New Understanding of the Relationship Between Solubility and Particle Size. J. Solut. Chem. 27, 521–531. https://doi.org/10.1023/A:1022678505433
Xie, B., Halter, T.J., Borah, B.M., Nancollas, G.H., 2014. Tracking Amorphous Precursor Formation and Transformation during Induction Stages of Nucleation. Cryst. Growth Des. 14, 1659–1665. https://doi.org/10.1021/cg401777x
Xie, B., Nancollas, G.H., 2010. How to control the size and morphology of apatite nanocrystals in bone. Proc. Natl. Acad. Sci. U. S. A. 107, 22369–22370. https://doi.org/10.1073/pnas.1017493108
Xin, R., Leng, Y., Wang, N., 2006. In situ TEM examinations of octacalcium phosphate to hydroxyapatite transformation. J. Cryst. Growth 289, 339–344. https://doi.org/10.1016/j.jcrysgro.2005.11.010
Yi, H., Balan, E., Gervais, C., Ségalen, L., Blanchard, M., Lazzeri, M., 2014. Theoretical study of the local charge compensation and spectroscopic properties of B-type carbonate defects in apatite. Phys. Chem. Miner. 41, 347–359. https://doi.org/10.1007/s00269-013-0654-9
Yin, X., Stott, M.J., 2003. Biological calcium phosphates and Posner's cluster. J. Chem. Phys. 118, 3717–3723. https://doi.org/10.1063/1.1539093
Young, R.A., 1993. The Rietveld method. International Union of Crystallograhy.
Young, R.A., Holcomb, D.W., 1984. Role of acid phosphate in hydroxyapatite lattice expansion. Calcif. Tissue Int. 36, 60–63.
Zhao, J., Liu, Y., Sun, W., Yang, X., 2012. First detection, characterization, and application of amorphous calcium phosphate in dentistry. J. Dent. Sci. 7, 316–323. https://doi.org/10.1016/j.jds.2012.09.001
Zhou, H., Lee, J., 2011. Nanoscale hydroxyapatite particles for bone tissue engineering. Acta Biomater. 7, 2769–2781. https://doi.org/10.1016/j.actbio.2011.03.019
Ziv, V., Weiner, S., 1994. Bone Crystal Sizes: A Comparison of Transmission Electron Microscopic and X-Ray Diffraction Line Width Broadening Techniques. Connect. Tissue Res. 30, 165–175. https://doi.org/10.3109/03008209409061969

List of Figures

List of Tables

Appendix

A1 – Terminology in the context of the thesis

"alteration"	intentionally or non-intentionally induced change of any parameter in the system.
"diagenesis"	a term originating in geology, defined as "the physical and chemical changes occurring during the conversion of sediment to sedimentary rock" (von Gumbel, 1868). It is, however not a synonym for a mechanism that produces the observed effects. In the literature a term "diagenetically altered bone" is often used to refer to bone material that was exposed to the unknown influence of the environment mostly in contact with soil of undefined kind.
"crystallinity"	in the literature there is a vogue concept of the state of the crystalline material that is often used for classification of the inferred physical properties of the material. There are even several empirical "crystallinity factors" that are defined based on observations of peak feature behaviour in measured diffraction pattern or spectroscopic profile. They are usually defined as specific peak amplitude (or peak area) and peak valley ratios. Although, different sources of microstructural changes result in the narrowing of peak width, and in this ways increase the empirical "crystallinity factor", this does not necessarily correlate to the real underlying physical reality of the material, this way rendering all correlations basically misleading or false. This term is misused since it does not include details about the sources of underlying effects.
"crystallite size"	dimensions of the coherently scattering (diffracting) domains
"peak decomposition"	procedure for spectral trace analysis using basis profile functions centred at positions of theoretical vibrational bands. A combination of distribution functions are summed to and fit to the measured peak profile in an optimization process.
"solvation"	IUPAC definition for any stabilizing interaction of a solute and the solvent or a similar interaction of solvent with groups of an insoluble material (i.e. the ionic groups of an ion-exchange resin). Such interactions involve electrostatic interaction, Van der Waals forces an hydrogen bond formation; Solvation is an

interaction of a solute with the solvent, which leads to stabilization of the solute species in the solution. In the solvated state an ion in a solution is surrounded or complexed by solvent molecules

"Microstructure analysis"

Microstructural analysis in the "FullProf" software with parameters used as in the following description:

- FWHM is calculated as observed (HGo) and instrumental (Hgi) Gaussian full-width-at-half-maximum and observed (HLo) and instrumental (HLi) Lorentzian (Cauchy) function.
- Integral breadths (β) is calculated using the De Keijser formula (de Keijser et al., 1982) and is in reciprocal lattice units (1/angstroms) x 1000.
- Apparent sizes is calculated according to Scherrer Formula.
- Strain = 1/2 * beta * d(hkl). The strain corresponds to 1/4 of the apparent strain defined by Stokes and Wilson (Stokes and Wilson, 1944). It is the so-called Maximum (upper limit) strain, related by a constant factor to the root-mean-square-strain (RMSS).
  In case of Gaussian distribution:
  $root - mean - square - strain = \sqrt{\frac{2}{\pi}} * strain$
- The apparent sizes/strains are calculated for each reflection using the formula:
  Apparent size = $1/(\beta_{size})$
  Max-strain (%%) = $1/2\ (\beta_{strain})$ * d(hkl)
- β_{size} :
  $FWHM^2\ H_{Gaussina\ size}{}^2 = IG/\cos^2(\vartheta)$
  $FWHM\ \ H_{Lorentzian\ size} = (\ Y + F(Sz))/\cos(\vartheta)$
  β_{strain}
  $FWHM^2\ H_{Gaussian\ strain}{}^2 = (U+[(1\text{-}z)DST]^2)\ \tan^2(\vartheta)$
  $FWHM\ \ H_{Lorentzain\ strain} = (X+ z\ DST)\ \tan(\vartheta)$
  "H" (width of the profile function) and "η" (eta-mixing parameter) are calculated from Thomson-Cox-Hastings formula (Thompson et al., 1987) and then $\beta_{pseudo\text{-}Voigt}$ is calculated:
  $$\beta_{pseudo-Voigt} = \frac{1}{2} * \frac{H}{\frac{\eta}{\pi} + \frac{(1-\eta)}{\sqrt{\frac{\pi}{ln2}}}}$$

- Parameters IG, Y,F,Sz,U,z,DST,X are scalars and represent free parameters for the refinement.
- Further notation used by "FullProf" are:
  betaG, betaL, beta:
  Gaussian, Lorentzian and total Sample Integral Breadth
  betaVo, HpVo, η:
  Integral Breadth, FWHM and η are values of the total observed pseudo-Voigt

A2 – Details of the automated Rietveld analysis Python code

The "AlgoRun" code is a wrapper around "FullProf", that can control, modify and execute refinement on one and many diffraction patters. The purpose of the code is to enable model comparison and refinement strategies execution automatically. All crystallographic structure refinements are done inside the "FullProf" software. At any refinement initial set-up of the refinement in "FullProf" is required. "AlgoRun" does not handle error messages of the main program "FullProf".

Requirements and download

At the time of writing the code requires python 2.7 and tested in an Linux operating system. The latest version of the code and the documentation can be downloaded from: https://github.com/bkocis/AlgoRun. Download a zip file or clone the repository using the "Clone or Download" button on the website. The updated documentation of the code and description is also available via the github repository.

Refinement folder organization

A few folders are need to be set up in order to enable access to data and refinement control files, as well as to define the output folder for the results. Before the refinement the folders of *"_data_files"*, *"_models"*, *"_strategies"* are needed together with the *"rules_and_settings.py"* file. Additional instrumental resolution files are also stored on this level. After the refinement are ran, folders of "*_results*" and "*_refinements*" are generated. The "*_refinements*" folder hold all the output files of "FullProf". The folder "*_results*" holds the selected parameter results (lattice constants, strain, size, etc.) in a table form indexed by the sample name.

Running the refinements

The code is executed from the command line by invoking the *"start.py"* script from the working directory containing the above described folders. The code runs in a command line, by invoking the "*start_algorRun.py*" file, which opens a dialogue in the terminal for the selection of the refinement mode. The available modes are:

[1] run refinements (assumes all files and folders are set) - returns a database
[2] evaluation using new rules (optionally generating new database)
[3] parametrisation

[4] setup folders and files for refinement

[5] scramble and make strategies from 'refinement step blocks' in '_blocks' folder

Mode [1] executes the refinement according to the predefined strategies found in the "_strategies" folder.

Mode [2] can be run on files that have been already refined, where only the results are evaluated base on a new set (modified) of rules. The rules and criteria for the acceptance of the fit results can be found in the *"rules_and_settings.py"* file.

Mode [3] is under development, and it is intended for refinements where a parameter's value is modified systematically in a range in order to map the response of the system. This functionality can be achieved also via setting the refinement strategies accordingly.

Mode [4] provides check and set-up of the folder structure (not yet operational).

Mode [5] runs a function that generated the refinement strategy files and stored them in the "_*strategies*" folder. This mode can use the folder "_blocks" that can include reusable sections (refinement steps). An example of a refinement step block would be the background parameters, structural parameter, or profile parameters.

In case that the python environment path is not set, the absolute path to the file is necessary. The full path to the script can be escaped when the code containing folder is added to the environment path of the operating system.

Working of the code

In the essence, the python script edits the text of the **.pcr* file by modifying it according to the instructions red from the strategy file. The instructions for the alterations on the **.pcr* file are read out from a file with the **.ctrl* extension. For each refinement step a specified section of the **.pcr* file text is modified. The scheme of a control file (**.ctrl* file) is shown in Table A2-1. After the **.pcr* file is modified an refinement is executed.

The code assumes that the the *.*pcr* file is set up correctly with all desired switches set. The script runs the predefined number of iterations after which it stores all the results in a sub-folders for better organization. Each refinement step can be accessed later on for inspection. Every step can be accessed the regular way, through FullProf's native "edpcr" editor as well.

Control file (.ctrl) containing the refinement step sequence*

A control file is defined as a text file with the **.ctrl* extension (Table A2-1). It

contains a sequence of steps that specifies exactly how the **.pcr* file is to be configured for every consecutive refinement run. At each step the code makes alterations to the **.pcr* file, then executes a refinement (defined number of iteration) before the next step makes the new set of alteration to the **.pcr* file. The structure of each step contains: "phase" - change a parameter in a particular phase in case of multiphase refinements, "parameter" - code word of a parameter, "value" - numerical value for the parameter, "lock" - code switch for locking of freeing a parameter for the fit. The exclamation mark is used to leave the value of the refinement of the code as is.

Table A2-1: Example of a control file. While editing, the numbering of the steps can be arbitrary, the correct order is restored by a function in the script.

Refinement control sequence	Description
#step 1 **phase**=1 **parameter**=a **value**=! **lock**=1.00 #step 2 **phase**=1 **parameter**=a,c **value**=9.81, 6.88 **lock**=0,1 ...	In the first step of the refinement for the first phase keep the unit cell parameter **a** value as it is, and change the refinement flag. In the second step the a new value of "9.81", "6.88" are assigned to **a and c,** respectively. The parameter **a** is fixed (with the code of 0.00), while the **c** parameter is let free for the refinement. The sequence of refinement steps can be as long as needed and each step can contain a arbitrary number of parameter.

Configuration file

The code can utilizes all the CPUs available on the PC by specifying the number of CPUs allocated for the refinements in the "*config.py*" file. AlgoRun executes multiple refinements simultaneously, nevertheless, the output stays organized.

In the "*config.py*" file a "switch" is defined in order to control the amount of data that is generated in the refinement and stored on the hard drive. In the case one wants to compare multiple refinement strategies on a larger number of diffraction patterns, the output folder "*_refinements*" can quickly grow to tens of GigaBites. The switch gives an option to store only the last steps of the refinement and so reducing

the amount of data stored on the hard disk. In this case the only the last step refinement is kept, previous steps are not stored and so can not be revisited.

Rules and sorting of results

For the evaluation of the results a rule based verification can be conducted over all results. In the "*rules_and_settings.py*" file rules can be defined as criteria for the validity of the fit. For example if the refinement return too high thermal factor values the refinement can be declared as non valid. One can define a range of parameter validity so that only reasonable results are summarized. This feature of the code is designed to compare multiple structural hypothesise and then sort them out by relevance.

Parametrization of a variable

It is possible to modify the **.pcr* file in a way that only relevant, selected parameters are let free while an influence parameter value is varied. In this mode a **.ctrl* file is generated with N steps, where the numerical value of a selected parameter is changed in a range (or as a function). For example the response of the refinement can be tested for a given range of lattice constants. The parametrized refinement can be run over any refinement step of the refinement.

A3 – Whole Powder Pattern Modelling (WPPM) refinements

Whole powder pattern modelling

An alternative method to examine powder diffraction patterns is through profile pattern synthesis described in literature as whole powder pattern modelling (WPPM) (Leoni et al., 2004; Scardi et al., 2010; Scardi and Leoni, 2006, 2002). According to this approach analytical functions are not used for the diffraction peak modelling, instead the code generates a full diffraction pattern model based on a direct parametrization of the microstructural factors that contribute to the diffraction peak broadening. It combines instrumental broadening and the sample's intrinsic microstructural properties. For each effect (size, dislocation, stacking faults, etc.) it generates a full pattern which is summed in Fourier space to avoid a convolution process in real space. Technically, the application requires the set of reflections of a crystallographic structure with corresponding integrated intensities. The code does not require crystallographic information about atomic positions, thermal factors, nor site occupancy parameters.

Domain shapes in WPPM

In the "PM2k" software used for the WPPM the domain shapes are given by one length parameter. In the case of a sphere, this would the radius, and in the case of a cylinder a parameter would be defined as the ratio of the equatorial and long axis. When the radius and length of the cylinder are equal, the shape resembles a sphere-like object, and at high ratio a needle-like object.

Domain size distribution in WPPM

In order to explore the applicability of the WPPM several domain shapes and size distribution settings have been tested. In the software the domain size can be modelled using distribution functions (log-normal, gamma, delta and York functions). The applicability of these distribution functions to describe domain size distributions relies on general theoretical concepts and experimental observations of particle distributions, such as those from TEM. In the case of the bone diffraction patterns evaluation, results of the log-normal (Fig.A3-1) and a delta-function type size distributions (Fig.A3-2 respectively) are summarised in the following sections.

The nanocrystallites in the bone material are associated with shapes described as a platelet with dimensions of roughly 6x10x20nm usually pictured as an

orthorhombic polyhedra, however, overall morphology of the crystallite habitus is not unanimously described as a platelet-like object (Kohn et al., 2002). A generic approach for accessing the domain shape is vie full profile fitting with the spherical crystallite model (Rogers and Daniels, 2002).

1. Spherical domain shape with log-normal particle size distribution

In first approximation the model of spherical domain shapes with a log-normal domain size distribution was tested to account for the broadening of the Bragg peaks. The fit of the diffraction pattern appears adequate, with respect to the singal-to-noise. The model with a log-normal distribution of sphere shaped domains results in a domain size distribution mean value around 10nm (Fig.A3-1). The fitted parameters are the mean value of the log-normal distribution (as an analytical function) and the squared value of it's variance. In this calculation for our case the estimated standard deviation for the fit values are high making the interpretation of the results difficult.

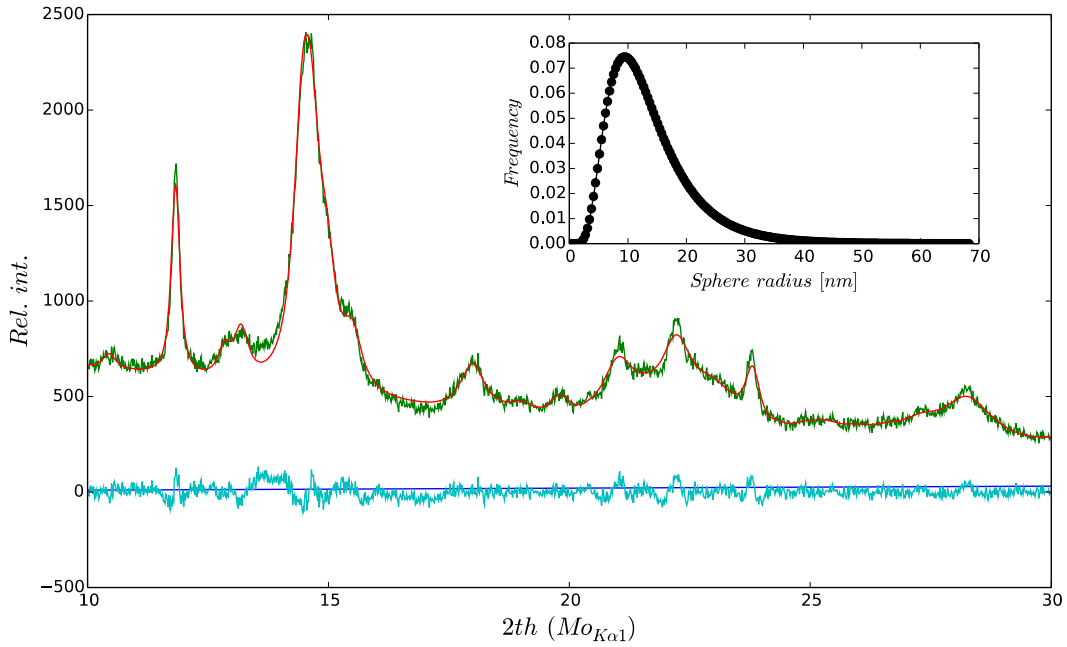

Figure A3-1: Diffraction pattern of untreated bone material sample with the WPPM model fit. The inset plot shows the calculated distribution of sphere shaped domains. The model with a log-normal distribution of sphere shaped domains results in a domain size distribution mean value around 10nm.

2. Case of delta function distribution of cylinders

Since in the WPPM software there are no disc or needle like domain shapes, the closest approximation that could model a phenomenological platelet like

crystallite could be cylinders (flat disc, or needle-like). Cylindrical domain shape was modelled with long axis along the 002 direction of the hydroxylapatite model with a delta function like domain size distribution (basically one value for the domain size). Cylindrical model in the WPPM is defined as a single length parameter domain shape with the axial length ratio as a free parameter. A model with cylindrical domain shape matches the diffraction pattern of the untreated bone material sample at a more satisfactory level (Fig.A3-2). The results are 17.4(2)nm long needles with domain diameter of 4.98(8)nm.

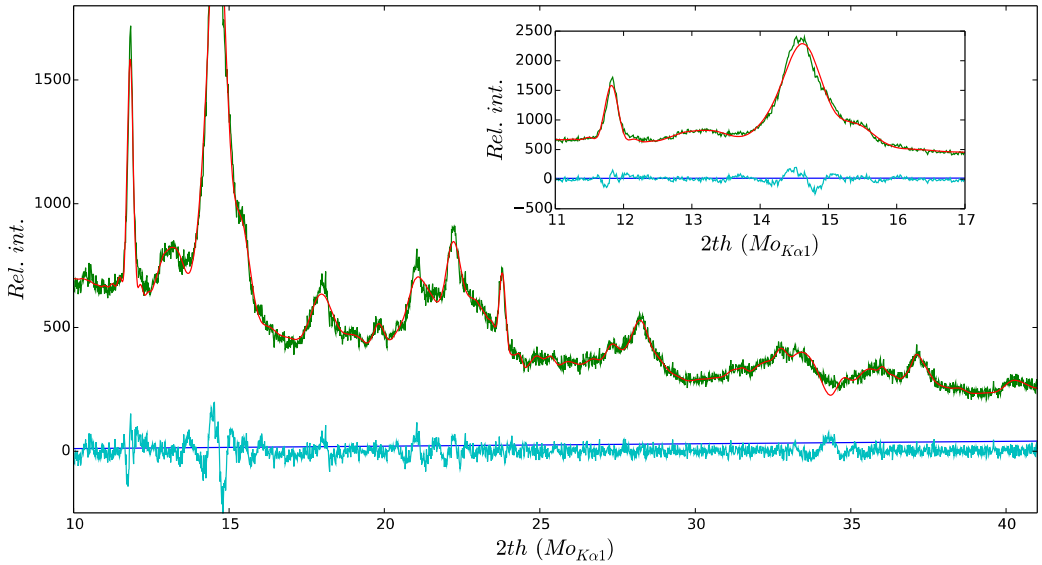

Figure A3-2: Cylindrical domain model with a Dirac delta function domain size distribution model. The inset plot shows a magnified section of the whole pattern.

Comparison of profile function refinement and WPPM methods

Bone samples annealed up to temperatures of 700°C have been evaluated with the WPPM refinement approach in order to test the methods applicability in the case of the poorly crystalline bone samples. A comparison between refinement methods using diffraction profile fitting (as implemented in "FullProf" (Rodríquez-Carvajal and Roisnel, 2004)) and the whole powder pattern modelling (as implemented in "PM2k" (Leoni et al., 2006)) was conducted on the same set of measurements. The obtained lattice parameters are listed in Table A3-1.

Table A3-1: Comparison of obtained lattice constants between peak fitting and whole powder pattern methods.

	Unit cell constant a		Unit cell constant c	
	FP*	WPPM*	FP*	WPPM*
21°C	9.441(1)	9.424	6.8843(4)	6.8841
200°C	9.4319(7)	9.423	6.8874(3)	6.8874
300°C	9.427(1)	9.4259	6.8901(5)	6.8907
400°C	9.4217(8)	9.4184	6.8903(3)	6.8879
500°C	9.4313(6)	9.4255	6.8950(3)	6.8912
600°C	9.4269(5)	9.4249	6.8906(3)	6.8910
700°C	9.4273(2)	9.4277	6.8838(1)	6.8845

* FP – full pattern decomposition using analytical pseudo-Voigt functions in FullProf;
* WPPM – Fourier transform based whole powder pattern modelling in PM2k

Conclusion

The whole powder pattern modelling (WPPM) approach with the PM2k software implementing the Fourier profile synthesis was not fully adequate for the evaluation of the nanocrystallites of the bone material. The crystalline structure of the nanoparticels of carbonated-calcium-phosphate apatite found in bone material has the tendency toward incorporating site vacancies and various degrees of carbonate incorporation. The origin of microstrain is in the case of this material of chemical origin. It was found that the options offered in the WPPM software do not cover these aspects.

For the modelling of the full diffraction pattern first a spherical domain shape was fitted. The whole pattern was successfully matched the data with the exception of the peak of the 002 reflection. In the temperature range up to 600°C the microstructure appears not to be affected by heat energy in a significant way. The spherical model fails to fit adequately the whole pattern since the 002 reflection is modelled as too broad. In the case of the samples treated at temperatures above 600°C size gain of the domains can be observed. For sample above 600°C the crystallite domain morphology resembles more an isotropic form such of a sphere.

A4 – Williamson-Hall plot in the Rietveld refinement of bone samples

According to the Williamson-Hall evaluation of the diffraction pattern the integral breadth of the peaks is plotted as a functions of the diffraction angle (momentum transfer vector). Linear regression in this space results the average apparent size from the intercept with the y-axis, and the slope gives the mean strain. The slope of the regression curve is interpreted as the magnitude of the strain present in the system. This is based on the assumption that the broadening due to size effect is reflection index independent, while the strain (maximum strain and root mean square strain) are hkl dependent (Ungár, 2001; Ungár et al., 1999). However, in the case of anisotropic broadening model the Williamson-Hall plot shows a scattered values for each reflection (all reflections shown in Fig.A4-1). The approach of using linear regression is not more applicable.

a.) b.)

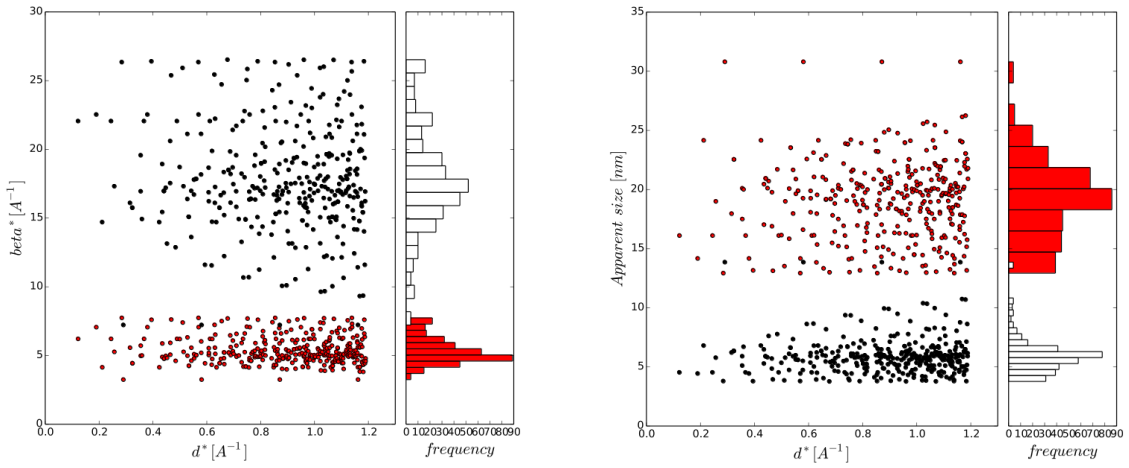

Figure A4-1: a.) Integral breadth plot - Williamson-Hall plot for two samples of different temperature treatment. The bone material that was exposed to high temperatures (in red) has narrower distribution of the integral breadths then the sample of bone material that was not annealed (in black). The shape of the integral breadth (beta) distribution is in the case of high temperature treated sample more asymmetric (red histogram on plot a); b.) Apparent size for each reflection – the sample annealed at 700°C (in red) shows apparent size in range from 15-30nm depending from reflection in the anisotropic model.

A5 – Data tables 1

Supplementary data for Chapter 4. The tables contain the XRD Rietveld refinement results and the additional data for the corresponding sample. The XRPD patterns were gathered on a General Electric Powder Diffractometer in a Bragg-Brentano set up in reflection mode. Cu_{Kapha1} radiation was used with a Ge(111) monochromator and a 1mm divergence slit. Additionally "knife-edge" slit was used directly over the sample surface at 3mm height for air-scattering reduction. In the case of bone material, this additional slit also reduces the high diffuse scattering at low angles. The data was analysed using the "Fullprof" software package (Rodríquez-Carvajal and Roisnel, 2004).

Table A5-1: Supplementary data table for Chapter 4 - Part 1 - Listing of the archaeological age of the sample, sample identifier context number, skeletal element and determined species of the sample.

Sample	**Archaeological dating**	**Context number**	**Skeletal element**	**Species**
1.106.15	850 v. Chr. bis 15 v. Chr.	Berching-Pollanten FZ 55325	Tibia/Tibiotarsus	Cervus elaphus
1.106.4	850 v. Chr. bis 15 v. Chr.	Berching-Pollanten 1984/757 Fz 55318	Mandibula	Bos taurus
1.106.9	850 v. Chr. bis 15 v. Chr.	Berching-Pollanten 1982/776 Fz 16996	Mandibula	Sus domesticus
1.114.11	850 v. Chr. bis 15 v. Chr.	Freising-Domberg, Fz. 1466 Iz. 264	Radius	Cervus elaphus
1.114.3	850 v. Chr. bis 15 v. Chr.	Freising-Domberg, Fz. 3892 Iz. 455	Mandibula	Bos taurus
1.114.7	850 v. Chr. bis 15 v. Chr.	Freising-Domberg, Fz. 1389 Iz. 9246	Mandibula	Sus domesticus
1.115.11	5600 v. Chr. bis 2200 v. Chr.	Griesstetten Kiste 11	Phalanx 1 ant.	Bos taurus
1.115.4	5600 v. Chr. bis 2200 v. Chr.	Griesstetten Kiste 5	Humerus	Sus domesticus
1.115.7	5600 v. Chr. bis 2200 v. Chr.	Griesstetten Kiste 12	Metacarpus III+IV	Cervus elaphus
1.127.1	3. Jh. v. Chr. bis 15 v. Chr.	Manching 7 aus Kiste 2	Phalanx 1 ant./post.	Cervus elaphus
1.127.12	3. Jh. v. Chr. bis 15 v. Chr.	Manching Kiste 262A	Mandibula	Sus domesticus
1.127.8	3. Jh. v. Chr. bis 15 v. Chr.	Manching Kiste 365	Mandibula	Bos taurus

1.131.1	4. Jt. v. Chr.	Pestenacker Kiste 9	Radius+Ulna (fused)	Cervus elaphus
1.131.11	4. Jt. v. Chr.	Pestenacker Kiste 8	Mandibula	Sus domesticus
1.131.9	4. Jt. v. Chr.	Pestenacker Kiste 7	Mandibula	Bos taurus
1.147.2	850 v. Chr. bis 15 v. Chr.	Wehringen Hochfeld, Fz 354	Humerus	Sus domesticus
1.147.6	850 v. Chr. bis 15 v. Chr.	Wehringen Hochfeld, Fz 360	Radius+Ulna (fused)	Bos taurus/Bos primigenius
1.147.9	850 v. Chr. bis 15 v. Chr.	Wehringen Hochfeld, Fz 360	Femur	Cervus elaphus
1.148.11	5600 v. Chr. bis 2200 v. Chr.	Schwabmunchen 1994/95, Fz. 54547	Metacarpus III+IV	Cervus elaphus
1.148.8	5600 v. Chr. bis 2200 v. Chr.	Schwabmunchen 1994/95, Fz. 54644	Mandibula	Bos taurus
1.201.1	850 v. Chr. bis 15 v. Chr.	Bergisel 2001 - 178	Mandibula	Bos taurus
1.201.7	850 v. Chr. bis 15 v. Chr.	Bergisel 2001 - 175	Tibia/Tibiotarsus	Sus domesticus
1.203.3	5600 v. Chr. bis 2200 v. Chr.	Brixlegg-Mariahilfbergl o. Nr. Neolithic fireplace	Femur	Bos taurus
1.203.5	5600 v. Chr. bis 2200 v. Chr.	Brixlegg-Mariahilfbergl o. Nr. Neolithic fireplace	Femur	Cervus elaphus
1.205.2	850 v. Chr. bis 15 v. Chr.	Fritzens-Pirchboden, G9-Schnitt C	Costa	Bos taurus
1.205.5	850 v. Chr. bis 15 v. Chr.	Fritzens-Pirchboden, SO-Eck Haus	Tibia/Tibiotarsus	Sus domesticus
1.217.3	5600 v. Chr. bis 2200 v. Chr.	Kirchbichl-Grattenbergl 18620/IIk2	Humerus	Sus domesticus
1.229.12	850 v. Chr. bis 15 v. Chr.	Mieming, LfdNr. 56/09	Metatarsus III+IV	Cervus elaphus
1.229.5	850 v. Chr. bis 15 v. Chr.	Mieming, LfdNr. 228/10	Mandibula	Bos taurus
1.229.7	850 v. Chr. bis 15 v. Chr.	Mieming, LfdNr. 349/10	Humerus	Sus domesticus
1.230.1	850 v. Chr. bis 15 v. Chr.	Pfaffenhofen-Hortenberg, Lfd.Nr.186/13	Humerus	Bos taurus
1.236.1	2200 v. Chr. bis 850 v. Chr.	Wiesing-Buchberg, Fundnr. 195/01	Mandibula	Bos taurus

1.236.6	2200 v. Chr. bis 850 v. Chr.	Wiesing-Buchberg, Fundnr. 193/01	Mandibula	Sus domesticus
1.237.1	Unknown	Ampass-Widumfeld G6/228	Mandibula	Bos taurus
1.237.11	Unknown	Ampass-Widumfeld, G6/4	Cranium with antler	Cervus elaphus
1.237.8	Unknown	Ampass-Widumfeld, G6/503	Mandibula	Sus domesticus
1.238.10	2200 v. Chr. bis 850 v. Chr.	Radfeld-Mauken Fnr Mauk D 158	Tibia/Tibiotarsus	Bos taurus
1.238.7	2200 v. Chr. bis 850 v. Chr.	Radfeld-Mauken Fnr Mauk D 143	Humerus	Sus domesticus
1.240.11	850 v. Chr. bis 15 v. Chr.	Hohe Birga Fz. Nr. 2/11	Humerus	Sus domesticus
1.240.7	850 v. Chr. bis 15 v. Chr.	Hohe Birga Fz. Nr. 10/10	Radius	Bos taurus
1.240.9	850 v. Chr. bis 15 v. Chr.	Hohe Birga Fz. Nr. 10/11	Metacarpus III+IV	Cervus elaphus
1.241.12	ca. 4500 v. Chr.- ca. 3800 v. Chr.	Thaur "Kiechlberg", 278	Metatarsus III+IV	Cervus elaphus
1.241.2	ca. 4500 v. Chr.- ca. 3800 v. Chr.	Thaur "Kiechlberg", 341	Femur	Sus domesticus
1.241.8	ca. 4500 v. Chr.- ca. 3800 v. Chr.	Thaur "Kiechlberg", 375	Metacarpus III+IV	Bos taurus
1.301.1	850 v. Chr. bis 15 v. Chr.	Brixen-Stufels "Hotel Dominik" 4540	Metatarsus III+IV	Cervus elaphus
1.301.7	850 v. Chr. bis 15 v. Chr.	Brixen-Stufels "Hotel Dominik" 4856	Mandibula	Sus domesticus
1.301.9	850 v. Chr. bis 15 v. Chr.	Brixen-Stufels "Hotel Dominik" 4403	Mandibula	Bos taurus
1.310.3	850 v. Chr. bis 15 v. Chr.	Sanzeno US 18	Mandibula	Sus domesticus
1.310.7	850 v. Chr. bis 15 v. Chr.	Sanzeno US 21	Radius	Bos taurus
1.311.4	850 v. Chr. bis 15 v. Chr.	Zambana - El Vato US 117	Tibia/Tibiotarsus	Sus domesticus
1.311.9				
1.312.2	850 v. Chr. bis 15 v. Chr.	Brixen-Stufels "Russo", n.sac. 294	Metacarpus III+IV	Bos taurus
1.312.5	850 v. Chr. bis 15 v. Chr.	Brixen-Stufels "Russo", n.sac. 257	Femur	Sus domesticus
1.314.1	850 v. Chr. bis 15 v. Chr.	Brixen-Stufels	Mandibula	Bos taurus

		"Eco-Bau", n.sac. 95		
1.314.7	850 v. Chr. bis 15 v. Chr.	Brixen-Stufels "Eco-Bau", n.sac. 154	Humerus	Cervus elaphus
4.108.2	2200 v. Chr. bis 850 v. Chr.	Eching-IKEA, Fz. 71674	Cranium with antler	Cervus elaphus
4.108.6	2200 v. Chr. bis 850 v. Chr.	Eching-IKEA, Fz. 71700	Tibia/Tibiotarsus	Bos taurus
4.108.9	2200 v. Chr. bis 850 v. Chr.	Eching-IKEA, Fz. 71957	Humerus	Sus domesticus
4.116.1	850 v. Chr. bis 15 v. Chr.	Grunwald-Parkgarage Fz.33	Mandibula	Bos taurus
4.116.8	850 v. Chr. bis 15 v. Chr.	Grunwald-Parkgarage, Fz. 331	Tibia/Tibiotarsus	Sus domesticus
4.137.1	15 v. Chr. bis 450 n. Chr.	Unterhaching-Am Rodelberg, Fz 119468	Mandibula	Bos taurus
4.137.12	15 v. Chr. bis 450 n. Chr.	Unterhaching-Am Rodelberg, Fz 119415	Radius	Cervus elaphus
4.137.14	15 v. Chr. bis 450 n. Chr.	Unterhaching-Am Rodelberg, Fz 119415	Humerus	Sus domesticus

Table A5-2: Supplementary data table for Chapter 4 - Part 2 - Listing of the average apparent size in the isotropic broadening model("avgappsz"), average apparent size in the anisotropic model ("avgappsz_aniso"), calcite weight percent as secondary phase, isotropic microstrain ("iso_str"), sizes along c-, and a-axis in the anisotropic model respectively, and the unit cell volume ("vol").

Sample	**avgappsz**	**avgappsz_aniso**	**calcite**	**iso_str**	**sz 002**	**sz 030**	**vol**
1.106.15	139.12	82.87	0.39	45.5517	666.1	84.2	530.481
1.106.4	128.64	57.63	0.49	41.6585	461.2	83.15	529.902
1.106.9	151.76	61.11	0.83	31.4657	483.51	99	531.183
1.114.11	106.96	27.5	1.64	44.2988	236.91	78.02	530.466
1.114.3	125.85	35.23	0.49	36.4129	295.47	89.44	531.092
1.114.7	157.57	55.53	0.44	29.5803	441.92	105.3	531.797
1.115.11	116.3	57.45	0.11	82.1387	463.3	74.22	527.944
1.115.4	153.39	82.21	0.25	52.7425	653.02	94.28	529.255
1.115.7	158.05	144.74	0.34	58.3596	1196.99	86.41	528.295
1.127.1	118.22	96.99	0.1	93.4162	803.21	67.61	529.196

1.127.12	115.44	33.97	0.37	53.6299	284.05	81.74	530.094
1.127.8	153.72	68.22	0.82	33.9485	538.11	98.17	531.032
1.131.1	114.05	38.12	0.15	85.0619	313.12	78.84	528.252
1.131.11	116.68	22.06	0.26	78.8558	204.81	89.8	527.059
1.131.9	121.1	32.2	0.33	69.2349	273.88	87.19	528.283
1.147.2	140.81	66.85	0.91	47.6463	531.92	89.36	530.202
1.147.6	142.05	50.52	0.93	33.1446	405.52	95.53	531.843
1.147.9	125.04	50.21	0.62	38.6025	403.57	82.81	531.288
1.148.11	131.77	46.1	0.6	60.8187	372.94	89.42	530.781
1.148.8	141.4	49.18	0.6	33.2463	396.03	95.6	530.449
1.201.1	125.36	43.55	0.38	42.5322	353.7	85.45	531.133
1.201.7	118.71	50.57	0.44	41.313	406.69	77.89	531.304
1.203.3	86.97	28.3	0.38	54.3562	236.36	61.28	531.008
1.203.5	102.26	39.75	0.4	51.0618	323.97	69	531.133
1.205.2	138.97	47.97	3.28	33.9452	386.69	94.15	531.145
1.205.5	144.56	60.49	0.89	34.7474	479.99	93.91	531.268
1.217.3	131.58	41.17	1.52	40.9327	337.81	91.28	530.831
1.229.12	102.94	28.22	0.28	48.9492	240.59	74.38	529.986
1.229.5	121.46	33.19	0.29	38.317	280.78	86.99	528.764
1.229.7	112.91	44	0.28	57.833	356.8	75.75	529.981
1.230.1	173.11	73.09	0.6	31.1425	570.35	110.59	531.344
1.236.1	134.37	61.12	0.44	38.4589	487.34	86.28	531.396
1.236.6	109.45	50.27	0.37	46.3014	406.2	71.12	530.846
1.237.1	113.79	41.58	0.38	39.0444	338.25	77.25	530.984
1.237.11	142.63	136.76	0.47	71.0743	1137.41	77.69	530.273
1.237.8	112.4	75.35	0.41	76.1065	616.92	67.37	528.932
1.238.10	90.13	26.64	0.42	56.0316	225.32	64.61	530.081
1.238.7	78.59	23.05	0.23	64.9586	196.3	56.77	530.123
1.240.11	102.27	31.87	0.35	56.9161	265.91	72.12	530.11
1.240.7	111.17	53.7	66.61	67.2494	433.74	71.43	530.393
1.240.9	115.94	57.51	57.02	60.6925	463.41	73.86	531.201
1.241.12	143.03	61.31	0.5	45.087	487.07	92.58	530.713
1.241.2	134.34	62.96	64.39	54.8577	502.42	85.77	530.497
1.241.8	131.12	42.44	1.69	53.3263	346.6	90.38	529.774
1.301.1	163.12	75.61	4.73	24.774	593.41	102.72	530.75
1.301.7	118.77	22.75	2.36	36.018	210.23	90.97	530.486
1.301.9	116.22	23.81	0.96	41.0854	216.28	88.03	530.285
1.310.3	133.14	58.31	0.83	37.5442	465.52	86.24	530.937
1.310.7	137.58	55.03	0.36	43.4112	439.32	90.57	530.114

1.311.4	120.2	49.07	0.32	61.2826	395.34	79.57	529.119
1.311.9	136.88	62.89	0.43	48.5261	501.11	87.62	530.033
1.312.2	145.96	53.5	0.63	39.3454	427.23	97.37	531.172
1.312.5	116.65	45.73	3.21	44.7228	369.84	78	530.55
1.314.1	130.59	33.59	1.13	22.1964	286.13	94.07	530.705
1.314.7	126.06	46.09	0.49	55.0451	372.38	85.03	530.531
4.108.2	143.96	75.48	0.27	65.6573	601.58	89.35	529.733
4.108.6	132.43	93.28	0.18	61.1149	761.81	77.76	528.816
4.108.9	117.62	43.94	2.29	66.1475	356.54	79.41	529.199
4.116.1	181.27	72.77	0.39	23.6275	565.94	116.54	531.665
4.116.8	134.46	53.77	0.51	49.6035	430.18	88.69	530.423
4.137.1	166.69	73.43	0.46	33.7032	574.84	105.88	531.866
4.137.12	154.81	96.14	0.5	46.3582	769.12	91.96	531.968
4.137.14	145.42	59.46	0.58	33.0238	471.69	94.85	532.297

Table A5-3: Supplementary data table for Chapter 4 - Part 3 - Additional context data of the samples; Latitude ("Nordl. Breite (Dez.-Grad)"), longitude ("Ostl. Lange (Dez.-Grad)"), hight above sea level ("Hohe (m NN)"), and strontium isotope ratio ("Sr 87/86")

Sample	**Nordl. Breite (Dez.-Grad)**	**Ostl. Lange (Dez.-Grad)**	**Hohe (m NN)**	**Sr 87/86**
1.106.15	49.1434410308	11.447722977	399.899658	0.710372
1.106.4	49.1434410308	11.447722977	399.899658	0.710335
1.106.9	49.1434410308	11.447722977	399.899658	0.71044
1.114.11	48.3985889889	11.747322036	459.446075	0.71123
1.114.3	48.3985889889	11.747322036	459.446075	0.711036
1.114.7	48.3985889889	11.747322036	459.446075	0.710071
1.115.11	49.0290289745	11.6006450169	390.86557	0.711815
1.115.4	49.0290289745	11.6006450169	390.86557	0.711453
1.115.7	49.0290289745	11.6006450169	390.86557	0.710458
1.127.1	48.715158971	11.5258119721	379.413574	0.709116
1.127.12	48.715158971	11.5258119721	379.413574	0.713489
1.127.8	48.715158971	11.5258119721	379.413574	0.709673
1.131.1	48.1459190324	10.9487730078	571.503052	0.709279
1.131.11	48.1459190324	10.9487730078	571.503052	0.709378
1.131.9	48.1459190324	10.9487730078	571.503052	0.709494
1.147.2	48.2516010012	10.8100550249	537.071899	0.708321
1.147.6	48.2516010012	10.8100550249	537.071899	0.70971
1.147.9	48.2516010012	10.8100550249	537.071899	0.709648

1.148.11	48.1658340152	10.7550509647	566.334473	0.709055
1.148.8	48.1658340152	10.7550509647	566.334473	0.70921
1.201.1	47.24694	11.4	725.3	0.711621
1.201.7	47.24694	11.4	725.3	0.711833
1.203.3	47.4312000163	11.8823330384	630.57373	0.709896
1.203.5	47.4312000163	11.8823330384	630.57373	0.713977
1.205.2	47.3106740322	11.589546036	805	0.711711
1.205.5	47.3106740322	11.589546036	805	0.710987
1.217.3	47.4953169655	12.0829500351	587.379578	0.711969
1.229.12	47.2820149641	10.9626130387	792	0.710411
1.229.5	47.2820149641	10.9626130387	792	0.710603
1.229.7	47.2820149641	10.9626130387	792	0.710389
1.230.1	47.293748036	11.0783320013	860.187317	0.714405
1.236.1	47.3954330105	11.7914329749	614.402527	0.711136
1.236.6	47.3954330105	11.7914329749	614.402527	0.711722
1.237.1	47.25903	11.45799	636	0.716648
1.237.11	47.25903	11.45799	636	0.716071
1.237.8	47.25903	11.45799	636	0.716576
1.238.10	47.43556	11.95222	1020	0.717008
1.238.7	47.43556	11.95222	1020	0.712299
1.240.11	47.240413	11.29595	855.3	0.718763
1.240.7	47.240413	11.29595	855.3	0.717661
1.240.9	47.240413	11.29595	855.3	0.715068
1.241.12	47.303528	11.447785	1026.3	0.712821
1.241.2	47.303528	11.447785	1026.3	0.709533
1.241.8	47.303528	11.447785	1026.3	0.709189
1.301.1	46.716672	11.66167	572	0.717958
1.301.7	46.716672	11.66167	572	0.716408
1.301.9	46.716672	11.66167	572	0.71625
1.310.3	46.3702059723	11.0801940411	683.026489	0.70879
1.310.7	46.3702059723	11.0801940411	683.026489	0.715912
1.311.4	46.1670210119	11.0811759811	193.750366	0.712619
1.311.9	46.1670210119	11.0811759811	193.750366	0.708511
1.312.2	46.71669	11.66044	573.6	0.717231
1.312.5	46.71669	11.66044	573.6	0.711785
1.314.1	46.718936	11.659806	553	0.71717
1.314.7	46.718936	11.659806	553	0.717101
4.108.2	48.2204370014	11.5322780237	482.697357	0.709111
4.108.6	48.2204370014	11.5322780237	482.697357	0.70943

4.108.9	48.2204370014	11.5322780237	482.697357	0.709553
4.116.1	48.037306	11.530509	599.2	0.708653
4.116.8	48.037306	11.530509	599.2	0.708673
4.137.1	48.060511	11.625689	560.9	0.708196
4.137.12	48.060511	11.625689	560.9	0.708603
4.137.14	48.060511	11.625689	560.9	0.708524

A6 – Data tables 2

Supplementary data for Chapter 6.2. The tables contain the detailed XRD Rietveld refinement results with the state and values for all used parameters. The XRPD patterns were gathered at the DESY synchrotron facility in Hamburg. The material contained in 1mm diameter capillaries was irradiated with 60keV photons of 0.20727nm wavelength. The diffraction data were collected on Perkin-Elmer 2D detectors of 0.5x0.5m dimension and pixel size of 200microns (0.2x0.2mm). The data was analysed using the "Fullprof" software package (Rodríquez-Carvajal and Roisnel, 2004).

1. Anisotropic broadening model

Table A6-1: Supplementary data table for Chapter 6.2 - Part 1 samples of hydrothermal treatment for 5-30min - Listing of the Rietveld refinement of ***anisotropic broadening model*** *with all parameters and their values.*

Parameters	**5min**	**10min**	**15min**	**30min**
Bov	0	0	0	0
Bov_std	0	0	0	0
Bragg_R_factor_ph1	4.61	4.55	4.97	5.13
Chi2	0.6301	0.6269	0.6045	0.6354
Dev_star	0.6289	0.631	0.6101	0.6469
Deviance	1570	1570	1520	1610
GoF	0.79	0.79	0.77	0.79
Npar	21	21	21	21
Re	13.1	13.3	14.1	13.8
Rf_factor_ph1	2.45	2.46	2.55	2.63
Rp	10.1	10.1	10.6	10.7
Rwp	10.4	10.5	11	11
SyCos	0	0	0	0
SyCos_err	0	0	0	0
SySin	0	0	0	0
SySin_err	0	0	0	0
U	0	0	0	0
U_std	0	0	0	0
V	0	0	0	0

V_std	0	0	0	0
W	0	0	0	0
W_std	0	0	0	0
X	0	0	0	0
X_std	0	0	0	0
Y	0	0	0	0
Y_std	0	0	0	0
Zero_shift	0	0	0	0
Zero_shift_err	0	0	0	0
ca1Biso	0.4	0.4	0.4	0.4
ca1Biso_std	0	0	0	0
ca1Mult	4	4	4	4
ca1Occ	98.1	98.1	98.1	98.1
ca1Occ_std	0	0	0	0
ca1Xpos	0.33333	0.33333	0.33333	0.33333
ca1Xpos_std	0	0	0	0
ca1Ypos	0.66667	0.66667	0.66667	0.66667
ca1Ypos_std	0	0	0	0
ca1Zpos	0.0034	0.0034	0.0034	0.0034
ca1Zpos_std	0	0	0	0
ca2Biso	0.7	0.7	0.7	0.7
ca2Biso_std	0	0	0	0
ca2Mult	6	6	6	6
ca2Occ	95.2	95.2	95.2	95.2
ca2Occ_std	0	0	0	0
ca2Xpos	0.247	0.247	0.247	0.247
ca2Xpos_std	0	0	0	0
ca2Ypos	0.993	0.993	0.993	0.993
ca2Ypos_std	0	0	0	0
ca2Zpos	0.25	0.25	0.25	0.25
ca2Zpos_std	0	0	0	0
cell_a	9.4401226	9.4391832	9.4386225	9.4387512
cell_a_err	0.0006164608	0.0006152654	0.0006326925	0.0006040714
cell_c	6.8886509	6.8891649	6.8898683	6.8900676
cell_c_err	0.0002761231	0.0002812507	0.0003236964	0.0002866183
o1-p1	1.55223	1.55208	1.55198	1.55202
o1-p1-o2	111.075	111.075	111.075	111.075
o1-p1-o2_err	0.01	0.011	0.011	0.011
o1-p1-o3	111.113	111.11	111.108	111.108

o1-p1-o3_err	0.008	0.008	0.008	0.008
o1-p1_err	0.00007	0.00007	0.00007	0.00007
o1Biso	1	1	1	1
o1Biso_std	0	0	0	0
o1Mult	6	6	6	6
o1Occ	100	100	100	100
o1Occ_std	0	0	0	0
o1Xpos	0.327	0.327	0.327	0.327
o1Xpos_std	0	0	0	0
o1Ypos	0.485	0.485	0.485	0.485
o1Ypos_std	0	0	0	0
o1Zpos	0.25	0.25	0.25	0.25
o1Zpos_std	0	0	0	0
o2-p1	1.52898	1.52883	1.52873	1.52876
o2-p1-o3	107.739	107.737	107.735	107.735
o2-p1-o3_err	0.007	0.007	0.007	0.007
o2-p1_err	0.0001	0.0001	0.0001	0.0001
o2Biso	1	1	1	1
o2Biso_std	0	0	0	0
o2Mult	6	6	6	6
o2Occ	100	100	100	100
o2Occ_std	0	0	0	0
o2Xpos	0.585	0.585	0.585	0.585
o2Xpos_std	0	0	0	0
o2Ypos	0.464	0.464	0.464	0.464
o2Ypos_std	0	0	0	0
o2Zpos	0.25	0.25	0.25	0.25
o2Zpos_std	0	0	0	0
o3-p1	1.54213	1.54215	1.54222	1.54226
o3-p1-o3	107.905	107.914	107.923	107.923
o3-p1-o3_err	0.007	0.007	0.007	0.007
o3-p1_err	0.00006	0.00006	0.00006	0.00006
o3Biso	1	1	1	1
o3Biso_std	0	0	0	0
o3Mult	12	12	12	12
o3Occ	100	100	100	100
o3Occ_std	0	0	0	0
o3Xpos	0.342	0.342	0.342	0.342
o3Xpos_std	0	0	0	0

o3Ypos	0.257	0.257	0.257	0.257
o3Ypos_std	0	0	0	0
o3Zpos	0.069	0.069	0.069	0.069
o3Zpos_std	0	0	0	0
o4-o4	0.79909	0.79915	0.79923	0.79925
o4-o4_err	0.00003	0.00003	0.00003	0.00003
o4Biso	1	1	1	1
o4Biso_std	0	0	0	0
o4Mult	4	4	4	4
o4Occ	51.9	51.9	51.9	51.9
o4Occ_std	0	0	0	0
o4Xpos	0	0	0	0
o4Xpos_std	0	0	0	0
o4Ypos	0	0	0	0
o4Ypos_std	0	0	0	0
o4Zpos	0.192	0.192	0.192	0.192
o4Zpos_std	0	0	0	0
p1-o1	1.55223	1.55208	1.55198	1.55202
p1-o1_err	0.00007	0.00007	0.00007	0.00007
p1-o2	1.52898	1.52883	1.52873	1.52876
p1-o2_err	0.0001	0.0001	0.0001	0.0001
p1-o3	1.54213	1.54215	1.54222	1.54226
p1-o3_err	0.00006	0.00006	0.00006	0.00006
p1Biso	1	1	1	1
p1Biso_std	0	0	0	0
p1Mult	6	6	6	6
p1Occ	91.8	91.8	91.8	91.8
p1Occ_std	0	0	0	0
p1Xpos	0.398	0.398	0.398	0.398
p1Xpos_std	0	0	0	0
p1Ypos	0.368	0.368	0.368	0.368
p1Ypos_std	0	0	0	0
p1Zpos	0.25	0.25	0.25	0.25
p1Zpos_std	0	0	0	0
size_002	136.43	135.99	124.17	136.5
size_011	49.08	48.93	48.52	51.79
size_030	41.74	42.31	44.39	44.7
size_110	58.88	60.68	63.27	62.32
size_112	73.28	72.44	71	75.62

strain_002	0	0	0	0
strain_011	0	0	0	0
strain_030	0	0	0	0
strain_110	0	0	0	0
strain_112	0	0	0	0
tet_vol	1.8767227814	1.8765032223	1.8764588557	1.8765893817
vol	531.643	531.577	531.568	531.598
vol_err	0.054	0.054	0.056	0.053
weight_fract_ph 1	100	100	100	100
weight_fract_ph 1_err	0.89	0.9	0.95	0.91

Table A6-2: Supplementary data table for Chapter 6.2 - Part 2 samples of hydrothermal treatment for 1-8 hours - Listing of the Rietveld refinement of ***anisotropic broadening model*** *with all parameters and their values.*

Parameters	**1h**	**2h**	**4h**	**6h**	**8h**
Bov	0	0	0	0	0
Bov_std	0	0	0	0	0
Bragg_R_factor_ph1	5.69	7.53	5.03	4.78	4.5
Chi2	0.5087	0.2086	0.8357	0.8868	0.6886
Dev_star	0.5216	0.2125	0.819	0.8653	0.6745
Deviance	1300	530	2040	2160	1680
GoF	0.71	0.45	0.91	0.94	0.83
Npar	21	21	21	21	21
Re	16.4	28.8	11.5	11	11.9
Rf_factor_ph1	2.93	3.91	3.03	2.8	2.73
Rp	11.6	15.2	9.93	9.66	9.35
Rwp	11.7	13.1	10.5	10.4	9.85
SyCos	0	0	0	0	0
SyCos_err	0	0	0	0	0
SySin	0	0	0	0	0
SySin_err	0	0	0	0	0
U	0	0	0	0	0
U_std	0	0	0	0	0
V	0	0	0	0	0
V_std	0	0	0	0	0
W	0	0	0	0	0

W_std	0	0	0	0	0
X	0	0	0	0	0
X_std	0	0	0	0	0
Y	0	0	0	0	0
Y_std	0	0	0	0	0
Zero_shift	0	0	0	0	0
Zero_shift_err	0	0	0	0	0
ca1Biso	0.4	0.4	0.4	0.4	0.4
ca1Biso_std	0	0	0	0	0
ca1Mult	4	4	4	4	4
ca1Occ	98.1	98.1	98.1	98.1	98.1
ca1Occ_std	0	0	0	0	0
ca1Xpos	0.33333	0.33333	0.33333	0.33333	0.33333
ca1Xpos_std	0	0	0	0	0
ca1Ypos	0.66667	0.66667	0.66667	0.66667	0.66667
ca1Ypos_std	0	0	0	0	0
ca1Zpos	0.0034	0.0034	0.0034	0.0034	0.0034
ca1Zpos_std	0	0	0	0	0
ca2Biso	0.7	0.7	0.7	0.7	0.7
ca2Biso_std	0	0	0	0	0
ca2Mult	6	6	6	6	6
ca2Occ	95.2	95.2	95.2	95.2	95.2
ca2Occ_std	0	0	0	0	0
ca2Xpos	0.247	0.247	0.247	0.247	0.247
ca2Xpos_std	0	0	0	0	0
ca2Ypos	0.993	0.993	0.993	0.993	0.993
ca2Ypos_std	0	0	0	0	0
ca2Zpos	0.25	0.25	0.25	0.25	0.25
ca2Zpos_std	0	0	0	0	0
cell_a	9.4337654	9.4259558	9.4290152	9.4296131	9.42945
cell_a_err	0.0006235134	0.0007757569	0.0002281596	0.0002004731	0.0002090548
cell_c	6.8892398	6.8888521	6.8895831	6.8899765	6.8894434
cell_c_err	0.0003310319	0.0004253665	0.000141535	0.0001233826	0.0001138354
o1-p1	1.55119	1.54991	1.5504	1.5505	1.55049
o1-p1-o2	111.075	111.075	111.075	111.075	111.075
o1-p1-o2_err	0.011	0.014	0.004	0.004	0.004
o1-p1-o3	111.102	111.091	111.094	111.094	111.095
o1-p1-o3_err	0.008	0.011	0.003	0.003	0.003
o1-p1_err	0.00007	0.0001	0.00002	0.00002	0.00002

o1Biso	1	1	1	1	1
o1Biso_std	0	0	0	0	0
o1Mult	6	6	6	6	6
o1Occ	100	100	100	100	100
o1Occ_std	0	0	0	0	0
o1Xpos	0.327	0.327	0.327	0.327	0.327
o1Xpos_std	0	0	0	0	0
o1Ypos	0.485	0.485	0.485	0.485	0.485
o1Ypos_std	0	0	0	0	0
o1Zpos	0.25	0.25	0.25	0.25	0.25
o1Zpos_std	0	0	0	0	0
o2-p1	1.52796	1.52669	1.52718	1.52727	1.52726
o2-p1-o3	107.73	107.721	107.723	107.724	107.724
o2-p1-o3_err	0.007	0.009	0.002	0.002	0.002
o2-p1_err	0.0001	0.00013	0.00003	0.00003	0.00003
o2Biso	1	1	1	1	1
o2Biso_std	0	0	0	0	0
o2Mult	6	6	6	6	6
o2Occ	100	100	100	100	100
o2Occ_std	0	0	0	0	0
o2Xpos	0.585	0.585	0.585	0.585	0.585
o2Xpos_std	0	0	0	0	0
o2Ypos	0.464	0.464	0.464	0.464	0.464
o2Ypos_std	0	0	0	0	0
o2Zpos	0.25	0.25	0.25	0.25	0.25
o2Zpos_std	0	0	0	0	0
o3-p1	1.54185	1.54136	1.54163	1.54172	1.541638
o3-p1-o3	107.945	107.988	107.976	107.976	107.972
o3-p1-o3_err	0.007	0.01	0.003	0.003	0.003
o3-p1_err	0.00006	0.00007	0.00002	0.00002	0.00002
o3Biso	1	1	1	1	1
o3Biso_std	0	0	0	0	0
o3Mult	12	12	12	12	12
o3Occ	100	100	100	100	100
o3Occ_std	0	0	0	0	0
o3Xpos	0.342	0.342	0.342	0.342	0.342
o3Xpos_std	0	0	0	0	0
o3Ypos	0.257	0.257	0.257	0.257	0.257
o3Ypos_std	0	0	0	0	0

o3Zpos	0.069	0.069	0.069	0.069	0.069
o3Zpos_std	0	0	0	0	0
o4-o4	0.79915	0.79911	0.799191	0.799238	0.799175
o4-o4_err	0.00003	0.00005	0.000016	0.000014	0.000013
o4Biso	1	1	1	1	1
o4Biso_std	0	0	0	0	0
o4Mult	4	4	4	4	4
o4Occ	51.9	51.9	51.9	51.9	51.9
o4Occ_std	0	0	0	0	0
o4Xpos	0	0	0	0	0
o4Xpos_std	0	0	0	0	0
o4Ypos	0	0	0	0	0
o4Ypos_std	0	0	0	0	0
o4Zpos	0.192	0.192	0.192	0.192	0.192
o4Zpos_std	0	0	0	0	0
p1-o1	1.55119	1.54991	1.5504	1.5505	1.55049
p1-o1_err	0.00007	0.0001	0.00002	0.00002	0.00002
p1-o2	1.52796	1.52669	1.52718	1.52727	1.52726
p1-o2_err	0.0001	0.00013	0.00003	0.00003	0.00003
p1-o3	1.54185	1.54136	1.54163	1.54172	1.541638
p1-o3_err	0.00006	0.00007	0.00002	0.00002	0.00002
p1Biso	1	1	1	1	1
p1Biso_std	0	0	0	0	0
p1Mult	6	6	6	6	6
p1Occ	91.8	91.8	91.8	91.8	91.8
p1Occ_std	0	0	0	0	0
p1Xpos	0.398	0.398	0.398	0.398	0.398
p1Xpos_std	0	0	0	0	0
p1Ypos	0.368	0.368	0.368	0.368	0.368
p1Ypos_std	0	0	0	0	0
p1Zpos	0.25	0.25	0.25	0.25	0.25
p1Zpos_std	0	0	0	0	0
size_002	135.95	181.47	205.17	228.36	282.83
size_011	57.77	80.1	100.86	111.27	123.53
size_030	51.49	68.43	82.88	88.18	87.32
size_110	68.52	85.05	107.2	113.54	110.26
size_112	82.11	111.19	128.59	140.48	158.01
strain_002	0	0	0	0	0
strain_011	0	0	0	0	0

strain_030	0	0	0	0	0
strain_110	0	0	0	0	0
strain_112	0	0	0	0	0
tet_vol	1.874358983	1.8711854332	1.8725579509	1.8729008214	1.8727203421
vol	530.973	530.064	530.464	530.562	530.503
vol_err	0.056	0.07	0.021	0.019	0.019
weight_fract_ph1	100	100	100	100	100
weight_fract_ph1_err	1.02	1.57	0.56	0.52	0.55

Table A6-3: Supplementary data table for Chapter 6.2 - Part 3 samples of hydrothermal treatment for 10-60 hours - Listing of the Rietveld refinement of ***anisotropic broadening model*** *with all parameters and their values.*

Parameters	**10h**	**12h**	**36h**	**60h**
Bov	0	0	0	0
Bov_std	0	0	0	0
Bragg_R_factor_ph1	4.3	4.44	4.98	6.33
Chi2	0.7922	1.075	1.082	2.661
Dev_star	0.7603	1.006	0.9744	1.61
Deviance	1890	2510	2430	4020
GoF	0.89	1	1	1.6
Npar	21	21	21	21
Re	11.5	10.7	14.5	14.7
Rf_factor_ph1	2.67	2.57	2.55	2.87
Rp	9.14	9.45	10.4	13.7
Rwp	10.3	11.1	15.1	23.9
SyCos	0	0	0	0
SyCos_err	0	0	0	0
SySin	0	0	0	0
SySin_err	0	0	0	0
U	0	0	0	0
U_std	0	0	0	0
V	0	0	0	0
V_std	0	0	0	0
W	0	0	0	0
W_std	0	0	0	0
X	0	0	0	0

X_std	0	0	0	0
Y	0	0	0	0
Y_std	0	0	0	0
Zero_shift	0	0	0	0
Zero_shift_err	0	0	0	0
ca1Biso	0.4	0.4	0.4	0.4
ca1Biso_std	0	0	0	0
ca1Mult	4	4	4	4
ca1Occ	98.1	98.1	98.1	98.1
ca1Occ_std	0	0	0	0
ca1Xpos	0.33333	0.33333	0.33333	0.33333
ca1Xpos_std	0	0	0	0
ca1Ypos	0.66667	0.66667	0.66667	0.66667
ca1Ypos_std	0	0	0	0
ca1Zpos	0.0034	0.0034	0.0034	0.0034
ca1Zpos_std	0	0	0	0
ca2Biso	0.7	0.7	0.7	0.7
ca2Biso_std	0	0	0	0
ca2Mult	6	6	6	6
ca2Occ	95.2	95.2	95.2	95.2
ca2Occ_std	0	0	0	0
ca2Xpos	0.247	0.247	0.247	0.247
ca2Xpos_std	0	0	0	0
ca2Ypos	0.993	0.993	0.993	0.993
ca2Ypos_std	0	0	0	0
ca2Zpos	0.25	0.25	0.25	0.25
ca2Zpos_std	0	0	0	0
cell_a	9.4298382	9.4257278	9.4257545	9.4241858
cell_a_err	0.0001972099	0.0001791052	0.0002091068	0.0003133179
cell_c	6.8894076	6.8881359	6.8881292	6.8900709
cell_c_err	0.0001122441	0.000108313	0.0001303365	0.0002090655
o1-p1	1.55054	1.54987	1.54988	1.54961
o1-p1-o2	111.075	111.075	111.075	111.075
o1-p1-o2_err	0.004	0.003	0.004	0.005
o1-p1-o3	111.096	111.092	111.092	111.085
o1-p1-o3_err	0.003	0.003	0.003	0.004
o1-p1_err	0.00002	0.00002	0.00002	0.00004
o1Biso	1	1	1	1
o1Biso_std	0	0	0	0

o1Mult	6	6	6	6
o1Occ	100	100	100	100
o1Occ_std	0	0	0	0
o1Xpos	0.327	0.327	0.327	0.327
o1Xpos_std	0	0	0	0
o1Ypos	0.485	0.485	0.485	0.485
o1Ypos_std	0	0	0	0
o1Zpos	0.25	0.25	0.25	0.25
o1Zpos_std	0	0	0	0
o2-p1	1.52731	1.52665	1.52666	1.5264
o2-p1-o3	107.725	107.722	107.722	107.716
o2-p1-o3_err	0.002	0.002	0.002	0.004
o2-p1_err	0.00003	0.00003	0.00003	0.00005
o2Biso	1	1	1	1
o2Biso_std	0	0	0	0
o2Mult	6	6	6	6
o2Occ	100	100	100	100
o2Occ_std	0	0	0	0
o2Xpos	0.585	0.585	0.585	0.585
o2Xpos_std	0	0	0	0
o2Ypos	0.464	0.464	0.464	0.464
o2Ypos_std	0	0	0	0
o2Zpos	0.25	0.25	0.25	0.25
o2Zpos_std	0	0	0	0
o3-p1	1.541653	1.541235	1.54124	1.54144
o3-p1-o3	107.97	107.983	107.983	108.008
o3-p1-o3_err	0.003	0.003	0.003	0.005
o3-p1_err	0.00002	0.000019	0.00002	0.00003
o3Biso	1	1	1	1
o3Biso_std	0	0	0	0
o3Mult	12	12	12	12
o3Occ	100	100	100	100
o3Occ_std	0	0	0	0
o3Xpos	0.342	0.342	0.342	0.342
o3Xpos_std	0	0	0	0
o3Ypos	0.257	0.257	0.257	0.257
o3Ypos_std	0	0	0	0
o3Zpos	0.069	0.069	0.069	0.069
o3Zpos_std	0	0	0	0

o4-o4	0.799172	0.799024	0.799023	0.79925
o4-o4_err	0.000013	0.000013	0.000015	0.00002
o4Biso	1	1	1	1
o4Biso_std	0	0	0	0
o4Mult	4	4	4	4
o4Occ	51.9	51.9	51.9	51.9
o4Occ_std	0	0	0	0
o4Xpos	0	0	0	0
o4Xpos_std	0	0	0	0
o4Ypos	0	0	0	0
o4Ypos_std	0	0	0	0
o4Zpos	0.192	0.192	0.192	0.192
o4Zpos_std	0	0	0	0
p1-o1	1.55054	1.54987	1.54988	1.54961
p1-o1_err	0.00002	0.00002	0.00002	0.00004
p1-o2	1.52731	1.52665	1.52666	1.5264
p1-o2_err	0.00003	0.00003	0.00003	0.00005
p1-o3	1.541653	1.541235	1.54124	1.54144
p1-o3_err	0.00002	0.000019	0.00002	0.00003
p1Biso	1	1	1	1
p1Biso_std	0	0	0	0
p1Mult	6	6	6	6
p1Occ	91.8	91.8	91.8	91.8
p1Occ_std	0	0	0	0
p1Xpos	0.398	0.398	0.398	0.398
p1Xpos_std	0	0	0	0
p1Ypos	0.368	0.368	0.368	0.368
p1Ypos_std	0	0	0	0
p1Zpos	0.25	0.25	0.25	0.25
p1Zpos_std	0	0	0	0
size_002	279.43	274.19	314.97	363.26
size_011	126	131.65	153.54	177.66
size_030	90	95.69	93.73	97.11
size_110	116.92	125.07	146.58	198.84
size_112	153.79	153.3	181.16	151.64
strain_002	0	0	0	0
strain_011	0	0	0	0
strain_030	0	0	0	0
strain_110	0	0	0	0

strain_112	0	0	0	0
tet_vol	1.8728386888	1.8708712348	1.870889592	1.8707919701
vol	530.543	529.983	529.986	529.959
vol_err	0.018	0.017	0.019	0.03
weight_fract_ph1	100	100	100	100
weight_fract_ph1 _err	0.54	0.51	0.65	1.05

2. Isotropic broadening model

Table A6-4: Supplementary data table for Chapter 6.2 - Part 1 samples of hydrothermal treatment for 5-30 minutes - Listing of the Rietveld refinement of ***isotropic broadening model*** *with all parameters and their values.*

Parameters	**5min**	**10min**	**15min**	**30min**
Bov	0	0	0	0
Bov_std	0	0	0	0
Bragg_R_factor _ph1	2.53	2.57	3	3.09
Chi2	0.3736	0.3841	0.3908	0.4087
Dev_star	0.3706	0.3869	0.3953	0.4194
Deviance	920	960	981	1040
GoF	0.61	0.62	0.62	0.64
Npar	31	31	31	31
Re	13.2	13.4	14.3	13.9
Rf_factor_ph1	1.04	1.05	1.22	1.29
Rp	7.26	7.37	8.07	7.97
Rwp	8.06	8.31	8.95	8.91
SyCos	0	0	0	0
SyCos_err	0	0	0	0
SySin	0	0	0	0
SySin_err	0	0	0	0
U	0	0	0	0
U_std	0	0	0	0
V	0	0	0	0
V_std	0	0	0	0
W	0	0	0	0
W_std	0	0	0	0
X	1.2557	1.27058	1.28793	1.21107

X_std	0.06512	0.06624	0.07163	0.06526
Y	0	0	0	0
Y_std	0	0	0	0
Zero_shift	0	0	0	0
Zero_shift_err	0	0	0	0
ca1Biso	0.4	0.4	0.4	0.4
ca1Biso_std	0	0	0	0
ca1Mult	4	4	4	4
ca1Occ	98.1	98.1	98.1	98.1
ca1Occ_std	0	0	0	0
ca1Xpos	0.33333	0.33333	0.33333	0.33333
ca1Xpos_std	0	0	0	0
ca1Ypos	0.66667	0.66667	0.66667	0.66667
ca1Ypos_std	0	0	0	0
ca1Zpos	0.01059	0.00978	0.00873	0.01002
ca1Zpos_std	0.0012	0.00122	0.00129	0.00123
ca2Biso	0.7	0.7	0.7	0.7
ca2Biso_std	0	0	0	0
ca2Mult	6	6	6	6
ca2Occ	95.2	95.2	95.2	95.2
ca2Occ_std	0	0	0	0
ca2Xpos	0.23998	0.23971	0.23999	0.24056
ca2Xpos_std	0.00063	0.00063	0.00067	0.00065
ca2Ypos	0.9856	0.98531	0.98491	0.98554
ca2Ypos_std	0.00087	0.00087	0.0009	0.00088
ca2Zpos	0.25	0.25	0.25	0.25
ca2Zpos_std	0	0	0	0
cell_a	9.4446564	9.443861	9.4438	9.4429216
cell_a_err	0.0008338972	0.0008348933	0.000854836	0.0008065368
cell_c	6.8862104	6.8870115	6.8876286	6.8883634
cell_c_err	0.0003557541	0.0003625858	0.0004075697	0.0003624872
o1-p1	1.54	1.54	1.52	1.52
o1-p1-o2	111.9	111.8	112	112.5
o1-p1-o2_err	1.9	1.9	2	1.9
o1-p1-o3	109.6	109.4	109.5	109.4
o1-p1-o3_err	1.5	1.5	1.6	1.5
o1-p1_err	0.02	0.02	0.02	0.02
o1Biso	1	1	1	1
o1Biso_std	0	0	0	0

o1Mult	6	6	6	6
o1Occ	100	100	100	100
o1Occ_std	0	0	0	0
o1Xpos	0.32733	0.32721	0.32646	0.32645
o1Xpos_std	0.00173	0.00174	0.00181	0.00174
o1Ypos	0.48493	0.48424	0.48233	0.48237
o1Ypos_std	0.00168	0.0017	0.00179	0.00171
o1Zpos	0.25	0.25	0.25	0.25
o1Zpos_std	0	0	0	0
o2-p1	1.575	1.57	1.563	1.577
o2-p1-o3	106.4	106.6	106.4	106.6
o2-p1-o3_err	1	1	1.1	1
o2-p1_err	0.016	0.016	0.017	0.016
o2Biso	1	1	1	1
o2Biso_std	0	0	0	0
o2Mult	6	6	6	6
o2Occ	100	100	100	100
o2Occ_std	0	0	0	0
o2Xpos	0.58708	0.58678	0.58545	0.58732
o2Xpos_std	0.0017	0.0017	0.00176	0.0017
o2Ypos	0.4597	0.4602	0.4588	0.45927
o2Ypos_std	0.00167	0.00168	0.00178	0.00171
o2Zpos	0.25	0.25	0.25	0.25
o2Zpos_std	0	0	0	0
o3-p1	1.468	1.471	1.475	1.474
o3-p1-o3	112.9	112.8	112.5	112.4
o3-p1-o3_err	0.8	0.8	0.9	0.8
o3-p1_err	0.009	0.009	0.01	0.009
o3Biso	1	1	1	1
o3Biso_std	0	0	0	0
o3Mult	12	12	12	12
o3Occ	100	100	100	100
o3Occ_std	0	0	0	0
o3Xpos	0.34242	0.34239	0.34204	0.34141
o3Xpos_std	0.00106	0.00107	0.00113	0.00108
o3Ypos	0.26713	0.26686	0.26614	0.26592
o3Ypos_std	0.00125	0.00125	0.00131	0.00126
o3Zpos	0.0723	0.07212	0.07194	0.07214
o3Zpos_std	0.00102	0.00103	0.00109	0.00104

o4-o4	0.7988	0.79889	0.79896	0.79905
o4-o4_err	0.00005	0.00005	0.00005	0.00005
o4Biso	1	1	1	1
o4Biso_std	0	0	0	0
o4Mult	4	4	4	4
o4Occ	51.9	51.9	51.9	51.9
o4Occ_std	0	0	0	0
o4Xpos	0	0	0	0
o4Xpos_std	0	0	0	0
o4Ypos	0	0	0	0
o4Ypos_std	0	0	0	0
o4Zpos	0.192	0.192	0.192	0.192
o4Zpos_std	0	0	0	0
p1-o1	1.54	1.54	1.52	1.52
p1-o1_err	0.02	0.02	0.02	0.02
p1-o2	1.575	1.57	1.563	1.577
p1-o2_err	0.016	0.016	0.017	0.016
p1-o3	1.468	1.471	1.475	1.474
p1-o3_err	0.009	0.009	0.01	0.009
p1Biso	1	1	1	1
p1Biso_std	0	0	0	0
p1Mult	6	6	6	6
p1Occ	91.8	91.8	91.8	91.8
p1Occ_std	0	0	0	0
p1Xpos	0.39458	0.39494	0.39442	0.39455
p1Xpos_std	0.00092	0.00093	0.00097	0.00094
p1Ypos	0.36622	0.36632	0.36621	0.3661
p1Ypos_std	0.00091	0.00091	0.00095	0.00092
p1Zpos	0.25	0.25	0.25	0.25
p1Zpos_std	0	0	0	0
size_002	634.82	658.11	514.97	612.63
size_011	133.6	138.6	143.19	142.89
size_030	63.2	65.59	70.96	68.67
size_110	63.2	65.59	70.96	68.67
size_112	237.63	234.59	225.24	241.27
strain_002	86.0642	87.084	88.2734	83.0057
strain_011	86.0642	87.084	88.2734	83.0057
strain_030	86.0642	87.084	88.2734	83.0057
strain_110	86.0642	87.084	88.2734	83.0056

strain_112	86.0642	87.084	88.2734	83.0057
tet_vol	1.77203962	1.7709694881	1.7569484609	1.7704326182
vol	531.965	531.938	531.978	531.936
vol_err	0.072	0.072	0.075	0.07
weight_fract_ph 1	100	100	100	100
weight_fract_ph 1_err	1.21	1.22	1.29	1.23

Table A6-5: Supplementary data table for Chapter 6.2 - Part 2 sample of hydrothermal treatment for 1-8 hours - Listing of the Rietveld refinement of ***isotropic broadening model*** *with all parameters and their values.*

Parameters	**1h**	**2h**	**4h**	**6h**	**8h**
Bov	0	0	0	0	0
Bov_std	0	0	0	0	0
Bragg_R_fact or_ph1	3.67	5.49	4.04	4.01	3.85
Chi2	0.3241	0.147	0.6163	0.6657	0.5019
Dev_star	0.3363	0.151	0.6003	0.6475	0.4922
Deviance	835	375	1490	1610	1220
GoF	0.57	0.38	0.78	0.81	0.7
Npar	31	31	31	31	31
Re	16.6	28.9	11.6	11.1	11.9
Rf_factor_ph1	1.64	2.77	2.2	2.11	2.14
Rp	8.7	12.3	8.52	8.4	7.86
Rwp	9.43	11.1	9.12	9.07	8.44
SyCos	0	0	0	0	0
SyCos_err	0	0	0	0	0
SySin	0	0	0	0	0
SySin_err	0	0	0	0	0
U	0	0	0	0	0
U_std	0	0	0	0	0
V	0	0	0	0	0
V_std	0	0	0	0	0
W	0	0	0	0	0
W_std	0	0	0	0	0
X	1.11375	0.73404	0.41107	0.34901	0.31175
X_std	0.07092	0.085	0.02427	0.02062	0.0197
Y	0	0	0	0	0

Y_std	0	0	0	0	0
Zero_shift	0	0	0	0	0
Zero_shift_err	0	0	0	0	0
ca1Biso	0.4	0.4	0.4	0.4	0.4
ca1Biso_std	0	0	0	0	0
ca1Mult	4	4	4	4	4
ca1Occ	98.1	98.1	98.1	98.1	98.1
ca1Occ_std	0	0	0	0	0
ca1Xpos	0.33333	0.33333	0.33333	0.33333	0.33333
ca1Xpos_std	0	0	0	0	0
ca1Ypos	0.66667	0.66667	0.66667	0.66667	0.66667
ca1Ypos_std	0	0	0	0	0
ca1Zpos	0.00824	0.00842	0.00415	0.00372	0.00435
ca1Zpos_std	0.00139	0.00214	0.00072	0.00066	0.00069
ca2Biso	0.7	0.7	0.7	0.7	0.7
ca2Biso_std	0	0	0	0	0
ca2Mult	6	6	6	6	6
ca2Occ	95.2	95.2	95.2	95.2	95.2
ca2Occ_std	0	0	0	0	0
ca2Xpos	0.2414	0.24263	0.24214	0.24236	0.24316
ca2Xpos_std	0.00074	0.00119	0.00038	0.00035	0.00038
ca2Ypos	0.98515	0.98478	0.98736	0.98802	0.98877
ca2Ypos_std	0.00096	0.00142	0.00049	0.00046	0.00049
ca2Zpos	0.25	0.25	0.25	0.25	0.25
ca2Zpos_std	0	0	0	0	0
cell_a	9.4373226	9.4275379	9.4296465	9.4300156	9.4298429
cell_a_err	0.0008200134	0.000941631	0.0002639539	0.0002276843	0.0002350558
cell_c	6.8873191	6.8878102	6.8894596	6.8900385	6.8894939
cell_c_err	0.000421436	0.0005256813	0.0001682409	0.0001444107	0.000133285
o1-p1	1.52	1.53	1.484	1.489	1.504
o1-p1-o2	113	114	112.9	112.9	112.8
o1-p1-o2_err	2	3	1.1	1	1.1
o1-p1-o3	109.5	110	110.4	110.5	110.8
o1-p1-o3_err	1.7	3	0.9	0.8	0.9
o1-p1_err	0.02	0.04	0.013	0.012	0.013
o1Biso	1	1	1	1	1
o1Biso_std	0	0	0	0	0
o1Mult	6	6	6	6	6
o1Occ	100	100	100	100	100

o1Occ_std	0	0	0	0	0
o1Xpos	0.32552	0.32364	0.32585	0.32544	0.3259
o1Xpos_std	0.00194	0.00299	0.00097	0.0009	0.00095
o1Ypos	0.48094	0.47942	0.47755	0.47772	0.47982
o1Ypos_std	0.00193	0.00301	0.001	0.00092	0.00098
o1Zpos	0.25	0.25	0.25	0.25	0.25
o1Zpos_std	0	0	0	0	0
o2-p1	1.589	1.59	1.528	1.526	1.524
o2-p1-o3	106.6	107	107.8	107.9	108.3
o2-p1-o3_err	1.2	1.8	0.6	0.6	0.6
o2-p1_err	0.018	0.03	0.01	0.008	0.009
o2Biso	1	1	1	1	1
o2Biso_std	0	0	0	0	0
o2Mult	6	6	6	6	6
o2Occ	100	100	100	100	100
o2Occ_std	0	0	0	0	0
o2Xpos	0.58916	0.5908	0.58235	0.58196	0.58272
o2Xpos_std	0.0019	0.00293	0.00099	0.00091	0.00098
o2Ypos	0.45968	0.45924	0.45892	0.45908	0.45964
o2Ypos_std	0.00194	0.00308	0.00101	0.00093	0.00099
o2Zpos	0.25	0.25	0.25	0.25	0.25
o2Zpos_std	0	0	0	0	0
o3-p1	1.474	1.485	1.508	1.515	1.519
o3-p1-o3	111.4	109.5	107.2	107	105.5
o3-p1-o3_err	0.9	1.5	0.5	0.5	0.5
o3-p1_err	0.01	0.016	0.006	0.005	0.006
o3Biso	1	1	1	1	1
o3Biso_std	0	0	0	0	0
o3Mult	12	12	12	12	12
o3Occ	100	100	100	100	100
o3Occ_std	0	0	0	0	0
o3Xpos	0.34142	0.3412	0.33813	0.33759	0.33697
o3Xpos_std	0.00121	0.00184	0.00062	0.00057	0.00061
o3Ypos	0.26481	0.26119	0.2572	0.25645	0.25492
o3Ypos_std	0.00142	0.00217	0.00073	0.00066	0.00071
o3Zpos	0.07321	0.07393	0.07378	0.07331	0.0745
o3Zpos_std	0.00121	0.00194	0.00066	0.00061	0.00065
o4-o4	0.79893	0.79898	0.799177	0.799245	0.799181
o4-o4_err	0.00005	0.00006	0.00002	0.000016	0.000015

o4Biso	1	1	1	1	1
o4Biso_std	0	0	0	0	0
o4Mult	4	4	4	4	4
o4Occ	51.9	51.9	51.9	51.9	51.9
o4Occ_std	0	0	0	0	0
o4Xpos	0	0	0	0	0
o4Xpos_std	0	0	0	0	0
o4Ypos	0	0	0	0	0
o4Ypos_std	0	0	0	0	0
o4Zpos	0.192	0.192	0.192	0.192	0.192
o4Zpos_std	0	0	0	0	0
p1-o1	1.52	1.53	1.484	1.489	1.504
p1-o1_err	0.02	0.04	0.013	0.012	0.013
p1-o2	1.589	1.59	1.528	1.526	1.524
p1-o2_err	0.018	0.03	0.01	0.008	0.009
p1-o3	1.474	1.485	1.508	1.515	1.519
p1-o3_err	0.01	0.016	0.006	0.005	0.006
p1Biso	1	1	1	1	1
p1Biso_std	0	0	0	0	0
p1Mult	6	6	6	6	6
p1Occ	91.8	91.8	91.8	91.8	91.8
p1Occ_std	0	0	0	0	0
p1Xpos	0.3948	0.39652	0.39532	0.39522	0.39612
p1Xpos_std	0.00105	0.00165	0.00055	0.0005	0.00054
p1Ypos	0.36629	0.36585	0.36671	0.36666	0.36754
p1Ypos_std	0.00102	0.00158	0.0005	0.00046	0.00049
p1Zpos	0.25	0.25	0.25	0.25	0.25
p1Zpos_std	0	0	0	0	0
size_002	450.25	469.1	309.06	335.02	449.09
size_011	151.03	180.26	181.41	192.3	205.32
size_030	78.02	96.64	114.79	120.3	116.48
size_110	78.02	96.64	114.79	120.3	116.48
size_112	251.08	283.05	213.9	222.94	249.44
strain_002	76.3353	50.3105	28.1742	23.921	21.367
strain_011	76.3353	50.3106	28.1742	23.921	21.367
strain_030	76.3353	50.3106	28.1742	23.921	21.367
strain_110	76.3353	50.3106	28.1742	23.921	21.367
strain_112	76.3353	50.3106	28.1742	23.921	21.367
tet_vol	1.7692398506	1.8004932313	1.753911017	1.7676437761	1.7854194982

vol	531.225	530.162	530.526	530.612	530.551
vol_err	0.073	0.085	0.025	0.021	0.021
weight_fract_ph1	100	100	100	100	100
weight_fract_ph1_err	1.37	2.05	0.68	0.63	0.67

Table A6-6: Supplementary data table for Chapter 6.2 - Part 3 sample of hydrothermal treatment for 10-60 hours - Listing of the Rietveld refinement of ***isotropic broadening model*** *with all parameters and their values.*

Parameters	**10h**	**12h**	**36h**	**60h**
Bov	0	0	0	0
Bov_std	0	0	0	0
Bragg_R_factor_ph1	3.83	3.92	5.14	6.87
Chi2	0.6334	0.8689	0.6585	2.263
Dev_star	0.5969	0.7864	0.6286	1.381
Deviance	1480	1950	1560	3380
GoF	0.79	0.93	0.81	1.5
Npar	31	31	31	31
Re	11.6	10.7	14.5	14.6
Rf_factor_ph1	2.1	2.02	2.51	3.4
Rp	7.92	8.25	9.58	13.2
Rwp	9.23	10	11.8	22
SyCos	0	0	0	0
SyCos_err	0	0	0	0
SySin	0	0	0	0
SySin_err	0	0	0	0
U	0	0	0	0
U_std	0	0	0	0
V	0	0	0	0
V_std	0	0	0	0
W	0	0	0	0
W_std	0	0	0	0
X	0.30448	0.32272	0.2371	0.20482
X_std	0.01899	0.01731	0.01896	0.03089
Y	0	0	0	0
Y_std	0	0	0	0

Zero_shift	0	0	0	0
Zero_shift_err	0	0	0	0
ca1Biso	0.4	0.4	0.4	0.4
ca1Biso_std	0	0	0	0
ca1Mult	4	4	4	4
ca1Occ	98.1	98.1	98.1	98.1
ca1Occ_std	0	0	0	0
ca1Xpos	0.33333	0.33333	0.33333	0.33333
ca1Xpos_std	0	0	0	0
ca1Ypos	0.66667	0.66667	0.66667	0.66667
ca1Ypos_std	0	0	0	0
ca1Zpos	0.00411	0.00419	0.00333	0.00396
ca1Zpos_std	0.00066	0.00061	0.00071	0.00116
ca2Biso	0.7	0.7	0.7	0.7
ca2Biso_std	0	0	0	0
ca2Mult	6	6	6	6
ca2Occ	95.2	95.2	95.2	95.2
ca2Occ_std	0	0	0	0
ca2Xpos	0.243	0.24304	0.24294	0.24185
ca2Xpos_std	0.00036	0.00033	0.00038	0.00062
ca2Ypos	0.9889	0.98942	0.99157	0.99146
ca2Ypos_std	0.00047	0.00043	0.00053	0.00082
ca2Zpos	0.25	0.25	0.25	0.25
ca2Zpos_std	0	0	0	0
cell_a	9.4301758	9.4260254	9.4257288	9.4243898
cell_a_err	0.0002219078	0.0001942587	0.0002153563	0.0003396271
cell_c	6.8895092	6.8882003	6.888535	6.8908563
cell_c_err	0.0001308112	0.0001216688	0.000142441	0.0002362554
o1-p1	1.501	1.503	1.463	1.475
o1-p1-o2	112.4	112.3	112	108.2
o1-p1-o2_err	1	0.9	1.1	1.7
o1-p1-o3	110.9	110.8	110.1	112.4
o1-p1-o3_err	0.8	0.7	0.9	1.4
o1-p1_err	0.012	0.011	0.013	0.02
o1Biso	1	1	1	1
o1Biso_std	0	0	0	0
o1Mult	6	6	6	6
o1Occ	100	100	100	100
o1Occ_std	0	0	0	0

o1Xpos	0.32578	0.32523	0.3257	0.3249
o1Xpos_std	0.00091	0.00082	0.00096	0.00155
o1Ypos	0.47947	0.47908	0.47585	0.47623
o1Ypos_std	0.00094	0.00084	0.00096	0.00149
o1Zpos	0.25	0.25	0.25	0.25
o1Zpos_std	0	0	0	0
o2-p1	1.525	1.534	1.523	1.56
o2-p1-o3	108.1	107.9	110.1	108.9
o2-p1-o3_err	0.6	0.5	0.6	0.9
o2-p1_err	0.008	0.008	0.009	0.013
o2Biso	1	1	1	1
o2Biso_std	0	0	0	0
o2Mult	6	6	6	6
o2Occ	100	100	100	100
o2Occ_std	0	0	0	0
o2Xpos	0.58251	0.58319	0.58086	0.58283
o2Xpos_std	0.00093	0.00083	0.00098	0.00138
o2Ypos	0.46058	0.46081	0.4614	0.47022
o2Ypos_std	0.00095	0.00086	0.00101	0.00159
o2Zpos	0.25	0.25	0.25	0.25
o2Zpos_std	0	0	0	0
o3-p1	1.517	1.517	1.549	1.508
o3-p1-o3	106.2	106.8	104.1	106
o3-p1-o3_err	0.5	0.4	0.5	0.9
o3-p1_err	0.005	0.005	0.006	0.009
o3Biso	1	1	1	1
o3Biso_std	0	0	0	0
o3Mult	12	12	12	12
o3Occ	100	100	100	100
o3Occ_std	0	0	0	0
o3Xpos	0.33809	0.33817	0.32983	0.3383
o3Xpos_std	0.00058	0.00053	0.0006	0.00098
o3Ypos	0.25584	0.25587	0.25028	0.25325
o3Ypos_std	0.00068	0.00061	0.0007	0.00114
o3Zpos	0.07394	0.07316	0.07267	0.07516
o3Zpos_std	0.00062	0.00057	0.00069	0.00115
o4-o4	0.799183	0.799031	0.799071	0.79934
o4-o4_err	0.000015	0.000014	0.000016	0.00002
o4Biso	1	1	1	1

o4Biso_std	0	0	0	0
o4Mult	4	4	4	4
o4Occ	51.9	51.9	51.9	51.9
o4Occ_std	0	0	0	0
o4Xpos	0	0	0	0
o4Xpos_std	0	0	0	0
o4Ypos	0	0	0	0
o4Ypos_std	0	0	0	0
o4Zpos	0.192	0.192	0.192	0.192
o4Zpos_std	0	0	0	0
p1-o1	1.501	1.503	1.463	1.475
p1-o1_err	0.012	0.011	0.013	0.02
p1-o2	1.525	1.534	1.523	1.56
p1-o2_err	0.008	0.008	0.009	0.013
p1-o3	1.517	1.517	1.549	1.508
p1-o3_err	0.005	0.005	0.006	0.009
p1Biso	1	1	1	1
p1Biso_std	0	0	0	0
p1Mult	6	6	6	6
p1Occ	91.8	91.8	91.8	91.8
p1Occ_std	0	0	0	0
p1Xpos	0.39579	0.39528	0.39435	0.39214
p1Xpos_std	0.00051	0.00046	0.00054	0.00083
p1Ypos	0.36725	0.36674	0.36671	0.36447
p1Ypos_std	0.00047	0.00042	0.00051	0.00079
p1Zpos	0.25	0.25	0.25	0.25
p1Zpos_std	0	0	0	0
size_002	432.15	439.85	424.53	480.17
size_011	210.17	225.58	242.07	275.88
size_030	122.07	133.94	150.96	172.76
size_110	122.07	133.94	150.96	172.76
size_112	238.05	244.03	256.78	191.99
strain_002	20.8689	22.1188	16.2503	14.0385
strain_011	20.8689	22.1188	16.2503	14.0385
strain_030	20.8688	22.1188	16.2503	14.0385
strain_110	20.8688	22.1188	16.2503	14.0385
strain_112	20.8689	22.1188	16.2503	14.0385
tet_vol	1.7810495686	1.7912413338	1.8008433614	1.773367828
vol	530.589	530.022	530.014	530.042

vol_err	0.02	0.018	0.02	0.033
weight_fract_ph1	100	100	100	100
weight_fract_ph1 _err	0.64	0.58	0.7	1.13

B. List of Publications

2014

Kocsis, B., Perez-Mato, J. M., Tasci, E. S., de la Flor, G. & Aroyo, M. I. (2014). A survey of the structural models proposed for PbZr1−xTixO3 using mode analysis, J. Appl. Cryst. 47, 1165-1179.

Perez-Mato, J. M., **Kocsis, B.**, Tasci, E.S., & Aroyo, M. I. (2014). Mode parameterization of structures with very low symmetry: PZT and magnetite, Acta Cryst. Section A: Foundations and Advances 70(a1):C501

2015

Gisela Grupe, Martin Grünewald, Markus Gschwind, Stefan Hölzl, **Balazs Kocsis**, Peer Kröger, Amei Lang, Markus Mauder, Christoph Mayr, George C. McGlynn, Carola Metzner-Nebelsick, Eirini Ntoutsi, Joris Peters, Matthias Renz, Simone Reuß, Wolfgang W. Schmahl, Frank Söllner, C. Sebastian Sommer, Bernd Steidl, Anita Toncala, Simon Trixl and Dominika Wycisk: Networking in Bioarchaeology: The example of the DFG Research Group FOR 1670 "Transalpine Mobility and Culture Transfer." In: Gisela Grupe, George McGlynn, Joris Peters (Hrsg.): Bioarchaeology beyond Osteology. Documenta Archaeobiologiae 12, 2015, pp 13-51.

2016

Schmahl W.W., **Kocsis B.**, Toncala A. and Grupe G.: Mineralogic Characterisation of Archaeological Bone. In: Grupe G. & McGlynn G.C. (Eds.): Isotopic Landscapes in Bioarchaeology. Berlin, Heidelberg: Springer, 2016, pp 91-110.

2017

Wolfgang W. Schmahl, **Balazs Kocsis**, Anita Toncala, Dominika Wycisk, Gisela Grupe,: The Crystalline State of Archaeological Bone Material. In: Grupe G, Grigat A, McGlynn GC (Eds): Across the Alps in Prehistory. Isotopic Mapping of the Brenner Passage by Bioarchaeology. Berlin, Heidelberg: Springer, 2017, pp 75-104

Gisela Grupe, Stefan Hölzl, **Balazs Kocsis**, Peer Kröger, Markus Mauder, Christoph Mayr, Eirini Ntoutsi, Wolfgang Schmahl, Frank Söllner, Anita Toncala and Dominika Wycisk: Isotopic Mapping and Migration Research. Based on Bioarchaeological Finds. The Interdisciplinary Project 'Transalpine Mobility and Culture Transfer'. In: Anke K. Scholz, Martin Bartelheim, Roland Hardenberg and Jörn Staecker (Eds.): ResourceCultures. Sociocultural Dynamics and the Use of Resources – Theories, Methods, Perspectives. RessourcenKulturen Band 5, Universität Tübingen 2017, pp 195-208.

2018

Greiner M, **Kocsis B**, Heining MF, Mayer K, Toncala A, Grupe G, Schmahl WW, 2018. Experimental cremation of bone: Crystallie size and lattice parameter evolution. In Endo K, Kugare T, Nagasawa H (eds): Biomineralization. From Molecular and Nanostructural Analysis to Environmental Science, Springer, Singapore, pp 21-29

2019

Greiner M, Rodriguez-Navarro A, Heining M, Mayer K, Kocsis B, Göhring A, Toncala A, Grupe G, Schmahl W, 2019. Bone incineration: An experimental study on mineral structure, colour and crystalline state, Journal of Archaeological Science: Report 25: 507-518

C. Acknowledgements

I thank to my family for patience, tolerance and support.

I thank to Prof. Dr. Jill Pasteris for the stimulating discussions during the scholar exchange program of DAAD.

I thank to Gisela Grupe for the collaboration on the "Transalpine mobility" project, as well as her colleagues at the Anthropology Department of the LMU.

I thank to colleagues and professors at the crystallography department of the Earth and Environmental Sciences Faculty in the Theresienstraße for the scientific collaboration and non-scientific discussions during lunch time.

Special acknowledgement to the thesis supervisor Prof. Dr Wolfgang Schmahl.